Measurements of Higgs boson properties in the diphoton decay channel with 36 fb^{-1} of pp collision data at $\sqrt{s}$ = 13 TeV with the ATLAS detector

The ATLAS Collaboration

Properties of the Higgs boson are measured in the two-photon final state using 36.1 fb^{-1} of proton–proton collision data recorded at $\sqrt{s}$ = 13 TeV by the ATLAS experiment at the Large Hadron Collider. Cross-section measurements for the production of a Higgs boson through gluon–gluon fusion, vector-boson fusion, and in association with a vector boson or a top-quark pair are reported. The signal strength, defined as the ratio of the observed to the expected signal yield, is measured for each of these production processes as well as inclusively. The global signal strength measurement of 0.99 ± 0.14 improves on the precision of the ATLAS measurement at $\sqrt{s}$ = 7 and 8 TeV by a factor of two. Measurements of gluon–gluon fusion and vector-boson fusion productions yield signal strengths compatible with the Standard Model prediction. Measurements of simplified template cross sections, designed to quantify the different Higgs boson production processes in specific regions of phase space, are reported. The cross section for the production of the Higgs boson decaying to two isolated photons in a fiducial region closely matching the experimental selection of the photons is measured to be 55 ± 10 fb, which is in good agreement with the Standard Model prediction of 64 ± 2 fb. Furthermore, cross sections in fiducial regions enriched in Higgs boson production in vector-boson fusion or in association with large missing transverse momentum, leptons or top-quark pairs are reported. Differential and double-differential measurements are performed for several variables related to the diphoton kinematics as well as the kinematics and multiplicity of the jets produced in association with a Higgs boson. These differential cross sections are sensitive to higher order QCD corrections and properties of the Higgs boson, such as its spin and CP quantum numbers. No significant deviations from a wide array of Standard Model predictions are observed. Finally, the strength and tensor structure of the Higgs boson interactions are investigated using an effective Lagrangian, which introduces additional CP-even and CP-odd interactions. No significant new physics contributions are observed.

Contents

1 Introduction

In July 2012, the ATLAS [1] and CMS [2] experiments announced the discovery of a Higgs boson [3, 4] using proton–proton collisions collected at center-of-mass energies $\sqrt{s}$ = 7 TeV and 8 TeV at the CERN Large Hadron Collider (LHC). Subsequent measurements of its properties were found to be consistent with those expected for the Standard Model (SM) Higgs boson [5] with a mass m_H = 125.09 ± 0.21(stat.) ± 0.11(syst.) GeV [6].

Following the modifications of the LHC to provide proton–proton collisions at a center-of-mass energy of $\sqrt{s}$ = 13 TeV, the Higgs sector can be probed more deeply: the data set collected in 2015 and 2016 allows inclusive Higgs boson measurements to be repeated with about two times better precision than to those done at $\sqrt{s}$ = 7 and 8 TeV with the Run 1 data set. The increased center-of-mass energy results in much larger cross sections for events at high partonic center-of-mass energy. This implies improved sensitivity to a variety of interesting physics processes, such as Higgs bosons produced at high transverse momentum or Higgs bosons produced in association with a top–antitop quark pair. The Higgs boson decay into two photons ($H \rightarrow \gamma\gamma$) is a particularly attractive way to study the properties of the Higgs boson and to search for deviations from the Standard Model predictions due to beyond-Standard Model (BSM) processes. Despite the small branching ratio, $(2.27 \pm 0.07) \times 10^{-3}$ for m_H = 125.09 GeV [7], a reasonably large signal yield can be obtained thanks to the high photon reconstruction and identification efficiency at the ATLAS experiment. Furthermore, due to the excellent photon energy resolution of the ATLAS calorimeter, the signal manifests itself as a narrow peak in the diphoton invariant mass ($m_{\gamma\gamma}$) spectrum on top of a smoothly falling background, and the Higgs boson signal yield can be measured using an appropriate fit to the $m_{\gamma\gamma}$ distribution of the selected events.

In this paper, the results of measurements of the Higgs boson properties in the diphoton decay channel are presented using 36.1 fb^{-1} of pp collision data collected at $\sqrt{s}$ = 13 TeV by the ATLAS detector in 2015 and 2016. All the measurements are performed under the assumption that the Higgs boson mass is 125.09 GeV, and are compared to Standard Model predictions. Three types of measurements are presented in this paper and are summarized in the remainder of this section: (i) measurements of the total Higgs boson production-mode cross sections and "signal strengths"; (ii) cross sections using the SM production modes as "templates" in simplified fiducial regions; and (iii) measurements of integrated or differential cross sections in fiducial phase-space regions closely matched to the experimental selection.

The rest of this paper is organized as follows. Section 2 provides a brief description of the ATLAS detector, and Section 3 describes the selected data set. The generation of simulated event samples is described in Section 4. Section 5 gives an overview of the event reconstruction and selection, and Section 6 explains the signal and background modeling used in the measurement. The sources of systematic uncertainties are detailed in Section 7. Section 8 describes the measurement of the total Higgs boson production-mode cross sections, signal strengths, and simplified template cross sections (STXS). Similarly, Section 9 describes the measurement of the fiducial and differential cross sections. Section 10 concludes with a brief summary of the main findings.

1.1 Higgs boson production-mode cross sections and signal strengths

In this paper, cross sections times branching ratio of the Higgs to two photons $B(H \to \gamma\gamma)$ are measured for inclusive Higgs boson production, as well as for several individual production processes: gluon–gluon fusion (ggH), vector-boson fusion (VBF), Higgs boson production in association with a vector boson (VH), and production of a Higgs boson in association with a top–antitop quark pair ($t\bar{t}H$) or a single top quark (t-channel and W-associated, respectively denoted as tHq and tHW, or in their sum as "tH"). In the SM, gluon–gluon fusion is the dominant production mechanism at the LHC, contributing to about 87% of the total cross section at $\sqrt{s}$ = 13 TeV [7]. Vector-boson fusion and associated production with either a vector boson, with a top–antitop quark pair or a bottom–antibottom quark pair correspond to 6.8%, 4.0%, 0.9%, and 0.9%, respectively, of the total Higgs boson production cross section.

The data are divided into 31 categories based on the reconstructed event properties to maximize the sensitivity to different production modes and the different regions of the simplified template cross sections, which are further described in Section 1.2. The categories are defined using the expected properties of the different production mechanisms: 10 categories aimed to measure gluon–gluon fusion properties, 4 categories to measure vector-boson fusion, 8 categories that target associated production with vector bosons with different final states, and 9 categories that target associated production with a top–antitop quark pair or a single top-quark. The definition of each category was optimized using simulated events and a full summary of the categories can be found in Section 8. In the sequence of the classification, priority is given to categories aimed at selecting signal events from processes with smaller cross sections.

In order to probe the production mechanisms independently of the $H \to \gamma\gamma$ branching ratio, ratios of the different production-mode cross sections normalized to gluon–gluon fusion are also reported, with their full experimental correlations. In addition, measurements of the signal strength μ, which is the ratio of the measured cross section to the SM prediction, are given for the different production processes as well as for the inclusive production. Finally, coupling-strength modifiers, which are scale factors of the tree-level Higgs boson couplings to the different particles or of the effective Higgs boson couplings to photons and gluons from loop-induced processes, are reported.

1.2 Simplified template cross sections

The measurements of cross sections separated by the production mode as presented in the previous section are extended to measurements in specific regions of phase space using the framework of the "simplified template cross sections" introduced in Refs. [7, 8]. These are reported as cross section times $B(H \to \gamma\gamma)$ for a Higgs boson absolute rapidity [1] $|y_H|$ less than 2.5 and with further particle-level requirements. The different production modes are separated in a theoretically motivated way using the SM modes ggH, VBF, VH and top-quark-associated production modes as "templates". The fiducial regions are defined in a "simplified" way using the measured kinematics and topology of the

---

[1] The ATLAS experiment uses a right-handed coordinate system with its origin at the nominal interaction point (IP) in the center of the detector and the z-axis along the beam pipe. The x-axis points from the IP to the center of the LHC ring, and the y-axis points upward. Cylindrical coordinates (r, ϕ) are used in the transverse plane, ϕ being the azimuthal angle around the z-axis. The pseudorapidity is defined in terms of the polar angle θ as $\eta = -\ln\tan(\theta/2)$. When dealing with massive particles, the rapidity $y = 1/2\ln[(E + p_z)/(E - p_z)]$ is used, where E is the energy and p_z is the z-component of the momentum. Angular separation is expressed in terms of $\Delta R = \sqrt{(\Delta\eta)^2 + (\Delta\phi)^2}$.

final state, defined by the Higgs boson, the hadronic jets and the vector bosons or top quarks in the event, to avoid large model-dependent extrapolations. The Higgs boson is treated as a stable final-state particle, which allows an easy combination with other decay channels. Similarly, vector bosons or top quarks are treated as stable particles, but the cases of leptonic and hadronic decays of the vector boson are distinguished.

In this paper a merged version of the so-called "stage-1" simplified template cross-section measurements are investigated. These measurements provide more information for theoretical reinterpretation compared to the signal strength measurements used in Run 1 and are defined to reduce the theoretical uncertainties typically folded into the signal strength results. In the full stage-1 proposal, template cross sections would be measured in 31 regions of phase space for $|y_H| < 2.5$, where the latter requirement reflects the experimental acceptance. The experimental categories used in this study (the same as those used for the signal strength measurements) have been optimized to provide the maximum sensitivity to such regions [7, 8].

Since the current data set is not large enough to probe all of the stage-1 cross sections with sufficiently small statistical uncertainties, regions with poor sensitivity or with large anti-correlations are merged together into ten regions: Six regions probe gluon-fusion Higgs boson production with zero, one, and two jets associated with them. Two regions probe VBF Higgs boson production and Higgs boson production associated with vector bosons that decay hadronically. A dedicated cross section is measured for Higgs boson production associated with vector bosons that decay via leptonic modes. The final cross section measures top-associated ($t\bar{t}H$ and tH) Higgs-boson production. To retain sensitivity to beyond the Standard Model Higgs boson production , the ≥ 1 jet, $p_T^H > 200$ GeV gluon–gluon fusion and $p_T^j > 200$ GeV VBF+VH regions are not merged with other regions. Here p_T^H and p_T^j denote the Higgs boson and leading jet transverse momenta, respectively, where the leading jet is the highest transverse momentum jet in a given event. However, due to their large anti-correlation, only the cross section for the summed yield of these two regions is quoted here, and thus a total of nine kinematic regions are reported. The experimental sensitivity to the difference in the yields of these two regions is expected to be small, and the corresponding result is treated as a nuisance parameter rather than a measurement.

Table 1 summarizes the ten probes merged stage-1 cross sections and details which of the full 31 stage-1 cross sections were merged (middle and last column). A detailed description of the full 31 cross section proposal can be found in Appendix A.

1.3 Fiducial integrated and differential cross sections

Fiducial integrated and differential cross sections have previously been measured at $\sqrt{s} = 8$ TeV in the $H \rightarrow \gamma\gamma$ decay channel by both the ATLAS [9] and the CMS [10] Collaborations. In this paper, fiducial cross sections are determined in a variety of phase-space regions sensitive to inclusive Higgs boson production and to explicit Higgs boson production mechanisms. The measurement of these cross sections provides an alternative way to study the properties of the Higgs boson and to search for physics beyond the Standard Model. For each fiducial region of an integrated cross-section measurement or bin of a differential distribution, the $H \rightarrow \gamma\gamma$ signal is extracted using a fit to the corresponding diphoton invariant mass spectrum. The cross sections are determined by correcting these yields for experimental inefficiencies and resolution effects, and by taking into account the integrated luminosity

Table 1: The particle-level kinematic regions of the stage-1 simplified template cross sections, along with the intermediate set of regions used for the measurements presented in this paper. All regions require $|y_H| < 2.5$. Jets are defined using the anti-k_t algorithm with radius parameter $R = 0.4$ and are required to have $p_T > 30$ GeV. The leading jet and Higgs boson transverse momenta are denoted by p_T^j and p_T^H, respectively. The transverse momentum of the Higgs boson and the leading and subleading jet is denoted as p_T^{Hjj} with the subleading jet being the second highest momentum jet in a given event. Events are considered "VBF-like" if they contain at least two jets with an invariant mass of $m_{jj} > 400$ GeV and a rapidity separation between the two jets of $|\Delta y_{jj}| > 2.8$. Events are considered "VH-like" if they contain at least two jets with an invariant mass of 60 GeV $< m_{jj} < 120$ GeV. All $qq' \to Hqq'$ VBF and VH events (with the vector boson V decaying hadronically) which are neither VBF nor VH-like are part of the "Rest" selection. For the $p_T^H > 200$ GeV gluon–gluon fusion and $p_T^j > 200$ GeV VBF + VH regions, only the sum of the corresponding cross sections is reported while the difference of the two is profiled in the fit. In total, the cross sections for nine kinematic regions are measured. The small contributions from $b\bar{b}H$ are merged with ggH. The process $gg \to ZH$ refers only to box and loop processes dominated by top and bottom quarks (see Section 4 for more details).

Process	Measurement region	Particle-level stage-1 region
ggH + $gg \to Z(\to qq)H$	0-jet	0-jet
	1-jet, $p_T^H < 60$ GeV	1-jet, $p_T^H < 60$ GeV
	1-jet, $60 \le p_T^H < 120$ GeV	1-jet, $60 \le p_T^H < 120$ GeV
	1-jet, $120 \le p_T^H < 200$ GeV	1-jet, $120 \le p_T^H < 200$ GeV
	$\ge$ 1-jet, $p_T^H > 200$ GeV	1-jet, $p_T^H > 200$ GeV
		$\ge$ 2-jet, $p_T^H > 200$ GeV
	$\ge$ 2-jet, $p_T^H < 200$ GeV or VBF-like	$\ge$ 2-jet, $p_T^H < 60$ GeV
		$\ge$ 2-jet, $60 \le p_T^H < 120$ GeV
		$\ge$ 2-jet, $120 \le p_T^H < 200$ GeV
		VBF-like, $p_T^{Hjj} < 25$ GeV
		VBF-like, $p_T^{Hjj} \ge 25$ GeV
$qq' \to Hqq'$ (VBF + VH)	$p_T^j < 200$ GeV	$p_T^j < 200$ GeV, VBF-like, $p_T^{Hjj} < 25$ GeV
		$p_T^j < 200$ GeV, VBF-like, $p_T^{Hjj} \ge 25$ GeV
		$p_T^j < 200$ GeV, VH-like
		$p_T^j < 200$ GeV, Rest
	$p_T^j > 200$ GeV	$p_T^j > 200$ GeV
VH (leptonic decays)	VH leptonic	$q\bar{q} \to ZH$, $p_T^Z < 150$ GeV
		$q\bar{q} \to ZH$, $150 < p_T^Z < 250$ GeV, 0-jet
		$q\bar{q} \to ZH$, $150 < p_T^Z < 250$ GeV, $\ge$ 1-jet
		$q\bar{q} \to ZH$, $p_T^Z > 250$ GeV
		$q\bar{q} \to WH$, $p_T^W < 150$ GeV
		$q\bar{q} \to WH$, $150 < p_T^W < 250$ GeV, 0-jet
		$q\bar{q} \to WH$, $150 < p_T^W < 250$ GeV, $\ge$ 1-jet
		$q\bar{q} \to WH$, $p_T^W > 250$ GeV
		$gg \to ZH$, $p_T^Z < 150$ GeV
		$gg \to ZH$, $p_T^Z > 150$ GeV, 0-jet
		$gg \to ZH$, $p_T^Z > 150$ GeV, $\ge$ 1-jet
Top-associated production	top	$t\bar{t}H$
		W-associated $tH(tHW)$
		t-channel $tH(tHq)$
$b\bar{b}H$	merged w/ ggH	$b\bar{b}H$

7

of the data. No attempt is made to separate individual production modes in favor of presenting fiducial regions enriched with a given production mode.

The inclusive fiducial region is defined at the particle level by two photons, not originating from the decay of a hadron, that have absolute pseudorapidity $|\eta| < 2.37$, excluding the region $1.37 < |\eta| < 1.52$,[2] with the leading (subleading) photon transverse momentum greater than 35% (25%) of $m_{\gamma\gamma}$. The two photons are required to be isolated from hadronic activity by imposing that the summed transverse momentum of charged stable particles (with a mean lifetime that satisfies $c\tau > 10$ mm) with $p_{\mathrm{T}} > 1$ GeV, within a cone of $\Delta R = 0.2$ centered on the photon direction, be less than 5% of the photon transverse momentum. This selection is applied to all the presented fiducial integrated and differential cross section results and the isolation criterion was tuned to mimic the detector level selection. One additional cross section and three cross-section limits are reported in smaller fiducial regions sensitive to specific Higgs boson production mechanisms:

- a VBF-enhanced region with two jets with large invariant mass and rapidity separation,

- a region of events containing at least one charged lepton[3],

- a region of events with large missing transverse momentum,

- and a region of events with a topology matching the presence of a top–antitop quark pair.

The fiducial cross section for different jet multiplicities are reported and compared to several predictions. Eleven fiducial differential cross sections are reported, for events belonging to the inclusive fiducial region as a function of the following observables:

- $p_{\mathrm{T}}^{\gamma\gamma}$ and $|y_{\gamma\gamma}|$, the transverse momentum and rapidity of the diphoton system,

- $p_{\mathrm{T}}^{j_1}$ and $|y_{j_1}|$, the transverse momentum and rapidity of the leading jet,

- $p_{\mathrm{T}}^{j_2}$ and $|y_{j_2}|$, the transverse momentum and rapidity of the subleading jet,

- $|\cos\theta^*|$, the cosine of the angle between the beam axis and the diphoton system in the Collins–Soper frame [11],

- $\Delta\phi_{jj}$ and $|\Delta y_{jj}|$, the difference in azimuthal angle and in rapidity between the leading and subleading jets,

- $|\Delta\phi_{\gamma\gamma,jj}|$, the difference in azimuthal angle between the dijet system formed by the leading and subleading jets and the diphoton system,

- and m_{jj}, the invariant mass of the leading and subleading jets.

Seven additional variables are reported in Appendix C. Inclusive Higgs boson production is dominated by gluon–gluon fusion, for which the transverse momentum of the Higgs boson is largely balanced by the emission of soft gluons and quarks. Measuring $p_{\mathrm{T}}^{\gamma\gamma}$ probes the perturbative QCD modeling of this production mechanism which is mildly sensitive to the bottom and charm quark Yukawa couplings of the Higgs boson [12]. The distribution at high transverse momentum is sensitive to new heavy particles coupling to the Higgs boson and to the top quark Yukawa coupling. The rapidity distribution of the Higgs boson is also sensitive to the modeling of the gluon–gluon fusion production mechanism, as

---

[2] This pseudorapidity interval corresponds to the transition region between the barrel and endcap sections of the ATLAS electromagnetic calorimeter, see Section 2.

[3] In this paper reconstructed charged leptons denote electrons and muons.

well as to the parton distribution functions (PDFs) of the colliding protons. The transverse momentum and absolute rapidity of the leading and subleading jets probe the perturbative QCD modeling and are sensitive to the relative contributions of the different Higgs production mechanisms. The angular variables $|\cos\theta^*|$ and $\Delta\phi_{jj}$ are sensitive to the spin and CP quantum numbers of the Higgs boson. The dijet rapidity separation $|\Delta y_{jj}|$, the dijet mass m_{jj} and the azimuthal difference between the dijet and diphoton system $|\Delta\phi_{\gamma\gamma,jj}|$ are sensitive to the VBF production mechanism. All fiducial differential cross sections are reported with their full statistical and experimental correlations and are compared to several predictions.

The strength and tensor structure of the Higgs boson interactions are investigated using an effective Lagrangian, which introduces additional CP-even and CP-odd interactions that can lead to deviations in the kinematic properties and event rates of the Higgs boson and of the associated jets from those in the Standard Model. This is done by a simultaneous fit to five differential cross sections, which are sensitive to the Wilson coefficients of four dimension-six CP-even or CP-odd operators of the Strongly Interacting Light Higgs formulation [13]. A similar analysis was carried out at $\sqrt{s} = 8$ TeV by the ATLAS Collaboration [14].

2 ATLAS detector

The ATLAS detector [1] covers almost the entire solid angle about the proton–proton interaction point. It consists of an inner tracking detector, electromagnetic and hadronic calorimeters, and a muon spectrometer.

Charged-particle tracks and interaction vertices are reconstructed using information from the inner detector (ID). The ID consists of a silicon pixel detector (including the insertable B-layer [15] installed before the start of Run 2), of a silicon microstrip detector, and of a transition radiation tracker (TRT). The ID is immersed in a 2 T axial magnetic field provided by a thin superconducting solenoid. The silicon detectors provide precision tracking over the pseudorapidity interval $|\eta| < 2.5$, while the TRT offers additional tracking and substantial discrimination between electrons and charged hadrons for $|\eta| < 2.0$.

The solenoid is surrounded by electromagnetic (EM) and hadronic sampling calorimeters allowing energy measurements of photons, electrons and hadronic jets and discrimination between the different particle types. The EM calorimeter is a lead/liquid-argon (LAr) sampling calorimeter. It consists of a barrel section, covering the pseudorapidity region $|\eta| < 1.475$, and of two endcap sections, covering $1.375 < |\eta| < 3.2$. The EM calorimeter is divided in three layers, longitudinally in depth, for $|\eta| < 2.5$, and in two layers for $2.5 < |\eta| < 3.2$. In the regions $|\eta| < 1.4$ and $1.5 < |\eta| < 2.4$, the first layer has a fine η segmentation to discriminate isolated photons from neutral hadrons decaying to pairs of close-by photons. It also allows, together with the information from the cluster barycenter in the second layer, where most of the energy is collected, a measurement of the shower direction without assumptions on the photon production point. In the range of $|\eta| < 1.8$ a presampler layer allows corrections to be made for energy losses upstream of the calorimeter. The hadronic calorimeter reconstructs hadronic showers using steel absorbers and scintillator tiles ($|\eta| < 1.7$), or either copper ($1.5 < |\eta| < 3.2$) or copper–tungsten ($3.1 < |\eta| < 4.9$) absorbers immersed in a LAr active medium.

A muon spectrometer surrounds the calorimeter. It comprises separate trigger ($|\eta| < 2.4$) and precision tracking chambers ($|\eta| < 2.7$) in the magnetic field provided by three large air-core toroids.

A two-level trigger system [16] was used during the $\sqrt{s}$ = 13 TeV data-taking period. Dedicated hardware implements the first-level (L1) trigger selection, using only a subset of the detector information and reducing the event rate to at most 100 kHz. Events satisfying the L1 requirements are processed by a high-level trigger executing, on a computer farm, algorithms similar to the offline reconstruction software, in order to reduce the event rate to approximately 1 kHz.

3 Data set

Events were selected using a diphoton trigger requiring the presence in the EM calorimeter of two clusters of energy depositions with transverse energy above 35 GeV and 25 GeV for the leading (highest transverse energy) and subleading (second highest transverse energy) cluster. In the high-level trigger the shape of the energy deposition of both clusters was required to be loosely consistent with that expected from an electromagnetic shower initiated by a photon. The diphoton trigger has an efficiency greater than 99% for events that satisfy the final event selection described in Section 5.

After the application of data quality requirements, the data set amounts to an integrated luminosity of 36.1 fb^{-1}, of which 3.2 fb^{-1} were collected in 2015 and 32.9 fb^{-1} were collected in 2016. The mean number of proton–proton interactions per bunch crossing is 14 in the 2015 data set and 25 in the 2016 data set.

4 Event simulation

Signal samples were generated for the main Higgs boson production modes using Monte Carlo event generators as described in the following. The mass and width of the Higgs boson were set in the simulation to m_H = 125 GeV and Γ_H = 4.07 MeV [17], respectively. The samples are normalized with the latest available theoretical calculations of the corresponding SM production cross sections, as summarized in Ref. [7] and detailed below. The normalization of all Higgs boson samples also accounts for the $H \rightarrow \gamma\gamma$ branching ratio of 0.227% calculated with HDECAY [18, 19] and PROPHECY4F [20–22].

Higgs boson production via ggH is simulated at next-to-next-to-leading-order (NNLO) accuracy in QCD using the POWHEG NNLOPS program [23], with the PDF4LHC15 PDF set [24]. The simulation achieves NNLO accuracy for arbitrary inclusive $gg \rightarrow H$ observables by reweighting the Higgs boson rapidity spectrum in Hj-MiNLO [25] to that of HNNLO [26]. The transverse momentum spectrum of the Higgs boson obtained with this sample was found to be compatible with the fixed-order HNNLO calculation [26] and the HRES2.3 calculation [27, 28] performing resummation at next-to-next-to-leading-logarithm accuracy matched to a NNLO fixed-order calculation (NNLL+NNLO). The HRES prediction includes the effects of the top and bottom quark masses up to NLO precision in QCD and uses dynamical renormalization (μ_R) and factorization (μ_F) scales, $\mu_F = \mu_R = 0.5\sqrt{m_H^2 + p_T^{H\,2}}$. The parton-level events produced by the POWHEG NNLOPS program are passed to PYTHIA8 [29] to provide parton showering, hadronization and underlying event, using the AZNLO set of parameters that are tuned to data [30]. The sample is normalized such that it reproduces the total cross section predicted by a next-to-next-to-next-to-leading-order (N^{3}LO) QCD calculation with NLO electroweak corrections applied [31–34].

Higgs boson production via VBF is generated at NLO accuracy in QCD using the Powheg-Box program [35–38] with the PDF4LHC15 PDF set. The parton-level events are passed to Pythia8 to provide parton showering, hadronization and the underlying event, using the AZNLO parameter set. The VBF sample is normalized with an approximate-NNLO QCD cross section with NLO electroweak corrections applied [39–41].

Higgs boson production via VH is generated at NLO accuracy in QCD through qq/qg-initiated production, denoted as $q\bar{q}' \to VH$, and through $gg \to ZH$ production using Powheg-Box [42] with the PDF4LHC15 PDF set. Higgs boson production through $gg \to ZH$ has two distinct sources: a contribution with two additional partons, $gg \to ZHq\bar{q}$, and a contribution without any additional partons in the final state, including box and loop processes dominated by top and bottom quarks. In the following, the $gg \to ZH$ notation refers only to this latter contribution. Pythia8 is used for parton showering, hadronization and the underlying event using the AZNLO parameter set. The samples are normalized with cross sections calculated at NNLO in QCD and NLO electroweak corrections for $q\bar{q}' \to VH$ and at NLO and next-to-leading-logarithm accuracy in QCD for $gg \to ZH$ [43–45].

Higgs boson production via $t\bar{t}H$ is generated at NLO accuracy in QCD using MG5_aMC@NLO [46] with the NNPDF3.0 PDF set [47] and interfaced to Pythia8 to provide parton showering, hadronization and the underlying event, using the A14 parameter set [48]. The $t\bar{t}H$ sample is normalized with a cross section calculation accurate to NLO in QCD with NLO electroweak corrections applied [49–52].

Higgs boson production via $b\bar{b}H$ is simulated using MG5_aMC@NLO [53] interfaced to Pythia8 with the CT10 PDF set [54], and is normalized with the cross-section calculation obtained by matching, using the *Santander* scheme, the five-flavor scheme cross section accurate to NNLO in QCD with the four-flavor scheme cross section accurate to NLO in QCD [55–57]. The sample includes the effect of interference with the gluon–gluon fusion production mechanism.

Associated production of a Higgs boson with a single top-quark and a W-boson (tHW) is generated at NLO accuracy, removing the overlap with the $t\bar{t}H$ sample through a diagram regularization technique, using MG5_aMC@NLO interfaced to Herwig++ [58–60], with the Herwig++ UEEE5 parameter set for the underlying event and the CT10 PDF set using the five-flavor scheme. Simulated Higgs boson events in association with a single top-quark, a b-quark and a light quark (tHq) are produced at LO accuracy in QCD using MG5_aMC@NLO interfaced to Pythia8 with the CT10 PDF set within the four-flavor scheme and using the A14 parameter set. The tHW and tHq samples are normalized with calculations accurate to NLO in QCD [61].

The generated Higgs boson events are passed through a Geant4 [62] simulation of the ATLAS detector [63] and reconstructed with the same analysis software used for the data.

Background events from continuum $\gamma\gamma$ production and $V\gamma\gamma$ production are simulated using the Sherpa event generator [64], with the CT10 PDF set and the Sherpa default parameter set for the underlying-event activity. The corresponding matrix elements for $\gamma\gamma$ and $V\gamma\gamma$ are calculated at leading order (LO) in the strong coupling constant α_S with the real emission of up to three or two additional partons, respectively, and are merged with the Sherpa parton shower [65] using the Meps@lo prescription [66].

The very large sample size required for the modeling of the $\gamma\gamma$ background processes is obtained through a fast parametric simulation of the ATLAS detector response [67]. For $V\gamma\gamma$ events the same full detector simulation as for the signal samples is used.

Table 2: Summary of the event generators and PDF sets used to model the signal and the main background processes. The SM cross sections σ for the Higgs production processes with m_H = 125.09 GeV are also given separately for $\sqrt{s}$ = 13 TeV, together with the orders of the calculations corresponding to the quoted cross sections, which are used to normalize the samples, after multiplication by the Higgs boson branching ratio to diphotons, 0.227%. The following versions were used: Pythia8 version 8.212 (processes) and 8.186 (pile-up overlay); Herwig++ version 2.7.1; Powheg-Box version 2; MG5_aMC@NLO version 2.4.3; Sherpa version 2.2.1

Process	Generator	Showering	PDF set	σ [pb] $\sqrt{s}$ = 13 TeV	Order of calculation of σ
ggH	Powheg NNLOPS	Pythia8	PDF4LHC15	48.52	N^{3}LO(QCD)+NLO(EW)
VBF	Powheg-Box	Pythia8	PDF4LHC15	3.78	NNLO(QCD)+NLO(EW)
WH	Powheg-Box	Pythia8	PDF4LHC15	1.37	NNLO(QCD)+NLO(EW)
$q\bar{q}' \rightarrow ZH$	Powheg-Box	Pythia8	PDF4LHC15	0.76	NNLO(QCD)+NLO(EW)
$gg \rightarrow ZH$	Powheg-Box	Pythia8	PDF4LHC15	0.12	NLO+NLL(QCD)
$t\bar{t}H$	MG5_aMC@NLO	Pythia8	NNPDF3.0	0.51	NLO(QCD)+NLO(EW)
$b\bar{b}H$	MG5_aMC@NLO	Pythia8	CT10	0.49	5FS(NNLO)+4FS(NLO)
t-channel tH	MG5_aMC@NLO	Pythia8	CT10	0.07	4FS(LO)
W-associated tH	MG5_aMC@NLO	Herwig++	CT10	0.02	5FS(NLO)
$\gamma\gamma$	Sherpa	Sherpa	CT10		
$V\gamma\gamma$	Sherpa	Sherpa	CT10		

Additional proton–proton interactions (pileup) are included in the simulation for all generated events such that the average number of interactions per bunch crossing reproduces that observed in the data. The inelastic proton–proton collisions were produced using Pythia8 with the A2 parameter set [68] that are tuned to data and the MSTW2008lo PDF set [69]. A summary of the used signal and background samples is shown in Table 2.

5 Event reconstruction and selection

5.1 Photon reconstruction and identification

The reconstruction of photon candidates is seeded by energy clusters in the electromagnetic calorimeter with a size of $\Delta\eta \times \Delta\phi$ = 0.075×0.125, with transverse energy E_T greater than 2.5 GeV [70]. The reconstruction is designed to separate electron from photon candidates, and to classify the latter as *unconverted* or *converted* photon candidates. Converted photon candidates are associated with the conversion of photons into electron–positron pairs in the material upstream the electromagnetic calorimeter. Conversion vertex candidates are reconstructed from either two tracks consistent with originating from a photon conversion, or one track that does not have any hits in the innermost pixel layer. These tracks are required to induce transition radiation signals in the TRT consistent with the electron hypothesis, in order to suppress backgrounds from non-electron tracks. Clusters without any matching track or conversion vertex are classified as unconverted photon candidates, while clusters with a matching conversion vertex are classified as converted photon candidates. In the simulation, the average reconstruction efficiency for photons with generated E_T above 20 GeV and generated pseudorapidity $|\eta| < 2.37$ is 98%.

The energy from unconverted and converted photon candidates is measured from an electromagnetic cluster of size $\Delta\eta \times \Delta\phi$ = 0.075×0.175 in the barrel region of the calorimeter, and $\Delta\eta \times \Delta\phi$ = 0.125×0.125 in the calorimeter endcaps. The cluster size is chosen sufficiently large to optimize the collection of energy of the particles produced in the photon conversion. The cluster electromagnetic energy is corrected in four steps to obtain the calibrated energy of the photon candidate, using a combination of simulation-based and data-driven correction factors [71]. The simulation-based calibration procedure was re-optimized for the 13 TeV data. Its performance is found to be similar with that of Run 1 [71] in the full pseudorapidity range, and is improved in the barrel–endcap transition region, due to the use of information from additional scintillation detectors in this region [72]. The uniformity corrections and the intercalibration of the longitudinal calorimeter layers are unchanged compared to Run 1 [71], and the data-driven calibration factors used to set the absolute energy scale are determined from $Z \to e^+e^-$ events in the full 2015 and 2016 data set. The energy response resolution is corrected in the simulation to match the resolution observed in data. This correction is derived simultaneously with the energy calibration factors using $Z \to e^+e^-$ events by adjusting the electron energy resolution such that the width of the reconstructed Z boson peak in the simulation matches the width observed in data [72].

Photon candidates are required to satisfy a set of identification criteria to reduce the contamination from the background, primarily associated with neutral hadrons in jets decaying into photon pairs, based on the lateral and longitudinal shape of the electromagnetic shower in the calorimeter [73]. Photon candidates are required to deposit only a small fraction of their energy in the hadronic calorimeter, and to have a lateral shower shape consistent with that expected from a single electromagnetic shower. Two working points are used: a *loose* criterion, primarily used for triggering and preselection purposes, and a *tight* criterion. The tight selection requirements are tuned separately for unconverted and converted photon candidates. Corrections are applied to the electromagnetic shower shape variables of simulated photons, to account for small differences observed between data and simulation. The variation of the photon identification efficiency associated with the different reconstruction of converted photons in the 2015 and 2016 data sets, due to the different TRT gas composition, has been studied with simulated samples and shown to be small. The efficiency of the tight identification criteria ranges from 84% to 94% (87% to 98%) for unconverted (converted) photons with transverse energy between 25 GeV and 200 GeV.

To reject the hadronic jet background, photon candidates are required to be isolated from any other activity in the calorimeter and the tracking detectors. The calorimeter isolation is computed as the sum of the transverse energies of positive-energy topological clusters [74] in the calorimeter within a cone of ΔR = 0.2 centered around the photon candidate. The transverse energy of the photon candidate is removed. The contributions of the underlying event and pileup are subtracted according to the method suggested in Ref. [75]. Candidates with a calorimeter isolation larger than 6.5% of the photon transverse energy are rejected. The track isolation is computed as the scalar sum of the transverse momenta of all tracks in a cone of ΔR = 0.2 with p_T > 1 GeV which satisfy some loose track-quality criteria and originate from the diphoton primary vertex, i.e. the most likely production vertex of the diphoton pair (see Section 5.2). For converted photon candidates, the tracks associated with the conversion are removed. Candidates with a track isolation larger than 5% of the photon transverse energy are rejected.

5.2 Event selection and selection of the diphoton primary vertex

Events are preselected by requiring at least two photon candidates with $E_T > 25$ GeV and $|\eta| <$ 2.37 (excluding the transition region between the barrel and endcap calorimeters of $1.37 < |\eta| <$ 1.52) that fulfill the loose photon identification criteria [70]. The two photon candidates with the highest E_T are chosen as the diphoton candidate, and used to identify the *diphoton primary vertex* among all reconstructed vertices, using a neural-network algorithm based on track and primary vertex information, as well as the directions of the two photons measured in the calorimeter and inner detector [76]. The neural-network algorithm selects a diphoton vertex within 0.3 mm of the true $H \rightarrow \gamma\gamma$ production vertex in 79% of simulated gluon–gluon fusion events. For the other Higgs production modes this fraction ranges from 84% to 97%, increasing with jet activity or the presence of charged leptons. The performance of the diphoton primary vertex neural-network algorithm is validated using $Z \rightarrow e^+e^-$ events in data and simulation, by ignoring the tracks associated with the electron candidates and treating them as photon candidates. Sufficient agreement between the data and the simulation is found. The diphoton primary vertex is used to redefine the direction of the photon candidates, resulting in an improved diphoton invariant mass resolution. The invariant mass of the two photons is given by $m_{\gamma\gamma} = \sqrt{2E_1E_2(1 - \cos\alpha)}$, where E_1 and E_2 are the energies of the leading and subleading photons and α is the opening angle of the two photons with respect to the selected production vertex.

Following the identification of the diphoton primary vertex, the leading and subleading photon candidates in the diphoton candidate are respectively required to have $E_T/m_{\gamma\gamma} > 0.35$ and 0.25, and to both satisfy the tight identification criteria as well as the calorimeter and track isolation requirements. Figure 1 compares the simulated per-event efficiency of the track- and calorimeter-based isolation requirement as a function of the number of primary vertex candidates with the per-event efficiency of the Run 1 algorithm described in Ref. [76], by using a MC sample of Higgs bosons produced by gluon-gluon fusion and decaying into two photons. The re-optimization of the thresholds applied to the transverse energy sum of the calorimeter energy deposits and to the transverse momentum scalar sum of the tracks in the isolation cone, as well as the reduction of the size of the isolation cone for the calorimeter-based isolation, greatly reduces the degradation of the efficiency as the number of reconstructed primary vertices increases in comparison to the Run 1 algorithm.

In total 332030 events are selected with diphoton candidates with invariant mass $m_{\gamma\gamma}$ between 105 GeV and 160 GeV. The predicted signal efficiency, assuming the SM and including the acceptance of the kinematic selection, is 42% (with the acceptance of the kinematic selection being 52%).

5.3 Reconstruction and selection of hadronic jets, *b*-jets, leptons and missing transverse momentum

Jets are reconstructed using the anti-k_t algorithm [77] with a radius parameter of 0.4 via the FASTJET package [78, 79]. The inputs to the algorithm are three-dimensional topological clusters of energy deposits in the calorimeter cells [74]. Jets are corrected on an event-by-event basis for energy deposits originating from pileup [80], then calibrated using a combination of simulation-based and data-driven correction factors, which correct for different responses to electromagnetic and hadronic showers of the calorimeter and inactive regions of the calorimeter [81, 82]. Jets are required to have $p_T > 25$ GeV for $|\eta| < 2.4$. The jet selection is tightened to $p_T > 30$ GeV within $|y| < 4.4$ for most event reconstruction categories and the measurement of fiducial integrated and differential cross sections (with exceptions
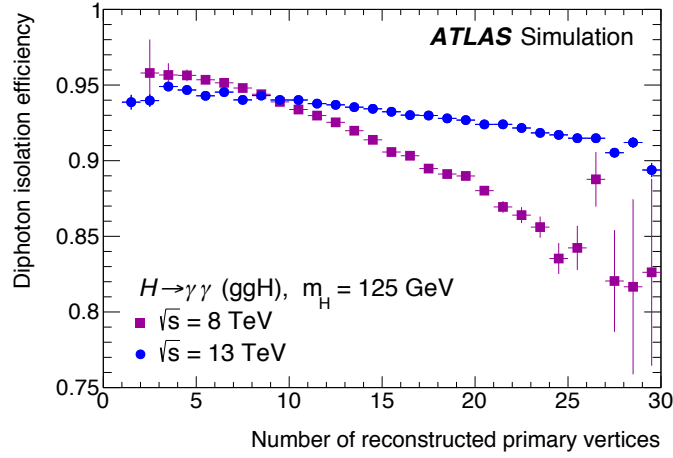
Figure 1: Efficiency for both photons to fulfill the isolation requirement as a function of the number of primary vertex candidates in each event, determined with a sample of simulated Higgs bosons with m_H = 125 GeV, produced in gluon–gluon fusion and decaying into two photons. Events are required to satisfy the kinematic selection described in Section 5.2 for the 8 TeV (violet squares) and 13 TeV (blue circles) simulated sample. The error bars show the statistical uncertainty of the generated samples. The Run 2 (Run 1) isolation requirement is based on the transverse energy deposited in the calorimeter in a ΔR = 0.2 (ΔR = 0.4) cone around the photon candidates. Both the Run 1 and Run 2 algorithms also use tracking information in a ΔR = 0.2 cone around the photon candidates.

noted in Sections 8.1 and 9.3). Jets that do not originate from the diphoton primary vertex are rejected, for $|\eta|$ < 2.4, using the jet vertex tagging algorithm (JVT) [83], which combines tracking information into a multivariate likelihood. For jets with p_T < 60 GeV and $|\eta|$ < 2.4 a *medium* working point is used, with an efficiency greater than 92% for non-pileup jets with p_T > 30 GeV. The efficiency of the JVT algorithm is corrected in the simulation to match that observed in the data. Jets are discarded if they are within ΔR = 0.4 of an isolated photon candidate, or within ΔR = 0.2 of an isolated electron candidate.

Jets consistent with the decay of a *b*-hadron are identified using a multivariate discriminant, having as input information from track impact parameters and secondary vertices [84, 85]. The chosen identification criterion has an efficiency of 70% for identifying jets originating from a *b*-quark. The efficiency is determined using a $t\bar{t}$ control region, with rejection factors of about 12 and 380 for jets originating from *c*-quarks and light quarks, respectively. Data-driven correction factors are applied to the simulation such that the *b*-tagging efficiencies of jets originating from *b*-quarks, *c*-quarks and light quarks are consistent with the ones observed in the data.

The reconstruction and calibration of electron candidates proceeds similarly as for photon candidates. Electromagnetic calorimeter clusters with a matching track in the inner detector are reconstructed as electron candidates and calibrated using dedicated corrections from the simulation and from data control samples. Electron candidates are required to have p_T > 10 GeV and $|\eta|$ < 2.47, excluding the region 1.37 < $|\eta|$ < 1.52. Electrons must satisfy *medium* identification criteria [86] using a likelihood-based discriminant.

Muon candidates are primarily built from tracks reconstructed in the inner detector and the muon spectrometer, but are complemented by candidates reconstructed only in the muon spectrometer that

15

are compatible with originating from the interaction point [87]. Muon candidates are required to have $p_T > 10$ GeV and $|\eta| < 2.7$, and satisfy *medium* identification criteria based on the number of hits in the silicon detectors, in the TRT and in the muon spectrometer. For the measurements of fiducial cross sections the electron and muon selections are tightened to $p_T > 15$ GeV.

Lepton candidates are discarded if they are within $\Delta R = 0.4$ of an isolated photon candidate or a jet. Isolation requirements are applied to all lepton candidates. Electron candidates are required to satisfy loose criteria for the calorimeter and track isolation, aimed at a combined efficiency of 99% independently of the candidate transverse momentum. Muon candidates are similarly required to satisfy loose criteria for the calorimeter and track isolation, in this case depending on the candidate transverse momentum, and aimed at a combined efficiency ranging from 95–97% at $p_T = 10–60$ GeV to 99% for $p_T > 60$ GeV.

Tracks associated with both the electron and muon candidates are required to be consistent with originating from the diphoton primary vertex by requiring their longitudinal impact parameter z_0 to satisfy $|z_0 \sin\theta| < 0.5$ mm and their unsigned transverse impact parameter $|d_0|$ relative to the beam axis to be respectively smaller than five or three times its uncertainty.

The lepton efficiency as well as energy/momentum scale and resolution are determined using the decays of Z bosons and J/ψ mesons in the full 2015 and 2016 data set using the methods described in Refs. [86, 87]. Lepton efficiency correction factors are applied to the simulation to improve the agreement with the data.

The magnitude of the missing transverse momentum E_T^{miss} is measured from the negative vectorial sum of the transverse momenta of all photon, electron and muon candidates and of all hadronic jets after accounting for overlaps between jets, photons, electrons, and muons, as well as an estimate of soft contributions based on tracks originating from the diphoton vertex which satisfy a set of quality criteria. A full description of this algorithm can be found in Refs. [88, 89]. The E_T^{miss} significance is defined as $E_T^{\text{miss}}/\sqrt{\sum E_T}$, where $\sum E_T$ is the sum of the transverse energies of all particles and jets used in the estimation of the missing transverse momentum in units of GeV.

6 Signal and background modeling of diphoton mass spectrum

The Higgs boson signal yield is measured through an unbinned maximum-likelihood fit to the diphoton invariant mass spectrum in the range $105\,\text{GeV} < m_{\gamma\gamma} < 160\,\text{GeV}$ for each event reconstruction category, fiducial region, or each bin of a fiducial differential cross section, as further discussed in Sections 8 and 9. The mass range is chosen to be large enough to allow a reliable determination of the background from the data, and at the same time small enough to avoid large uncertainties from the choice of the background parameterization. The signal and background shapes are modeled as described below, and the background model parameters are freely floated in the fit to the $m_{\gamma\gamma}$ spectra.

6.1 Signal model

The Higgs boson signal manifests itself as a narrow peak in the $m_{\gamma\gamma}$ spectrum. The signal distribution is empirically modeled as a double-sided Crystal Ball function, consisting of a Gaussian central part and power-law tails on both sides. The Gaussian core of the Crystal Ball function is parameterized

by the peak position ($m_H + \Delta\mu_{\rm CB}$) and the width ($\sigma_{\rm CB}$). The non-Gaussian contributions to the mass resolution arise mostly from converted photons $\gamma \to e^+e^-$ with at least one electron losing a significant fraction of its energy through bremsstrahlung in the inner detector material. The parametric form for a given reconstructed category or bin i of a fiducial cross section measurement, for a Higgs boson mass m_H, can be written as:

$$f_i^{\rm sig}(m_{\gamma\gamma}; \Delta\mu_{{\rm CB},i}, \sigma_{{\rm CB},i}, \alpha_{{\rm CB},i}^{\pm}, n_{{\rm CB},i}^{\pm}) = \mathcal{N}_c \begin{cases} e^{-t^2/2} & -\alpha_{{\rm CB},i}^{-} \le t \le \alpha_{{\rm CB},i}^{+} \\ \left(\frac{n_{{\rm CB},i}^{-}}{|\alpha_{{\rm CB},i}^{-}|}\right)^{n_{{\rm CB},i}^{-}} e^{-|\alpha_{{\rm CB},i}^{-}|^2/2} \left(\frac{n_{{\rm CB},i}^{-}}{\alpha_{{\rm CB},i}^{-}} - \alpha_{{\rm CB},i}^{-} - t\right)^{-n_{{\rm CB},i}^{-}} & t < -\alpha_{{\rm CB},i}^{-} \\ \left(\frac{n_{{\rm CB},i}^{+}}{|\alpha_{{\rm CB},i}^{+}|}\right)^{n_{{\rm CB},i}^{+}} e^{-|\alpha_{{\rm CB},i}^{+}|^2/2} \left(\frac{n_{{\rm CB},i}^{+}}{\alpha_{{\rm CB},i}^{+}} - \alpha_{{\rm CB},i}^{+} - t\right)^{-n_{{\rm CB},i}^{+}} & t > \alpha_{{\rm CB},i}^{+} \end{cases} ,$$

where $t = (m_{\gamma\gamma} - m_H - \Delta\mu_{{\rm CB},i})/\sigma_{{\rm CB},i}$, and $\mathcal{N}_c$ is a normalization factor. The non-Gaussian parts are parameterized by $\alpha_{{\rm CB},i}^{\pm}$ and $n_{{\rm CB},i}^{\pm}$ separately for the low- ($-$) and high-mass ($+$) tails.

The parameters of the model that define the shape of the signal distribution are determined through fits to the simulated signal samples. The parameterization is derived separately for each reconstructed category or fiducial region of the integrated or differential cross-section measurement. Figure 2 shows an example for two categories with different mass resolution: the improved mass resolution in the central region of the detector (defined by requiring $|\eta| \le 0.95$ for both selected photons) with respect to the forward region (defined by requiring one photon with $|\eta| \le 0.95$ and one photon with $0.95 < |\eta| < 2.37$) results in better discriminating power against the non-resonant background and in turn in a smaller statistical error of the extracted Higgs boson signal yield. The effective signal mass resolution of the two categories, defined as half the width containing 68% (90%) of the signal events, is 1.6 (2.7) GeV and 2.1 (3.8) GeV, respectively, and the mass resolution for all used categories can be found in Appendix E.

6.2 Background composition and model

The diphoton invariant mass model for the background used to fit the data is determined from studies of the bias in the signal yield in signal+background fits to large control samples of data or simulated background events.

Continuum $\gamma\gamma$ production is simulated with the SHERPA event generator as explained in Section 4, neglecting any interference effects with the $H \to \gamma\gamma$ signal. The γj and jj backgrounds are obtained by reweighting this sample using an $m_{\gamma\gamma}$ dependent linear correction function obtained from the fraction of $\gamma\gamma$ to γj and $\gamma\gamma$ to jj background events in data, respectively.

For very low rate categories targeting $t\bar{t}H$ or tH events, in which the background simulation suffers from very large statistical uncertainties, various background-enriched control samples are directly obtained from the data by either reversing photon identification or isolation criteria, or by loosening or removing completely b-tagging identification requirements on the jets, and normalizing to the data in the $m_{\gamma\gamma}$ sidebands of the events satisfying the nominal selection. For low rate categories targeting associated vector boson production, background control samples are obtained by summing the distributions from the main background processes: Those of $\gamma\gamma$ and $V\gamma\gamma$ events are obtained directly from the simulation, while the $m_{\gamma\gamma}$ distributions of γj and jj events are obtained from data control samples in which the nominal selection is applied except that at least one (for γj) or both (for

17
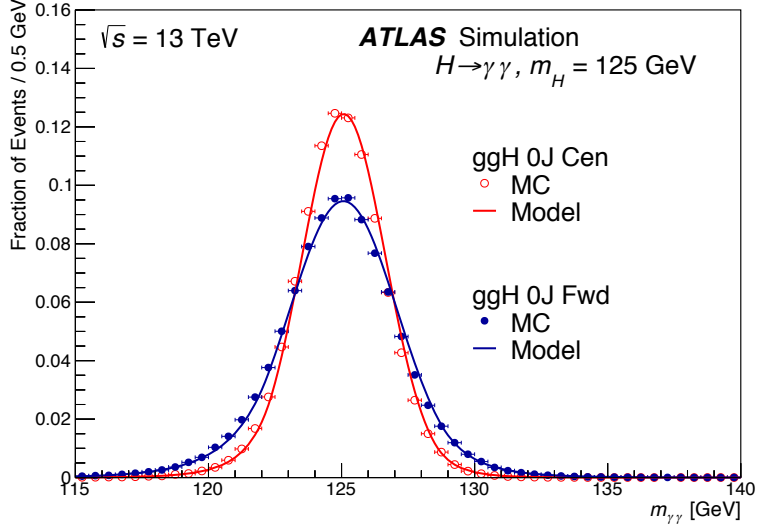
Figure 2: The diphoton mass signal shapes of two gluon–gluon fusion categories that are later introduced in Section 8.1 are shown: ggH 0J Fwd aims to select gluon–gluon fusion events with no additional jet and at least one photon in the pseudorapidity region $|\eta| > 0.95$; ggH 0J Cen applies a similar selection, but requires both photons to have $|\eta| \leq 0.95$ in order to have a better energy resolution. The simulated sample (labeled as MC) is compared to the fit model and contains simulated events from all Higgs boson production processes described in Section 4 with $m_H = 125$ GeV.

jj) of the two photon candidates fail to meet either the identification or isolation criteria. Except for the $V\gamma\gamma$ component, which is normalized with its theoretical cross section, the other contributions are normalized according to their relative fractions determined in data as described in the following.

The measurement of the background fractions in data is performed for each category or fiducial region. The relative fractions of $\gamma\gamma$, γj and jj background events are determined using a double two-dimensional sideband method [90, 91]. The nominal identification and isolation requirement are loosened for both photon candidates, and the data are split into 16 orthogonal regions defined by diphoton pairs in which one or both photons satisfy or fail to meet identification and/or isolation requirements. The region in which both photons satisfy the nominal identification and isolation requirements corresponds to the nominal selection of Section 5, while the other 15 regions provide control regions, whose $\gamma\gamma$, γj and jj yields are related to those in the signal region via the efficiencies for photons and for hadronic jets to satisfy the photon identification and isolation requirements. The $\gamma\gamma$, γj and jj yields in the signal region are thus obtained, together with the efficiencies for hadronic jets, by solving a linear system of equations using as inputs the observed yields in the 16 regions and the photon efficiencies predicted by the simulation. In the VH categories, a small extra contribution from $V\gamma\gamma$ events with an electron originating from the decay of the vector boson V which is incorrectly reconstructed as a photon, is also estimated from the simulation and subtracted before applying the two-dimensional sideband method. The dominant systematic uncertainties in the measured background fractions are due to the definition of the background control regions. The yields and relative fractions of the $\gamma\gamma$, γj and jj backgrounds are shown in Figure 3 as a function of $m_{\gamma\gamma}$ for the selected events. The fractions of these background sources in the inclusive diphoton sample are $(78.7 \, ^{+1.8}_{-5.2})\%$, $(18.6 \, ^{+4.2}_{-1.6})\%$ and $(2.6 \, ^{+0.5}_{-0.4})\%$, respectively. The uncertainties in the measured background
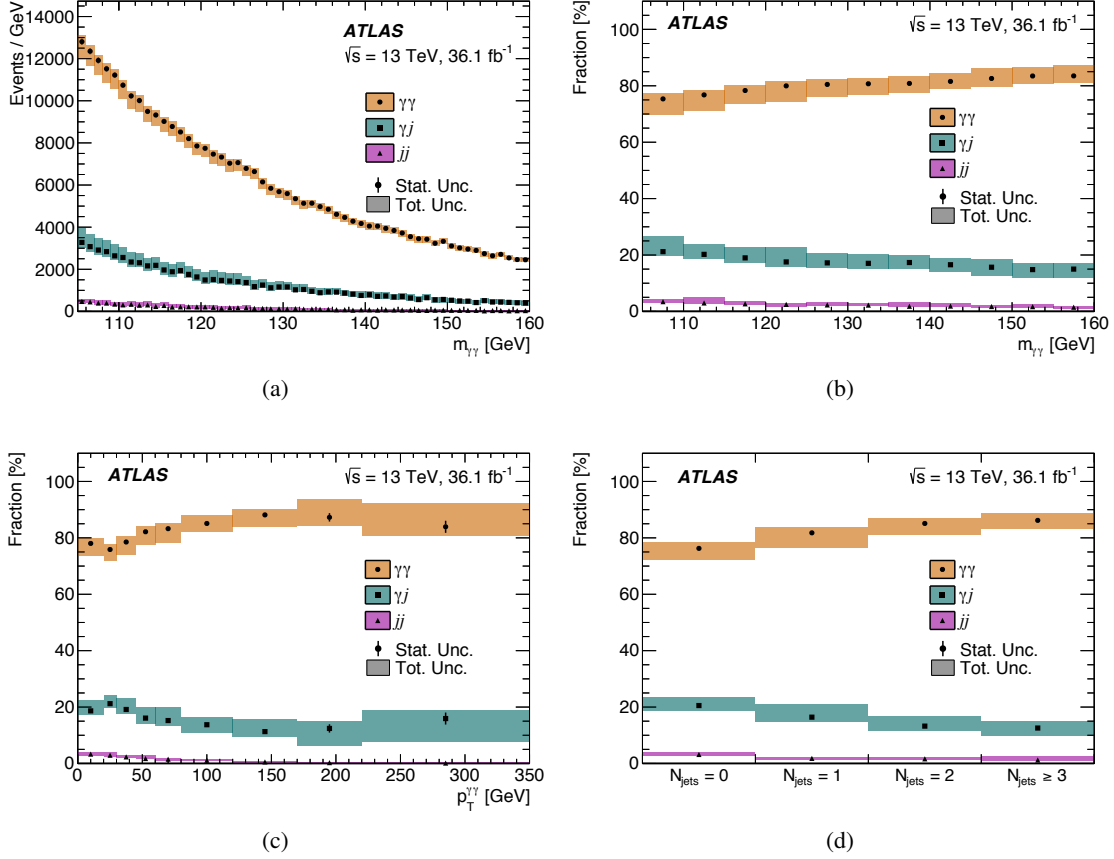
Figure 3: The data-driven determination of (a) event yields and (b) event fractions for $\gamma\gamma$, γj and $j j$ events as a function of $m_{\gamma\gamma}$ after the final selection outlined in Section 5. The event fractions for two differential observables, (c) $p_T^{\gamma\gamma}$ and (d) N_{jets} defined for jets with a $p_T > 30$ GeV are shown as well. The shaded regions show the total uncertainty of the measured yield and fraction, and the error bars show the statistical uncertainties.

fractions are systematically dominated. These results are comparable to previous results at $\sqrt{s} = 7$ and 8 TeV [9, 76]. In addition the purity is shown as a function of the p_T of the diphoton system, and the number of reconstructed jets with $p_T > 30$ GeV.

The functional form used to model the background $m_{\gamma\gamma}$ distribution in the fit to the data is chosen, in each region, to ensure a small bias in the extracted signal yield relative to its experimental precision, following the procedure described in Ref. [3]. The potential bias (*spurious signal*) is estimated as the maximum of the absolute value of the fitted signal yield, using a signal model with mass between 121 and 129 GeV, in fits to the background control regions described before.

The spurious signal is required, at 95% confidence level (CL), to be less than 10% of the expected SM signal yield or less than 20% of the expected statistical uncertainty in the SM signal yield. In the case when two or more functions satisfy those requirements, the background model with the least number of parameters is chosen.

Prior to the final fit to the data, the selected model is tested against a model from the same family of functions but with one more degree of freedom (for instance, the exponential of a second-order

19

polynomial is tested against an exponential of a third-order polynomial) to check, using only events in the diphoton invariant mass sidebands (*i.e.* excluding the range 121 GeV $< m_{\gamma\gamma} <$ 129 GeV), if the data favors a more complex model. A test statistic is built from the χ^2 values and number of degrees of freedom of two binned fits to the data with the two background models. The expected distribution of the test statistic is built from pseudo-data assuming that the function with fewer degrees of freedom is the true underlying model. The value of the test statistic obtained in the data is compared to such distribution, and the simpler model is rejected in favor of the more complex one if the *p*-value of such comparison is lower than 5%. The background distribution of all regions is found to be well modeled by at least one of the following functions: an exponential of a first- or second-order polynomial, a power law, or a third-order Bernstein polynomial.

6.3 Statistical model

The data are interpreted following the statistical procedure summarized in Ref. [92] and described in detail in Ref. [93]. An extended likelihood function is built from the number of observed events and invariant diphoton mass values of the observed events using the analytic functions describing the distributions of $m_{\gamma\gamma}$ in the range 105–160 GeV for the signal and the background.

The likelihood for a given reconstructed category, fiducial region, or differential bin *i* of the integrated or differential cross-section measurement is a marked Poisson probability distribution,

$$\mathcal{L}_i = \text{Pois}(n_i|N_i(\boldsymbol{\theta})) \cdot \prod_{j=1}^{n_i} f_i(m_{\gamma\gamma}^j, \boldsymbol{\theta}) \cdot G(\boldsymbol{\theta}),$$

where n_i (N_i) is the observed (expected) number of selected candidates, $f_i(m_{\gamma\gamma}^j)$ is the value of the probability density function (pdf) of the invariant mass distribution evaluated for each candidate *j*, $\boldsymbol{\theta}$ are nuisance parameters and $G(\boldsymbol{\theta})$ is a set of unit Gaussian constraints on a subset of the nuisance parameters, as described in the following. The likelihood for the measurements of the total Higgs boson production-mode cross sections and signal strengths is given by the product of the likelihood functions of each event reconstruction category. For the fiducial integrated and differential cross-section measurements the likelihood of all bins *i* in a spectrum is taken.

The number of expected candidates is the sum of the signal and background yields, denoted by N_i^{sig} and N_i^{bkg}, and the fitted spurious signal yield, $N_i^{\text{spur}} \cdot \theta_i^{\text{spur}}$,

$$N_i = N_i^{\text{sig}} + N_i^{\text{bkg}} + N_i^{\text{spur}} \cdot \theta_i^{\text{spur}}.$$

In more detail, the invariant mass distribution for each category has signal and background components,

$$f_i(m_{\gamma\gamma}^j) = \left[(N_i^{\text{sig}} + N_i^{\text{spur}} \cdot \theta_i^{\text{spur}}) \cdot f_i^{\text{sig}}(m_{\gamma\gamma}^j, \boldsymbol{\theta}_i^{\text{sig}}) + N_i^{\text{bkg}} \cdot f_i^{\text{bkg}}(m_{\gamma\gamma}^j, \boldsymbol{\theta}_i^{\text{bkg}}) \right] / N_i,$$

where $\boldsymbol{\theta}_i^{\text{sig}}$ and $\boldsymbol{\theta}_i^{\text{bkg}}$ are nuisance parameters associated with systematic uncertainties affecting the resolutions and positions (Section 7.1) of the invariant mass distributions of the signal f_i^{sig} (further detailed in Section 6.1) or the shape of the background f_i^{bkg} (as explained in Section 6.2), respectively.

Systematic uncertainties are incorporated into the likelihood function by multiplying the relevant parameter of the statistical model by a factor

$$F_{\mathrm{G}}(\sigma, \theta) = (1 + \sigma \cdot \theta)$$

in the case of a Gaussian pdf for the effect of an uncertainty of size σ or, for cases where a negative model parameter does not make physical sense (e.g. the uncertainty in the integrated luminosity), by a factor

$$F_{\mathrm{LN}}(\sigma, \theta) = e^{\sqrt{\ln(1+\sigma^2)}\theta}$$

for a log-normal pdf. In both cases the corresponding component of the constraint product $G(\theta)$ is a unit Gaussian centered at zero for the nuisance parameter θ. The systematic uncertainties affecting the yield and mass resolution use the log-normal form while a Gaussian form is used for all others. When two uncertainties are considered fully correlated they share the same nuisance parameter. Systematic uncertainties with partial correlations are decomposed into their uncorrelated and fully correlated components before being assigned to nuisance parameters.

All measured Higgs boson signal yields are determined with the profile likelihood ratio test statistic

$$\Lambda(\nu) = -2\ln \frac{\mathcal{L}(\nu, \hat{\boldsymbol{\theta}}_\nu)}{\mathcal{L}(\hat{\nu}, \hat{\boldsymbol{\theta}})}, \tag{1}$$

where $\hat{\nu}$ and $\hat{\boldsymbol{\theta}}$ are the values of the parameter of interest (e.g. a signal strength or a simplified template cross section) and nuisance parameters that unconditionally maximize the likelihood while $\hat{\boldsymbol{\theta}}_\nu$ are the values of the nuisance parameters that maximize the likelihood on the condition that the parameter of interest is held fixed to a given value ν. In the asymptotic approximation, which is valid for all the results presented here, $\Lambda(\nu)$ may be interpreted as an increase in χ^2 from its minimum value [92] such that approximate confidence intervals are easily constructed. The total uncertainty in ν is thus obtained from the ν values such that $\Lambda(\nu) = 1$ with all other parameters "profiled" (*i.e.* set to the values that maximize the likelihood for those values of ν). Theory uncertainties in the parameters of interest are found by fixing the nuisance parameters associated with experimental uncertainties and subtracting in quadrature the statistical uncertainty. The statistical uncertainty is similarly determined, by fixing all nuisance parameters to their best-fit values, except for those describing the background shape and normalization. The experimental uncertainty is found by subtracting in quadrature the theory and the statistical uncertainties from the total uncertainty.

6.4 Limit setting in the absence of a signal

In the absence of a significant signal yield in the measured production process categories or fiducial regions, upper limits on the corresponding signal strength or cross section are placed. For production-mode measurements, the limit is set by treating all other parameters of the fit as nuisance parameters. For the fiducial regions, each measurement is split into two orthogonal categories, one of which contains the events in the specified fiducial region and one that contains the events that are outside of it. The diphoton spectrum in both sets of events are simultaneously analyzed to extract the desired limit.

For category-based measurements the 95% CL upper limit on the parameter of interest ν is determined using the $\mathrm{CL_s}$ prescription [94]. For this, the agreement between data and the expected yield for the

hypothesized value of the parameter of interest ν is quantified by the test statistic, q_ν, defined as

$$q_\nu = \begin{cases} \Lambda(\nu) & 0 < \hat{\nu} \leq \nu, \\ 0 & \nu < \hat{\nu} \end{cases}, \tag{2}$$

where $\hat{\nu} \geq 0$ is the fitted parameter of interest. The observed value of the test statistic, q_{obs}, is determined from the ratio of the likelihood obtained by fixing the number of signal events to that predicted for a given value of the parameter of interest, to the likelihood normalized by allowing the number of signal events to float in the fit. The asymptotic behavior of Eq. (2) is well known [92]. For fiducial measurements the 95% CL upper limit are determined using a one-sided Gaussian interpretation of the observed cross section.

7 Systematic uncertainties

Several sources of systematic uncertainty are considered in this measurement. They can be grouped into three categories: (i) uncertainties associated with the parameterization of the signal and background when fitting the $m_{\gamma\gamma}$ spectrum, (ii) experimental uncertainties arising either from the extraction of the signal in a given category or from migrations between categories, and (iii) theoretical and modeling uncertainties in each category, causing migrations between categories, or affect the fiducial acceptance.

The origin of the uncertainties and their treatment are discussed in detail below and summarized in Table 3.[4]

The analysis based on event reconstruction categories and those of fiducial cross sections treat yield and migration uncertainties differently: whereas the former incorporate them directly into the likelihood function (cf. Section 6.3), the latter incorporate them at a later stage as part of the correction factor (introduced in Section 9.2) or the luminosity. Modeling uncertainties were also estimated with different approaches as discussed further in Sections 7.3 and 7.4. A summary of the impact of the uncertainties on the measurement is given in Sections 8.2.2 and 9.5.6.

7.1 Systematic uncertainties in the signal and background modeling from fitting the $m_{\gamma\gamma}$ spectrum

Systematic uncertainties associated with the signal and background parameterizations are treated in a similar way for all the measurements. These include systematic uncertainties in the photon energy scale and resolution, and the uncertainties due to the specific choice of background model.

The fit to the $m_{\gamma\gamma}$ spectra is performed for a Higgs boson mass of $m_H = 125.09 \pm 0.24\,\mathrm{GeV}$ [6]. The uncertainties in the photon energy scale and resolution impact the signal model, as the photon energy scale shifts the position of the peak and the assumed energy resolution broadens or narrows the signal peak relative to its nominal width. Uncertainties in the photon energy scale are included as nuisance parameters associated with Gaussian constraint terms in the likelihood functions. Uncertainties in the photon energy resolution are included as nuisance parameters, and are typically among the dominant

---

[4] The breakdown of uncertainties differs from those used in the Run 1 measurement Ref. [76] as more updated recommendations for experimental and theory uncertainties are used.

Table 3: Summary of the sources of systematic uncertainties for results based on event reconstruction categories or fiducial integrated and differential cross sections. The columns labels "Category Likelihood" and "Fiducial Likelihood" provide an overview about which terms are part of the Likelihood (✓) or incorporated at a later stage (-). Both sets of results incorporate uncertainties associated with the Higgs boson mass, photon energy scale and resolution, and uncertainties associated with the choice of the background function into the likelihood function, either using log normal ($F_{\mathrm{LN}}(\sigma_i, \theta_i)$) or Gaussian constraints ($F_{\mathrm{G}}(\sigma_i, \theta_i)$) with σ_i denoting the systematic uncertainty (i is the index to each of the unique nuisance parameters θ). When acting on $N_{\mathrm{S}}^{\mathrm{tot}}$ the uncertainty value is the same for all processes, whereas the uncertainty has a different value for each signal process for the case denoted $N_{\mathrm{S}}^{\mathrm{p}}$. The number of nuisance parameters, N_{NP}, for the spurious signal uncertainty varies, e.g. for the category-based results 31 independent error sources are present and for the differential measurements one source per measured bin is included.

		Systematic uncertainty source	N_{NP}	Constraint	Category Likelihood	Fiducial Likelihood
Theory		ggH QCD	9	$N_{\mathrm{S}}^{\mathrm{ggH}}\, F_{\mathrm{LN}}(\sigma_i, \theta_i)$	✓	-
		Missing higher orders (non-ggH)	6	$N_{\mathrm{S}}^{\mathrm{p}}\, F_{\mathrm{LN}}(\sigma_i, \theta_i)$	✓	-
		$B(H \to \gamma\gamma)$	1	$N_{\mathrm{S}}^{\mathrm{tot}}\, F_{\mathrm{LN}}(\sigma_i, \theta_i)$	✓	-
		PDF	30	$N_{\mathrm{S}}^{\mathrm{p}}\, F_{\mathrm{LN}}(\sigma_i, \theta_i)$	✓	-
		α_{S}	1	$N_{\mathrm{S}}^{\mathrm{p}}\, F_{\mathrm{LN}}(\sigma_i, \theta_i)$	✓	-
		UE/PS	5	$N_{\mathrm{S}}^{\mathrm{p}}\, F_{\mathrm{LN}}(\sigma_i, \theta_i)$	✓	-
Experimental	Yield	Heavy flavor content	1	$N_{\mathrm{S}}^{\mathrm{p}}\, F_{\mathrm{LN}}(\sigma_i, \theta_i)$	✓	-
		Luminosity	1	$N_{\mathrm{S}}^{\mathrm{tot}}\, F_{\mathrm{LN}}(\sigma_i, \theta_i)$	✓	-
		Trigger	1	$N_{\mathrm{S}}^{\mathrm{tot}}\, F_{\mathrm{LN}}(\sigma_i, \theta_i)$	✓	-
		Photon identification	1	$N_{\mathrm{S}}^{\mathrm{p}}\, F_{\mathrm{LN}}(\sigma_i, \theta_i)$	✓	-
		Photon isolation	2	$N_{\mathrm{S}}^{\mathrm{p}}\, F_{\mathrm{LN}}(\sigma_i, \theta_i)$	✓	-
	Migration	Flavor tagging	14	$N_{\mathrm{S}}^{\mathrm{p}}\, F_{\mathrm{LN}}(\sigma_i, \theta_i)$	✓	-
		Jet	20	$N_{\mathrm{S}}^{\mathrm{p}}\, F_{\mathrm{LN}}(\sigma_i, \theta_i)$	✓	-
		Jet flavor composition	7	$N_{\mathrm{S}}^{\mathrm{p}}\, F_{\mathrm{LN}}(\sigma_i, \theta_i)$	✓	-
		Jet flavor response	7	$N_{\mathrm{S}}^{\mathrm{p}}\, F_{\mathrm{LN}}(\sigma_i, \theta_i)$	✓	-
		Electron	3	$N_{\mathrm{S}}^{\mathrm{p}}\, F_{\mathrm{LN}}(\sigma_i, \theta_i)$	✓	-
		Muon	11	$N_{\mathrm{S}}^{\mathrm{p}}\, F_{\mathrm{LN}}(\sigma_i, \theta_i)$	✓	-
		Missing transverse momentum	3	$N_{\mathrm{S}}^{\mathrm{p}}\, F_{\mathrm{LN}}(\sigma_i, \theta_i)$	✓	-
		Pileup	1	$N_{\mathrm{S}}^{\mathrm{p}}\, F_{\mathrm{LN}}(\sigma_i, \theta_i)$	✓	-
		Photon energy scale	40	$N_{\mathrm{S}}^{\mathrm{p}}\, F_{\mathrm{LN}}(\sigma_i, \theta_i)$	✓	-
Mass		ATLAS-CMS m_H	1	$\mu_{\mathrm{CB}}\, F_{\mathrm{G}}(\sigma_i, \theta_i)$	✓	✓
		Photon energy scale	40	$\mu_{\mathrm{CB}}\, F_{\mathrm{G}}(\sigma_i, \theta_i)$	✓	✓
		Photon energy resolution	9	$\sigma_{\mathrm{CB}}\, F_{\mathrm{LN}}(\sigma_i, \theta_i)$	✓	✓
Background		Spurious signal	Varies	$N_{\mathrm{spur},c}\, \theta_{\mathrm{spur},c}$	✓	✓

sources of systematic uncertainty in the measurement. The systematic uncertainties in the photon energy resolution and scale follow those in Refs. [71, 72]. The overall energy scale factors and their uncertainties have been determined using $Z \rightarrow e^+e^-$ events collected during 2015 and 2016. Compared to Ref. [72], several systematic uncertainties were re-evaluated with the 13 TeV data, including uncertainties related to the observed LAr cell non-linearity, the material simulation, the intercalibration of the first and second layer of the calorimeter, and the pedestal corrections. The typical impact of the photon energy scale uncertainties is to shift the peak position by between $\pm 0.21\%$ and $\pm 0.36\%$ of the nominal peak position, whereas the typical impact of the photon energy resolution uncertainty is to change the width of the signal distribution by between $\pm 6\%$ and $\pm 13\%$ of the nominal width. The size of both uncertainties is dependent on the energy, rapidity and jet activity of the selected photon pair.

An additional uncertainty in the signal peak position is added as a nuisance parameter in the fit, reflecting the uncertainty in the measurement of the Higgs boson mass of 0.24 GeV [6]. The uncertainty in the Higgs boson mass is dominated by the statistical component, and the systematic component has contributions from both the ATLAS and the CMS muon momentum and electromagnetic energy scale uncertainties. Therefore, the correlation between this uncertainty and the photon energy scale uncertainty in the measurements presented here is considered negligible. A variation of the signal mass by ± 0.24 GeV (without including this uncertainty in the fit) is found to impact the measured global signal strength or the diphoton fiducial cross section by less than $\pm 0.1\%$.

The uncertainty due to the choice of background function is taken to be the spurious signal yield obtained when fitting the $m_{\gamma\gamma}$ spectrum reconstructed from background-only simulated samples (or signal-suppressed control regions in data), as discussed in Section 6.

7.2 Experimental systematic uncertainties affecting the expected event yields

There are two categories of uncertainties: 1) those in the expected overall signal yield and 2) those that cause migrations of events between categories and bins, as well as into and out of the photon fiducial selection.

The sources of uncertainties in the expected signal yield consist of:

- The luminosity delivered to the ATLAS experiment. The uncertainty in the combined 2015+2016 integrated luminosity is 3.2%. It is derived, following a methodology similar to that detailed in Ref. [95], from a calibration of the luminosity scale using x–y beam-separation scans performed in August 2015 and May 2016.

- The efficiency of the diphoton trigger. Its uncertainty is estimated to be 0.4% by comparing the trigger efficiencies determined using a bootstrap method [16] in data and simulation.

- The photon identification efficiency. Its uncertainty is estimated to be 1.6% and is obtained by varying the efficiency scale factors within their uncertainties, derived from control samples of photons from radiative Z boson decays and from inclusive γ events, and of electrons from $Z \rightarrow e^+ e^-$ decays.

- The photon track isolation efficiency. Its uncertainty is estimated to be 0.8% and is derived from measurements of the efficiency correction factors using inclusive photon control samples.

24

- The photon calorimeter isolation efficiency. Its uncertainty is estimated to be 0.1% and is obtained from the difference between applying and not applying corrections derived from inclusive photon events to the calorimeter isolation variable in the simulation.

Uncertainties which affect the calibration of photons, jets, and leptons cause migrations between categories and bins, as well as migrations into and out of the fiducial acceptance. These include:

- The modeling of pileup in the simulation. The corresponding uncertainty is derived by varying the average number of pileup events in the simulation by an amount consistent with data. The typical size ranges from 1.4% up to 5.6% depending on the category or fiducial cross section bin.

- Uncertainties in the photon energy scale and resolution. These uncertainties cause migrations into and out of the fiducial volume or between the event reconstruction categories and impact the expected number of events. The calibration of the absolute energy scale is derived using $Z \rightarrow e^+ e^-$ decays. The impact of the corresponding uncertainties is small, however, for all measurements, and ranges for instance between 0.2% for events with a low diphoton p_T up to 1.9% for events with a high diphoton p_T.

- Uncertainties in the jet energy calibration and the jet energy resolution. Uncertainties in the jet energy scale and resolution are estimated by varying the jet energies by an amount commensurate with the differences observed between 13 TeV data and simulation in the transverse momentum balance in dijet, γ + jet and Z + jet events [81, 82, 96]. The typical size of this uncertainty ranges from 2.8% to 15%.

- Uncertainties due to the efficiency of the jet vertex tagger. Such uncertainties are estimated by shifting the associated corrections applied to the simulation by an amount allowed by the data. For the measurement of the fiducial integrated and differential cross sections, uncertainties associated with the modeling of pileup jets in the simulation are estimated by recalculating the correction factor after removing 20% of pileup jets at random, which is commensurate with the observed differences in data and simulation for jets tagged as low-JVT (pileup) and high-JVT (hard scatter). Its typical size ranges from nil to 0.3%.

- Uncertainties associated with the efficiency of the b-tagging algorithm. They have been estimated to be typically of the order of 3% and are determined using $t\bar{t}$ events in 13 TeV data for jets containing the decay of a b-quark, using the method outlined in Ref. [97]. The corresponding uncertainties in the identification of jets originating from c-quarks, light quarks and gluons are taken directly from Run 1 studies [97], with additional uncertainties to cover the extrapolation to Run 2 conditions.

- Uncertainties in the electron [86] and muon [87] reconstruction, identification and isolation efficiencies. They have been obtained from dilepton decays of Z bosons and J/ψ mesons collected in Run 2, using a tag-and-probe technique. The typical size of these uncertainties is about 0.6% for electrons and about 0.5% for muons in the relevant categories or fiducial regions.

- Uncertainties in the electron [98] and muon [87] energy and momentum scale and resolution. They are determined from comparisons between the reconstructed invariant mass in data and simulation of dileptons from decays of Z bosons or J/ψ mesons. The impact is negligible for all measurements.

- Uncertainties associated with energy scales and resolutions of photons, jets and leptons are propagated to the E_T^{miss} uncertainty, together with the uncertainty in the contribution to E_T^{miss} from charged-particle tracks not associated with high-p_T leptons, jets, or photon conversions [89]. This results in a typical migration uncertainties ranging from 4.0% to 4.8% for relevant categories or fiducial regions.

7.3 Theoretical and modeling uncertainties for results based on event reconstruction categories

The overall theoretical cross-section uncertainties affect the signal strength measurements, which are ratios of the observed to predicted event yields, but not the cross-section measurements which do not rely on absolute predictions. Modeling uncertainties that alter the kinematic properties of the events, such as the Higgs boson transverse momentum or the jet multiplicity, have an impact on both types of measurements.

The theoretical modeling uncertainties in the per-category acceptance of each production process affect the measurement of production-mode cross sections and signal strengths. Uncertainties due to the choice of parton distribution functions and the value of α_S are estimated using the PDF4LHC15 recommendations [24] with the nominal `PDF4LHC_nlo_30_as` PDF set. Samples using the CT10 PDF set are reweighted to PDF4LHC15 to estimate these uncertainties. For the gluon–gluon fusion process, the total production-mode cross section has been calculated at N^3LO precision in QCD and has an uncertainty of 3.9%, as determined by QCD-scale variations and including top, bottom, and charm quark mass effect uncertainties. However, the perturbative uncertainty becomes significantly larger in different kinematic regions, e.g. when requiring additional jets or high Higgs boson p_T. To take this effect into account nine uncertainty sources are included:

- Four sources [7] account for uncertainties in the jet multiplicities due to missing higher-order corrections: two accounting for yield uncertainties (with uncertainties up to 8.9% in each STXS region) and two accounting for migrations between jet multiplicity bins (with uncertainties up to 18% in each STXS region), using the STWZ [99] and BLPTW [99–101] predictions as an input. For more details see Table 20 of Ref. [7].

- Three uncertainty sources parameterize modeling uncertainties in the Higgs boson p_T. The first two encapsulate the migration uncertainty between the intermediate and high p_T region with events with at least one jet. The third uncertainty parameterizes top-quark mass effects in the gluon–gluon fusion loop, where the difference between the LO and NLO predictions is taken as an uncertainty due to missing higher-order corrections. This introduces a negligible uncertainty at low Higgs boson p_T and a sizable uncertainty of the order of 30% at $p_T > 500$ GeV.

- Two sources account for the uncertainty in the acceptance of gluon–gluon fusion events in the VBF categories, due to missing QCD higher-orders in the calculation. Such uncertainties are estimated by variations of the renormalization and factorization scales in MCFM [102] by a factor of two around the nominal scale of $\mu_r = \mu_f = m_H$. The two sources account for the uncertainty in the overall normalization of $H + 2$ jet and $H + \geq 3$ jet events as well as for the uncertainty due to the multivariate requirement on $|\Delta\phi_{\gamma\gamma,jj}|$ (cf. Section 8.1.4), which suppresses additional jet activity. The uncertainty estimation uses an extension of the Stewart–Tackmann method [103, 104] and typically ranges between 20% and 32%.

The applicability of these uncertainties to PowHEG NNLOPS was tested by comparing the STWZ+BLPTW and the MCFM cross section predictions in variables relevant for the definition of the simplified cross-section bins, and reasonable agreement was found. In addition, the ggH acceptance of PowHEG NNLOPS of all categories based on BDT classifiers is compared to the acceptance derived from the MG5_AMC@NLO prediction or Refs. [46, 105] which includes up to two jets at NLO accuracy using the FxFx merging scheme [106]. Sufficient agreement was found for all categories and no additional modeling uncertainties are assigned based on these comparisons. [5]

Finally, in the categories targeting production in association with top quarks, the normalization of each of the ggH, VBF, and VH production mechanisms is assigned an uncertainty of 100%, motivated by comparisons of data with simulation in $t\bar{t}b\bar{b}$ [108] and Vb [109, 110] productions, but this has little impact on the final results.

The uncertainty in the modeling of the parton shower, underlying event and hadronization affects all measurements (labeled as "UE/PS" in the following). It is estimated by taking the relative difference in acceptance at particle level after switching the parton showering algorithm from PYTHIA8 to HERWIG7 in the ggH, VBF, and VH samples and from HERWIG++ to PYTHIA8 in the $t\bar{t}H$ sample, respectively. These differences are treated as four independent uncertainty sources. Additionally, for ggH the effect of the eigenvector tunes from the AZNLO set are merged to provide one additional uncertainty component.

The theoretical modeling uncertainties in the measurement of signal strengths include all of the sources that affect the measurement of the production-mode cross sections, plus additional uncertainties in the overall normalization of each production mechanism. Uncertainties in the overall normalization of each production process from missing higher-order QCD effects and the choice of parton distribution function are specified as part of the theoretical calculations used to normalize the simulated samples. The normalization uncertainty from the $H \rightarrow \gamma\gamma$ branching ratio is taken from HDECAY and PROPHECY4F.

7.4 Theoretical and modeling uncertainties for fiducial integrated and differential results

The theoretical modeling uncertainty in the detector correction factor (introduced in Section 9.2) used to measure the fiducial integrated and differential cross sections is taken to be the envelope of the following three sources:

1. The uncertainty in the relative contributions of the different Higgs boson production mechanisms. This uncertainty is estimated by varying the fraction of the ggH, VBF, VH and $t\bar{t}H$ processes by an amount commensurate with the 68% confidence levels of the measured production mode cross-section ratios [5]. The variations of each production mechanism are carried out simultaneously and include the known correlations between the measured production mode

---

[5] Recent measurements of QCD and electroweak (VBF) Z-boson production in association with two jets in Ref. [107] show large deviations between the data and the predictions for the QCD Zjj background at large m_{jj}. These differences are significantly larger than the 30–40% uncertainties assigned here to the ggH background in the experimental categories targeting VBF Higgs boson production. Increasing this uncertainty to 100% results in an increase in the theory uncertainty in the VBF signal strengths or simplified template cross sections by a factor of about two, while the increase in the total uncertainty is about 10%, as it is dominated by the statistical component.

cross-section ratios. These uncertainties range from 0.1% to 31%, depending on the fiducial region or differential variable, increasing typically in bins and regions sensitive to $t\bar{t}H$-production.

2. The uncertainty in the detector correction factor due to a possible mismodeling of the Higgs boson transverse momentum and rapidity distributions is estimated by reweighting the Higgs boson distributions in simulation to match those observed in the data. The resulting uncertainties range from 0.1% to 4.5%, increasing in fiducial regions and bins with high jet multiplicities.

3. The uncertainty in the modeling of the parton shower, underlying event, and hadronization. This uncertainty is derived as described in Section 7.3 and the size of this uncertainty ranges from from 0.1% up to 30%, with the highest uncertainties in fiducial regions with large missing transverse energy.

Typically differential measurements involving only the photon kinematics are less affected by these model uncertainties than measurements using selections on jets or missing transverse momentum.

7.5 Illustration of model errors for simplified template cross section and fiducial cross section measurements

To illustrate the difference between the two approaches of assigning theory and model errors used for category based results and the fiducial cross section results, the theoretical modeling uncertainties in the corresponding zero-jet ggF-dominated and VBF-dominated regions are compared.

The simplified template cross section defined as $gg \rightarrow H$ events with $|y_H| < 2.5$ and no jets derives its sensitivity from the two categories requiring no jet and either one or both photons reconstructed in the barrel region of the electromagnetic calorimeter (defined by $|\eta| \leq 0.95$). The total theory uncertainty is dominated by the uncertainty in the choice of parton distribution functions (1.5%), in the value of α_S (1.4%), and in the modeling of the parton shower, underlying event, and hadronization (1.7%), and amounts to a relative uncertainty of 2.7%. The fiducial zero-jet cross section, in contrast, has only a modeling uncertainty of 0.1%, dominated by the possible mismodeling of the Higgs boson transverse momentum and rapidity distributions.

The simplified template cross section defined as $qq \rightarrow Hqq$ events with $|y_H| < 2.5$ and no jets with $p_{\mathrm{T}}^j < 200$ GeV derives its sensitivity from four VBF categories employing multivariate methods to distinguish VBF events from background processes. The total theory uncertainty is dominated by the modeling uncertainties in the parton shower, underlying event, and hadronization (9%) and in the remaining ggH contamination (5%), and amounts to a relative uncertainty of 13%. In contrast, the fiducial VBF cross section, defined by a dijet mass m_{jj} of at least 400 GeV, a large rapidity separation $|\Delta y_{jj}| > 2.8$, and an azimuthal difference between the Higgs boson and the dijet pair of $|\Delta\phi_{\gamma\gamma,jj}| > 2.6$, has only a modeling uncertainty of 4.5%, dominated by the composition variation of the fractions of the ggH, VBF, VH and $t\bar{t}H$ processes (4.5%).

8 Measurement of total production-mode cross sections, signal strengths, and simplified template cross sections

8.1 Event categorization

The events satisfying the diphoton selection discussed in Section 5.2 are classified, in accord with the reconstructed event kinematics and topology, into 31 exclusive categories that are optimized for the best separation of the Higgs boson production processes and for the maximum sensitivity to the phase space regions defined by the stage 1 of the simplified template cross-section framework. A combined fit to the event reconstruction categories is then performed to determine nine simplified template cross sections (with $|y_H| < 2.5$), as well as production-mode cross sections and signal strength interpretations of the data. The categorization proceeds from the production modes with the smallest expected cross sections to the production modes with largest expected cross sections, in the order described below. In categories with definitions based on jet properties, jets with transverse momenta greater than 30 GeV are used, unless explicitly stated otherwise.

8.1.1 $t\bar{t}H$ and tH enriched categories

Nine categories enriched in events produced in association with a top quark are defined to target the $t\bar{t}H$, tHq, and tHW production modes. These categories are separated into a hadronic channel, where top quarks in the event decay to hadrons via $t \rightarrow Wb \rightarrow qq'b$; and a leptonic channel, where at least one top quark decays to a charged lepton via $t \rightarrow Wb \rightarrow \ell\nu b$. The single top quark categories are optimized for sensitivity to SM tH production, and are expected to provide additional sensitivity to anomalous values of the top quark Yukawa coupling.

Three categories target the leptonic channel by requiring the presence of at least one prompt lepton and at least one b-tagged jet with transverse momentum greater than 25 GeV. Two of these categories target tH production while the third one is optimized for $t\bar{t}H$ events. Both tH categories veto events with more than one prompt lepton. The first of these categories ("tH lep 0fwd") contains events with at most three central jets ($|\eta| < 2.5$) and a veto on forward jets ($|\eta| > 2.5$). The second tH category ("tH lep 1fwd") is defined by events with at most four central jets and at least 1 forward jet. The "ttH lep" category includes events with at least two central jets, while no requirement is applied to the forward jets. To suppress ZH events with $Z \rightarrow \ell\ell$, same-flavor dilepton candidates with an invariant mass within 10 GeV of the Z boson mass are vetoed.

Six categories target the hadronic decay channel by selecting events with no prompt leptons and at least three jets, of which at least one is b-tagged. Four of these categories ("ttH had BDT1" to "ttH had BDT4") are defined by means of a boosted decision tree (BDT) trained to identify $t\bar{t}H$ signal against ggH and multijet background. The BDT exploits five kinematic variables: H_T, the scalar sum of jet transverse momenta, $m_{\text{all jets}}$, the mass of all jets, as well as the number of all jets, central jets ($|\eta| < 2.5$), and b-tagged jets. The training uses $t\bar{t}H$ and ggH simulated events and a data-driven multijet background sample defined by diphoton events with at least three jets and in which at least one photon fails to meet either identification or isolation requirements. Using the BDT response as a discriminating variable, events are separated into four categories with an expected fraction of $t\bar{t}H$ events (among all Higgs boson events in this category) of 95%, 89%, 86%, and 79%, respectively. Two additional hadronic categories enhanced in tH production ("tH had 4j1b" and "tH had 4j2b")
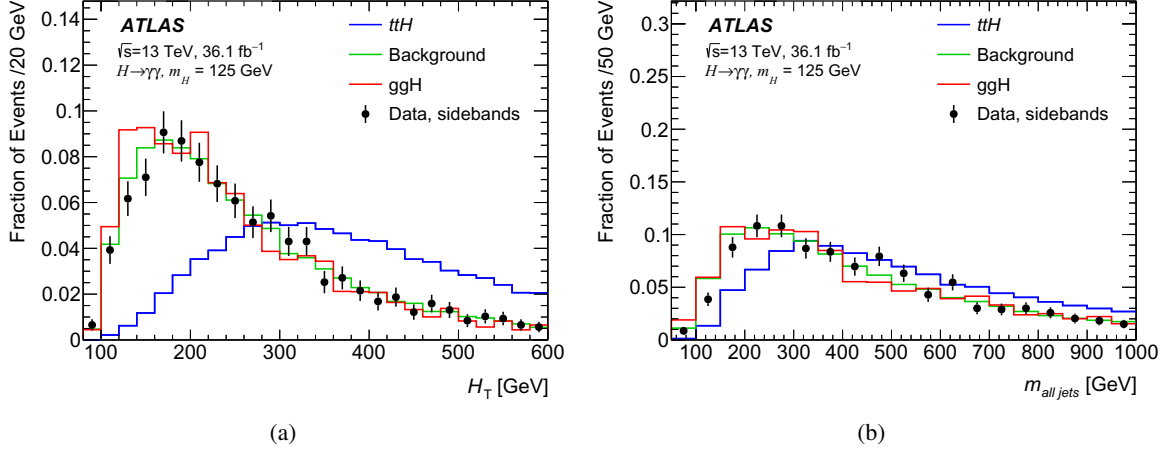
Figure 4: The normalized distributions for the expected background of two kinematic variables used for the selection of the hadronic $t\bar{t}H$ categories: (a) H_T and (b) $m_{\text{all jets}}$ for events after the first step of the selection (see text) for simulated $H \to \gamma\gamma$ events produced via $t\bar{t}H$ (blue) and gluon–gluon fusion (red), for the expected background derived from the data control region (green) described in the text and events from data with $105\,\text{GeV} < m_{\gamma\gamma} < 120\,\text{GeV}$ or $130\,\text{GeV} < m_{\gamma\gamma} < 160\,\text{GeV}$ (black dots with error bars showing the statistical uncertainty).

are included, defined by events with exactly four jets with transverse momentum greater than 25 GeV and split by events with exactly one or two b-tagged jets, respectively. The distributions of two of the discriminating variables are shown in Figure 4.

8.1.2 VH leptonic enriched categories

Five categories are enriched in Higgs boson production in association with a vector boson, based on different decays of the vector bosons.

The VH dilepton category ("VH dilep") targets ZH production with $Z \to \ell\ell$ by requiring the presence of two same-flavor opposite-sign leptons with an invariant mass between 70 GeV and 110 GeV. Two additional VH one-lepton categories target WH production with $W \to \ell\nu$. Events are requested to contain exactly one selected electron or muon. To suppress ZH events with Z bosons decaying to ee, in which an electron is misidentified as a photon, a veto is applied to events in which the invariant mass of the selected electron and any of the two signal photons is between 84 GeV and 94 GeV. Events are then split into two regions, where the p_T of the lepton+E_T^{miss} system is higher ("VH lep High") or lower ("VH lep Low") than 150 GeV. An additional requirement on the E_T^{miss} significance, defined as $E_T^{\text{miss}}/\sqrt{\sum E_T}$, of at least 1.0 is applied to events in the low lepton+E_T^{miss} p_T category.

Two VH missing transverse momentum categories target ZH production with $Z \to \nu\nu$ and $W \to \ell\nu$ where the lepton was not reconstructed or failed to meet the selection criteria. One category ("VH MET Low") requires $80\,\text{GeV} < E_T^{\text{miss}} < 150\,\text{GeV}$ and E_T^{miss} significance greater than 8. The other category ("VH MET High") requires $E_T^{\text{miss}} > 150\,\text{GeV}$ and E_T^{miss} significance greater than 9, or $E_T^{\text{miss}} > 250\,\text{GeV}$.
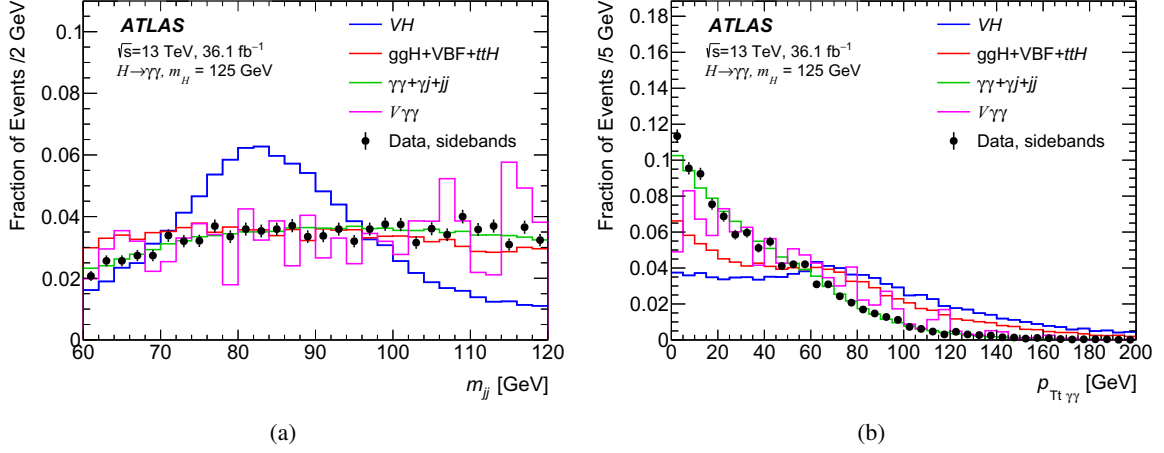
Figure 5: The normalized distributions of two kinematic variables used for the selection of the VH hadronic categories: (a) m_{jj} and (b) $p_{\mathrm{Tt}}^{\gamma\gamma}$ for events after the first step of the VH hadronic category preselection (see text) for simulated $H \to \gamma\gamma$ events produced in association with hadronically decaying vector bosons (blue) or through ggH, VBF or $t\bar{t}H$ processes (red), for the expected background from data (γj, jj) and simulation ($\gamma\gamma$, $V\gamma\gamma$) control samples (green, purple), and for events from data with 105 GeV$< m_{\gamma\gamma} < $ 120 GeV or 130 GeV$< m_{\gamma\gamma} < $ 160 GeV (black dots with error bars showing the statistical uncertainty).

8.1.3 BSM enriched and VH hadronic categories

To provide sensitivity to potential beyond SM contributions, a category ("jet BSM") defined by events with a leading jet with transverse momentum greater than 200 GeV is included in the event selection. This category includes SM events in the typical VBF topology, boosted $V(\to jj)H$ production where the vector boson is reconstructed as a single jet, as well as events produced in gluon–gluon fusion with an energetic jet.

Two VH hadronic categories target VH production with a hadronically decaying vector boson. Events are required to have at least two jets with $60 < m_{jj} < 120$ GeV. A BDT classifies the events using the following information: the dijet invariant mass, the component $p_{\mathrm{Tt}}^{\gamma\gamma}$ of the diphoton $\vec{p}_{\mathrm{T}}$ transverse to its thrust axis in the transverse plane, the rapidity difference between the dijet and the diphoton system, and the cosine $\cos\theta^*_{\gamma\gamma,jj}$ where $\theta^*_{\gamma\gamma,jj}$ is the angle between the diphoton systems momentum and the direction of motion of the diphoton–dijet system in the Collins–Soper frame. The training uses VH events as signal, and a mixture of simulated signals (everything except VH events), simulated $\gamma\gamma$ events, and γj and jj data control samples as background. Using the BDT response as a discriminating variable, events are classified into two categories ("VH had tight" and "VH had loose") with an expected fraction of signal events due to VH production of 42% and 25%, respectively.

Figure 5 shows the distributions of m_{jj} and $p_{\mathrm{Tt}}^{\gamma\gamma}$ in signal and background events and in events selected in data from the $m_{\gamma\gamma}$ sidebands. The variables show good separation between VH events and both the other signal events and background events.

8.1.4 VBF enriched categories

Four categories are defined to enhance the sensitivity to vector boson fusion production. Events are required to contain at least two hadronic jets, and the selections applied are based on the two leading jets (j_1, j_2) in the event. The pseudorapidity separation $|\Delta\eta_{jj}|$ between the two leading jets is required to be greater than 2. In addition $|\eta_{\gamma\gamma} - 0.5(\eta_{j1} + \eta_{j2})|$ is required to be less than 5, with $\eta_{\gamma\gamma}$ denoting the pseudorapidity of the diphoton system. The events are first split into two regions based on the value of the transverse momentum p_T^{Hjj} of the vector sum of the momenta of the reconstructed Higgs boson and of the two leading jets. This variable is highly correlated with the p_T of the third jet due to momentum balance. The signal in the $p_T^{\gamma\gamma jj} < 25$ GeV "low p_T^{Hjj}" region is dominated by exclusive two-jet-like events, while the signal in the $p_T^{\gamma\gamma jj} > 25$ GeV "high p_T^{Hjj}" region is dominated by inclusive $\geq$ 3-jet like events. This choice minimizes the otherwise large ggH jet-migration uncertainties in this phase space and is similar to a central-jet veto that separates contributions from ggH and VBF.

A BDT is then used to classify events in each region, using six kinematic variables: m_{jj}, $|\Delta\eta_{jj}|$, $p_{Tt}^{\gamma\gamma}$, the absolute azimuthal difference of the diphoton and the dijet system $|\Delta\phi_{\gamma\gamma,jj}|$, the minimum angular separation between either of the two signal photons and either of the two leading jets $\Delta R_{\gamma j}^{\min}$, and $|\eta_{\gamma\gamma} - 0.5(\eta_{j1} + \eta_{j2})|$. A requirement of $|\Delta\phi_{\gamma\gamma,jj}|$ to be near π effectively vetoes additional jets in the event by restricting the phase space for additional emissions and, to avoid large theoretical uncertainties, the BDT does not use shape information for events with $|\Delta\phi_{\gamma\gamma,jj}| > 2.94$ by merging these events into one bin. The training of the BDT uses VBF events as signal, and a mixture of simulated gluon–gluon fusion and $\gamma\gamma$ events and of γj and jj data control samples as background. Four exclusive categories are defined with "loose" and "tight" requirements on the BDT classifier in the two p_T^{Hjj} regions. The "tight" category in the $p_T^{Hjj} > 25$ GeV region has an expected fraction of VBF events among all Higgs boson events in this category of 49%, while the "loose" category has an expected fraction of VBF events of 20%. In the $p_T^{Hjj} < 25$ GeV region the "tight" category has an expected fraction of VBF events of 85%, whereas the "loose" category has an expected fraction of 61%.

Figure 6 shows the distributions of $|\Delta\eta_{jj}|$ and $|\Delta\phi_{\gamma\gamma,jj}|$ in simulated $H \rightarrow \gamma\gamma$ events, background events from simulated diphotons and data control samples of γj and jj events, and events selected from the $m_{\gamma\gamma}$ sidebands in data. The variables show good separation between VBF events and both gluon–gluon fusion events and background events.

8.1.5 Untagged categories

The remaining "untagged" events are dominated by events produced through gluon–gluon fusion and they are further split into ten categories. The untagged events are first separated by jet multiplicity into events with zero jets, exactly one jet, or at least two jets. The zero-jet events are split into two categories with either two photons in the "central" pseudorapidity region $|\eta| < 0.95$, in which the energy resolution is better ("ggH 0J Cen"), or with at least one photon in the "forward" region $|\eta| > 0.95$ which has worse energy resolution ("ggH 0J FWD"). The exclusive one-jet ("ggH 1J") and inclusive two-jet ("ggH 2J") categories are further split into regions of diphoton transverse momentum with $p_T^{\gamma\gamma} \in [0, 60)$ ("Low"), $[60, 120)$ ("Med"), $[120, 200)$ ("High") or > 200 GeV("BSM"), the latter of which is particularly sensitive to the presence of BSM physics in the loop diagrams associated with the gluon–gluon fusion production mode.
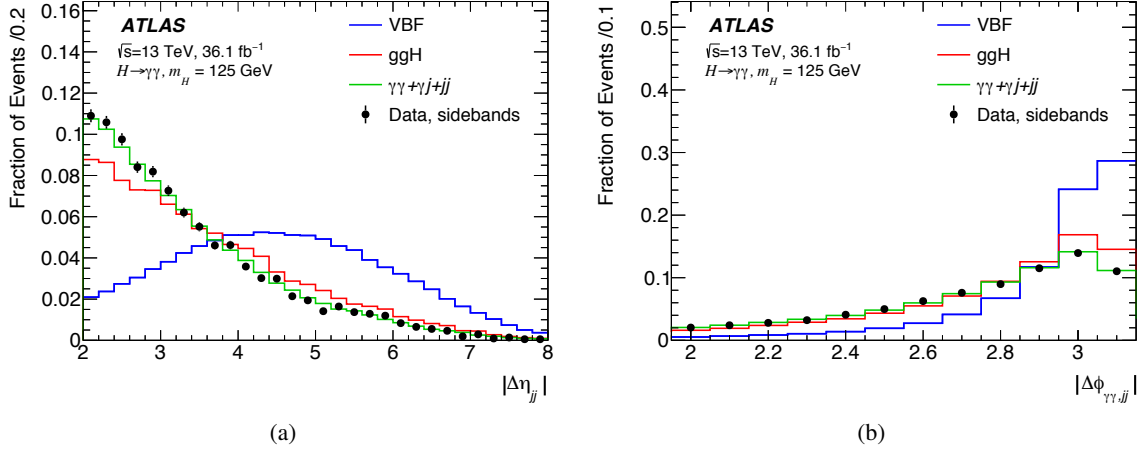
Figure 6: The normalized distributions for the expected background of two kinematic variables used for the selection of the VBF categories: (a) $|\Delta\eta_{jj}|$ and (b) $|\Delta\phi_{\gamma\gamma,jj}|$ for events after the first step of the selection (see text) for simulated $H \rightarrow \gamma\gamma$ events produced via vector-boson fusion (blue) and gluon–gluon fusion (red), for the expected background from data (γj, jj) and simulation ($\gamma\gamma$) control samples (green), and for events from data with $105\,\text{GeV} < m_{\gamma\gamma} < 120\,\text{GeV}$ or $130\,\text{GeV} < m_{\gamma\gamma} < 160\,\text{GeV}$ (black dots with error bars showing the statistical uncertainty).

8.1.6 Categorization summary

A summary of the selection requirements defining each category is provided in Table 4. The predicted signal efficiencies times acceptance and the event fractions per production mode for each category are given in Table 5. The fractions of signal events in each reconstructed category originating from a given simplified template cross-section region are shown in Figure 7. The defined ggH categories exhibit high purities as they are defined with a near one-to-one correspondence with the STXS regions despite small contaminations arising primarily from pileup and selection inefficiencies. The $qq \rightarrow Hqq$ bins are more ambiguous however still retain much of the diagonal structure. On the other hand, the VH leptonic and top categories are not sensitive to all of the STXS regions of interest, necessitating a merging. Finally, the fractions of signal events in each category from a given production mode are shown in Figure 8.

More information about the number of background events, the purity and the SM signal composition can be found in Tables 27 and 28 in Appendix E.

33

Table 4: Shorthand label and event selection defining each of the 31 event reconstruction categories for the measurement of the signal strengths and simplified template cross sections. The labels denote the predominant production process or kinematic properties the category targets. Jets are required to have $p_\mathrm{T} > 30\,\mathrm{GeV}$ unless otherwise noted. The categories are mutually exclusive and the criteria are applied in descending order of the shown categories.

Category	Selection
tH lep 0fwd	$N_\mathrm{lep} = 1$, $N_\mathrm{jets}^\mathrm{cen} \leq 3$, $N_{b-\mathrm{tag}} \geq 1$, $N_\mathrm{jets}^\mathrm{fwd} = 0$ ($p_\mathrm{T}^\mathrm{jet} > 25\,\mathrm{GeV}$)
tH lep 1fwd	$N_\mathrm{lep} = 1$, $N_\mathrm{jets}^\mathrm{cen} \leq 4$, $N_{b-\mathrm{tag}} \geq 1$, $N_\mathrm{jets}^\mathrm{fwd} \geq 1$ ($p_\mathrm{T}^\mathrm{jet} > 25\,\mathrm{GeV}$)
ttH lep	$N_\mathrm{lep} \geq 1$, $N_\mathrm{jets}^\mathrm{cen} \geq 2$, $N_{b-\mathrm{tag}} \geq 1$, $Z_{\ell\ell}$ veto ($p_\mathrm{T}^\mathrm{jet} > 25\,\mathrm{GeV}$)
ttH had BDT1	$N_\mathrm{lep} = 0$, $N_\mathrm{jets} \geq 3$, $N_{b-\mathrm{tag}} \geq 1$, $\mathrm{BDT}_\mathrm{ttH} > 0.92$
ttH had BDT2	$N_\mathrm{lep} = 0$, $N_\mathrm{jets} \geq 3$, $N_{b-\mathrm{tag}} \geq 1$, $0.83 < \mathrm{BDT}_\mathrm{ttH} < 0.92$
ttH had BDT3	$N_\mathrm{lep} = 0$, $N_\mathrm{jets} \geq 3$, $N_{b-\mathrm{tag}} \geq 1$, $0.79 < \mathrm{BDT}_\mathrm{ttH} < 0.83$
ttH had BDT4	$N_\mathrm{lep} = 0$, $N_\mathrm{jets} \geq 3$, $N_{b-\mathrm{tag}} \geq 1$, $0.52 < \mathrm{BDT}_\mathrm{ttH} < 0.79$
tH had 4j1b	$N_\mathrm{lep} = 0$, $N_\mathrm{jets}^\mathrm{cen} = 4$, $N_{b-\mathrm{tag}} = 1$ ($p_\mathrm{T}^\mathrm{jet} > 25\,\mathrm{GeV}$)
tH had 4j2b	$N_\mathrm{lep} = 0$, $N_\mathrm{jets}^\mathrm{cen} = 4$, $N_{b-\mathrm{tag}} \geq 2$ ($p_\mathrm{T}^\mathrm{jet} > 25\,\mathrm{GeV}$)
VH dilep	$N_\mathrm{lep} \geq 2$, $70\,\mathrm{GeV} \leq m_{\ell\ell} \leq 110\,\mathrm{GeV}$
VH lep High	$N_\mathrm{lep} = 1$, $|m_{e\gamma} - 89\,\mathrm{GeV}| > 5\,\mathrm{GeV}$, $p_\mathrm{T}^{\ell + E_\mathrm{T}^\mathrm{miss}} > 150\,\mathrm{GeV}$
VH lep Low	$N_\mathrm{lep} = 1$, $|m_{e\gamma} - 89\,\mathrm{GeV}| > 5\,\mathrm{GeV}$, $p_\mathrm{T}^{\ell + E_\mathrm{T}^\mathrm{miss}} < 150\,\mathrm{GeV}$, $E_\mathrm{T}^\mathrm{miss}$ significance > 1
VH MET High	$150\,\mathrm{GeV} < E_\mathrm{T}^\mathrm{miss} < 250\,\mathrm{GeV}$, $E_\mathrm{T}^\mathrm{miss}$ significance > 9 or $E_\mathrm{T}^\mathrm{miss} > 250\,\mathrm{GeV}$
VH MET Low	$80\,\mathrm{GeV} < E_\mathrm{T}^\mathrm{miss} < 150\,\mathrm{GeV}$, $E_\mathrm{T}^\mathrm{miss}$ significance > 8
jet BSM	$p_\mathrm{T,j1} > 200\,\mathrm{GeV}$
VH had tight	$60\,\mathrm{GeV} < m_\mathrm{jj} < 120\,\mathrm{GeV}$, $\mathrm{BDT}_\mathrm{VH} > 0.78$
VH had loose	$60\,\mathrm{GeV} < m_\mathrm{jj} < 120\,\mathrm{GeV}$, $0.35 < \mathrm{BDT}_\mathrm{VH} < 0.78$
VBF tight, high p_T^{Hjj}	$|\Delta\eta_{jj}| > 2$, $|\eta_{\gamma\gamma} - 0.5(\eta_\mathrm{j1} + \eta_\mathrm{j2})| < 5$, $p_\mathrm{T}^{Hjj} > 25\,\mathrm{GeV}$, $\mathrm{BDT}_\mathrm{VBF} > 0.47$
VBF loose, high p_T^{Hjj}	$|\Delta\eta_{jj}| > 2$, $|\eta_{\gamma\gamma} - 0.5(\eta_\mathrm{j1} + \eta_\mathrm{j2})| < 5$, $p_\mathrm{T}^{Hjj} > 25\,\mathrm{GeV}$, $-0.32 < \mathrm{BDT}_\mathrm{VBF} < 0.47$
VBF tight, low p_T^{Hjj}	$|\Delta\eta_{jj}| > 2$, $|\eta_{\gamma\gamma} - 0.5(\eta_\mathrm{j1} + \eta_\mathrm{j2})| < 5$, $p_\mathrm{T}^{Hjj} < 25\,\mathrm{GeV}$, $\mathrm{BDT}_\mathrm{VBF} > 0.87$
VBF loose, low p_T^{Hjj}	$|\Delta\eta_{jj}| > 2$, $|\eta_{\gamma\gamma} - 0.5(\eta_\mathrm{j1} + \eta_\mathrm{j2})| < 5$, $p_\mathrm{T}^{Hjj} < 25\,\mathrm{GeV}$, $0.26 < \mathrm{BDT}_\mathrm{VBF} < 0.87$
ggH 2J BSM	≥ 2 jets, $p_\mathrm{T}^{\gamma\gamma} \geq 200\,\mathrm{GeV}$
ggH 2J High	≥ 2 jets, $p_\mathrm{T}^{\gamma\gamma} \in [120, 200]\,\mathrm{GeV}$
ggH 2J Med	≥ 2 jets, $p_\mathrm{T}^{\gamma\gamma} \in [60, 120]\,\mathrm{GeV}$
ggH 2J Low	≥ 2 jets, $p_\mathrm{T}^{\gamma\gamma} \in [0, 60]\,\mathrm{GeV}$
ggH 1J BSM	$= 1$ jet, $p_\mathrm{T}^{\gamma\gamma} \geq 200\,\mathrm{GeV}$
ggH 1J High	$= 1$ jet, $p_\mathrm{T}^{\gamma\gamma} \in [120, 200]\,\mathrm{GeV}$
ggH 1J Med	$= 1$ jet, $p_\mathrm{T}^{\gamma\gamma} \in [60, 120]\,\mathrm{GeV}$
ggH 1J Low	$= 1$ jet, $p_\mathrm{T}^{\gamma\gamma} \in [0, 60]\,\mathrm{GeV}$
ggH 0J Fwd	$= 0$ jets, one photon with $|\eta| > 0.95$
ggH 0J Cen	$= 0$ jets, two photons with $|\eta| \leq 0.95$

Table 5: Signal efficiencies times acceptance, ϵ, and expected signal event fractions per production mode, f, in each category for $\sqrt{s} = 13$ TeV and $m_H = 125.09$ GeV. The second-to-last row shows the total efficiency per production process summed over the categories. Values labeled as 'nil' correspond to efficiencies or fractions that are smaller than 0.05%. The total number of expected signal events, N_S, in the last row corresponds to an integrated luminosity of 36.1 fb^{-1}.

| | ggH | | VBF | | WH | | ZH | | ttH | | $b\bar{b}H$ | | tHq | | tHW | | All |
Category	$\epsilon[\%]$	$f[\%]$	$\epsilon[\%]$	$f[\%]$	$\epsilon[\%]$	$f[\%]$	$\epsilon[\%]$	$f[\%]$	$\epsilon[\%]$	$f[\%]$	$\epsilon[\%]$	$f[\%]$	$\epsilon[\%]$	$f[\%]$	$\epsilon[\%]$	$f[\%]$	N_S
ggH 0J Cen	8.9	97.3	1.2	1.1	1.4	0.4	1.9	0.4	nil	nil	8.2	0.9	nil	nil	nil	nil	333.5
ggH 0J Fwd	15.5	97.0	2.4	1.2	3.0	0.5	3.7	0.4	nil	nil	14.7	0.9	0.2	nil	0.1	nil	579.5
ggH 1J Low	7.2	90.5	5.7	5.7	5.0	1.7	4.4	1.0	0.1	nil	9.1	1.1	0.5	nil	0.2	nil	289.9
ggH 1J Med	3.6	83.5	6.4	11.7	4.2	2.6	4.1	1.6	0.1	nil	1.9	0.4	0.6	nil	0.3	nil	156.2
ggH 1J High	0.7	76.0	1.9	17.5	1.1	3.4	1.4	2.7	0.1	0.1	0.3	0.3	0.2	nil	0.1	nil	31.5
ggH 1J BSM	nil	72.4	0.1	16.9	0.1	6.0	0.2	4.2	nil	0.3	nil	nil	nil	0.1	nil	nil	2.2
ggH 2J Low	1.8	79.1	2.7	9.6	3.7	4.5	4.1	3.1	2.2	1.1	5.4	2.3	3.9	0.3	1.9	nil	81.1
ggH 2J Med	1.5	77.6	3.1	12.2	3.2	4.4	3.8	3.2	2.6	1.5	1.6	0.7	4.5	0.4	2.4	nil	72.4
ggH 2J High	0.6	75.8	1.3	12.8	1.4	4.9	1.9	4.0	1.4	2.0	0.1	0.1	2.2	0.4	1.6	0.1	29.2
ggH 2J BSM	0.2	76.2	0.3	10.3	0.4	4.9	0.6	4.6	0.6	3.0	0.1	0.2	0.8	0.6	1.3	0.2	7.6
VBF Hjj Low loose	0.2	32.3	4.5	66.7	0.1	0.3	0.1	0.3	nil	nil	0.1	0.2	0.3	0.1	nil	nil	19.4
VBF Hjj Low tight	nil	12.9	4.2	86.7	nil	0.1	nil	0.1	nil	nil	nil	nil	0.3	0.1	nil	nil	13.8
VBF Hjj High loose	0.3	69.9	1.4	23.8	0.4	2.2	0.5	1.8	0.4	0.9	0.4	0.7	1.8	0.6	0.5	nil	16.5
VBF Hjj High tight	0.3	47.0	3.4	48.2	0.2	1.2	0.4	1.3	0.4	0.8	0.2	0.3	4.4	1.2	0.6	nil	20.2
VHhad loose	0.3	67.2	0.3	4.9	2.4	14.6	2.9	11.0	0.6	1.6	0.2	0.4	0.8	0.3	0.8	0.1	16.5
VHhad tight	0.2	52.4	0.1	3.4	3.0	23.8	3.5	18.0	0.6	1.9	nil	0.1	0.5	0.2	1.0	0.1	12.3
jet BSM	0.4	59.9	2.4	25.8	1.6	5.9	1.9	4.4	2.0	3.0	0.1	0.1	3.1	0.6	5.1	0.2	26.7
VHMET Low	nil	11.9	nil	0.4	0.1	23.4	0.6	63.2	nil	0.5	nil	0.3	nil	0.2	nil	nil	0.6
VHMET High	nil	1.3	nil	0.1	0.3	22.8	1.4	66.2	0.3	8.3	nil	nil	0.1	0.6	0.8	0.7	1.3
VHlep Low	nil	11.4	nil	1.1	4.4	68.0	0.8	8.1	1.3	8.5	0.2	0.9	1.8	1.6	2.2	0.4	6.4
VHlep High	nil	0.2	nil	nil	1.2	76.5	0.1	4.6	0.6	16.2	nil	nil	0.3	1.2	1.6	1.3	1.5
VHdilep	nil	nil	nil	nil	nil	nil	1.4	95.8	0.1	4.0	nil	nil	nil	nil	0.1	0.2	0.9
tHhad 4j2b	nil	23.8	nil	2.8	nil	1.6	0.1	13.5	0.6	39.0	0.1	8.2	1.2	10.5	0.3	0.6	0.6
tHhad 4j1b	nil	35.4	nil	4.0	0.1	4.3	0.3	7.9	2.2	36.3	0.2	2.2	3.8	8.5	2.6	1.3	2.5
ttHhadBDT4	nil	7.0	nil	0.8	nil	1.4	0.2	4.5	4.8	79.4	nil	0.3	1.9	4.3	4.7	2.4	2.5
ttHhadBDT3	nil	3.5	nil	0.5	nil	1.0	nil	3.1	1.3	86.1	nil	0.5	0.3	3.1	1.1	2.2	0.6
ttHhadBDT2	nil	3.6	nil	0.3	nil	0.8	nil	1.6	3.8	89.3	nil	0.2	0.6	1.8	3.4	2.4	1.8
ttHhadBDT1	nil	1.2	nil	0.1	nil	0.1	nil	0.7	3.4	95.0	nil	0.1	0.2	0.7	2.5	2.1	1.4
ttHlep	nil	nil	nil	nil	nil	0.2	nil	0.1	5.6	96.0	nil	0.1	0.4	1.0	5.0	2.6	2.4
tHlep 1fwd	nil	1.8	nil	0.2	nil	1.4	nil	0.9	2.1	79.4	nil	0.2	2.6	13.5	2.3	2.6	1.1
tHlep 0fwd	nil	4.1	nil	0.2	0.1	5.6	nil	2.8	1.9	75.7	nil	0.9	1.5	8.2	2.1	2.5	1.0
Total ϵ [%]	41.8	-	41.3	-	37.6	-	40.5	-	39.1	-	42.8	-	38.9	-	44.5	-	41.8
Events	1518.4		119.1		37.1		25.2		16.0		14.8		2.2		0.5		1733.2	

35
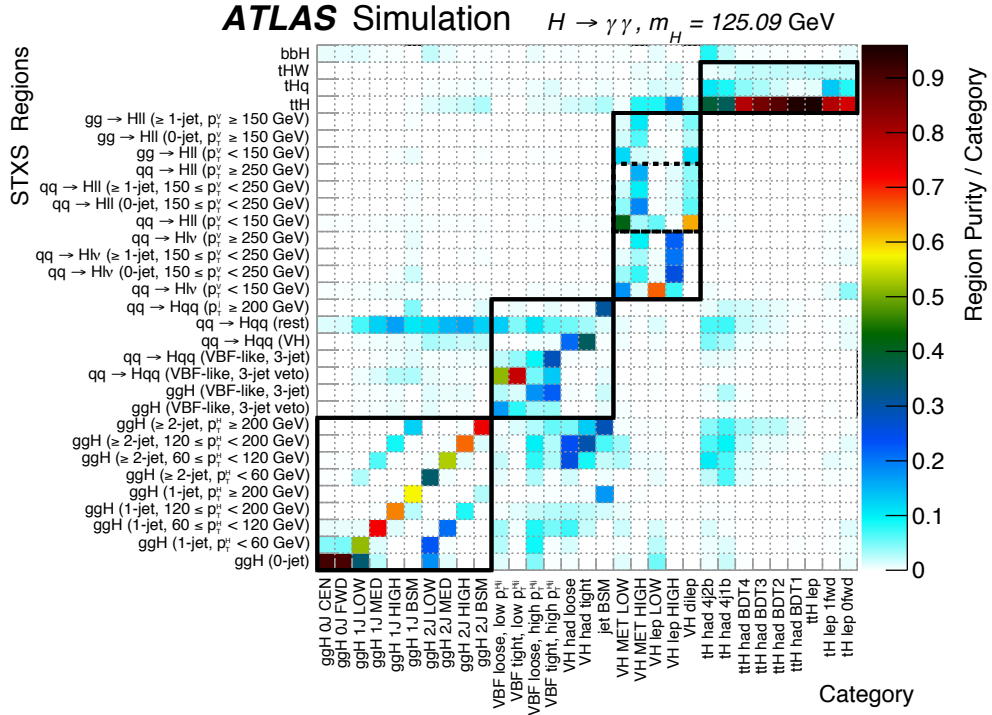
Figure 7: The fraction of signal events assigned to each reconstructed category (*x* axis and listed in Table 4) and originating from a given region (listed in Table 1) of the stage-1 simplified template cross section framework (*y* axis). The black lines separate the $t\bar{t}H$ and tH, VH leptonic, VH hadronic and VBF enriched, and untagged categories, along with the simplified template cross-section regions they are most sensitive to. The color shows the purity of the region per category.

Figure 8: The expected composition of the selected Higgs boson events, in terms of the different production modes, for each reconstructed category.

8.2 Production mode measurements

Using the 31 categories, total and production mode specific signal strength measurements are carried out. Measurements of total production cross sections and simplified template cross sections are reported. The simplified template cross sections are measured in a merged scheme introduced in Section 1.2 and summarized in Table 1. In addition, the result of coupling-strength fits are reported.

8.2.1 Observed Data

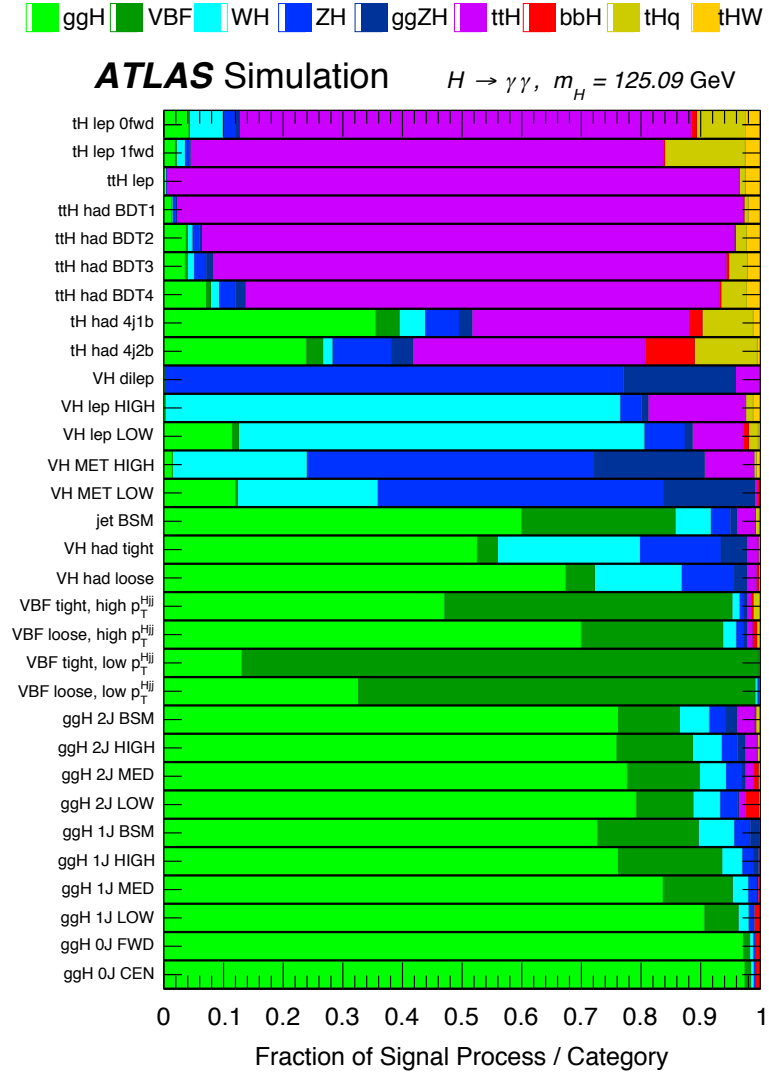The observed invariant mass distribution of the selected diphoton pairs of all categories as defined in Table 4, is shown in Figure 9. Figure 10 shows the invariant mass distributions for the sums of the categories most sensitive to the different production modes. In all cases, for illustration purposes, events in each category are weighted according to the expected signal (S_{90}) to background (B_{90}) ratio in a $m_{\gamma\gamma}$ region containing 90% of the expected signal yield, using a weight of the form $\ln(1 + S_{90}/B_{90})$. The results of signal-plus-background fits to these spectra, displaying both the total sum and the background-only components, are shown, as well as the residuals between the data and the background component. Both the signal-plus-background and background-only distributions shown are obtained from the sum of the individual distributions in each category weighted in the same way as the data points. In the fit of Figure 9 a single signal strength μ affecting simultaneously all production modes has been assumed, while in the fits of Figure 10 the four signal strengths μ_{ggH}, μ_{VBF}, μ_{VH} and $\mu_{\mathrm{ttH+tH}}$ are allowed to vary separately, as described in the following section. The observed mass peak of the Higgs boson, constrained in the fit as $m_H = 125.09 \pm 0.24$ GeV, is well within 68% CL of the Run 1 ATLAS+CMS combined measurement.

8.2.2 Signal strengths

The signal strengths, *i.e.* the ratios of the measured Higgs boson production-mode cross sections times diphoton branching ratio to the SM predictions for each production mode, are measured with the extended likelihood analysis described in Section 6.3. In the likelihood the signal yield $N_{\mathrm{sig},m}^i$ in each category i for a particular production mode m is expressed as the product of the integrated luminosity $\int L\,dt$, the signal strength μ_m for that production mode, the expected SM Higgs boson production mode cross section times branching ratio to diphotons, and the acceptance times efficiency ϵ (Table 5) for signal events from that production mode in the selected category ($N_{\mathrm{sig,m}}^i = \mu_m \times \int L\,dt \times \sigma_m^{\mathrm{SM}} \times B(H \to \gamma\gamma) \times \epsilon_m^i$).

A global signal strength μ is measured assuming the ratios between different production processes to be as predicted by the SM. The profile of the negative log-likelihood ratio $\lambda(\mu)$ of the global signal strength of all Higgs processes μ for $m_H = 125.09 \pm 0.24$ GeV is shown in Figure 11.

The measured central value and 68% CL interval for μ is found to be:

$$\mu = 0.99\,^{+0.15}_{-0.14} = 0.99\,\pm 0.12\,(\mathrm{stat.})\,^{+0.06}_{-0.05}\,(\mathrm{exp.})\,^{+0.07}_{-0.05}\,(\mathrm{theo.})\,,$$

well compatible with the SM prediction ($\mu = 1$). This result confirms the ATLAS Run-1 diphoton signal strength measurement of $\mu = 1.17 \pm 0.23\,(\mathrm{stat.})\,^{+0.10}_{-0.08}\,(\mathrm{exp.})\,^{+0.12}_{-0.08}\,(\mathrm{theo.})$ with around a factor of two improvement in each component of the uncertainty. The Run-1 result was obtained using the NNLO
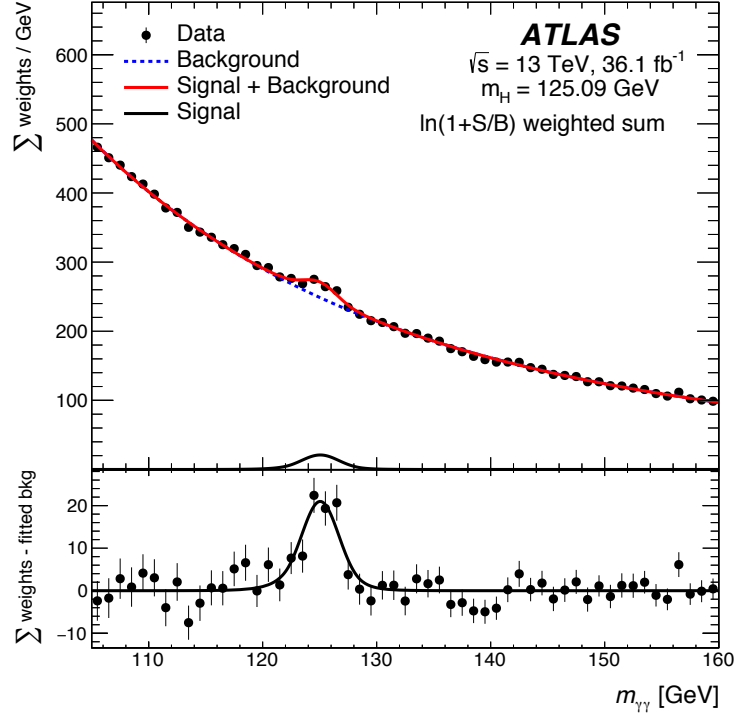
Figure 9: Weighted diphoton invariant mass spectrum observed in the 2015 and 2016 data at 13 TeV. Each event is weighted by the $\ln(1 + S_{90}/B_{90})$ ratio of the expected signal (S_{90}) and background (B_{90}) of the 90% signal quantile in the category to which it belongs to. The values of S_{90} and B_{90} used for each category are shown in Table 27 of Appendix E. The error bars represent 68% confidence intervals of the weighted sums. The solid red curve shows the fitted signal-plus-background model when the Higgs boson mass is constrained to be 125.09 ± 0.24 GeV. The background component of the fit is shown with the dotted blue curve. The signal component of the fit is shown with the solid black curve. Both the signal-plus-background and background-only curves reported here are obtained from the sum of the individual curves in each category weighted by the logarithm of unity plus the signal-to-background ratio. The bottom plot shows the residuals between the data and the background component of the fitted model.

SM prediction for ggH production [17, 111], which is about 10% lower than the N^3LO calculation used here (see Section 4). The impact of the main sources of systematic uncertainty (presented in Table 3 and Section 7) in the measured global signal strength is summarized in Table 6. The distinction between yield and migration uncertainties adopted in Table 3 is used and the uncertainties are grouped into theory uncertainties, experimental uncertainties, mass resolution and scale, background shape, and luminosity.

In addition to the global signal strength, the signal strengths of the primary production processes are evaluated by exploiting the sensitivities of the analysis categories of Table 4 to specific production processes. The measured signal strengths are shown together with the global signal strengths discussed above in Figure 12 and found to be:
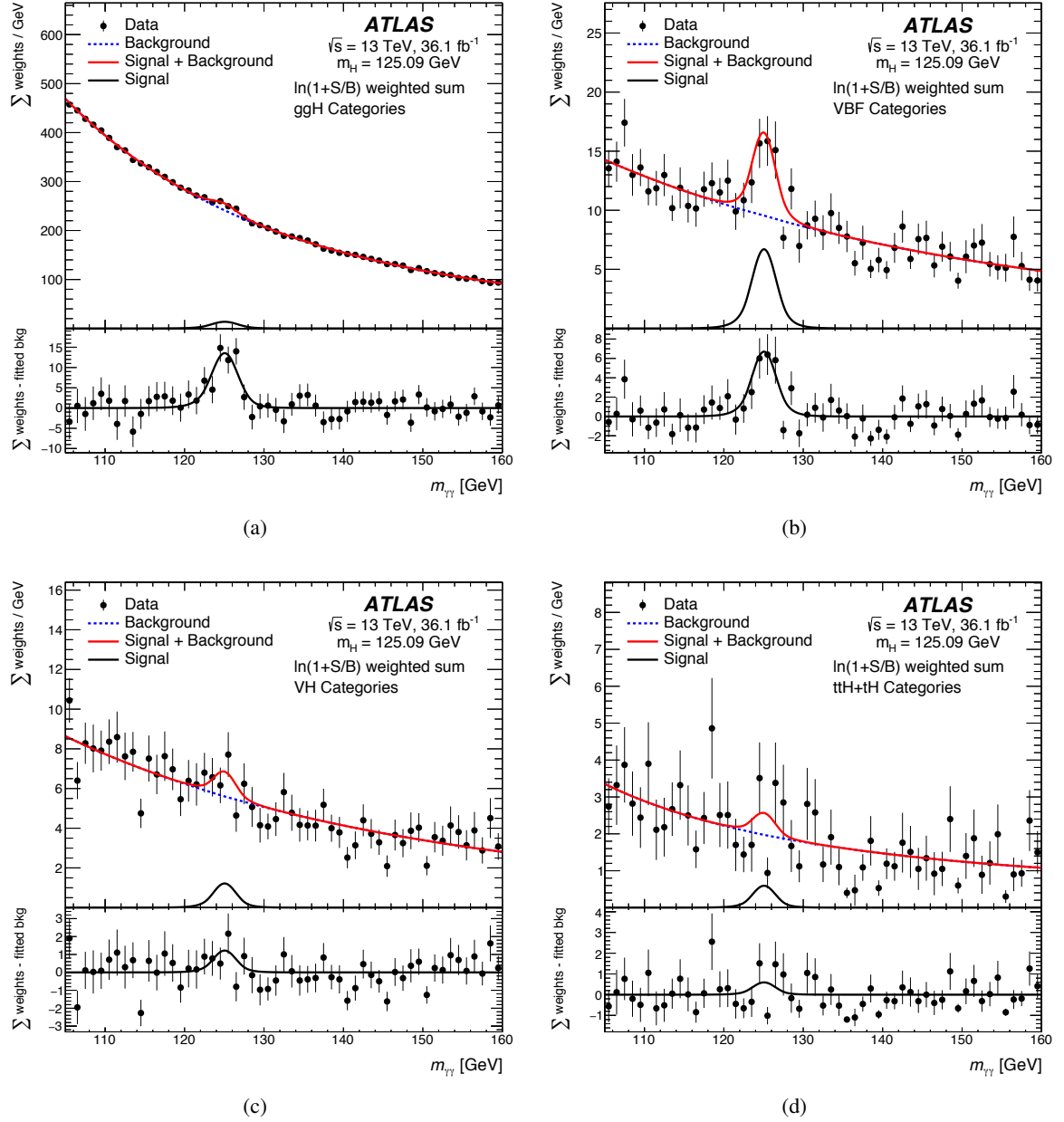
Figure 10: Weighted diphoton invariant mass spectra observed in the 13 TeV data for events belonging to: (a) "untagged" categories and the "jet BSM" category, in which the expected signal is produced mainly through gluon–gluon fusion, (b) VBF categories, (c) VH categories and (d) $t\bar{t}H$ categories. Each event is weighted by the $\ln(1 + S_{90}/B_{90})$ ratio of the expected signal (S_{90}) and background (B_{90}) of the 90% signal quantile in the category it belongs to. The values of S_{90} and B_{90} used for each category are shown in Table 27 of Appendix E. The error bars represent 68% confidence intervals of the weighted sums. The solid red curve shows the fitted signal-plus-background model when the Higgs boson mass is constrained to be 125.09 ± 0.24 GeV. The background component of the fit is shown with the dotted blue curve. The signal component of the fit is shown with the solid black curve. Both the signal-plus-background and background-only curves reported here are obtained from the sum of the individual curves in each category weighted by the logarithm of unity plus the signal-to-background ratio. The bottom plot shows the residuals between the data and the background component of the fitted model.

Figure 11: Observed negative log-profile likelihood Λ of the global signal strength μ. The three likelihood contours shown correspond to all theory and experimental nuisance parameters fixed (Stat.), all experimental nuisance parameters fixed (Theo.), and with all nuisance parameters floating (Total). The intersections of the solid curves and horizontal lines at $\Lambda = 1$ and $\Lambda = 4$ indicate the 1 and 2 σ confidence intervals of the corresponding result.

Table 6: Main systematic uncertainties $\sigma_\mu^{\text{syst.}}$ in the combined signal strength parameter μ. The values for each group of uncertainties are determined by subtracting in quadrature from the total uncertainty the change in the 68% CL range of μ when the corresponding nuisance parameters are fixed to their best fit values. The experimental uncertainty in the yield does not include the luminosity contribution, which is accounted for separately. The uncertainties correspond to the sources detailed in Table 3.

Uncertainty Group	$\sigma_\mu^{\text{syst.}}$
Theory (QCD)	0.041
Theory ($B(H \to \gamma\gamma)$)	0.028
Theory (PDF+α_S)	0.021
Theory (UE/PS)	0.026
Luminosity	0.031
Experimental (yield)	0.017
Experimental (migrations)	0.015
Mass resolution	0.029
Mass scale	0.006
Background shape	0.027

Figure 12: Summary of the signal strengths measured for the different production processes (ggH, VBF, VH and top) and globally ($\mu_{\text{Run}-2}$), compared to the global signal strength measured at 7 and 8 TeV ($\mu_{\text{Run}-1}$) [76]. The black and orange error bars show the total and statistical uncertainties. The signal strength $\mu_{\text{Run}-1}$ was derived assuming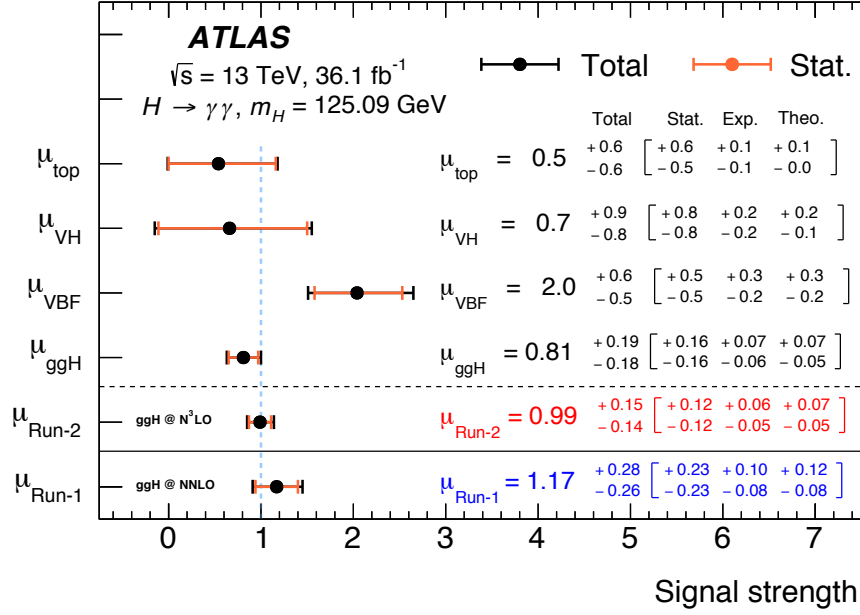 the Higgs production-mode cross section based on Refs. [17, 111]. Uncertainties smaller than 0.05 are displayed as 0.0. In the more recent theoretical predictions used in this analysis [7, 32], the gluon–gluon fusion production-mode cross section is larger by approximately 10%. In this measurement, the $b\bar{b}H$ contributions are scaled with ggH ($\mu_{\text{bbH}} = \mu_{\text{ggH}}$), and the tH and $t\bar{t}H$ productions are measured together ($\mu_{\text{top}} = \mu_{\text{ttH}+\text{tH}}$). Associated production with Z or W bosons is assumed to be scaled by a single signal strength parameter ($\mu_{\text{VH}} = \mu_{\text{ZH}} = \mu_{\text{WH}}$).

$$\mu_{\text{ggH}} = 0.81\,^{+0.19}_{-0.18} = 0.81\,\pm 0.16\,(\text{stat.})\,^{+0.07}_{-0.06}\,(\text{exp.})\,^{+0.07}_{-0.05}\,(\text{theo.})$$
$$\mu_{\text{VBF}} = 2.0\,^{+0.6}_{-0.5} = 2.0\,\pm 0.5\,(\text{stat.})\,^{+0.3}_{-0.2}\,(\text{exp.})\,^{+0.3}_{-0.2}\,(\text{theo.})$$
$$\mu_{\text{VH}} = 0.7\,^{+0.9}_{-0.8} = 0.7\,\pm 0.8\,(\text{stat.})\,^{+0.2}_{-0.2}\,(\text{exp.})\,^{+0.2}_{-0.1}\,(\text{theo.})$$
$$\mu_{\text{top}} = 0.5\,^{+0.6}_{-0.6} = 0.5\,^{+0.6}_{-0.5}\,(\text{stat.})\,^{+0.1}_{-0.1}\,(\text{exp.})\,^{+0.1}_{-0.0}\,(\text{theo.})$$

For Higgs boson production via VH the signal strength is assumed to be scaled by a single parameter (*i.e.* $\mu_{\text{VH}} = \mu_{\text{ZH}} = \mu_{\text{WH}}$). The $b\bar{b}H$ contributions are scaled with ggH (*i.e.* $\mu_{\text{bbH}} = \mu_{\text{ggH}}$), and the tH and $t\bar{t}H$ productions are measured together rather than separately (*i.e.* $\mu_{\text{top}} = \mu_{\text{ttH}+\text{tH}}$).

The ggH signal strength is 1 σ below the Standard Model prediction, while the VBF signal strength is 2.2 σ above the prediction. The expected and observed significances Z_0 of VBF production are reported in Table 7: the significance of the observed VBF signal is close to 5 σ.

Since no significant evidence is observed for VH and top-associated Higgs boson production, upper limits at 95% CL are reported for their signal strengths, as shown in Table 8 and Figure 13. The accuracy

Table 7: Expected and observed significances of the VBF, VH and top quark associated production mode signal strengths.

Measurement	Expected Z_0	Observed Z_0
μ_{VBF}	2.6 σ	4.9 σ
μ_{VH}	1.4 σ	0.8 σ
μ_{top}	1.8 σ	1.0 σ

Table 8: Observed and expected upper limits at 95% CL on the signal strengths μ_{VH} and μ_{top}. The median expected limits are given for either the case when the true value of the signal strength under study is the SM value ($\mu_i = 1$) or zero. The $\pm 1\,\sigma$ and $\pm 2\,\sigma$ intervals for the expected upper limit in the case $\mu_i = 0$ are also reported.

Measurement	Observed	Expected Limit ($\mu_i = 1$)	Expected Limit ($\mu_i = 0$)	$+2\sigma$	$+1\sigma$	-1σ	-2σ
μ_{VH}	2.3	2.5	1.5	3.1	2.2	1.1	0.8
μ_{top}	1.7	2.3	1.2	2.6	1.8	0.9	0.6

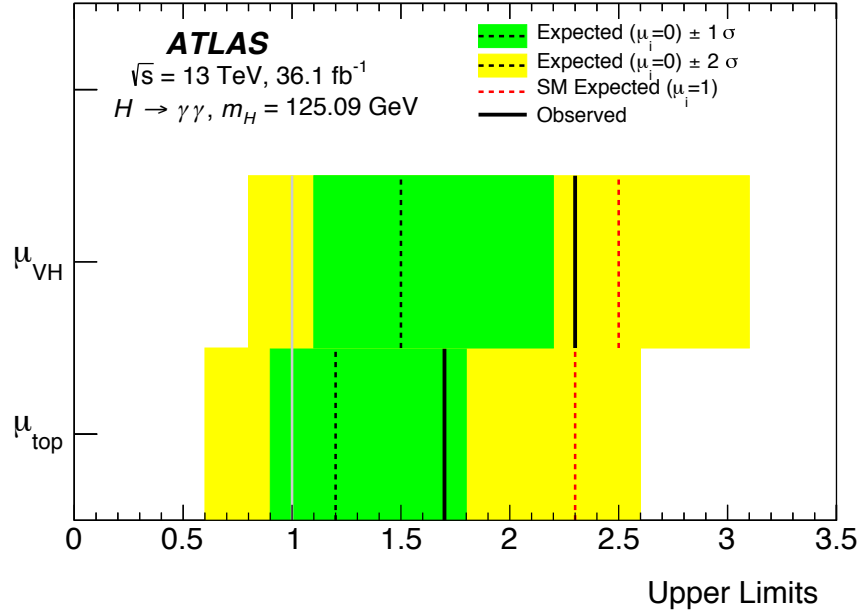Figure 13: Summary of asymptotic limits for the signal strengths of the associated production processes (VH and top).

of the asymptotic approximation was validated using ensembles of pseudo-experiments. Appendix F provides separate limits on μ_{ZH} and μ_{WH}, and Appendix G.1 shows the expected uncertainties for the inclusive and production-mode specific signal strengths reported in Figure 12.

Table 9: Best-fit values and uncertainties of the production-mode cross sections times branching ratio. The SM predictions [7] with their uncertainties are shown for each production process. Uncertainties smaller than 0.05 are displayed as 0.0.

Process ($|y_H| < 2.5$)	Result [fb]	Uncertainty [fb]				SM prediction [fb]
		Total	Stat.	Exp.	Theo.	
ggH	82	$^{+19}_{-18}$	±16	$^{+7}_{-6}$	$^{+5}_{-4}$	102^{+5}_{-7}
VBF	16	$^{+5}_{-4}$	±4	±2	$^{+3}_{-2}$	8.0 ± 0.2
VH	3	±4	$^{+4}_{-3}$	±1	$^{+1}_{-0}$	4.5 ± 0.2
Top	0.7	$^{+0.9}_{-0.7}$	$^{+0.8}_{-0.7}$	$^{+0.2}_{-0.1}$	$^{+0.2}_{-0.0}$	1.3 ± 0.1

8.2.3 Production-mode cross sections

The production-mode cross sections for $m_H = 125.09 \pm 0.24$ GeV in a region with Higgs-boson rapidity $|y_H| < 2.5$, multiplied by the branching ratio of the Higgs boson decay to diphotons, are evaluated in the following way. The fitted value of σ_{top} corresponds to the sum of $t\bar{t}H$, tHq, and tHW production-mode cross sections under the assumption that their relative ratios are as predicted by the SM. The VH production-mode cross section value is fitted under the assumption that the ratio of the WH and ZH production mode cross sections is as predicted by the SM and includes both production from quark and gluon initial states. Such results are obtained through signal+background fits to the diphoton invariant mass distribution in each category by expressing, in the likelihood, the signal yield $N^i_{\text{sig},m}$ in each category i for a particular production mode m as $N_{\text{sig},m} = \int L \, dt \times \sigma_m^{\text{SM}} \times B^{\text{SM}}(H \to \gamma\gamma) \times \epsilon^i_m$ using the same notation as in Section 8.2.2.

The production-mode cross sections are summarized in Figure 14 and Table 9.

The 68% and 95% CL two-dimensional contours of $\sigma_{\text{ggH}} \times B(H \to \gamma\gamma)$ and $\sigma_{\text{VBF}} \times B(H \to \gamma\gamma)$ are shown in Figure 15, profiling $\sigma_{\text{VH}} \times B(H \to \gamma\gamma)$ and $\sigma_{\text{top}} \times B(H \to \gamma\gamma)$ in the fits. The SM expectation of $\sigma_{\text{ggH}} \times B(H \to \gamma\gamma)$ vs $\sigma_{\text{VBF}} \times B(H \to \gamma\gamma)$ is within the 95% CL contour of this measurement.

To remove the impact of possible deviations in the $H \to \gamma\gamma$ branching ratio, ratios of the production-mode cross sections to the ggH cross section are also extracted. Such ratios, normalized for convenience
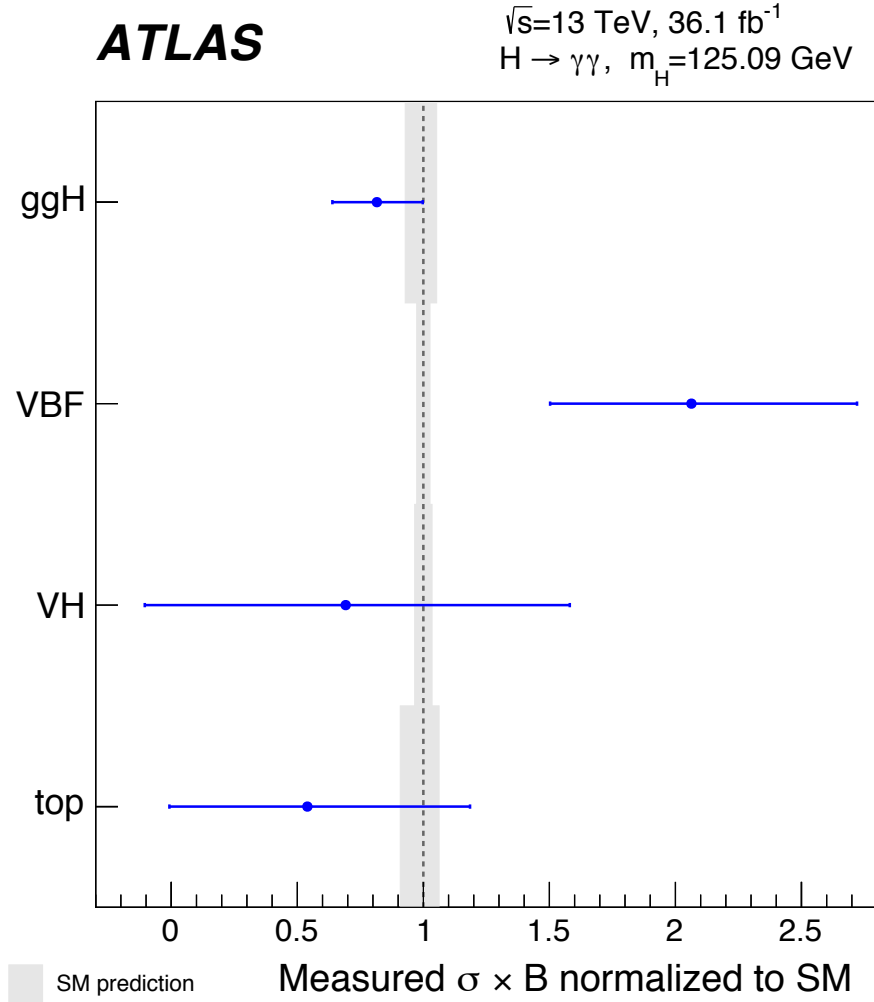
Figure 14: Summary plot of the measured production-mode cross sections times the Higgs to diphoton branching ratio. For illustration purposes the central values have been divided by their SM expectations but no additional theory uncertainties have been added to the uncertainty of the ratio. The uncertainties in the predicted SM cross sections are shown in gray bands in the plot. The fitted value of σ_{top} corresponds to the sum of $t\bar{t}H$, tHq, and tHW production-mode cross sections under the assumption that their relative ratios are as predicted by the SM. The VH production mode cross-section values are determined under the assumption that the ratio of the WH and ZH production-mode cross sections is as predicted by the SM and includes production from both the quark and gluon initial states. The $b\bar{b}H$ contributions are merged with ggH.
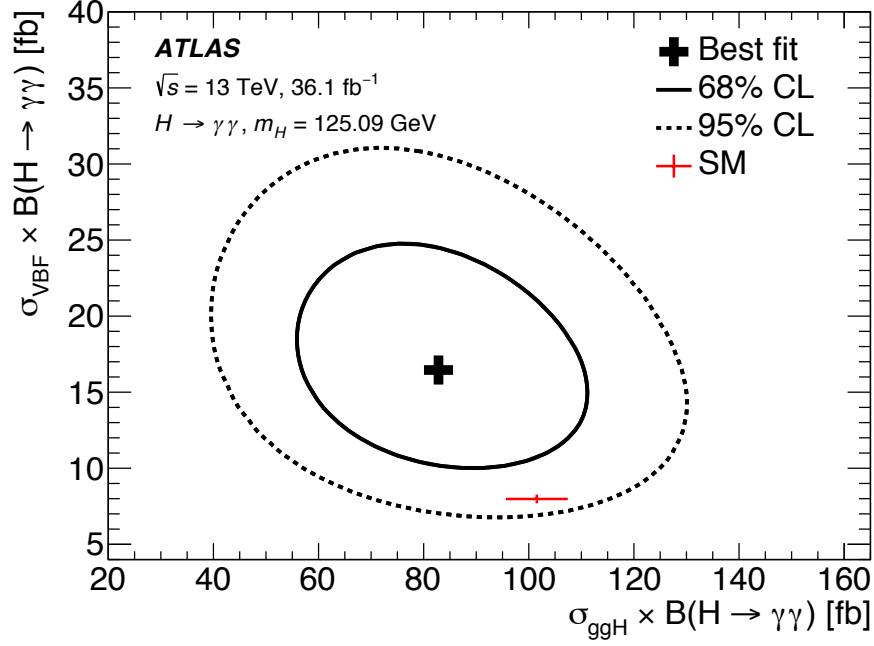
Figure 15: Likelihood contours in the $(\sigma_{ggH} \times B(H \rightarrow \gamma\gamma), \sigma_{VBF} \times B(H \rightarrow \gamma\gamma))$ plane, compared to the Standard Model prediction (red cross) for a Higgs boson mass $m_H = 125.09$ GeV.

of presentation to the central values of their SM predictions, are[6]

$$\frac{\sigma_{VBF}/\sigma_{ggH}}{(\sigma_{VBF}/\sigma_{ggH})^{SM}} = 2.5 \, {}^{+1.3}_{-0.9} = 2.5 \, {}^{+1.1}_{-0.8} \, (\text{stat.}) \, {}^{+0.5}_{-0.3} \, (\text{exp.}) \, {}^{+0.5}_{-0.3} \, (\text{theo.})$$

$$\frac{\sigma_{VH}/\sigma_{ggH}}{(\sigma_{VH}/\sigma_{ggH})^{SM}} = 0.9 \, {}^{+1.3}_{-1.0} = 0.9 \, {}^{+1.2}_{-0.9} \, (\text{stat.}) \, {}^{+0.3}_{-0.3} \, (\text{exp.}) \, {}^{+0.2}_{-0.1} \, (\text{theo.})$$

$$\frac{\sigma_{top}/\sigma_{ggH}}{(\sigma_{top}/\sigma_{ggH})^{SM}} = 0.7 \, {}^{+0.8}_{-0.7} = 0.7 \, {}^{+0.8}_{-0.7} \, (\text{stat.}) \, {}^{+0.2}_{-0.1} \, (\text{exp.}) \, {}^{+0.2}_{-0.0} \, (\text{theo.})$$

The ratios are also given in Table 10, along with their statistical, experimental and theoretical uncertainties without the normalization to the central values of the SM predictions. Both the measurements of the ggH and VBF production modes and the evaluations of the VH and top production modes agree within 1–2 σ with the SM expectations. Appendix G.2 provides the expected uncertainties for the production mode cross sections.

8.2.4 Simplified template cross sections

As the current data are not yet sensitive to all of the 31 regions with $|y_H| < 2.5$ (assuming SM acceptance) of the "stage-1" scheme of the simplified template cross-section framework, simplified

---

[6] The quoted theory uncertainty only accounts for the uncertainty in the acceptance. The production cross-section uncertainties are not included in the uncertainty budget. Uncertainties smaller than 0.05 are displayed as 0.0.

Table 10: Ratios of the production-mode cross sections with respect to the ggH cross section and uncertainties are shown. The SM predictions [7] with their uncertainties are shown for each production process.

Process ($|y_H| < 2.5$)	Result	Uncertainty				SM prediction
		Total	Stat.	Exp.	Theo.	
$\sigma_{\mathrm{VBF}}/\sigma_{\mathrm{ggH}}$	0.20	$+0.10$ -0.07	$\left(\begin{array}{c}+0.09\\-0.06\end{array}\right.$	$+0.04$ -0.02	$\left.\begin{array}{c}+0.04\\-0.02\end{array}\right)$	$0.078^{+0.005}_{-0.006}$
$\sigma_{\mathrm{VH}}/\sigma_{\mathrm{ggH}}$	0.04	$+0.06$ -0.05	$\left(\begin{array}{c}+0.06\\-0.04\end{array}\right.$	$+0.01$ -0.01	$\left.\begin{array}{c}+0.01\\-0.01\end{array}\right)$	$0.045^{+0.004}_{-0.005}$
$\sigma_{\mathrm{top}}/\sigma_{\mathrm{ggH}}$	0.009	$+0.010$ -0.009	$\left(\begin{array}{c}+0.010\\-0.009\end{array}\right.$	$+0.002$ -0.001	$\left.\begin{array}{c}+0.002\\-0.001\end{array}\right)$	$0.012^{+0.001}_{-0.002}$

Table 11: Best-fit values and uncertainties of the simplified template cross sections times branching ratio. The SM predictions [7] are shown for each region.

Measurement region ($|y_H| < 2.5$)	Result	Uncertainty			SM prediction
		Total	Stat.	Syst.	
ggH, 0 jet	37	$+16$ -15	$\left(\pm14\right.$	$\left.\begin{array}{c}+6\\-5\end{array}\right)$ fb	63 ± 5 fb
ggH, 1 jet, $p_T^H < 60$ GeV	13	$+13$ -12	$\left(\pm12\right.$	$\left.\begin{array}{c}+5\\-4\end{array}\right)$ fb	15 ± 2 fb
ggH, 1 jet, $60 \leq p_T^H < 120$ GeV	5	±6	$\left(\pm6\right.$	$\left.\begin{array}{c}+2\\-1\end{array}\right)$ fb	10 ± 2 fb
ggH, 1 jet, $120 \leq p_T^H < 200$ GeV	2.8	$+1.7$ -1.6	$\left(\begin{array}{c}+1.6\\-1.5\end{array}\right.$	$\left.\begin{array}{c}+0.7\\-0.5\end{array}\right)$ fb	1.7 ± 0.3 fb
ggH, ≥ 2 jet	20	$+9$ -8	$\left(\pm8\right.$	$\left.\begin{array}{c}+4\\-3\end{array}\right)$ fb	11 ± 2 fb
$qq \rightarrow Hqq, p_T^j < 200$ GeV	15	$+6$ -5	$\left(\pm5\right.$	$\left.\begin{array}{c}+3\\-2\end{array}\right)$ fb	10 ± 0.5 fb
ggH $+ qq \rightarrow Hqq, \mathrm{BSM - like}$	2.0	±1.4	$\left(\pm1.3\right.$	$\left.\pm0.6\right)$ fb	1.8 ± 0.4 fb
VH, leptonic	0.7	$+1.4$ -1.3	$\left(\begin{array}{c}+1.4\\-1.2\end{array}\right.$	$\left.\begin{array}{c}+0.4\\-0.3\end{array}\right)$ fb	1.4 ± 0.1 fb
Top	0.7	$+0.8$ -0.7	$\left(\begin{array}{c}+0.8\\-0.7\end{array}\right.$	$\left.\begin{array}{c}+0.2\\-0.1\end{array}\right)$ fb	1.3 ± 0.1 fb

template cross sections are reported for 10 phase space regions obtained from merging the initial 31 as described in Section 1.2 and Table 1. To retain sensitivity to BSM Higgs boson production, the $p_T^H > 200$ GeV gluon–gluon fusion and $p_T^j > 200$ GeV VBF regions are not merged with other regions. This scheme has been chosen to reduce strong anti-correlations between the measured cross sections and to keep measurements near or below 100% total uncertainty. In the likelihood, the signal yield N_{sig}^i in each category i is the sum over the yields $N_{\mathrm{sig},r}^i$ expected from each of the 9 regions r of phase space, where $N_{\mathrm{sig},r}^i = \int L \, \mathrm{d}t \times \sigma_r^{\mathrm{SM}} \times B^{\mathrm{SM}}(H \rightarrow \gamma\gamma) \times \epsilon_r^i$ and the additional region corresponds to the difference of the cross sections for the $p_T^H > 200$ GeV gluon–gluon fusion and $p_T^j > 200$ GeV VBF regions. The observed cross sections are reported in Table 11. These measurements have been defined to minimize theoretical uncertainties and are strongly dominated by experimental uncertainty, hence only the total systematic uncertainty is reported.
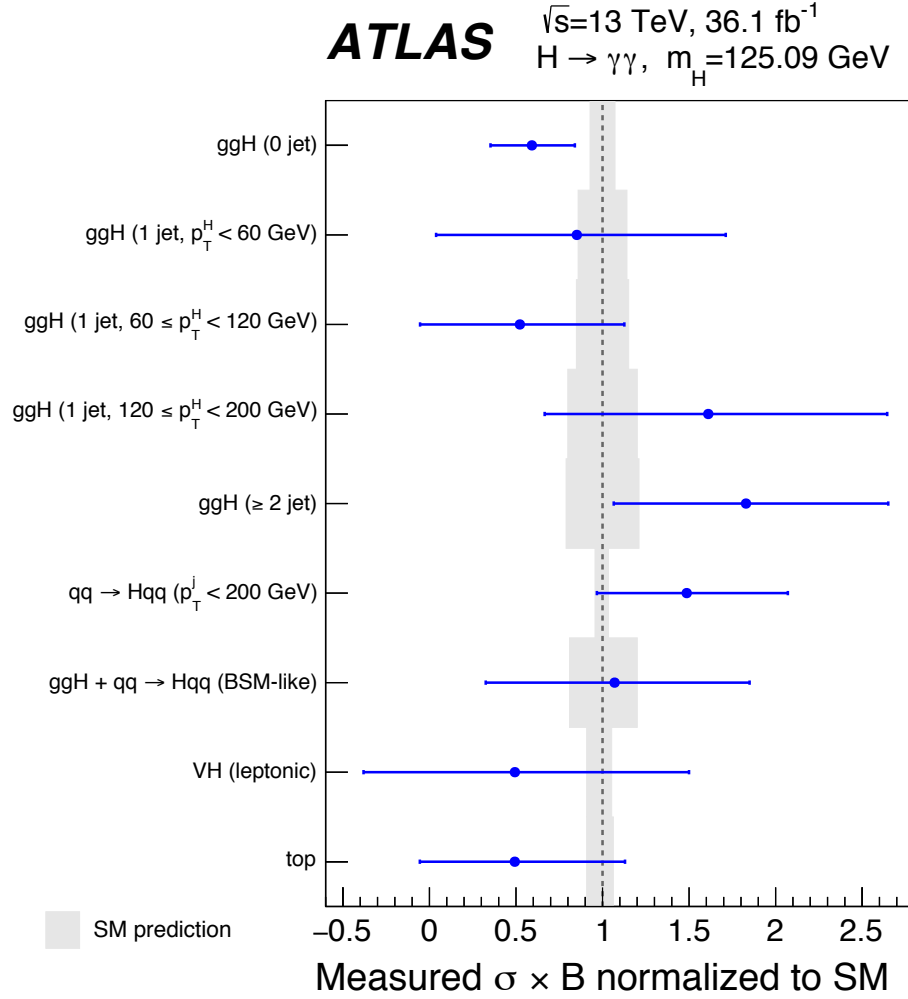
Figure 16: Summary plot of the measured simplified template cross sections times the Higgs to diphoton branching ratio. For illustration purposes the central values have been divided by their SM expectations but no additional theory uncertainties have been included in the uncertainty of the ratio due to this. The uncertainties in the predicted SM cross sections are shown in gray in the plot. The definition of the measured regions can be found in Table 1. The fitted value of $\sigma(\text{top})$ corresponds to the sum of $t\bar{t}H$ and tH production-mode cross sections under the assumption that their relative ratios are as predicted by the SM. The $\sigma(\text{VH, leptonic})$ cross-section values are determined under the assumption that the ratio of the WH and ZH production mode cross sections is as predicted by the SM and includes production from both the quark and gluon initial states. The $b\bar{b}H$ contributions are merged with ggH.

The evaluated cross sections including their correlations are summarized in Figures 16 and 17. The expected Standard Model correlations can be found in Appendix H. All observed cross sections are in agreement with the Standard Model values. The Standard Model prediction is determined using the generators in Section 4 and the theory uncertainties due to missing higher-order corrections and due to the chosen PDF set are constructed as described in Section 7.3. The largest deviation ($1.7\,\sigma$) from the SM prediction is found in the ggH, 0 jet bin. The difference of the cross sections for the $p_\text{T}^H > 200\,\text{GeV}$ ggH and $p_\text{T}^j > 200\,\text{GeV}$ VBF regions is found to be $4.8^{+2.9}_{-2.7}$ fb.
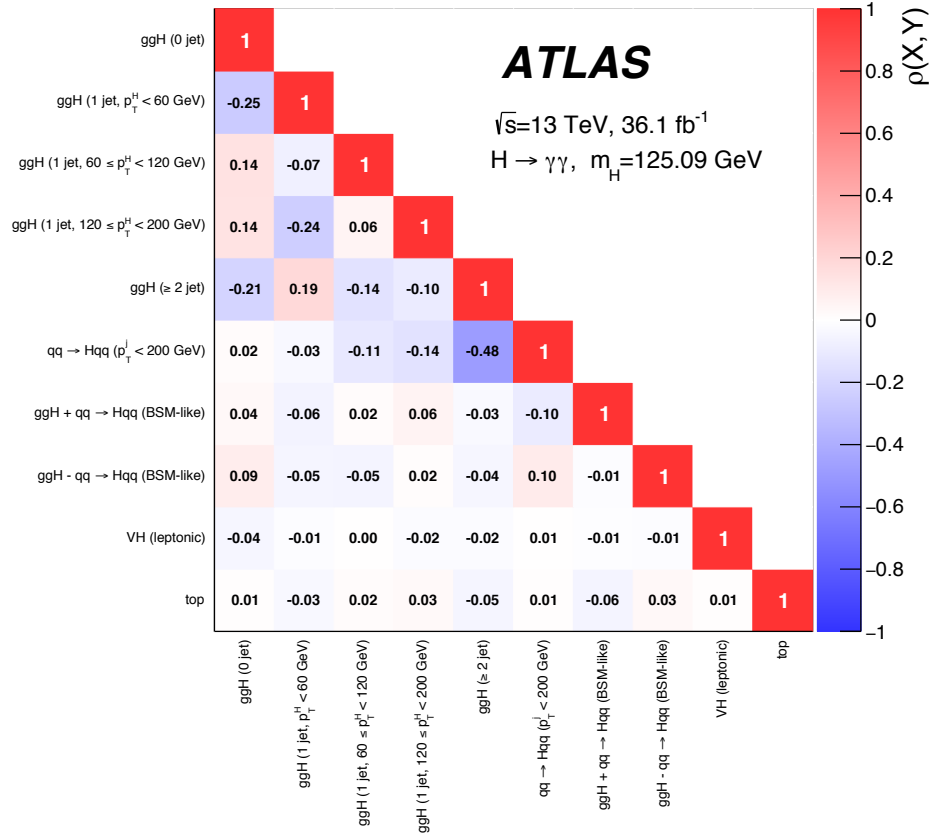
Figure 17: Observed correlations between the measured simplified template cross sections, including both the statistical and systematic uncertainties. The color indicates the size of the correlation.

Table 12: Observed and expected upper limits at 95% CL on the simplified template cross section times the Higgs to diphoton branching ratio in the BSM sensitive phase space with $p_T^j > 200$ GeV. The median expected limits are given for either the case when the true value of the cross section under study is SM-like ($\sigma = \sigma_{SM}$) or zero. The $\pm 1\,\sigma$ and $\pm 2\,\sigma$ intervals for the expected upper limit ($\sigma = 0$ fb) are also reported.

Measurement	Observed	Expected Limit ($\sigma = \sigma_{SM}$)	Expected Limit ($\sigma = 0$ fb)	$+2\sigma$	$+1\sigma$	-1σ	-2σ
$ggH + qq \to Hqq$, BSM $-$ like	4.4 fb	4.3 fb	2.7 fb	5.3 fb	3.8 fb	2.0 fb	1.5 fb

Limits at 95% CL on the ggH + $qq \to Hqq$ BSM-like ($p_T^j > 200$ GeV) bin are set, profiling all other parameters, as shown in Table 12. Appendix G.3 provides the expected uncertainties for all quoted simplified template cross sections.

In Appendix B additional measurements are reported for a "minimally merged" set of 15 cross sections of kinematic regions defined by the requirement that the fits to expected event yields be stable even in the presence of large uncertainties or correlations.

8.2.5 Coupling-strength fits

Following the tree-level-motivated framework and benchmark models recommended in Ref. [17], measurements of Higgs boson coupling-strength modifiers κ_j are implemented. In the narrow width approximation for the Higgs boson, the cross section $\sigma(i \to H \to \gamma\gamma)$ can be parameterized as

$$\sigma(i \to H \to \gamma\gamma) = \frac{\sigma_i(\vec{\kappa})\,\Gamma^{\gamma\gamma}(\vec{\kappa})}{\Gamma_H},$$

where Γ_H is the total width of the Higgs boson and $\Gamma^{\gamma\gamma}$ is the partial decay width to two photons. A set of coupling-strength modifiers, $\vec{\kappa}$, is introduced to parameterize possible deviations from the SM predictions of the Higgs boson coupling to SM bosons and fermions. For a given production process or decay mode j, a coupling-strength modifier κ_j is defined such that:

$$\kappa_j^2 = \sigma_j/\sigma_{j,\text{SM}} \quad \text{or} \quad \kappa_\gamma^2 = \Gamma^{\gamma\gamma}/\Gamma_{\text{SM}}^{\gamma\gamma},$$

where all κ_j values equal unity in the SM. Here, by construction, the SM cross sections and branching ratio include the best available higher-order QCD and EW corrections. This higher-order accuracy is not necessarily preserved for κ_j values different from unity, but the dominant higher-order QCD corrections factorize to a large extent from any rescaling of the coupling strengths and are therefore assumed to remain valid over the entire range of κ_j values considered.

Individual coupling-strength modifiers corresponding to tree-level Higgs boson couplings to different particles are introduced as well as two effective coupling-strength modifiers, κ_g and κ_γ, which describe the loop processes for ggH production and $H \to \gamma\gamma$ decay. This is possible because BSM particles that might be present in these loops are not expected to appreciably change the kinematics of the corresponding process. The $gg \to H$ and $H \to \gamma\gamma$ loop processes can thus be studied through these effective coupling-strength modifiers, providing sensitivity to potential BSM particles in the loops. In contrast, the $gg \to ZH$ process, which occurs at LO through box and triangular loop diagrams, is always taken into account by resolving the loop in terms of the corresponding coupling-strength modifiers (κ_Z and κ_t). No decays to particles other than those predicted in the SM are assumed to take place. These considerations and the limited sensitivity of the data available in this analysis lead to introducing two distinct models.

In the first model, the two parameters κ_g and κ_γ introduced above are tested assuming that all other couplings are as in the SM. The 68% and 95% CL two-dimensional contours of both effective couplings are shown in Figure 18(a) and the best fit values and uncertainties are $\kappa_g = 0.76^{+0.17}_{-0.14}$ and $\kappa_\gamma = 1.16^{+0.14}_{-0.14}$.

In a second model, universal coupling-strength modifiers, κ_F (for all fermions) and κ_V (for all bosons), are defined that resolve the $gg \to H$ and $H \to \gamma\gamma$ loops:

$$\kappa_F = \kappa_t = \kappa_b = \kappa_\tau = \kappa_\mu\,,$$
$$\kappa_V = \kappa_W = \kappa_Z\,.$$

The 68% and 95% CL two-dimensional contours of both parameters are shown in Figure 18(b) and the best fit values and uncertainties are $\kappa_F = 0.64^{+0.18}_{-0.14}$ and $\kappa_V = 0.92^{+0.08}_{-0.07}$. Due to the very limited sensitivity to κ_b, κ_τ and κ_μ, the shown CLs would not change if these coupling-strength modifiers would be fixed to the SM expectation.
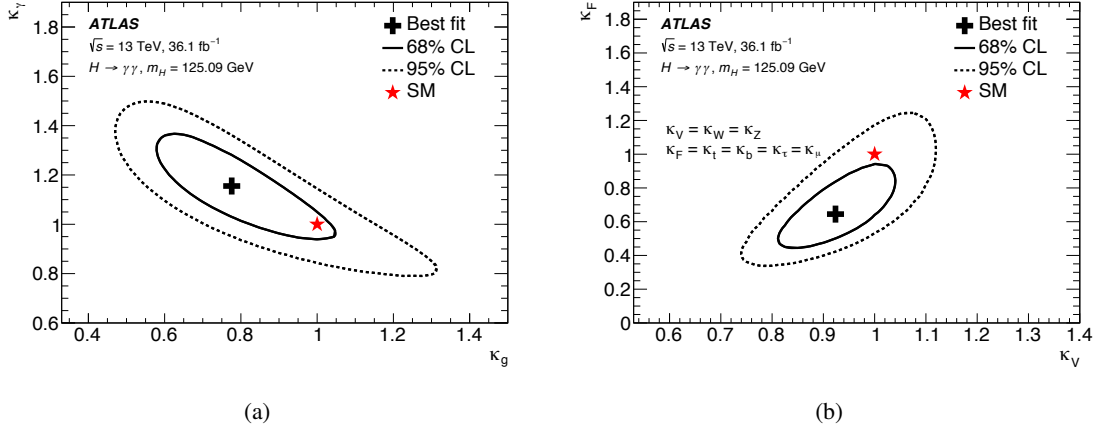
Figure 18: Likelihood contours in (a) the $(\kappa_g, \kappa_\gamma)$ plane, and (b) the (κ_V, κ_F) plane, compared to the Standard Model prediction (red star) for a Higgs boson mass $m_H = 125.09$ GeV. In (a), all coupling-strength modifiers other than κ_g and κ_γ are fixed to their SM value. In (b), the $gg \to H$ and $H \to \gamma\gamma$ loops are resolved in terms of two universal coupling-strength modifiers κ_F and κ_V, under the assumption that $\kappa_V = \kappa_W = \kappa_Z$ and $\kappa_F = \kappa_t = \kappa_b = \kappa_\tau = \kappa_\mu$.

Table 13: Best-fit values and uncertainties of $\kappa_{g\gamma}$, λ_{Vg}, and λ_{tg}.

Parameter	Result	Uncertainty			
		Total	Stat.	Exp.	Theo.
$\kappa_{g\gamma}$	0.90	± 0.10	± 0.09	± 0.04	$^{+0.04}_{-0.03}$
λ_{Vg}	1.41	$^{+0.31}_{-0.26}$	$^{+0.28}_{-0.23}$	$^{+0.10}_{-0.07}$	$^{+0.04}_{-0.03}$
λ_{tg}	0.8	$^{+0.4}_{-0.6}$	$^{+0.4}_{-0.6}$	± 0.1	$^{+0.1}_{-0.0}$

The SM prediction is found within the 68% CL contour for the first model and within the 95% CL contour for the second model.

Finally, a set of three ratios is constructed to probe the loop vertices (κ_g, κ_γ), total width (κ_H), and the vector and top couplings (κ_t and κ_V respectively): $\kappa_{g\gamma} = \kappa_g\kappa_\gamma/\kappa_H$, $\lambda_{Vg} = \kappa_V/\kappa_g$, and $\lambda_{tg} = \kappa_t/\kappa_g$. The parameter λ_{tg} is allowed to be negative to exploit the sensitivity to the relative sign from the tH and $gg \to ZH$ processes. The expected and observed sensitivities to the relative sign are illustrated in Figure 19. The bottom quark Yukawa coupling strength is kept fixed to the top quark Yukawa coupling strength ($\lambda_{bg} = \lambda_{tg}$); this contribution is irrelevant to the λ_{tg} measurement as there is no sensitivity to $b\bar{b}H$ in the analysis. All other parameters are assumed to be positive without losing generality. The inclusion of κ_H in the parameterization allows for non-SM decays of the Higgs boson, but this parameter is not determined directly. The best fit values of these coupling ratios are summarized in Table 13.
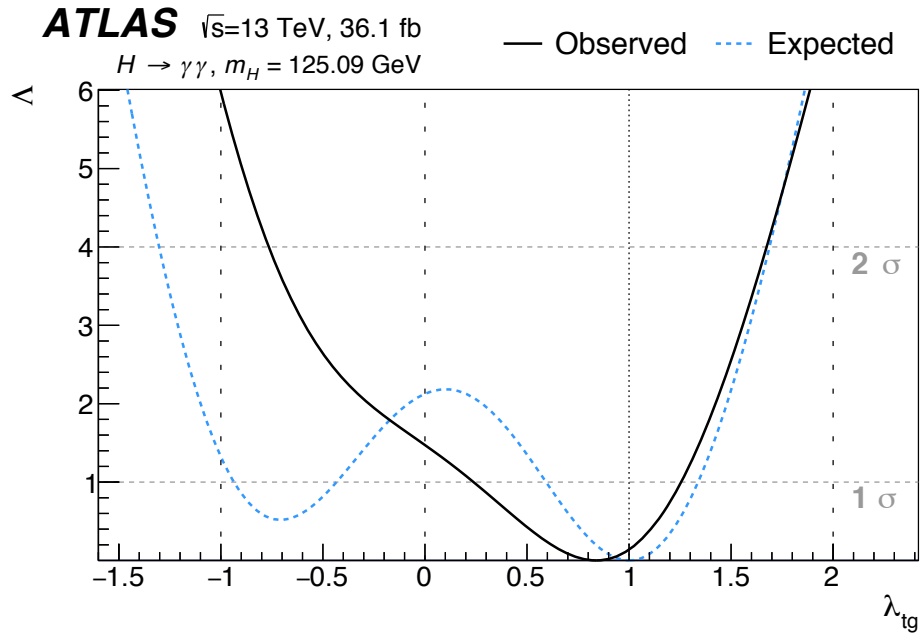
Figure 19: The profile of negative log-likelihood Λ of the observed and expected coupling-strength modifier ratio $\lambda_{tg} = \kappa_t/\kappa_g$. The parameters $\kappa_{g\gamma}$ and λ_{Vg} are also profiled within the fit. The intersections of the solid and dashed curves with the horizontal dashed line at $\Lambda = 1$ and $\Lambda = 4$ indicate the 1 and 2 σ confidence intervals of the observed and expected results, respectively.

9 Measurement of fiducial integrated and differential cross sections

The measurement of fiducial integrated and differential cross sections provides an alternative way to study the properties of the Higgs boson and to search for physics beyond the Standard Model. The fiducial volumes are defined to closely mimic the detector-level photon and object selections described in Section 5. This reduces the model-dependence of the quoted cross sections in contrast to the per production mode simplified template cross-section measurements of Section 8.2.4. The cross sections are determined by correcting measured signal yields for experimental inefficiencies and resolution effects, and by taking into account the integrated luminosity of the data. Rather than separating individual production modes, fiducial regions are defined such that they are enriched with a given production mode: Fiducial cross sections are measured in a variety of phase space regions, sensitive to for instance gluon–gluon fusion Higgs boson production, vector-boson fusion production, but also to production of the Higgs boson in association with charged leptons, top quarks and neutrinos. Differential and double-differential cross sections are reported for variables related to the diphoton kinematics and the jet activity produced in the Higgs boson events. The observed signal yields are corrected for detector effects resulting in cross sections measured at the particle level. The full statistical and systematic correlations between measured distributions are determined and are available in HEPDATA along with the central values of the measured fiducial and differential cross sections to allow future comparisons and interpretations.

9.1 Particle-level fiducial definition of the Higgs boson diphoton cross sections

The fiducial volume at particle level is defined using particles with a mean lifetime $c\tau > 10$ mm. Only photons and leptons which do not originate from the decay of hadrons are considered.[7] The two highest-p_T photons with $|\eta| < 2.37$ – excluding $1.37 < |\eta| < 1.52$ – are selected as the diphoton system. The leading (subleading) photon is required to satisfy $p_T/m_{\gamma\gamma} > 0.35$ (0.25), where $m_{\gamma\gamma} = m_H = 125.09$ GeV. Furthermore, for each photon the scalar p_T-sum of charged particles with $p_T > 1$ GeV within a cone of $\Delta R = 0.2$ around the photon is required to be less than 5% of the photon p_T. The lepton four-momentum is defined as the combination of an electron (or muon) and all nearby photons within $\Delta R < 0.1$ that do not originate from the decay of a hadron. Muons are required to have $p_T > 15$ GeV and $|\eta| < 2.7$. Electrons are required to have $p_T > 15$ GeV and $|\eta| < 2.47$, excluding the region $1.37 < |\eta| < 1.52$, and are rejected if the distance ΔR to a photon with $p_T > 15$ GeV is less than 0.4. Jets are reconstructed from all particles, excluding muons and neutrinos, using the anti-k_t algorithm with a radius parameter of 0.4. Unless stated otherwise, jets are required to have $p_T > 30$ GeV, $|y| < 4.4$ and to be well separated from photons with $p_T > 15$ GeV ($\Delta R > 0.4$) and electrons ($\Delta R > 0.2$). The acceptance for the VBF-enhanced fiducial region (introduced in Section 9.2) is increased by loosening the p_T cut to 25 GeV. Jets are considered to originate from a b-hadron if there is a b-hadron with $p_T > 5$ GeV within a cone of size $\Delta R = 0.4$ around the jet.

The missing transverse momentum is defined as the vector sum of neutrino transverse momenta, for neutrinos that do not originate from the decay of a hadron. The particle-level fiducial definition is summarized in Table 14.

---

[7] Leptons originating from the decay of τ leptons are only considered if the τ lepton itself did not originate from the decay of hadrons.

Table 14: Summary of the particle-level definitions of the five fiducial integrated regions described in the text. The photon isolation $p_T^{iso,0.2}$ is defined analogously to the reconstructed-level track isolation as the transverse momentum of the system of charged particles within $\Delta R < 0.2$ of the photon.

Objects	Definition
Photons	$\|\eta\| < 1.37$ or $1.52 < \|\eta\| < 2.37$, $p_T^{iso,0.2}/p_T^\gamma < 0.05$
Jets	anti-k_t, $R = 0.4$, $p_T > 30$ GeV, $\|y\| < 4.4$
Leptons, ℓ	e or μ, $p_T > 15$ GeV, $\|\eta\| < 2.47$ for e (excluding $1.37 < \|\eta\| < 1.52$) and $\|\eta\| < 2.7$ for μ

Fiducial region	Definition
Diphoton fiducial	$N_\gamma \geq 2$, $p_T^{\gamma_1} > 0.35\, m_{\gamma\gamma} = 43.8$ GeV, $p_T^{\gamma_2} > 0.25\, m_{\gamma\gamma} = 31.3$ GeV
VBF-enhanced	Diphoton fiducial, $N_j \geq 2$ with $p_T^{jet} > 25$ GeV,
	$m_{jj} > 400$ GeV, $\|\Delta y_{jj}\| > 2.8$, $\|\Delta\phi_{\gamma\gamma,jj}\| > 2.6$
$N_{\text{lepton}} \geq 1$	Diphoton fiducial, $N_\ell \geq 1$
High E_T^{miss}	Diphoton fiducial, $E_T^{\text{miss}} > 80$ GeV, $p_T^{\gamma\gamma} > 80$ GeV
$t\bar{t}H$-enhanced	Diphoton fiducial, $\left(N_j \geq 4, N_{b\text{-jets}} \geq 1\right)$ or $\left(N_j \geq 3, N_{b\text{-jets}} \geq 1, N_\ell \geq 1\right)$

9.2 Fiducial integrated and differential cross sections

The cross section (σ_i) in a fiducial integrated region, and the differential cross section ($d\sigma_i/dx$) in a bin of variable x, are given by

$$\sigma_i = \frac{N_i^{\text{sig}}}{c_i \int L\, dt} \qquad \text{and} \qquad \frac{d\sigma_i}{dx} = \frac{N_i^{\text{sig}}}{c_i\, \Delta x_i \int L\, dt},$$

where N_i^{sig} is the number of signal events as introduced in Section 6.3, $\int L\, dt$ is the integrated luminosity of the data set, c_i is a correction factor that accounts for detector inefficiency and resolution, and Δx_i is the bin width. The correction factors are determined using the simulated samples discussed in Section 4. This bin-by-bin method showed similar performance to that of the non-regularized inversion of the full migration matrix and of regularized methods [112–114] within the current statistical accuracy and systematic uncertainties.

The correction factor is 0.75 ± 0.03 in the diphoton fiducial region, defined to unfold all signal events to the fiducial definition of Section 9.1, which is dominated by the photon identification and isolation efficiency. The correction factor also accounts for migrations caused by detector energy resolution and migration in and out of the fiducial phase space due to detector effects. In addition, the correction factor removes a small fraction (0.5% for the diphoton fiducial region) of reconstructed $H \to ff\gamma$ Dalitz decays.[8]

The correction factor is different in fiducial regions defined by associated jet activity, for example, taking values of 0.66 and 0.87 for the $t\bar{t}H$ and VBF fiducial regions defined in the next section, respectively. For the diphoton fiducial region the uncertainty in the correction factor is dominated by the theoretical modeling uncertainty. For the $t\bar{t}H$ and VBF fiducial regions the uncertainties in the correction factors are dominated by uncertainties associated with the knowledge of the jet energy scale and energy resolution, as well as the theoretical modeling. A more complete breakdown is given in Section 9.5.6 and Table 16.
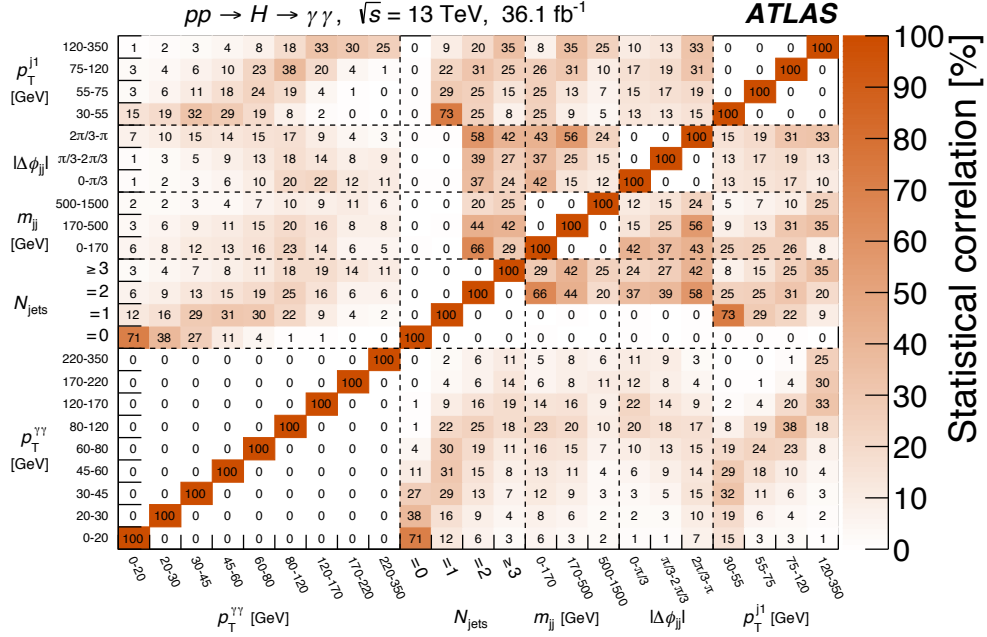
---

[8] Here f denotes any fermion but the top quark.

Figure 20: The observed statistical correlations between $p_T^{\gamma\gamma}$, N_{jets}, m_{jj}, $|\Delta\phi_{jj}|$, and $p_T^{j_1}$ are shown. These correlations were determined from an ensemble of 100,000 bootstrapped data sets which are each reanalyzed using an unbinned maximum-likelihood fit of the diphoton invariant mass spectrum to extract the correlations.

The measured differential cross sections in different observables are partially statistically correlated, since they correspond to the same data set in a given fiducial region. These correlations are obtained using a random sampling with replacement method on the detector-level data, often referred to as 'bootstrapping' [115]. Bootstrapped event samples are constructed from the data by assigning each event a weight pulled from a Poisson distribution with unit mean. All measured differential distributions are then reconstructed using the weighted events, and the signal yields in each bin of a differential distribution are determined using an unbinned maximum-likelihood fit of the diphoton invariant mass spectrum. The procedure is repeated with statistically independent weights and the correlation between two bins of different distributions is determined from the obtained cross sections. Figure 20 shows as an illustration the determined correlations between $p_T^{\gamma\gamma}$, N_{jets}, m_{jj}, $|\Delta\phi_{jj}|$, and $p_T^{j_1}$: the lowest $p_T^{\gamma\gamma}$ bin, reconstructing events with a Higgs boson p_T between 0 and 20 GeV, is highly correlated with the zero-jet bin. The lowest $p_T^{j_1}$ bin, reconstructing events with a jet p_T between 30 and 55 GeV, is strongly correlated with the one-jet bin. And the lowest m_{jj} bin, reconstructing events with at least two jets and a dijet mass between 0 and 170 GeV, is strongly correlated with the two jet bin. The systematic correlations are obtained by fully correlating identical error sources described in Section 7 across bins and observables to construct the corresponding systematic covariance matrix. Knowledge of these correlations allows to simultaneously analyze all fiducial regions, differential and double differential cross sections. This is illustrated later in Section 9.5.8 with a simultaneous fit of the shown five variables of Figure 20 to set limits on new physics contributions.

## 9.3 Measurements of cross sections of fiducial integrated regions

Cross sections in five fiducial integrated regions are measured that target either specific Higgs boson production mechanisms or are sensitive to the presence of physics beyond the Standard Model. The selection criteria defining these regions are summarized in Table 14 and a description of each region follows:

1. Diphoton fiducial: This region unfolds all signal events after the selection presented in Section 5.

2. VBF-enhanced: This region retains all events with at least two jets and with an invariant dijet mass m_{jj} of at least 400 GeV, a large rapidity separation $|\Delta y_{jj}| > 2.8$, and an azimuthal difference between the Higgs boson and the dijet pair of $|\Delta\phi_{\gamma\gamma,jj}| > 2.6$. All variables are computed using the two highest-p_T jets in the event with $p_\mathrm{T} > 25$ GeV with matching detector-level cuts.

3. $N_\mathrm{lepton} \geq 1$: This region retains events that contain at least one electron or one muon with $p_\mathrm{T} > 15$ GeV. For electrons the pseudo-rapidity needs to satisfy $|\eta| < 2.47$ (excluding $1.37 < |\eta| < 1.52$) and for muons $|\eta| < 2.7$ is required. Such events are enriched in Higgs bosons produced in association with a vector boson.

4. High $E_\mathrm{T}^\mathrm{miss}$: This region retains events with missing transverse momentum $E_\mathrm{T}^\mathrm{miss} > 80$ GeV and $p_\mathrm{T}^{\gamma\gamma} > 80$ GeV is defined to study VH production and possible contributions of Higgs boson production with dark matter particles. The simultaneous requirement that the Higgs boson system balances the missing transverse momentum reduces the fraction of selected events at detector level without particle-level $E_\mathrm{T}^\mathrm{miss} > 80$ GeV.

5. $t\bar{t}H$-enhanced: This region retains events with either at least one lepton and three jets or no leptons and four jets to study Higgs boson production in association with top quarks. In addition, one of the jets needs to be identified as originating from a bottom quark.

The expected composition of Higgs boson events in the Standard Model after reconstruction and at particle level is summarized in Figure 21. At particle level the VBF-enhanced fiducial region contains about 65% VBF and 32% ggH events. The particle-level $N_\mathrm{lepton} \geq 1$ region is dominated by WH (47%), $t\bar{t}H$ (37%) and ZH (13%) production. The particle-level high $E_\mathrm{T}^\mathrm{miss}$ region is populated by about equal amounts of WH, ZH, and $t\bar{t}H$ (32%, 30%, and 35%). Finally, the particle-level $t\bar{t}H$-enhanced region contains about 80% $t\bar{t}H$ events.

The fitted invariant mass spectra for all regions are shown in Figures 22 and 23. The results of signal-plus-background fits to these spectra is shown, displaying both the total sum and the background-only component as well as the residuals between the data and the background. In the diphoton fiducial region, the Higgs boson signal is clearly visible on the falling non-resonant background. In total, $1491 \pm 248\,\text{(stat.)} \pm 64\,\text{(syst.)}$ Higgs boson signal events are extracted. Clear evidence for Higgs boson production is observed in the VBF-enhanced region with $117 \pm 26\,\text{(stat.)} \pm 4\,\text{(syst.)}$ signal events, corresponding to an observed significance of 4.2 standard deviations.

The remaining three regions all show positive signal yields with large, predominantly statistical, uncertainties: 14 ± 11, 19 ± 11, 6 ± 15 for the $N_\mathrm{lepton} \geq 1$, high $E_\mathrm{T}^\mathrm{miss}$, and $t\bar{t}H$-enhanced fiducial regions, respectively, and the error corresponds to the sum of the statistical and systematic uncertainties.
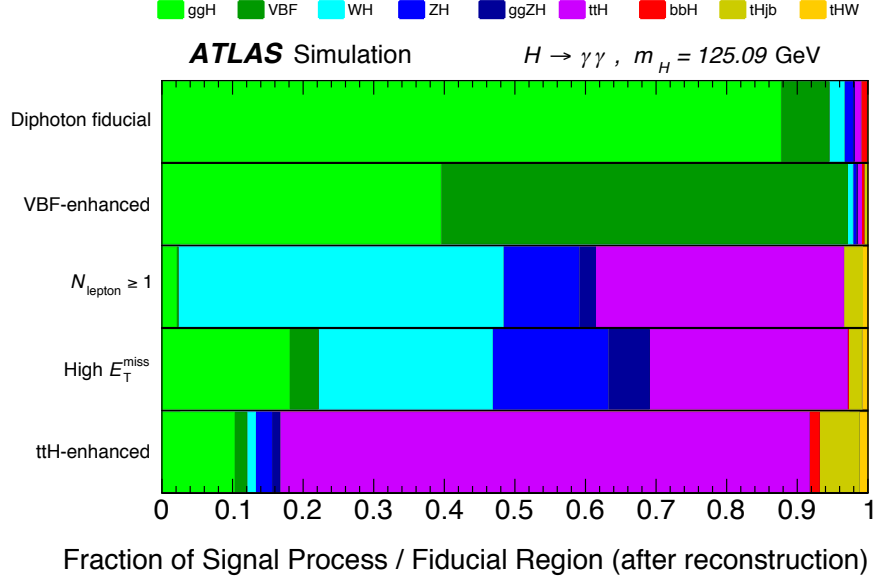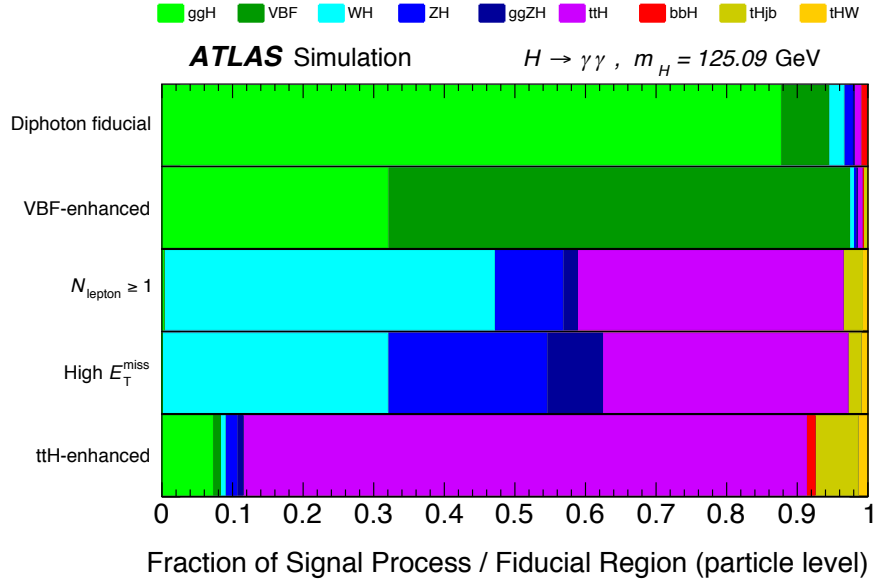
Figure 21: The expected composition of Higgs boson events in each fiducial region (a) after the reconstruction and (b) at particle-level. Details about the reconstruction can be found in Section 5 and the definition of the particle-level fiducial volume is given in Section 9.1.
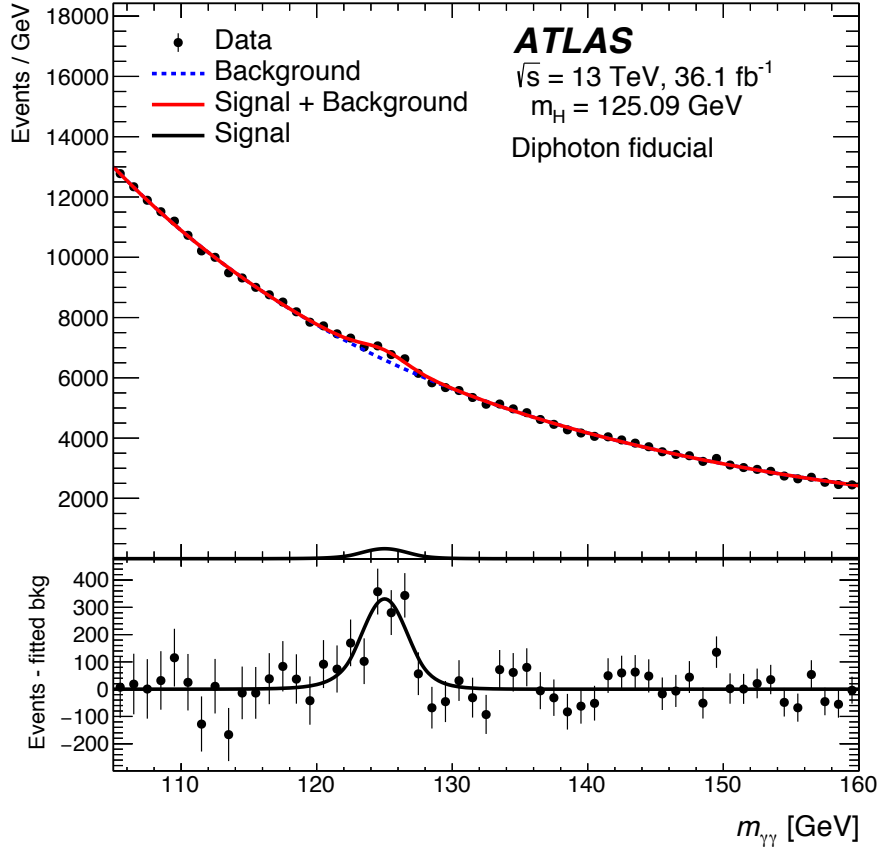
Figure 22: Diphoton invariant mass $m_{\gamma\gamma}$ spectrum observed in the 2015 and 2016 data at $\sqrt{s}$ = 13 TeV for events in the diphoton fiducial region. The solid red curve shows the fitted signal-plus-background model when the Higgs boson mass is constrained to be 125.09 ± 0.24 GeV. The background component of the fit is shown with the dotted blue curve. The signal component of the fit is shown with the solid black curve. The bottom plot shows the residuals between the data and the background component of the fitted model.

The cross section for $pp \to H \to \gamma\gamma$ measured in the diphoton fiducial region is

$$\sigma_{\text{fid}} = 55 \pm 9\,(\text{stat.}) \pm 4\,(\text{exp.}) \pm 0.1\,(\text{theo.})\,\text{fb},$$

which is to be compared with the Standard Model prediction of 64 ± 2 fb. The gluon–gluon fusion contribution to the Standard Model prediction and its uncertainty are taken to be the N^3LO QCD and NLO EW prediction of Refs. [7, 24, 31–34] corrected for the $H \to \gamma\gamma$ branching ratio and the fiducial acceptance. The fiducial acceptance is defined using the PowHEG NNLOPS prediction for gluon–gluon fusion [23]. The contributions to the Standard Model prediction from the VBF, VH, $b\bar{b}H$ and $t\bar{t}H$ production mechanisms are determined using the particle-level predictions normalized with theoretical calculations as discussed in Section 4, and are collectively referred to as XH. The measured cross section is compatible with the Standard Model prediction and the observed ggH coupling strength measured in Section 8, as the diphoton fiducial region is dominated by gluon–gluon fusion production.
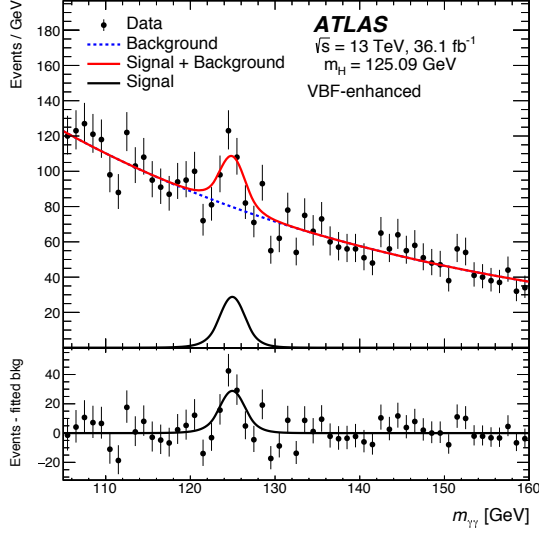
(a) VBF-enhanced
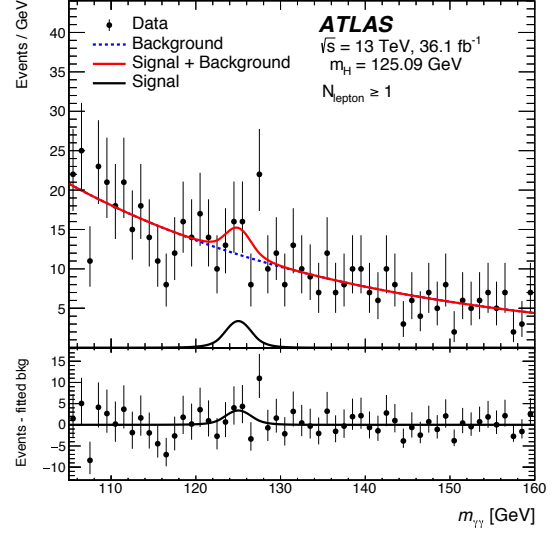
(b) $N_{\text{lepton}} \geq 1$
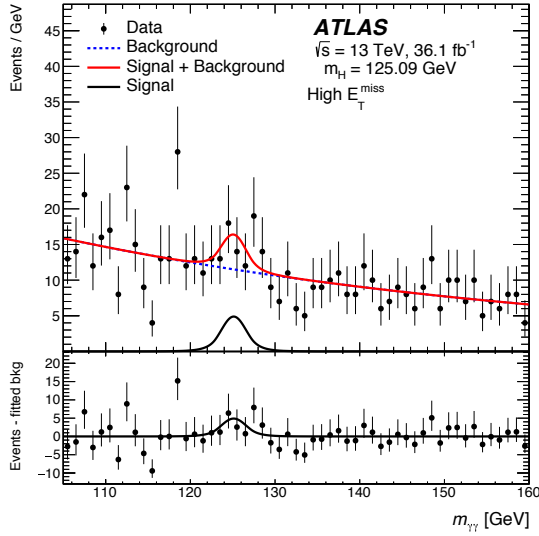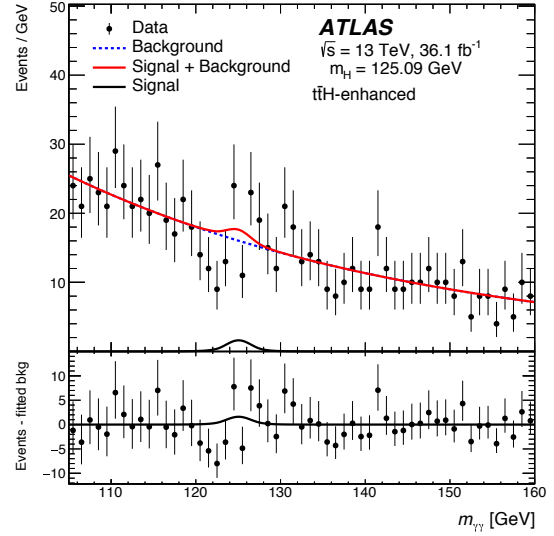
(c) High $E_{\text{T}}^{\text{miss}}$

(d) $t\bar{t}H$-enhanced

Figure 23: Diphoton invariant mass $m_{\gamma\gamma}$ spectra observed in the 2015 and 2016 data at $\sqrt{s}$ = 13 TeV for events in the (a) VBF-enhanced, (b) $N_{\text{lepton}} \geq 1$, (c) high $E_{\text{T}}^{\text{miss}}$, and (d) $t\bar{t}H$-enhanced fiducial regions. The solid red curve shows the fitted signal-plus-background model when the Higgs boson mass is constrained to be 125.09 ± 0.24 GeV. The background component of the fit is shown with the dotted blue curve. The signal component of the fit is shown with the solid black curve. The bottom plot shows the residuals between the data and the background component of the fitted model.

Table 15: The measured cross sections in the diphoton, VBF-enhanced, $N_{\text{lepton}} \geq 1$, high $E_{\text{T}}^{\text{miss}}$, and $t\bar{t}H$-enhanced fiducial regions. The gluon–gluon fusion contribution to the Standard Model prediction of the diphoton fiducial region is taken to be the N^3LO prediction of Refs. [7, 24, 31–34] corrected for the $H \rightarrow \gamma\gamma$ branching ratio and the fiducial acceptance. The gluon–gluon fusion contribution to the Standard Model for all the other regions is taken from the PowHEG NNLOPS prediction normalized with the N^3LO prediction and includes all theory uncertainties related to gluon–gluon fusion as discussed in Section 7.3. The contributions to the Standard Model prediction from VBF, VH $t\bar{t}H$ and $b\bar{b}H$ production mechanisms are determined using the particle-level predictions described in Section 4 normalized with theoretical calculations.

Fiducial region	Measured cross section	SM prediction	
Diphoton fiducial	55 ± 9 (stat.) ± 4 (exp.) ± 0.1 (theo.) fb	64 ± 2 fb	[N^3LO + XH]
VBF-enhanced	3.7 ± 0.8 (stat.) ± 0.5 (exp.) ± 0.2 (theo.) fb	2.3 ± 0.1 fb	[default MC + XH]
$N_{\text{lepton}} \geq 1$	≤ 1.39 fb 95% CL	0.57 ± 0.03 fb	[default MC + XH]
High $E_{\text{T}}^{\text{miss}}$	≤ 1.00 fb 95% CL	0.30 ± 0.02 fb	[default MC + XH]
$t\bar{t}H$-enhanced	≤ 1.27 fb 95% CL	0.55 ± 0.06 fb	[default MC + XH]

The cross section of the VBF-enhanced region is measured to be

$$\sigma_{\text{VBF-enhanced}} = 3.7 \pm 0.8 \,(\text{stat.}) \pm 0.5 \,(\text{exp.}) \pm 0.2 \,(\text{theo.}) \,\text{fb},$$

which is to be compared with the Standard Model prediction of 2.3 ± 0.1 fb. The gluon–gluon fusion part of the SM prediction is constructed from the PowHEG NNLOPS prediction for gluon–gluon fusion normalized with the N^3LO in QCD and NLO EW prediction of Refs. [7, 24, 31–34]. This prediction is labeled as "default MC" in the following and includes all theory uncertainties related to gluon–gluon fusion as discussed in Section 7.3.

For the $N_{\text{lepton}} \geq 1$, high $E_{\text{T}}^{\text{miss}}$, and $t\bar{t}H$-enhanced fiducial regions, limits on the cross sections are reported at the 95% CL.[9]

Figure 24 and Table 15 summarize measured cross sections of the fiducial regions and limits, and compare both to the Standard Model expectations, constructed as outlined above. The PowHEG NNLOPS prediction, without any additional corrections, is also shown. The uncertainty band is estimated using a set of scale variations and includes PDF uncertainties from eigenvector variations. The Standard Model predictions of all fiducial regions are in agreement with the corresponding measured cross sections.

---

[9] The quoted CL values were obtained using the unfolded cross sections and their corresponding uncertainties assuming Gaussian errors.
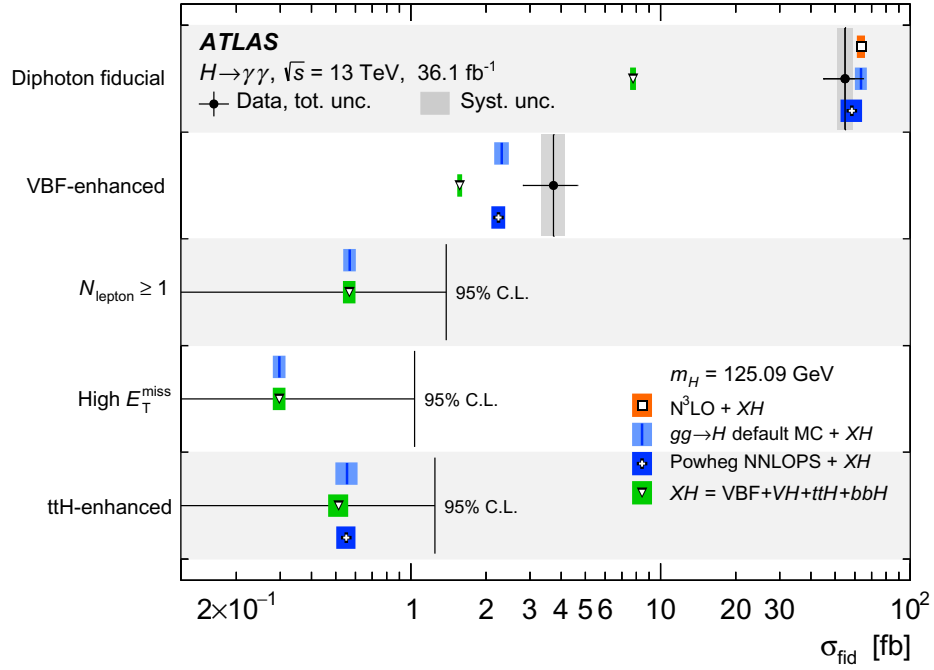
Figure 24: The measured cross sections or cross-section upper limits of the diphoton, VBF-enhanced, $N_{\text{lepton}} \geq 1$, high $E_{\text{T}}^{\text{miss}}$, and $t\bar{t}H$-enhanced fiducial regions are shown. The intervals on the vertical axis each represent one of these fiducial regions. The data are shown as filled (black) circles. The error bar on each measured cross section represents the total uncertainty in the measurement, with the systematic uncertainty shown as a dark gray rectangle. Each cross section limit is shown at the 95% confidence level. The measured cross sections are compared to a range of predictions and a detailed description of each prediction can be found in the text. All comparisons include the SM predictions arising from VBF, VH, $t\bar{t}H$, and $b\bar{b}H$, which are collectively labeled as XH.

9.4 Measurements of cross sections of inclusive and exclusive jet multiplicities

The production of Higgs bosons in association with jets is sensitive to the theoretical modeling in QCD and to the contribution of different Higgs boson production mechanisms. In the SM, events with zero or one jet are dominated by gluon–gluon fusion production. In events with two jets the contributions from VBF and VH production modes become more important. Higgs boson production in association with top quarks ($t\bar{t}H$) can be probed in events with the highest jet multiplicities. In BSM scenarios, the jet multiplicity distribution is sensitive to new heavy particles coupling to the Higgs boson and vector bosons. For the measurements presented here, jet multiplicity bins with zero, one, two, and at least three jets with p_T larger than 30 GeV and absolute rapidity $|y| < 4.4$ are defined. In addition, jet multiplicity bins with a p_T larger than 50 GeV are defined for zero, one, or at least two jets. The measured cross sections are compared to a range of predictions of gluon–gluon fusion production:

- The parton-level N³LO QCD and NLO EW prediction of Refs. [7, 24, 31–34]. This prediction is shown for the inclusive zero-jet cross section.

- The parton-level JVE+N³LO prediction of Ref. [116], which includes NNLL resummation in QCD of the p_T of the leading jet which is matched to the N³LO total cross section. This prediction is shown for the inclusive one-jet cross section.

- The parton-level STWZ-BLPTW predictions of Refs. [99, 101], which include NNLL′+NNLO resummation for the p_T of the leading jet in QCD, combined with a NLL′+NLO resummation in QCD for the subleading jet.[10] The numerical predictions for $\sqrt{s} = 13$ TeV are taken from Ref. [7]. This prediction is shown for the inclusive zero-, one- and two-jet cross sections as well as for the exclusive zero- and one-jet cross sections.

- The parton-level NNLOJET prediction of Refs. [117, 118] is a fixed-order NNLO prediction in QCD for inclusive H+one-jet production. This prediction is shown for the inclusive one-, two-jet, and three-jet cross sections as well as for the exclusive one- and two-jet cross sections.

- The parton-level GoSam prediction of Refs. [119, 120], which provides the fixed-order loop contributions accurate at NLO in QCD in the inclusive H + zero-jet, H + one-jet, H + two-jet, and H + three-jet regions. The real-emission contributions at fixed order in QCD are provided by Sherpa [64]. This prediction is shown for the inclusive one-, two-jet, and three-jet cross sections as well as for the exclusive one- and two-jet cross sections.

- The default MC prediction (Powheg NNLOPS normalized with the N³LO in QCD and NLO EW cross section) introduced in Section 9.3. This prediction is shown for all measured inclusive and exclusive jet cross sections.

- The Powheg NNLOPS prediction which is already described in Section 4. This prediction is shown for all measured inclusive and exclusive jet cross sections.

- The Sherpa (Meps@Nlo) prediction of Refs. [64, 65, 120–129] is accurate to NLO in QCD in the inclusive H + zero-jet, H + one-jet, H + two-jet, and H + three-jet regions and includes top-quark mass effects. The one-loop corrections are incorporated from GoSam [119, 120] and the different jet multiplicity regions are merged using the Meps@Nlo multijet merging technique. This prediction is shown for all measured inclusive and exclusive jet cross sections.

---

[10] The prime indicates that the leading contributions from N³LL (resp. NNLL) are included along with the full NNLL (resp. NLL) corrections.

- The MG5_ₐMC@NLO prediction of Refs. [46, 105], which includes up to two jets at NLO accuracy using the FxFx merging scheme [106]. The central merging scale is taken to be 30 GeV. The generated events are passed to Pythia8 [29] to provide parton showering and hadronization to create the full final state (without underlying event). This prediction is shown for all measured inclusive and exclusive jet cross sections.

All predictions but NNLOJET and Sherpa (Meps@Nlo) use the NNLO PDF set following the PDF4LHC15 recommendations. The NNLOJET prediction uses the CT14 NNLO PDF set [130] and Sherpa (Meps@Nlo) uses the NNPDF3.0PDF set [47]. GoSam, Sherpa (Meps@Nlo), and NNLOJET apply the kinematic selection on the final-state photons. For all other predictions, the fiducial acceptance is determined using Powheg NNLOPS. The cross sections of all parton-level predictions are multiplied with isolation correction factors to account for the efficiency of the fiducial photon isolation criterion. The additional uncertainties in the isolation correction are determined by studying multiple event generators and/or event generator tunes, and are included in the uncertainty bands of the parton-level predictions. No correction factors nor additional uncertainties to account for the impact of hadronization and the underlying event activity are applied, so the theory uncertainties in the parton-level predictions may be incomplete, but example values for such corrections and their uncertainties can be found in Table 24 in Appendix D. All other acceptance and correction factors along with their associated uncertainties can also be found in Appendix D.

No K-factors are applied to the predictions and the contributions from XH are also included in the comparison using the corresponding generators and cross sections described in Section 4.

Figure 25(a) shows exclusive and inclusive zero-, one- and two-jet cross sections and the inclusive three-jet cross section for jets defined with $p_{\rm T} > 30$ GeV. Figure 25(b) shows the exclusive zero- and one- and the inclusive two-jet cross section with $p_{\rm T} > 50$ GeV. The measured cross sections are in agreement with the Standard Model predictions, although there is a 1.5 σ deficit in the $N_{\rm jets}=$ 0 cross section for jets defined with $p_{\rm T} > 30$ GeV. As shown in Figure 20, there is a sizeable positive correlation between zero-jet and low-$p_{\rm T}^{\gamma\gamma}$ events, and a similar deficit is observed there (cf. Section 9.5.1).

9.5 Measurements of differential and double-differential cross sections

Eleven fiducial differential cross sections are measured that characterize the Higgs boson production kinematics, the kinematics of jets produced in association with the Higgs boson, the spin and CP quantum numbers of the Higgs boson and variables sensitive to the VBF production mechanism. In addition, two double-differential cross sections are reported. The measurement of seven additional variables can be found in Appendix C.

9.5.1 Measurements of cross sections probing the Higgs boson production kinematics

Measuring the transverse momentum of the diphoton system, $p_{\rm T}^{\gamma\gamma}$, probes the perturbative QCD modeling of the ggH production mechanism which is mildly sensitive to the bottom- and charm-quark Yukawa couplings [12]. The distribution at high transverse momentum is sensitive to new heavy particles coupling to the Higgs boson and to the top-quark Yukawa coupling. The rapidity distribution of the diphoton system, $|y_{\gamma\gamma}|$, is also sensitive to the modeling of the ggH production mechanism. The
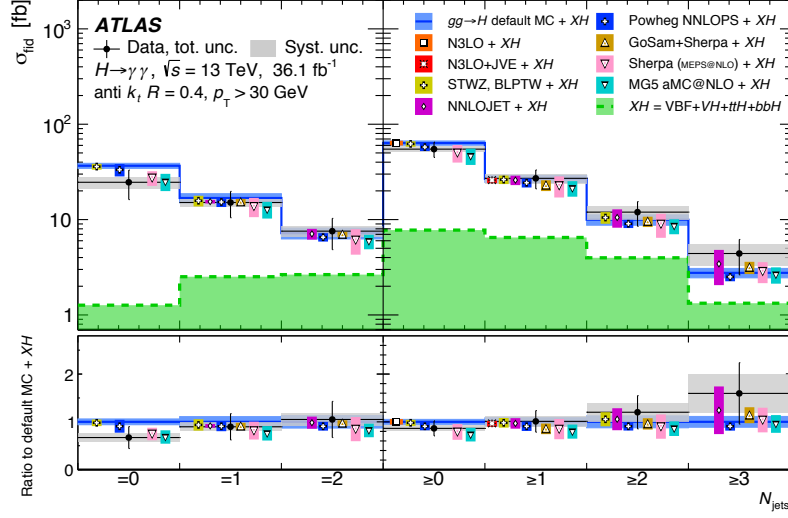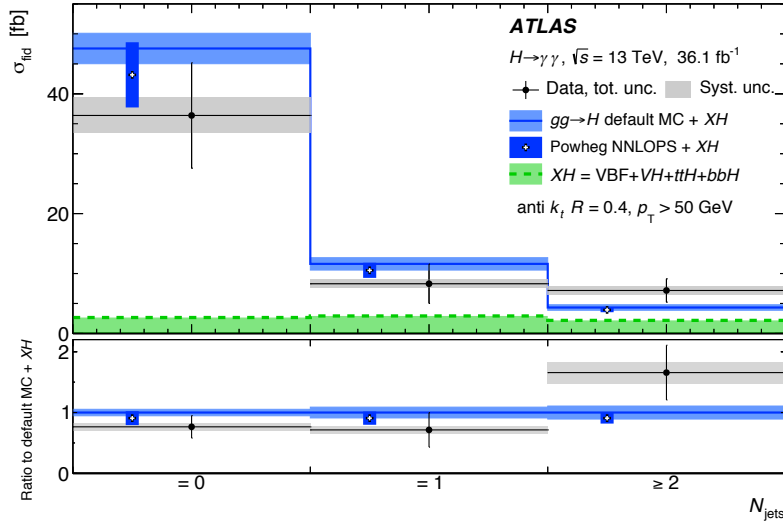
Figure 25: Cross sections for $pp \to H \to \gamma\gamma$ as a function of inclusive and exclusive jet multiplicities for jets with (a) $p_T > 30$ GeV and (b) $p_T > 50$ GeV. The data are shown as filled (black) circles. The vertical error bar on each data point represents the total uncertainty in the measured cross section and the shaded (gray) band is the systematic component. The measured differential cross sections are compared to a range of predictions and details can be found in the text. The width of the bands of each prediction reflects the total theoretical uncertainty. The small contribution from VBF, VH, $t\bar{t}H$, and $b\bar{b}H$ is also shown as a (green) histogram and denoted by XH.

differential cross sections for $pp \to H \to \gamma\gamma$ as a function of $p_T^{\gamma\gamma}$ and $|y_{\gamma\gamma}|$ are shown in Figure 26. The chosen bin widths are a compromise between retaining a sufficiently significant signal and providing spectra with good granularity. Each bin is chosen such that it retains an expected significance of at least two standard deviations, estimated using the Powheg NNLOPS and additional predictions described in Section 4 as well as using a fit to $m_{\gamma\gamma}$ sidebands. The measurements are compared to several predictions of gluon–gluon fusion:

- The default MC prediction (Powheg NNLOPS normalized with the N³LO in QCD and NLO EW cross section) introduced in Section 9.3.

- Hres [131, 132], which provides predictions at NNLO with p_T^H resummation at NNLL and differentially in $p_T^{\gamma\gamma}$. Finite top-, bottom-, and charm-quark masses are included at NLO accuracy. The renormalization and factorization scales are chosen to be $\frac{1}{2}\sqrt{m_H^2 + (p_T^H)^2}$, and the two resummation scales are chosen to be $m_H/2$ and $2m_b$.

- RadISH+NNLOjet [133], which provides predictions using a p_T^H resummation to NNLL and matching to the one-jet NNLO differential spectrum from NNLOJET [117, 118]. The shown $p_T^{\gamma\gamma}$ RadISH+NNLOjet prediction does include corrections from the finite top and bottom quark masses.

- SCETlib+MCFM8 which provides predictions at NNLO+NNLL$'_\varphi$ accuracy derived by applying a resummation of the virtual corrections to the gluon form factor [134, 135] and differentially in $|y_{\gamma\gamma}|$ and $|\cos\theta^*|$.[11] The underlying NNLO predictions are obtained using MCFM8 with zero-jettiness subtractions [136, 137].

No additional K-factors are applied to the predictions, which all use the NNLO PDF set following the PDF4LHC15 recommendations, and the fiducial acceptance for RadISH+NNLOjet is determined using Powheg NNLOPS. The SCETlib+MCFM8 and Hres predictions include the kinematic acceptance and are corrected and apply correction factors accounting for the photon isolation efficiency as described in Section 9.4. As also mentioned in Section 9.4, no correction factors to account for the impact of hadronization and the underlying-event activity are used. The SM prediction shows a slight excess at low transverse momentum and low rapidity, and shows a slight deficit at large transverse momentum. The slightly harder Higgs boson transverse momentum shown in Figure 26 is consistent with the ATLAS Run 1 measurements in both the $H \to \gamma\gamma$ and $H \to ZZ^* \to 4\ell$ decay channels [9, 138] and the measured zero-jet cross section. The Standard Model prediction is in agreement with the measured distributions.

9.5.2 Measurements of cross sections probing the jet kinematics

The transverse momentum and absolute rapidity of the leading jet, $p_T^{j_1}$ and $|y_{j_1}|$, as well as the transverse momentum and absolute rapidity of the subleading jet, $p_T^{j_2}$ and $|y_{j_2}|$, are sensitive to the theoretical modeling and to the relative contributions of the different Higgs boson production mechanisms. The transverse momentum distribution of the leading jet probes the emission of energetic quarks and gluons. In events with two jets, the contributions of VBF and VH productions become more important. The differential cross sections for $pp \to H \to \gamma\gamma$ as a function of $p_T^{j_1}$, $|y_{j_1}|$, $p_T^{j_2}$, and $|y_{j_2}|$ are shown in Figure 27. The chosen bin widths are a compromise between keeping migrations between bins

---

[11] The subscript φ refers to the fact that the applied resummation is to the gluon form factor.

Figure 26: The differential cross sections for $pp \rightarrow H \rightarrow \gamma\gamma$ as a function of (a) $p_T^{\gamma\gamma}$ and (b) $|y_{\gamma\gamma}|$ are shown and compared to the SM expectations.

small whilst retaining enough statistical power to measure the differential spectra. The measured $p_T^{j_1}$ spectrum shown in Figure 27(a) is compared to the default MC prediction as introduced in the previous section as well as to the NNLOJET and SCETLIB(STWZ) [99, 135] predictions. Both the NNLOJET and SCETLIB predictions are corrected using isolation correction factors to account for the impact of the isolation efficiency. In addition, the NNLOJET prediction is corrected for the kinematic acceptance and the uncertainties in these corrections is included in the uncertainty bands of both NNLOJET and SCETLIB. The first bin of the leading jet p_T spectrum represents zero-jet events that do not contain any jet with $p_T >$ 30 GeV. The predicted p_T distributions slightly exceed the measured distribution at low transverse momentum and all show a slight deficit at large transverse momentum. Both are compatible with the observed slightly harder Higgs boson transverse momentum distribution. The measured $|y_{j_1}|$ distribution shown in Figure 27(b) is compared to the default MC and the NNLOJET predictions: Both show a slight excess at low rapidity. In Figure 27(c) the measured subleading jet p_T distribution is shown. The first bin of p_T^{j2} represents one-jet events that do not contain two or more jets with $p_T >$ 30 GeV. The measured distribution is compared to the default MC, SHERPA (MEPS@NLO), and GOSAM predictions, as introduced in Section 9.4. Finally, in Figure 27(d) the subleading jet rapidity distribution, $|y_{j_2}|$, is shown and compared to the expectation from the default MC, SHERPA (MEPS@NLO), and GOSAM predictions. The SM predictions are in agreement with the measured distributions and no significant deviations are seen.

9.5.3 Measurements of cross sections probing spin and CP

The absolute value of the cosine of the angle between the beam axis and the photons in the Collins–Soper frame [11] of the Higgs boson, $|\cos\theta^*|$, can be used to study the spin of the Higgs boson. The

66

Figure 27: The differential cross sections for $pp \to H \to \gamma\gamma$ as a function of (a) $p_T^{j_1}$, (b) $|y_{j_1}|$, (c) $p_T^{j_2}$, and (d) $|y_{j_2}|$ are shown and compared to the SM expectations. The data and theoretical predictions are presented in the same way as in Figure 26. In addition, the NNLOJET and SCETLIB(STWZ) predictions, the NNLOJET prediction, and the SHERPA (MEPS@NLO) and GOSAM predictions, described in the text, are displayed in (a), (b) and (c+d), respectively.

azimuthal angle between the two leading jets, $\Delta\phi_{jj}$,[12] in events containing two or more jets is sensitive to the charge conjugation and parity properties of the Higgs boson interactions with gluons and weak bosons in the gluon–gluon fusion and the VBF production channels, respectively [139–142].

The differential cross sections for $pp \rightarrow H \rightarrow \gamma\gamma$ as a function of $|\cos\theta^*|$ and $\Delta\phi_{jj}$ are shown in Figure 28. For a scalar particle $|\cos\theta^*|$, shows a strong drop around 0.6 due to the fiducial requirement on the photon system, whereas for a spin-2 particle, an enhancement would be present in precisely this region. The charge conjugation and parity properties of the Higgs boson are encoded in the azimuthal angle between the jets: For example, in gluon–gluon fusion, its distribution for a CP-even coupling has a dip at $\pm\frac{\pi}{2}$ and present peaks at 0 and $\pm\pi$, whereas for a purely CP-odd coupling it would present as peaks at $\pm\frac{\pi}{2}$ and dips at 0 and $\pm\pi$. For VBF the SM prediction for $\Delta\phi_{jj}$ is approximately constant with a slight rise towards $\Delta\phi_{jj}= \pm\pi$. Any additional anomalous CP-even or CP-odd contribution to the interaction between the Higgs boson and weak bosons would manifest itself as an additional oscillatory component, and any interference between the SM and anomalous couplings can produce distributions peaked at either $\Delta\phi_{jj}= 0$ or $\Delta\phi_{jj}= \pm\pi$ [139, 141, 142]. The shape of the distribution is therefore sensitive to the relative contribution of gluon–gluon fusion and vector-boson fusion, as well as to the tensor structure of the interactions between the Higgs boson and gluons or weak bosons. This is exploited in Section 9.5.8 to set limits on new physics contributions. To quantify the structure of the azimuthal angle between the two jets, a ratio is defined as

$$A_{|\Delta\phi_{jj}|} = \frac{\sigma(|\Delta\phi_{jj}| < \frac{\pi}{3}) - \sigma(\frac{\pi}{3} < |\Delta\phi_{jj}| < \frac{2\pi}{3}) + \sigma(|\Delta\phi_{jj}| > \frac{2\pi}{3})}{\sigma(|\Delta\phi_{jj}| < \frac{\pi}{3}) + \sigma(\frac{\pi}{3} < |\Delta\phi_{jj}| < \frac{2\pi}{3}) + \sigma(|\Delta\phi_{jj}| > \frac{2\pi}{3})},$$

which is motivated by a similar ratio presented in Ref. [141]. The measured ratio in data as determined by measuring $|\Delta\phi_{jj}|$ in three bins is

$$A_{|\Delta\phi_{jj}|}^{\mathrm{meas}} = 0.45_{-0.24}^{+0.18}\,(\mathrm{stat.})\,_{-0.11}^{+0.10}\,(\mathrm{syst.})\,.$$

This value can be compared to the SM prediction from the default MC simulation. The predicted value is $A_{|\Delta\phi_{jj}|}^{\mathrm{SM}} = 0.44 \pm 0.01$, consistent with the measured ratio.

In summary, the measured $|\cos\theta^*|$ and $\Delta\phi_{jj}$ distributions are consistent with Standard Model predictions for a CP-even scalar particle.

9.5.4 Cross sections probing the VBF production mode

The distribution of the dijet rapidity separation, $|\Delta y_{jj}|$, the azimuthal angle between the dijet and diphoton systems, $|\Delta\phi_{\gamma\gamma,jj}|$, and the invariant mass of the leading and subleading jets, m_{jj} for events with two or more jets are sensitive to the differences between the gluon–gluon fusion and VBF production mechanisms. In vector-boson fusion, the t-channel exchange of a W/Z boson typically results in two moderate-p_{T} jets that are well separated in rapidity. Furthermore, quark/gluon radiation in the rapidity interval between the two jets is suppressed in the VBF process when compared to the gluon–gluon fusion process, because there is no color flow between the two jets. The $|\Delta\phi_{\gamma\gamma,jj}|$ distribution for VBF production is therefore expected to be steeper and more peaked towards $|\Delta\phi_{\gamma\gamma,jj}| = \pi$ than for gluon–gluon fusion.

---

[12] To preserve the sign information, the azimuthal angles of the jets are ordered according to the jet with the highest rapidity. This definition of $\Delta\phi_{jj}$ is invariant under a redefinition of the ordering by choosing the opposite beam axis, as explained in Ref. [139].
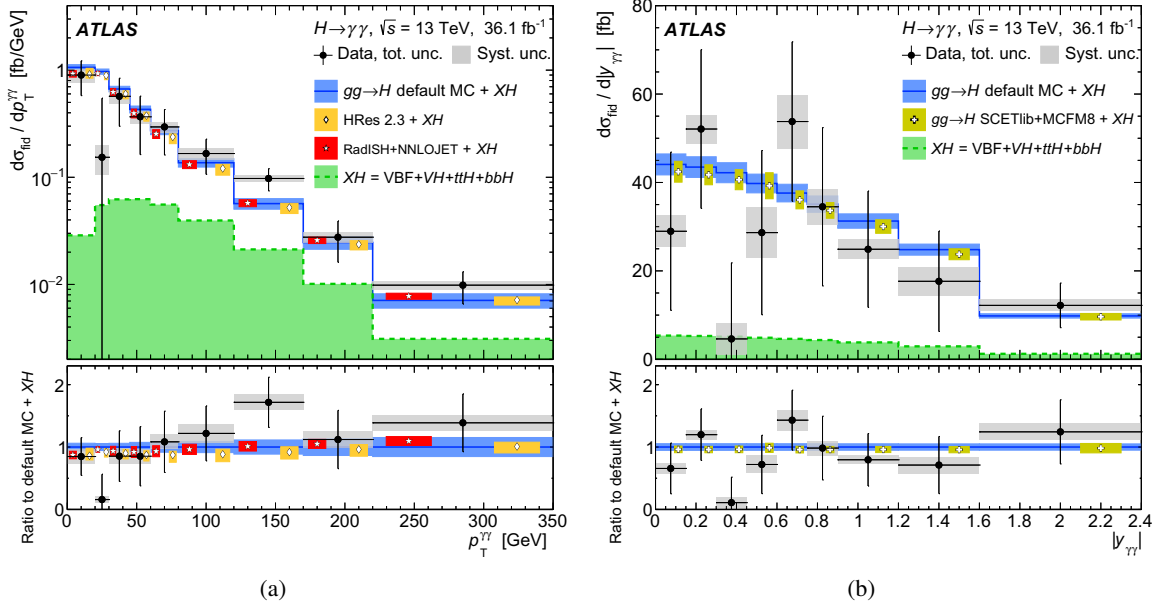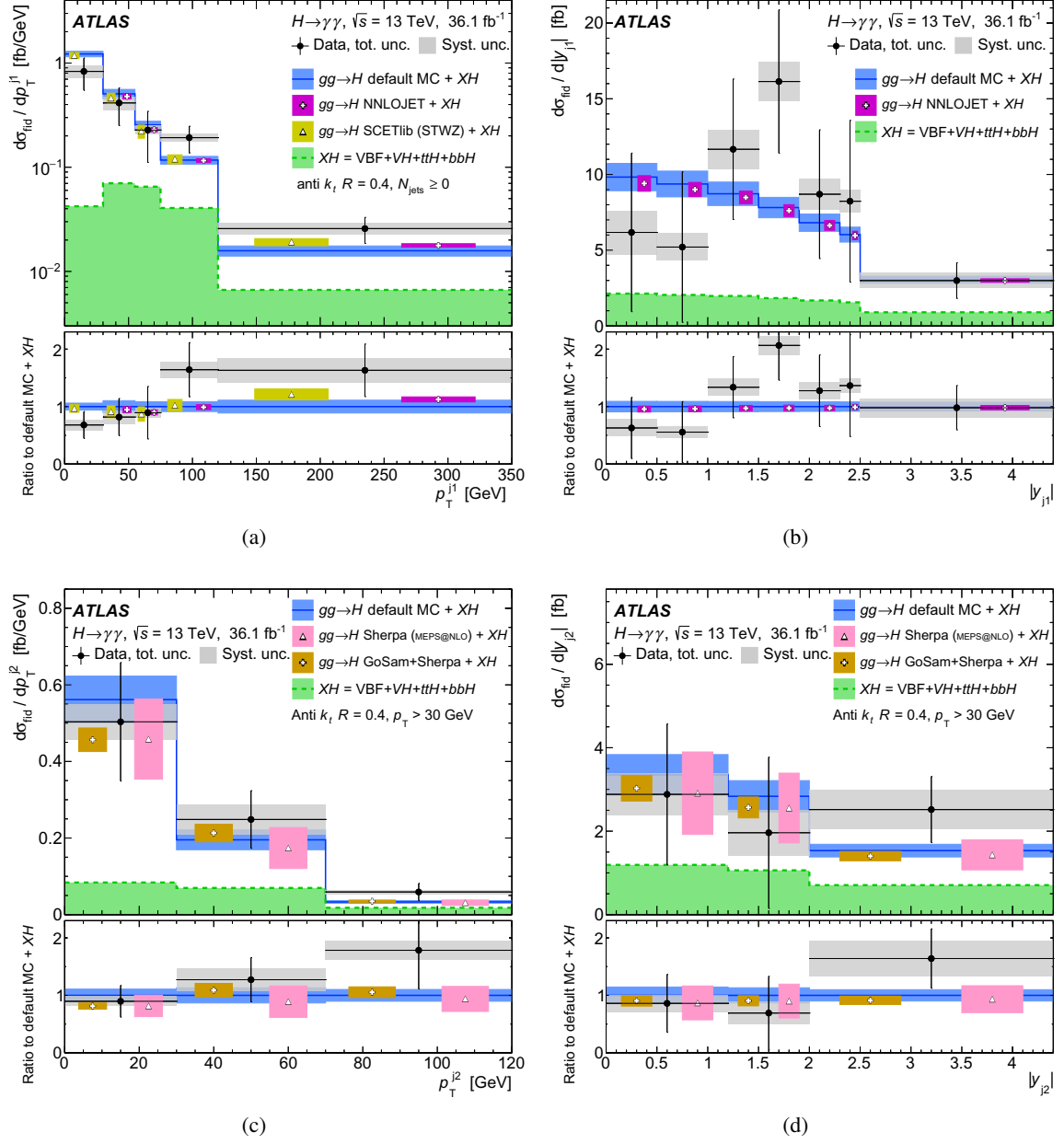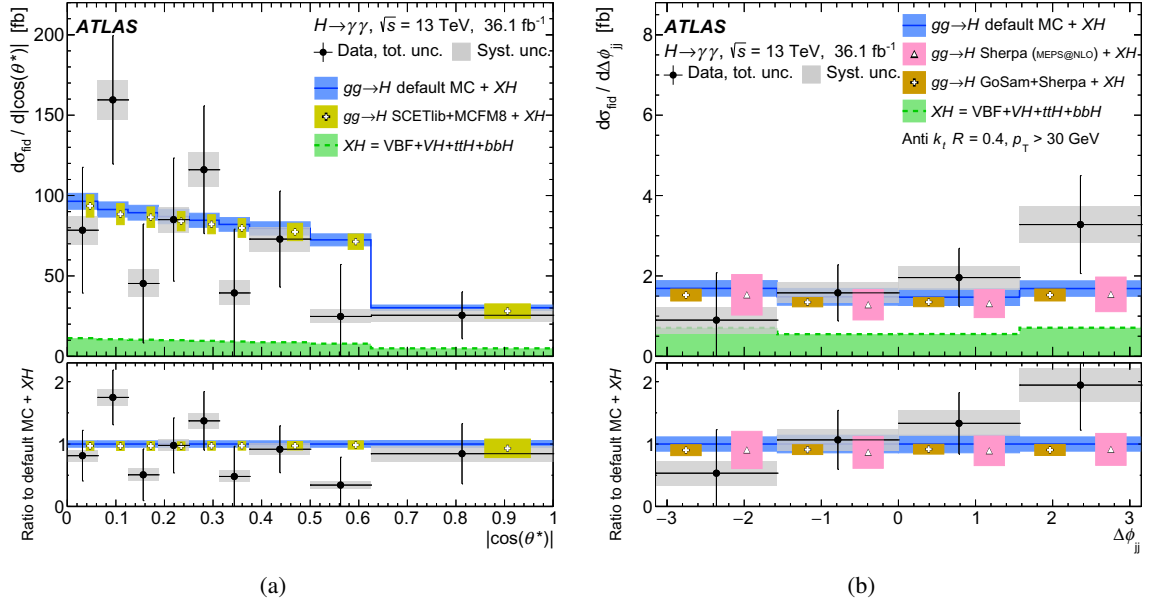
Figure 28: The differential cross sections for $pp \rightarrow H \rightarrow \gamma\gamma$ as a function of (a) $|\cos \theta^*|$ and (b) $\Delta\phi_{jj}$ are shown and compared to the SM expectations. The data and theoretical predictions are presented in the same way as in Figure 26. In addition, the SCETlib+MCFM8 prediction and the Sherpa (Meps@Nlo) and GoSam predictions, described in the text, are displayed in (a) and (b), respectively.

The differential cross sections for $pp \rightarrow H \rightarrow \gamma\gamma$ as a function of $|\Delta y_{jj}|$, $|\Delta\phi_{\gamma\gamma,jj}|$, and m_{jj} are shown for events with at least two jets with $p_T > 30$ GeV in Figure 29. These variables are used to discriminate between gluon–gluon fusion and the VBF production of the Higgs boson and enter the multivariate classifier introduced in Section 8.1.4 that defines the categories used for the simplified template cross-section and coupling measurements. The measured distributions are in agreement to the default MC, Sherpa (Meps@Nlo), and the GoSam predictions. The accuracy of the fixed-order parton-level prediction from GoSam breaks down in the lowest bin of $\pi - |\Delta\phi_{\gamma\gamma,jj}|$ and the measured cross section moderately exceeds the SM predictions at high m_{jj} values.

9.5.5 Double-differential cross sections

The double-differential cross section for $pp \rightarrow H \rightarrow \gamma\gamma$ as a function of $p_T^{\gamma\gamma}$ and N_{jets}, for jets with $p_T > 30$ GeV, and $p_T^{\gamma\gamma}$ and $|\cos \theta^*|$ are shown in Figure 30. These cross sections are sensitive to the modeling of the Higgs boson kinematic, its production mechanisms, and its spin-CP properties. Both double-differential cross sections are in agreement with the Standard Model expectation.

9.5.6 Impact of systematic uncertainties on results

A summary of the uncertainties in the measured cross sections of the fiducial regions are shown in Table 16. As an example concerning the differential measurements, a breakdown of the systematic uncertainties in the differential cross sections as a function of $p_T^{\gamma\gamma}$ and N_{jets} is shown in Figure 31. The measurements are dominated by the statistical uncertainties. For the systematic uncertainties,
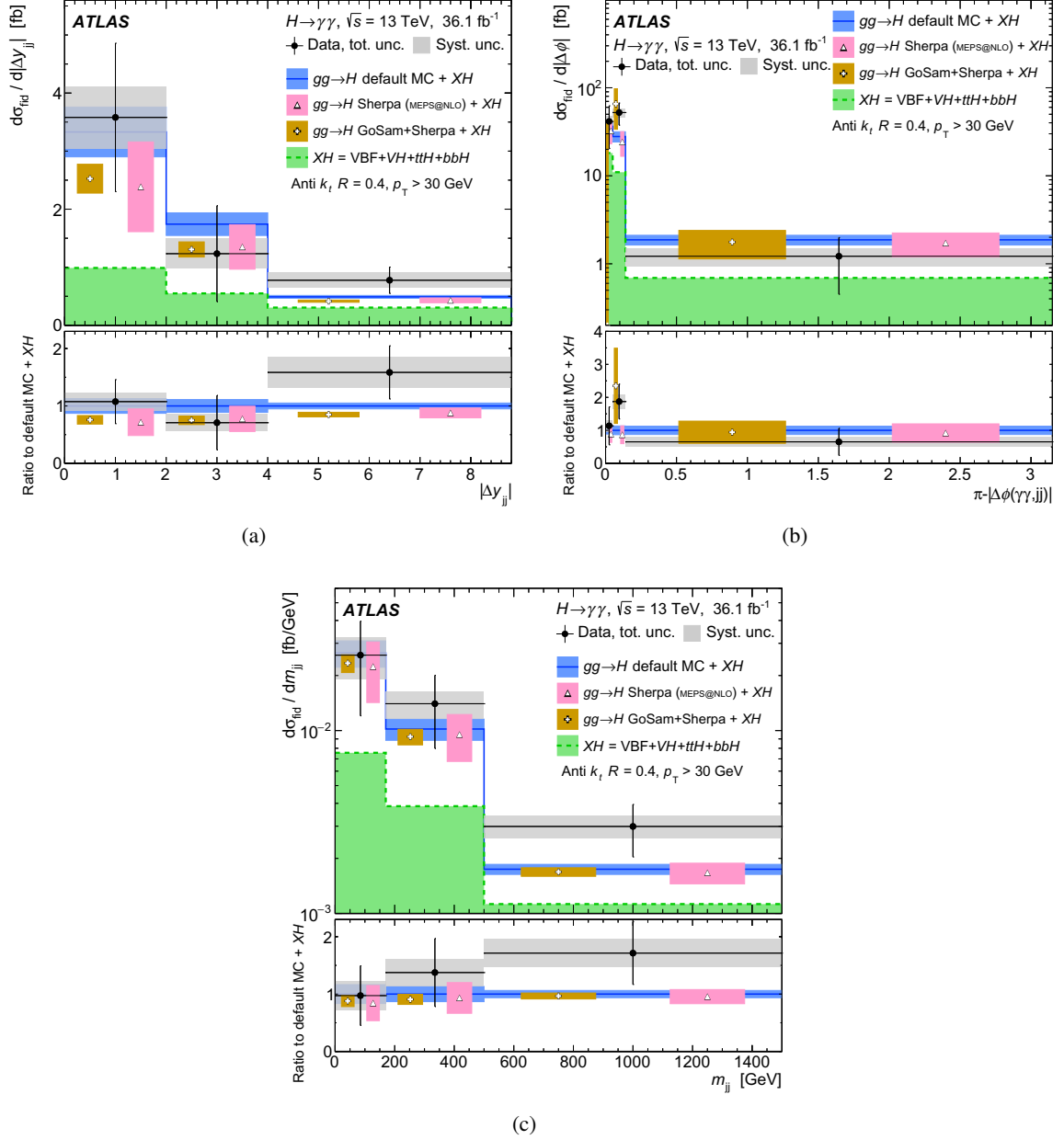
Figure 29: The differential cross sections for $pp \to H \to \gamma\gamma$ as a function of (a) $|\Delta y_{jj}|$, (b) $\pi - |\Delta\phi_{\gamma\gamma,jj}|$, and (c) m_{jj} are shown and compared to the SM expectations. The data and theoretical predictions are presented in the same way as in Figure 26. In addition, the SHERPA (MEPS@NLO) and GOSAM predictions are shown for all three cross sections.
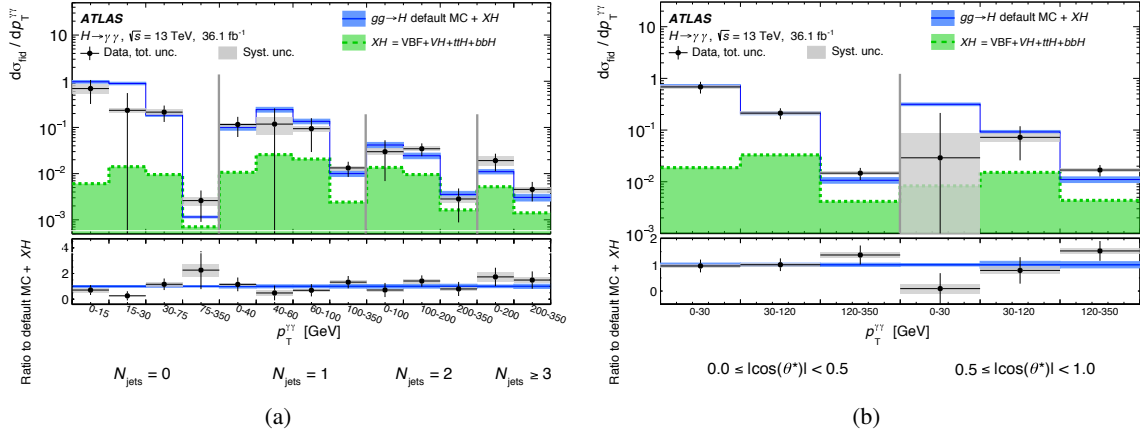
Figure 30: The double-differential cross section for $pp \to H \to \gamma\gamma$ as a function of (a) $p_T^{\gamma\gamma}$ and N_{jets}, for jets with $p_T > 30$ GeV, and (b) $p_T^{\gamma\gamma}$ and $|\cos\theta^*|$ separating the two regions of $|\cos\theta^*| < 0.5$ and $|\cos\theta^*| > 0.5$ from each other. The data and theoretical predictions are presented in the same way as in Figure 26.

Table 16: The expected uncertainties, expressed in percent, in the cross sections measured in the diphoton fiducial, VBF-enhanced, $N_{\text{lepton}} \geq 1$, $t\bar{t}H$-enhanced, and high E_T^{miss} regions. The fit systematic uncertainty includes the effect of the photon energy scale and resolution, and the impact of the background modeling on the signal yield. The theoretical modeling uncertainty is defined as the envelope of the signal composition, the modeling of Higgs boson transverse momentum and rapidity distribution, and the uncertainty of parton shower and the underlying event (labeled as "UE/PS") as described in Section 7.4.

Source	Uncertainty in fiducial cross section				
	Diphoton	VBF-enhanced	$N_{\text{lepton}} \geq 1$	$t\bar{t}H$-enhanced	High E_T^{miss}
Fit (stat.)	17%	22%	72%	176%	53%
Fit (syst.)	6%	9%	27%	138%	13%
Photon energy scale & resolution	4.3%	3.5%	3.1%	10%	4.1%
Background modeling	4.2%	7.8%	26.7%	138%	12.2%
Photon efficiency	1.8%	1.8%	1.8%	1.8%	1.9%
Jet energy scale/resolution	-	8.9%	-	4.5%	6.9%
b-jet flavor tagging	-	-	-	3%	-
Lepton selection	-	-	0.7%	0.2%	-
Pileup	1.1%	2.9%	1.3%	2.5%	2.5%
Theoretical modeling	0.1%	4.5%	4.0%	8.1%	31%
Signal composition	0.1%	4.5%	3.1%	8.1%	25%
Higgs boson p_T^H & $|y_H|$	0.1%	0.9%	0.2%	0.7%	0.1%
UE/PS	-	0.3%	0.7%	1.1%	31%
Luminosity	3.2%	3.2%	3.2%	3.2%	3.2%
Total	18%	26%	77%	224%	63%

the uncertainty in the fitted signal yield, due to the background modeling and the photon energy resolution, is typically more important than the uncertainty in the correction factor due to the theoretical modeling. The jet energy scale and resolution uncertainties become increasingly important for high-jet multiplicities and in the $t\bar{t}H$- and VBF-enhanced phase space.
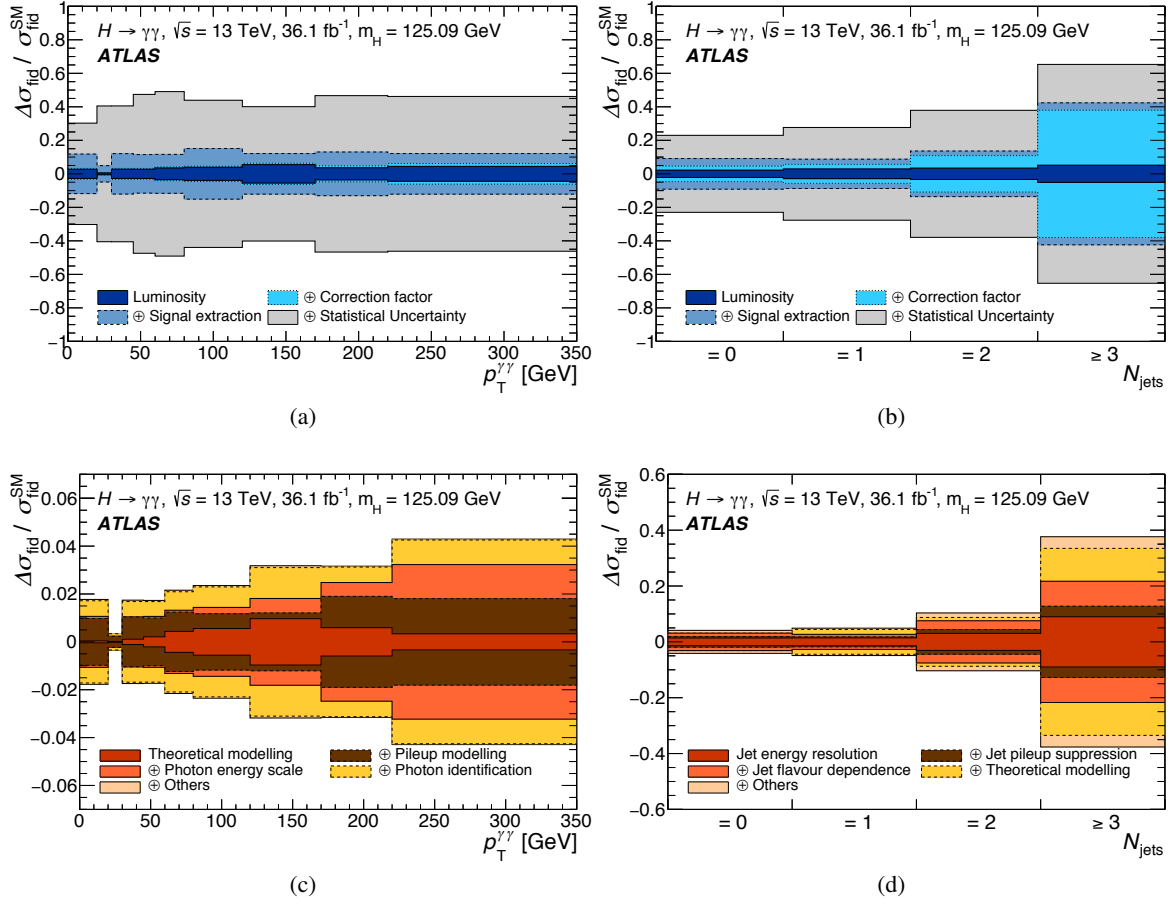
Figure 31: The relative size of systematic uncertainties associated with the signal extraction, the correction factors (experimental and theoretical modeling) and the luminosity on the differential cross sections are shown as a function of (a) $p_{\mathrm{Tt}}^{\gamma\gamma}$ and (b) N_{jets}. The statistical uncertainty associated with the signal extraction is also shown as a gray band. For completeness, the relevant components of the uncertainties in the correction factors are shown as a function of (c) $p_{\mathrm{Tt}}^{\gamma\gamma}$ and (d) N_{jets}.

Table 17: Probabilities from a χ^2 test for the comparison between data and the default SM prediction.

Distribution	Default MC Prediction
$p_T^{\gamma\gamma}$	51%
$|y_{\gamma\gamma}|$	57%
$p_T^{j_1}$	32%
$|y_{j_1}|$	66%
$p_T^{j_2}$	61%
$|y_{j_2}|$	56%
$|\cos\theta^*|$	47%
$\Delta\phi_{jj}$	64%
$|\Delta y_{jj}|$	53%
$|\Delta\phi_{\gamma\gamma,jj}|$	43%
m_{jj}	54%
$N_{\text{jets}}(p_T > 30 \text{ GeV})$	56%
$N_{\text{jets}}(p_T > 50 \text{ GeV})$	19%

9.5.7 Compatibility of measured distributions with the Standard Model

The compatibility between the measured distributions and the Standard Model is tested by comparing the first and second moments of the measured distributions. Figure 32 shows the first and second moments (mean and RMS) of the distributions and compares them to the moments of the default MC prediction, as calculated from the measured and predicted cross-section bins. The theory uncertainties are constructed as outlined in Section 7.3. The measured Higgs boson transverse momentum has somewhat higher first and second moments than the Standard Model prediction, which is consistent with the previous observations [9, 138]. The leading-jet p_T spectrum shows the same feature. In addition a χ^2 test is carried out for all distributions reported in Section 9: The resulting p-values are reported in Table 17, which confirms that within the current uncertainties the data are in agreement with the SM predictions.
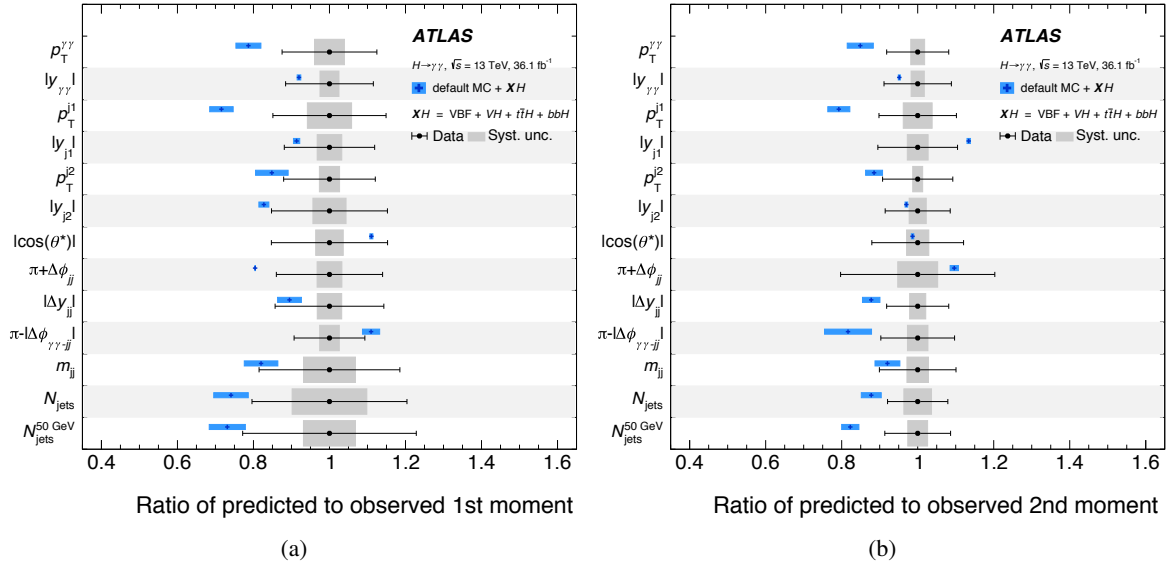
Figure 32: (a) The ratio of the first moment (mean) of each differential distribution predicted by the Standard Model to that observed in the data. The SM moment is calculated by using the default MC distributions for gluon–gluon fusion and the other production mechanisms. (b) The ratio of the second moment (RMS) of each differential distribution predicted by the Standard Model to that observed in the data. The intervals on the vertical axes each represent one of the differential distributions. The band for the theoretical prediction represents the corresponding uncertainty in that prediction (see text for details). The error bar on the data represents the total uncertainty in the measurement, with the gray band representing only the systematic uncertainty.

9.5.8 Search for anomalous Higgs-boson interactions using an effective field theory approach

The strength and tensor structure of the Higgs-boson interactions can be investigated using an effective field theory approach, which introduces additional CP-even and CP-odd interactions that change the event rates and the kinematic properties of the Higgs boson and associated jet spectra from those in the Standard Model. The parameters of the effective field theory are probed using a fit to five of the most relevant differential cross sections. The effective Lagrangian of Ref. [143] is used which adds dimension-six operators of the Strongly Interacting Light Higgs formulation [13] to the Standard Model interactions. The $H \rightarrow \gamma\gamma$ differential cross sections are mainly sensitive to the operators that affect the Higgs boson interactions with gauge bosons and the relevant terms in the Lagrangian can be specified by

$$\mathcal{L}_{\text{eff}} = \quad \bar{c}_g O_g + \bar{c}_{HW} O_{HW} + \bar{c}_{HB} O_{HB}$$
$$+ \tilde{c}_g \tilde{O}_g + \tilde{c}_{HW} \tilde{O}_{HW} + \tilde{c}_{HB} \tilde{O}_{HB},$$

where $\bar{c}_i$ and $\tilde{c}_i$ are dimensionless Wilson coefficients specifying the strength of the new CP-even and CP-odd interactions, respectively, and the dimension-six operators O_i and $\tilde{O}_i$ are those described in Refs. [143, 144]. In the SM, all of the Wilson coefficients are equal to zero. The O_g and $\tilde{O}_g$ operators introduce new interactions between the Higgs boson and two gluons and can be probed through the gluon–gluon fusion Higgs production mechanism. The O_{HW} and $\tilde{O}_{HW}$ operators introduce new HWW, HZZ and $HZ\gamma$ interactions. The HZZ and $HZ\gamma$ interactions are also impacted by O_{HB} and $\tilde{O}_{HB}$. The O_{HW}, $\tilde{O}_{HW}$, O_{HB} and $\tilde{O}_{HB}$ operators can be probed through vector-boson fusion and associated production. Other operators in the full effective Lagrangian of Ref. [143] can also modify Higgs-boson interactions but are not considered here due to the lack of sensitivity of the $H \rightarrow \gamma\gamma$ decay channel. Combinations of some of the CP-even operators have been constrained using global fits to experimental data from LEP and the LHC [143, 145, 146].

The effective Lagrangian has been implemented in FeynRules [144].[13] Parton-level event samples are produced for specific values of Wilson coefficients by interfacing the universal file output from FeynRules to the MG5_aMC@NLOevent generator [46]. Higgs bosons are produced via gluon–gluon fusion with up to two additional partons in the final state using leading-order matrix elements.

The generated events are passed to Pythia8 [29] to provide parton showering, hadronization and underlying event and the zero-, one- and two-parton events are merged using the MLM matching scheme [148] to create the full final state. Event samples containing a Higgs boson produced either in association with a vector boson or via vector-boson fusion are produced using leading-order matrix elements and passed through the Pythia8 generator. For each production mode, the Higgs boson mass is set to 125 GeV and events are generated using the NNPDF2.3LO PDF set [47] and the A14 parameter set [48]. All other Higgs boson production modes are assumed to occur as predicted by the SM.

Event samples are produced for different values of a given Wilson coefficient. The particle-level differential cross sections are produced using Rivet [149]. The Professor method [150] is used to

---

[13] The implementation in Ref. [144] involves a redefinition of the gauge boson propagators that results in unphysical amplitudes unless certain physical constants are also redefined. The original implementation did not include the redefinition of these physical constants. However, the impact of redefining the physical constants is found to be negligible on the predicted cross sections across the range of Wilson coefficients studied. The relative change in the predicted Higgs boson cross sections as functions of the different Wilson coefficients is also found to agree with that predicted by the Higgs characterization framework [147], with less than 2% variation across the parameter ranges studied.

interpolate between these samples, for each bin of each distribution, to provide a parameterization of the effective Lagrangian prediction. The parameterization function is determined using 11 samples when studying a single Wilson coefficient, whereas 25 samples are used when studying two Wilson coefficients simultaneously. As the Wilson coefficients enter the effective Lagrangian in a linear fashion, second-order polynomials are used to predict the cross sections in each bin. The method was validated by comparing the differential cross sections obtained with the parameterization function to the predictions obtained with dedicated event samples generated at the specific point in parameter space.

The model implemented in FeynRules fixes the Higgs boson width to be that of the SM, $\Gamma_H = 4.07$ MeV [17]. The cross sections are scaled by $\Gamma_H/(\Gamma_H + \Delta\Gamma)$, where $\Delta\Gamma$ is the change in partial widths due to a specific choice of Wilson coefficient. The change in partial widths is determined for each Higgs coupling using the partial-width calculator in MG5_aMC@NLOand normalized to reproduce the SM prediction from HDECAY [18].

The leading-order predictions obtained from MG5_aMC@NLOare reweighted to account for higher-order QCD and electroweak corrections to the SM process, assuming that these corrections factorize from the new physics effects. The differential cross section as a function of variable X for a specific choice of Wilson coefficient, c_i, is given by

$$\frac{\mathrm{d}\sigma}{\mathrm{d}X} = \sum_j \left(\frac{\mathrm{d}\sigma_j}{\mathrm{d}X}\right)^{\mathrm{ref}} \cdot \left(\frac{\mathrm{d}\sigma_j}{\mathrm{d}X}\right)^{\mathrm{MG5}}_{c_i} \Big/ \left(\frac{\mathrm{d}\sigma_j}{\mathrm{d}X}\right)^{\mathrm{MG5}}_{c_i=0},$$

where the summation j is over the different Higgs boson production mechanisms, 'MG5' labels the interpolated MG5_aMC@NLOprediction and 'ref' labels a reference sample for SM Higgs boson production. For the reference sample the default MC simulation is used.

The measured differential cross sections of $p_\mathrm{T}^{\gamma\gamma}$, N_jets, m_{jj}, $|\Delta\phi_{jj}|$, and $p_\mathrm{T}^{j_1}$ are compared in Figure 33(a) to the SM hypothesis and to two non-SM hypotheses, specified by $\bar{c}_g = 2 \times 10^{-4}$ and $\bar{c}_{HW} = 0.05$, respectively. The new CP-odd gluon–gluon fusion operator results in a large increase in rate and the additional CP-even WH operator leads to a larger number of Higgs boson with sizeable p_T and an increased number of zero-jet events.

The ratios of the expected differential cross sections to the SM predictions for some representative values of the Wilson coefficients are shown in Figure 33(b). The impact of the $\bar{c}_g$ and $\tilde{c}_g$ coefficients are presented for the gluon–gluon fusion production: it displays a large change in the overall cross-section normalization. The $\tilde{c}_g$ coefficient also changes the shape of the $\Delta\phi_{jj}$ distribution, which is expected from consideration of the tensor structure of CP-even and CP-odd interactions [139, 141]. In contrast, the impact of the $\bar{c}_{HW}$ and $\tilde{c}_{HW}$ coefficients are presented specifically for the VBF+VH production channel: one expects large shape changes in all of the studied distributions and the $\Delta\phi_{jj}$ distribution is known to discriminate between CP-even and CP-odd interactions in the VBFproduction channel [140].

Limits on Wilson coefficients are set by constructing a likelihood function

$$\mathcal{L} = \frac{1}{\sqrt{(2\pi)^k |C|}} \exp\left(-\frac{1}{2} \left(\vec{\sigma}_{\mathrm{data}} - \vec{\sigma}_{\mathrm{pred}}\right)^T C^{-1} \left(\vec{\sigma}_{\mathrm{data}} - \vec{\sigma}_{\mathrm{pred}}\right)\right),$$

where $\vec{\sigma}_{\mathrm{data}}$ and $\vec{\sigma}_{\mathrm{pred}}$ are k-dimensional vectors from the measured and predicted differential cross sections of the five analyzed observables, $C = C_{\mathrm{stat}} + C_{\mathrm{syst}} + C_{\mathrm{theo}}$ is the $k \times k$ total covariance

(a)

(b)
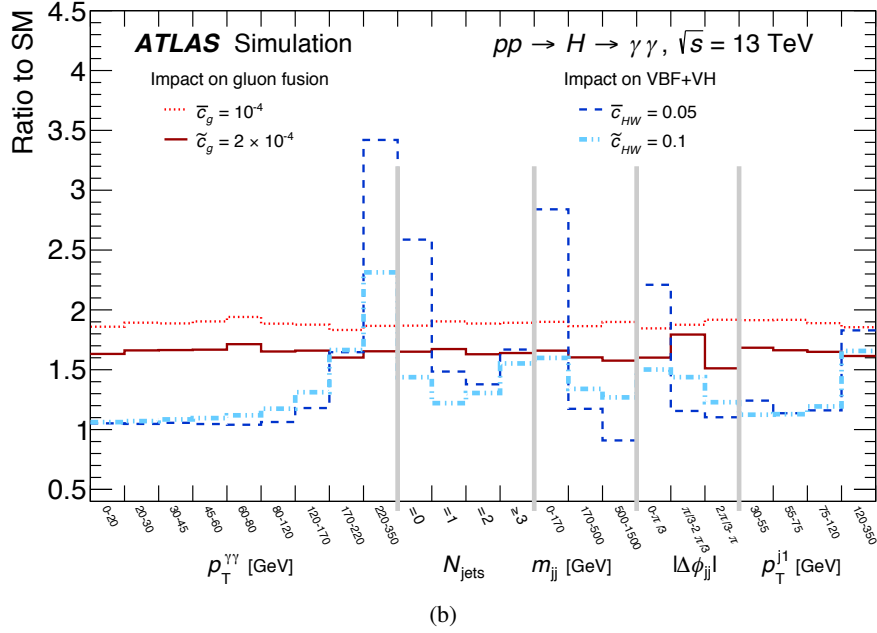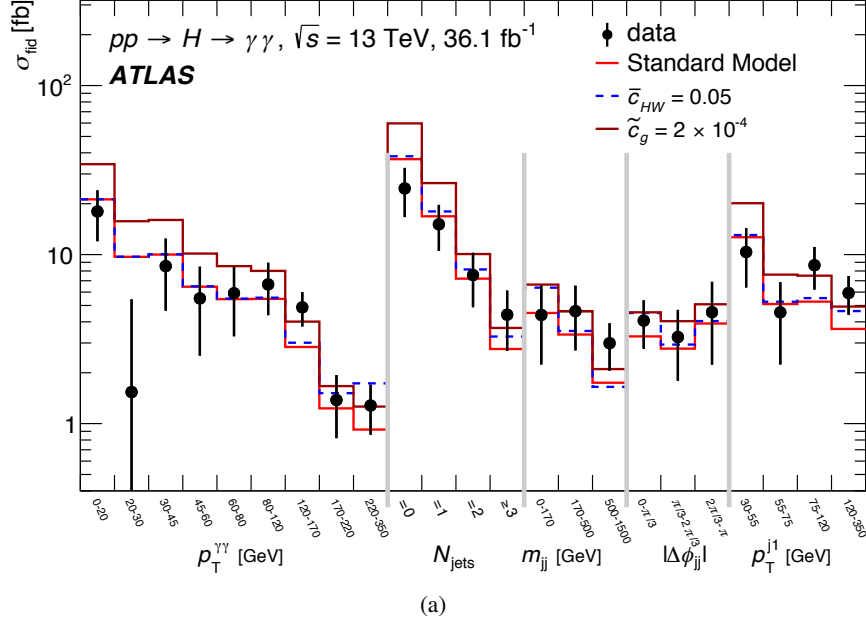
Figure 33: (a) The measured differential cross sections as a function of $p_T^{\gamma\gamma}$, N_{jets}, m_{jj}, $|\Delta\phi_{jj}|$, and $p_T^{j_1}$ are compared to the SM hypothesis and two non-SM hypotheses with $\bar{c}_g = 1 \times 10^{-4}$ and $\bar{c}_{HW} = 0.05$, respectively. (b) Ratios of differential cross sections, as predicted for specific choices of Wilson coefficient, to the differential cross sections predicted by the SM: the impact of non-zero $\bar{c}_g$ and $\tilde{c}_g$ is shown relative to the SM ggH prediction, while the impact of non-zero $\bar{c}_{HW}$ and $\tilde{c}_{HW}$ is shown relative to the SM VBF+VH prediction.

matrix defined by the sum of the statistical, systematic and theoretical covariances, and $|C|$ denotes its determinant. The theory covariance is constructed as outlined in Section 7.3 and includes no additional uncertainty to account for the factorization assumption in Eq. 9.5.8. Based on this likelihood, one can construct a χ^2 test to test the compatibility of the five distributions with the SM and a probability of 93% is found. In what follows, the likelihood function is numerically maximized to determine $\mathcal{L}_{\max}$ and confidence limits for one or several Wilson coefficients are determined via

$$1 - \mathrm{CL} = \int_{-2\ln \mathcal{L}(c_i)+2\ln \mathcal{L}_{\max}}^{\infty} \mathrm{d}x\, f(x),$$

with $\mathcal{L}(c_i)$ denoting the likelihood value evaluated for a given Wilson coefficient value c_i, and $f(x)$ denoting the distribution of the test statistic. The coverage of the confidence limit is determined using ensembles of pseudo-experiments. Form factors are sometimes used to regularize the change of the cross section above a momentum scale Λ_{FF}. This was investigated by reweighting the VBF+VH samples using form-factor predictions from VBFNLO [151]. The impact on the $\bar{c}_{HW}$ and $\tilde{c}_{HW}$ limits is negligible for $\Lambda_{\mathrm{FF}} > 1$ TeV.

In Table 18, the observed and expected 95% CL limits for four Wilson coefficient fits are given. The limit for $\bar{c}_g$ is derived by fixing all other Wilson coefficients to zero. This additional interaction can interfere with the corresponding SM interaction and destructive interference causes the gluon–gluon fusion production-mode cross section to be zero at $\bar{c}_g \sim -2.2\times 10^{-4}$. The $\tilde{c}_g$ coefficient is also derived after setting all Wilson coefficients to zero. Due to the CP conjugate structure of the interaction, no interference with the SM process is possible. The 95% CL limit for $\bar{c}_{HW}$ is obtained after setting $\bar{c}_{HB} = \bar{c}_{HW}$ to ensure that the partial width for $H \to Z\gamma$ is unchanged from the SM prediction (Values of $|\bar{c}_{HW} - \bar{c}_{HB}| > 0.03$ lead to a very large decay rate for the $H \to Z\gamma$ process that is contradicted by the experimental constraints reported by ATLAS [152, 153]) and setting all other Wilson coefficients to zero. Finally, the 95% CL limit for $\tilde{c}_{HW}$ is given after setting $\tilde{c}_{HB} = \tilde{c}_{HW}$ to ensure a SM decay rate for $H \to Z\gamma$ and all other Wilson coefficients to zero. The observed limits are improved by about a factor of two compared to the Run 1 analysis of Ref. [14].

Figure 34 shows the 68% and 95% confidence regions obtained from scanning $\bar{c}_{HW}$ and $\tilde{c}_{HW}$ simultaneously, with the other two Wilson coefficients set to $\bar{c}_{HB} = \bar{c}_{HW}$ and $\tilde{c}_{HB} = \tilde{c}_{HW}$. All other Wilson coefficients are fixed at zero. The $\bar{c}_{HW}$ and $\tilde{c}_{HW}$ Wilson coefficients produce large shape changes in all distributions, as shown in Figure 33, and the obtained limits are strongest when fitting all five distributions simultaneously. The shape of the observed 68% confidence regions thus results from both shape and yield differences between data and expectations: the operators proportional to $\bar{c}_{HW}$ can destructively interfere with the SM contributions, a negative value of $\bar{c}_{HW}$ reduces the overall predicted cross section in the zero-jet and the lowest m_{jj} bins, where deficits are observed in the data. The operators proportional to $\tilde{c}_{HW}$ can only increase the cross section from its SM value and can increase the predicted cross sections in the higher jet bins and the tails of the distributions (cf. Figure 33). If only shape information is used to constrain the Wilson coefficients, the reported limits on $\bar{c}_{HW}$ and $\tilde{c}_{HW}$ weaken by about 20% and 50%, respectively. As also shown in Figure 34, these results display significant improvements on similar limits obtained from the Run-1 analysis [14]. All reported results assume that QCD effects and new physics effects factorise. This assumption cannot be avoided with the current state-of-the-art implementation of the effective Lagrangian of Ref. [143]. The full statistical and systematic correlations between measured distributions and all measured fiducial and differential cross sections are available in HepData to allow future interpretations with better models.

Table 18: Observed allowed ranges at 95% CL for the $\bar{c}_g$ and $\bar{c}_{HW}$ Wilson coefficients and the CP-conjugate coefficients. Limits on $\bar{c}_g$ and $\tilde{c}_g$ are each derived with all other Wilson coefficients set to zero. Limits on $\bar{c}_{HW}$ and $\tilde{c}_{HW}$ are derived with $\bar{c}_{HB} = \bar{c}_{HW}$ and $\tilde{c}_{HB} = \tilde{c}_{HW}$, respectively.

Coefficient	Observed 95% CL limit	Expected 95% CL limit
$\bar{c}_g$	$[-0.8, 0.1] \times 10^{-4} \cup [-4.6, -3.8] \times 10^{-4}$	$[-0.4, 0.5] \times 10^{-4} \cup [-4.9, -4.1] \times 10^{-4}$
$\tilde{c}_g$	$[-1.0, 0.9] \times 10^{-4}$	$[-1.4, 1.3] \times 10^{-4}$
$\bar{c}_{HW}$	$[-5.7, 5.1] \times 10^{-2}$	$[-5.0, 5.0] \times 10^{-2}$
$\tilde{c}_{HW}$	$[-0.16, 0.16]$	$[-0.14, 0.14]$
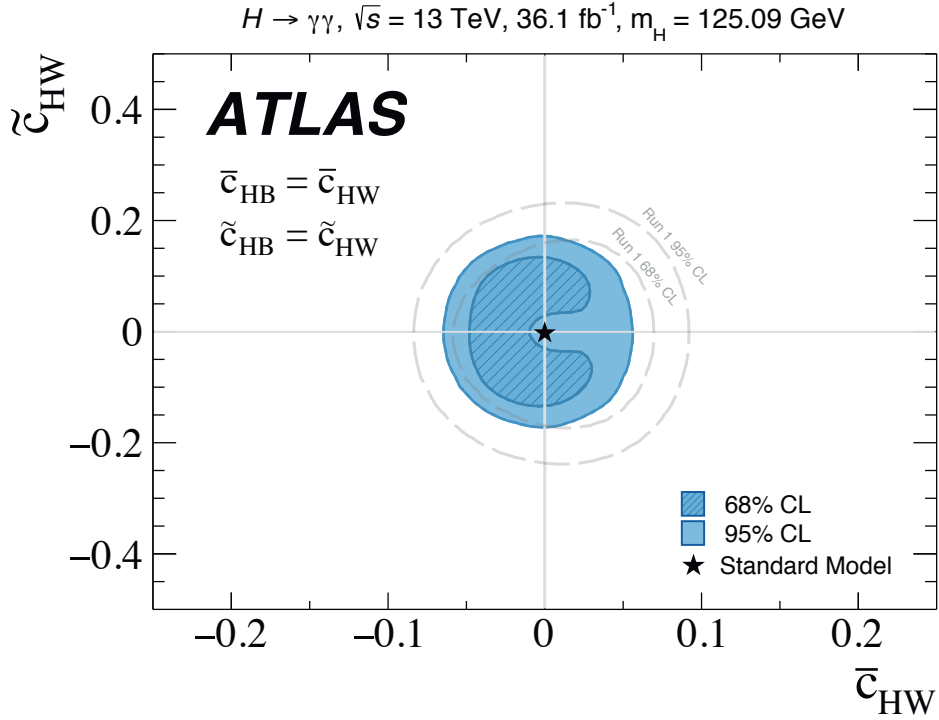
Figure 34: The observed 68% (dark) and 95% (light) confidence level regions from the simultaneous fit to the $\bar{c}_{HW}$ and $\tilde{c}_{HW}$ Wilson coefficients. The values of $\bar{c}_{HB}$ and $\tilde{c}_{HB}$ are set to be equal to $\bar{c}_{HW}$ and $\tilde{c}_{HW}$, respectively, and all other Wilson coefficients are set to zero, except for $\bar{c}_{HB}$ and $\tilde{c}_{HB}$ which are set to be equal to $\bar{c}_{HW}$ and $\tilde{c}_{HW}$, respectively. The SM expectation at $(0, 0)$ is also shown, together with the Run-1 confidence regions reported in Ref. [14].

10 Summary and conclusions

Measurements of Higgs boson cross sections in the Higgs boson to diphoton decay channel are performed using pp collision data recorded by the ATLAS experiment at the LHC. The data were taken at a center-of-mass energy of $\sqrt{s} = 13$ TeV and correspond to an integrated luminosity of 36.1 fb^{-1}. All measurements assume a Higgs boson mass of 125.09 ± 0.24 GeV. The measured signal strength relative to the Standard Model expectation is found to be:

$$\mu = 0.99\ ^{+0.15}_{-0.14}\ .$$

Signal strengths of the main production modes are measured separately via event reconstruction categories that are designed to be sensitive to the specific production modes. They are found to be:

$$\mu_{\mathrm{ggH}} = 0.81\ ^{+0.19}_{-0.18},\quad \mu_{\mathrm{VBF}} = 2.0\ ^{+0.6}_{-0.5},\quad \mu_{\mathrm{VH}} = 0.7\ ^{+0.9}_{-0.8},\quad \text{and}\quad \mu_{\mathrm{top}} = 0.5\ ^{+0.6}_{-0.6}\ .$$

The total uncertainties of both the global and the production mode signal strengths is dominated by their respective statistical uncertainties. The global signal strength measurement improves on the precision of the previous ATLAS measurement in the diphoton channel by a factor of two [154]. The ggH (VBF) signal strength is measured to be $1\,\sigma$ below ($2\,\sigma$ above) the Standard Model expectation. The precision of the coupling-strength measurements involving top quarks improves by about a factor of three compared to the previous ATLAS measurement in the diphoton channel [154]. These improvements result from a combination of the larger Higgs boson sample collected at $\sqrt{s} = 13$ TeV, from the use of multivariate techniques to target the VBF, VH, and top-quark associated production modes more efficiently, from the improved precision of the ggH Standard Model theory predictions, and from a significant reduction of some of the experimental uncertainties such as the photon energy resolution. Production mode cross-section measurements for a Higgs boson of rapidity $|y_H| < 2.5$ for gluon–gluon fusion, vector-boson fusion, and Higgs boson production in association with vector bosons or a top quark pair are reported:

$$\sigma_{\mathrm{ggH}} = 82^{+19}_{-18}\,\mathrm{fb},\quad \sigma_{\mathrm{VBF}} = 16^{+5}_{-4}\,\mathrm{fb},\quad \sigma_{\mathrm{VH}} = 3 \pm 4\,\mathrm{fb},\quad \text{and}\quad \sigma_{\mathrm{top}} = 0.7^{+0.9}_{-0.7}\,\mathrm{fb}\ .$$

These values can be compared to the Standard Model expectations of

$$\sigma^{\mathrm{SM}}_{\mathrm{ggH}} = 102^{+5}_{-7}\,\mathrm{fb},\quad \sigma^{\mathrm{SM}}_{\mathrm{VBF}} = 8 \pm 0.2\,\mathrm{fb},\quad \sigma^{\mathrm{SM}}_{\mathrm{VH}} = 5 \pm 0.2\,\mathrm{fb},\quad \sigma^{\mathrm{SM}}_{\mathrm{top}} = 1.3 \pm 0.1\,\mathrm{fb},$$

and show a similar level of agreement as that obtained with the coupling-strength measurements.

Nine measurements of so-called simplified template cross sections, designed to measure the different Higgs boson production processes in specific regions of phase space, are reported:

$$\sigma(\mathrm{ggH}, 0\ \mathrm{jet}) = 37^{+16}_{-15}\,\mathrm{fb},$$
$$\sigma(\mathrm{ggH}, 1\ \mathrm{jet}, p_{\mathrm{T}}^{H} < 60\ \mathrm{GeV}) = 13^{+13}_{-12}\,\mathrm{fb},$$
$$\sigma(\mathrm{ggH}, 1\ \mathrm{jet}, 60 \leq p_{\mathrm{T}}^{H} < 120\ \mathrm{GeV}) = 5 \pm 6\,\mathrm{fb},$$
$$\sigma(\mathrm{ggH}, 1\ \mathrm{jet}, 120 \leq p_{\mathrm{T}}^{H} < 200\ \mathrm{GeV}) = 2.8^{+1.7}_{-1.6}\,\mathrm{fb},$$
$$\sigma(\mathrm{ggH}, \geq 2\ \mathrm{jet}) = 20^{+9}_{-8}\,\mathrm{fb},$$
$$\sigma(qq \to Hqq, p_{\mathrm{T}}^{j} < 200\ \mathrm{GeV}) = 15^{+6}_{-5}\,\mathrm{fb},$$
$$\sigma(ggH + qq \to Hqq, \mathrm{BSM} - \mathrm{like}) = 2.0 \pm 1.4\,\mathrm{fb},$$
$$\sigma(\mathrm{VH}, \mathrm{leptonic}) = 0.7^{+1.4}_{-1.3}\,\mathrm{fb},$$
$$\sigma(\mathrm{top}) = 0.7^{+0.8}_{-0.7}\,\mathrm{fb}\ .$$

All reported results show agreement with the Standard Model expectation.

Higgs boson coupling-strength modifiers are reported and two models are investigated: the first one reports results on effective coupling-strength modifiers for Higgs boson production in gluon–gluon fusion and decay, κ_g and κ_γ, respectively. They are found to be:

$$\kappa_g = 0.76^{+0.17}_{-0.14}, \quad \text{and} \quad \kappa_\gamma = 1.16^{+0.14}_{-0.14}.$$

The second model resolves the Higgs boson production and decay loops in terms of the more fundamental fermionic and vector boson couplings under the assumption of universal coupling-strength modifiers for all fermions and vector bosons, namely κ_V and κ_F, respectively. They are found to be:

$$\kappa_V = 0.92^{+0.08}_{-0.07}, \quad \text{and} \quad \kappa_F = 0.64^{+0.18}_{-0.14}.$$

Fiducial cross-section measurements are reported for a Higgs boson decaying into two isolated photons with transverse momentum greater than 35% and 25% of the diphoton invariant mass (corresponding to a photon p_T of 43.8 GeV and 31.3 GeV), and with $|\eta| < 2.37$, excluding the region of $1.37 < |\eta| < 1.52$. The total fiducial cross section is measured to be

$$\sigma_{\text{fid}} = 55 \pm 9 \,(\text{stat.}) \pm 4 \,(\text{exp.}) \pm 0.1 \,(\text{theo.}) \,\text{fb},$$

and is in agreement with the Standard Model expectation of 64 ± 2 fb. Additional cross sections in fiducial regions probing Higgs boson production from vector-boson fusion or associated with large missing transverse momentum, leptons or top quarks are reported. The cross section for the VBF-enhanced region is measured to be

$$\sigma_{\text{VBF-enhanced}} = 3.7 \pm 0.8 \,(\text{stat.}) \pm 0.5 \,(\text{exp.}) \pm 0.2 \,(\text{theo.}) \,\text{fb},$$

which is to be compared with the Standard Model prediction of 2.3 ± 0.1 fb. The larger measured cross section is consistent with the VBF signal-strength measurement reported above, if one scales the expected SM contributions from VBF (about 65%) and ggH (about 35%) in this fiducial region with the corresponding measured signal strengths. For the remaining fiducial regions, limits at 95% CL are reported

$$\sigma_{N_{\text{lepton}} \geq 1} < 1.39 \,\text{fb}, \quad \sigma_{\text{High }E_T^{\text{miss}}} < 1.00 \,\text{fb}, \quad \text{and} \quad \sigma_{t\bar{t}H-\text{enhanced}} < 1.27 \,\text{fb},$$

which can be compared with the Standard Model expectations of 0.57 ± 0.03 fb, 0.30 ± 0.02 fb, and 0.55 ± 0.06 fb, respectively.

The fiducial cross sections for different jet multiplicities is reported and compared to several theoretical predictions. Eleven differential cross sections and two double-differential cross sections are reported for events belonging to the inclusive diphoton fiducial region, as a function of kinematic variables of the diphoton system or of jets produced in association with the Higgs boson. The reported cross sections are sensitive to the Higgs boson production kinematics, the jet kinematics, the spin and CP quantum numbers of the Higgs boson, and the VBF production mechanism. All measured differential cross sections are compared to predictions and no significant deviation from the Standard Model expectation is observed. The full statistical and systematic correlations between measured distributions are determined and are available in HEPDATA along with the central values of the measured fiducial and differential cross sections to allow future comparisons and interpretations.

The strength and tensor structure of the Higgs boson interactions is investigated using five differential variables and an effective Lagrangian, which introduces additional CP-even and CP-odd interactions. No significant new physics contributions are observed and the reported 68% and 95% limits on such contributions have improved by a factor of two in comparison to the previous ATLAS measurement.

The measurements presented in this paper lay the foundation for further studies. All reported results are statistically limited and their precision will further improve with the full data set to be recorded during Run 2 of the LHC.

Acknowledgments

Appendix

A Simplified template cross-section framework

As introduced in Section 1.2, this paper includes cross-section measurements using the so called "stage-1" of the simplified template cross-section framework [7, 8]. In the full stage-1 proposal, template cross sections are defined in 31 regions of phase space with $|y_H| < 2.5$. These regions have been chosen to minimize the dependence on theoretical uncertainties and isolate possible BSM effects, while maximizing the experimental sensitivity.

The 31 regions of particle-level phase space corresponding to the stage 1 of the template cross-section approach are the following [7, 8]:

- Gluon–gluon fusion (11 regions). Gluon–gluon fusion events, together with $gg \rightarrow ZH$ events followed by hadronic decays of the Z boson, are split according to the number of jets in the event in 0, 1, and $\geq$ 2-jet events. Jets are reconstructed from all stable particles[14] with lifetime greater than 10 ps using the anti-k_t algorithm [77] with a jet radius parameter $R = 0.4$ and must have $p_T > 30$ GeV. The region containing two or more jets is split into two, with one of the two subregions ("VBF-like") containing events with a topology similar to vector-boson fusion events (invariant mass of the leading-p_T jet pair $m_{jj} > 400$ GeV, and rapidity separation between the two jets $|\Delta y_{jj}| > 2.8$). The one-jet and non-VBF-like two-jet regions are further split according to the transverse momentum of the Higgs boson in "low" (0–60 GeV), "medium" (60–120 GeV), "high" (120–200 GeV) and "BSM" (> 200 GeV) regions. The VBF-like events are further split into exclusive two-jet-like and inclusive three-jet-like events through a requirement on the transverse momentum p_T^{Hjj} of the system formed by the two photons and the two leading-p_T jets ($p_T^{Hjj} < 25$ GeV or $p_T^{Hjj} > 25$ GeV, respectively). The separation between events with zero, one, or two or more jets probes perturbative QCD predictions. Events containing a very high transverse momentum Higgs-boson of more than 200 GeV are sensitive to BSM contributions, such as those from loop-induced amplitudes mediated by hypothetical particles heavier than the top-quark.

- Vector-boson fusion (5 regions). Vector-boson fusion events, and VH events followed by hadronic V-boson decays, are first split according to the p_T of the leading jet. Events that contain at least one jet with a transverse momentum greater than 200 GeV, which are sensitive to BSM contributions, are measured separately in a "VBF BSM" category. The remaining events are separated into VBF-like events, VH-like events, and events that have a ggH-like topology (referred to as "Rest"). VBF-like events satisfy the same m_{jj} and $|\Delta y_{jj}|$ requirements as for the gluon–gluon fusion VBF-like category and are similarly split into "two-jet" and "$\geq$ 3-jet" events by requiring $p_T^{Hjj} < 25$ GeV or $p_T^{Hjj} > 25$ GeV, respectively. VH-like events are selected by requiring that they have at least two jets and an invariant mass of 60 GeV $< m_{jj} < 120$ GeV.

- Associated production with vector bosons decaying to leptons (11 regions). VH events are first split according to their production mode ($q\bar{q}' \rightarrow WH$, $q\bar{q} \rightarrow ZH$, or $gg \rightarrow ZH$). Events are separated further into regions of the vector boson transverse momentum p_T^V, and of jet multiplicity. For $gg \rightarrow ZH$, two regions are defined with p_T^V ("low": 0–150 GeV, and "high":

---

[14] The Higgs boson is treated as stable and consequently its decay products are removed from the jet finding.

> 150 GeV). The "high-p_T^V" $gg \to ZH$ region is further split into zero-jet and $\geq$ 1-jet regions. Regions sensitive to BSM contributions with $p_\mathrm{T}^V > 250$ GeV are defined for the $q\bar{q} \to VH$ production modes and two further p_T^V regions are defined ("low": 0–150 GeV, and "high": 150–250 GeV). The "high-p_T^V" $q\bar{q} \to VH$ region is finally split into zero-jet and $\geq$ 1-jet regions.

- Associated production with top and bottom quarks (4 regions). $t\bar{t}H$, t-channel tH, W-associated tH, and $b\bar{b}H$ events are classified according to their production mode, with no further separation into specific regions of phase space.

Table 19 summarizes the acceptances for each of the stage-1 STXS $gg \to H$ regions, and for five $qq \to Hqq$ regions, split into their VBF, WH, and ZH respective contributions. The table also lists the summed acceptance for the 11 VH leptonic regions, separately for the $gg \to ZH$, $q\bar{q}' \to WH$ and $q\bar{q} \to ZH$ processes. Finally, the acceptances are shown for the rarer production processes: $t\bar{t}H$, t-channel tH, W-associated tH, and $b\bar{b}H$. All STXS regions require $|y_H| < 2.5$ and are determined using the samples summarized in Table 2.

Table 19: The SM acceptances of stage-1 STXS regions useful to the results presented in this paper. For the $gg \rightarrow H$ regions each acceptance is relative to inclusive $gg \rightarrow H$ production; for all other regions, each acceptance is relative to the inclusive process shown at the top of the column. All regions require $|y_H| < 2.5$.

$gg \rightarrow H$ regions	0-jet	1-jet	$\geq$ 2-jet
$p_\mathrm{T}^H < 60$ GeV	0.562	0.134	0.025
$60\,\mathrm{GeV} \leq p_\mathrm{T}^H < 120$ GeV	-	0.093	0.038
$120\,\mathrm{GeV} \leq p_\mathrm{T}^H < 200$ GeV	-	0.015	0.020
$p_\mathrm{T}^H \geq 200$ GeV	-	0.003	0.009
VBF-like			
$\quad p_\mathrm{T}^{Hjj} < 25$ GeV	-	-	0.006
$\quad p_\mathrm{T}^{Hjj} \geq 25$ GeV	-	-	0.007

$qq \rightarrow Hqq$ regions	VBF	$q\bar{q}' \rightarrow WH$	$q\bar{q} \rightarrow ZH$
$p_\mathrm{T}^j \geq 200$ GeV	0.043	0.027	0.029
$p_\mathrm{T}^j < 200$ GeV			
$\quad$ VH-like	0.023	0.189	0.224
$\quad$ Rest	0.556	0.368	0.363
$\quad$ VBF-like			
$\quad\quad p_\mathrm{T}^{Hjj} < 25$ GeV	0.235	0.002	0.002
$\quad\quad p_\mathrm{T}^{Hjj} \geq 25$ GeV	0.074	0.007	0.008

VH, leptonic region	$gg \rightarrow ZH$	$q\bar{q}' \rightarrow WH$	$q\bar{q} \rightarrow ZH$
	0.289	0.286	0.265

Top region	$t\bar{t}H$	t-ch. tH	W-assoc. tH
	0.987	0.921	0.989

Beauty region	$b\bar{b}H$		
	0.945		

Table 20: The kinematic regions of the stage 1 of the simplified template cross sections, along with the intermediate (minimally merged set of) regions used for the measurements presented in this appendix. The VH-like, VBF-like, and rest regions are defined as in Table 1 and Appendix A. All regions require $|y_H| < 2.5$. The leading jet transverse momentum is denoted by p_T^j. In total, the cross sections for fifteen kinematic regions are measured.

Process	Measurement region	Particle-level stage 1 region
ggH + $gg \to Z(\to qq)H$	0-jet	0-jet
	1-jet, $p_T^H < 60$ GeV	1-jet, $p_T^H < 60$ GeV
	1-jet, $60 \le p_T^H < 120$ GeV	1-jet, $60 \le p_T^H < 120$ GeV
	1-jet, $120 \le p_T^H < 200$ GeV	1-jet, $120 \le p_T^H < 200$ GeV
	1-jet, $p_T^H > 200$ GeV	1-jet, $p_T^H > 200$ GeV
	$\ge$ 2-jet, $p_T^H < 60$ GeV	$\ge$ 2-jet, $p_T^H < 60$ GeV
	$\ge$ 2-jet, $60 \le p_T^H < 120$ GeV	$\ge$ 2-jet, $60 \le p_T^H < 120$ GeV
	$\ge$ 2-jet, $120 \le p_T^H < 200$ GeV	$\ge$ 2-jet, $120 \le p_T^H < 200$ GeV
	$\ge$ 2-jet, $p_T^H > 200$ GeV	$\ge$ 2-jet, $p_T^H > 200$ GeV
	VBF-like	VBF-like, $p_T^{Hjj} < 25$ GeV
		VBF-like, $p_T^{Hjj} \ge 25$ GeV
$qq' \to Hqq'$ (VBF + VH)	$p_T^j < 200$ GeV, VBF-like	$p_T^j < 200$ GeV, VBF-like, $p_T^{Hjj} < 25$ GeV
		$p_T^j < 200$ GeV, VBF-like, $p_T^{Hjj} \ge 25$ GeV
	$p_T^j < 200$ GeV, VH+Rest	$p_T^j < 200$ GeV, VH-like
		$p_T^j < 200$ GeV, Rest
	$p_T^j > 200$ GeV, BSM-like	$p_T^j > 200$ GeV
VH (leptonic decays)	VH leptonic	$q\bar{q} \to ZH$, $p_T^Z < 150$ GeV
		$q\bar{q} \to ZH$, $150 < p_T^Z < 250$ GeV, 0-jet
		$q\bar{q} \to ZH$, $150 < p_T^Z < 250$ GeV, $\ge$ 1-jet
		$q\bar{q} \to ZH$, $p_T^Z > 250$ GeV
		$q\bar{q} \to WH$, $p_T^W < 150$ GeV
		$q\bar{q} \to WH$, $150 < p_T^W < 250$ GeV, 0-jet
		$q\bar{q} \to WH$, $150 < p_T^W < 250$ GeV, $\ge$ 1-jet
		$q\bar{q} \to WH$, $p_T^W > 250$ GeV
		$gg \to ZH$, $p_T^Z < 150$ GeV
		$gg \to ZH$, $p_T^Z > 150$ GeV, 0-jet
		$gg \to ZH$, $p_T^Z > 150$ GeV, $\ge$ 1-jet
Top-associated production	top	$t\bar{t}H$
		tHW
		tHq
$b\bar{b}H$	merged w/ ggH	$b\bar{b}H$

B Minimally merged simplified template cross sections

In this appendix, the measurement for a minimally merged set of fifteen simplified template cross section regions is presented. The merged regions are defined in Table 20 and the extracted cross sections are summarized in Table 21 and Figure 35.

Table 21: Best-fit values and uncertainties of the simplified template cross sections times branching ratio, as defined in Table 20. The SM predictions [7] are shown for each region.

Measurement region ($|y_H| < 2.5$)	Result	Uncertainty				SM prediction
		Total	Stat.	Syst.		
ggH, 0 jet	38	$^{+16}_{-15}$	±14	$^{+6}_{-5}$	fb	63 ± 5 fb
ggH, 1 jet, $p_T^H < 60$ GeV	23	$^{+14}_{-13}$	±13	$^{+5}_{-4}$	fb	15 ± 2 fb
ggH, 1 jet, $60 \leq p_T^H < 120$ GeV	11	±8	±7	$^{+3}_{-2}$	fb	10 ± 2 fb
ggH, 1 jet, $120 \leq p_T^H < 200$ GeV	4.0	$^{+2.1}_{-1.9}$	±1.8	$^{+0.9}_{-0.6}$	fb	1.7 ± 0.3 fb
ggH, 1 jet, $p_T^H \geq 200$ GeV	2.6	$^{+1.6}_{-1.2}$	$^{+1.3}_{-1.1}$	$^{+0.8}_{-0.5}$	fb	0.4 ± 0.1 fb
ggH, ≥ 2 jet, $p_T^H < 60$ GeV	0	±8	±8	$^{+3}_{-2}$	fb	3 ± 1 fb
ggH, ≥ 2 jet, $60 \leq p_T^H < 120$ GeV	12	$^{+8}_{-7}$	±7	$^{+3}_{-2}$	fb	4 ± 1 fb
ggH, ≥ 2 jet, $120 \leq p_T^H < 200$ GeV	7.9	$^{+3.5}_{-3.4}$	±3.3	$^{+1.1}_{-0.9}$	fb	2.3 ± 0.6 fb
ggH, ≥ 2 jet, $p_T^H \geq 200$ GeV	2.6	$^{+1.6}_{-1.4}$	$^{+1.5}_{-1.4}$	$^{+0.6}_{-0.5}$	fb	1.0 ± 0.3 fb
ggH, VBF $-$ like	6.2	$^{+5.0}_{-4.5}$	±4.1	±1.2	fb	1.5 ± 0.3 fb
$qq \rightarrow Hqq$, VBF $-$ like	3.8	$^{+2.5}_{-2.3}$	$^{+2.2}_{-2.0}$	±1.2	fb	2.7 ± 0.2 fb
$qq \rightarrow Hqq$, VH + Rest	-19	±22	$^{+21}_{-20}$	$^{+6}_{-7}$	fb	7.7 ± 0.4 fb
$qq \rightarrow Hqq$, $p_T^j > 200$ GeV	-3.2	$^{+1.9}_{-2.0}$	±1.7	$^{+0.7}_{-0.9}$	fb	0.5 ± 0.1 fb
VH, leptonic	0.7	$^{+1.4}_{-1.2}$	$^{+1.4}_{-1.2}$	$^{+0.4}_{-0.3}$	fb	1.4 ± 0.1 fb
Top	0.7	$^{+0.8}_{-0.7}$	$^{+0.8}_{-0.7}$	$^{+0.2}_{-0.1}$	fb	1.3 ± 0.1 fb

88
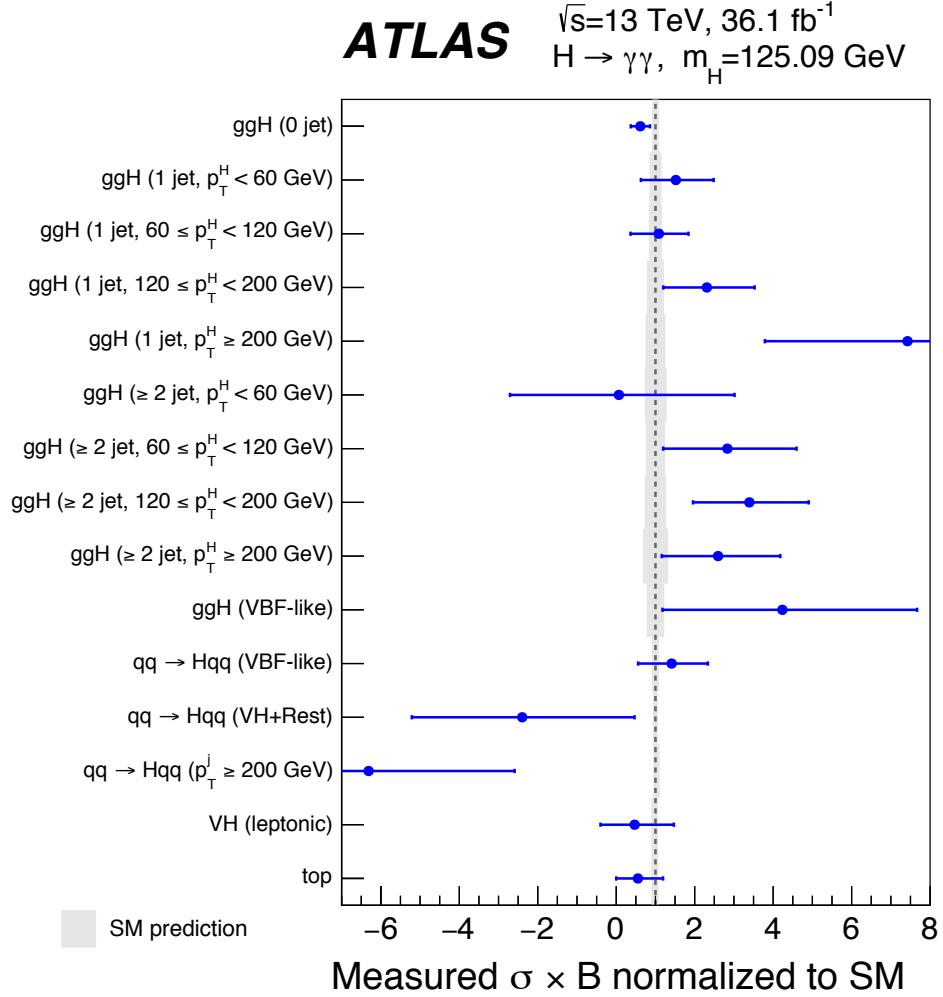
Figure 35: Summary plot of the measured simplified template cross sections times the Higgs to diphoton branching ratio, as defined in Table 20. For illustration purposes, the central values have been divided by their SM expectations but no additional SM uncertainties have been folded into the measurement. The uncertainties in the SM predicted cross sections are shown in gray in the plot. The fitted value of σ(top) corresponds to the sum of the $t\bar{t}H$, tHq, and tHW production-mode cross sections under the assumption that their relative ratios are as predicted by the SM. The σ(VH, leptonic) cross-section values are determined under the assumption that the ratio of the WH and ZH production mode cross sections is as predicted by the SM and includes production from both the quark and gluon initial states. The $b\bar{b}H$ contributions are merged with ggH.

C Additional unfolded differential cross sections

This appendix presents additional measurements and comparisons to theoretical predictions to those discussed in Section 9.5.

Figure 36 shows differential cross sections as a function of $p_{\mathrm{Tt}}^{\gamma\gamma}$, the orthogonal component of the diphoton momentum when projected on the axis given by the difference of the 3-momenta of the two photons, as well as $|\Delta y_{\gamma\gamma}|$, the rapidity separation of the two photons.

Figure 37 shows differential cross sections as a function of H_{T}, the scalar sum of all reconstructed jets in a given event with $p_{\mathrm{T}} > 30$ GeV, the absolute value of the azimuthal difference $|\Delta\phi_{jj}|$ between the leading and subleading jet in events with at least two jets, and the vectorial sum of the transverse momentum of the diphoton system and the leading and subleading jet system, $p_{\mathrm{T}}^{\gamma\gamma jj}$, in events with at least two jets.

Figure 38 displays measurements of the beam-thrust-like variables $\tau_{C,j1}$ and $\sum \tau_{C,j}$. For a given jet, τ is defined by

$$\tau = \frac{m_{\mathrm{T}}}{2\cosh y^*}, \quad y^* = y - y_{\gamma\gamma}, \qquad m_{\mathrm{T}} = \sqrt{p_{\mathrm{T}}^2 + m^2}, \tag{3}$$

where y is the jet rapidity and m is the jet mass. The variable $\tau_{C,j1}$ refers to the highest-τ jet, and $\sum \tau_{C,j}$ is the scalar sum of τ for all jets with $\tau > 8$ GeV. For large jet rapidities, τ corresponds to the small light-cone component of the jet, $p_{\mathrm{jet}}^+ = E_{\mathrm{jet}} - |p_{z,\mathrm{jet}}|$, while the sum is closely related to the beam-thrust global event shape [156], as measured in the diphoton rest frame.

Figure 39 shows the first and second moments of each of the additional differential distributions. The data are compared to a variety of theoretical predictions. In general, the SM predictions are in agreement with the measured distributions.

D Diphoton acceptance, photon isolation and non-perturbative correction factors for parton-level gluon–gluon fusion calculations

This appendix presents the diphoton acceptance factors that are applied to parton-level calculations of Higgs production via gluon–gluon fusion, in order to correctly account for the diphoton selection criteria applied to the Higgs-boson decay products, are shown in Table 22 for the fiducial and differential cross sections presented in Section 9.5 and Appendix C. Multiplicative isolation efficiency and non-perturbative correction factors that account for the efficiency of the photon isolation criterion and the impact of hadronization and underlying-event activity are presented in Tables 23 and 24, respectively. The isolation efficiency is defined as the fraction of selected diphoton events (i.e. within the kinematic acceptance) that also satisfy the isolation criteria, and is determined using samples before including hadronization and the underlying-event activity. The non-perturbative correction factors are defined as the ratios of cross sections produced with and without hadronization and the underlying event. The default non-perturbative correction is taken as the central value of an envelope formed from multiple event generators and/or event generator tunes, with the uncertainty taken to be the maximal deviation observed in the envelope. Table 25 also provides the combined non-perturbative and isolation correction with a total uncertainty that takes into account the correlations between the uncertainties of
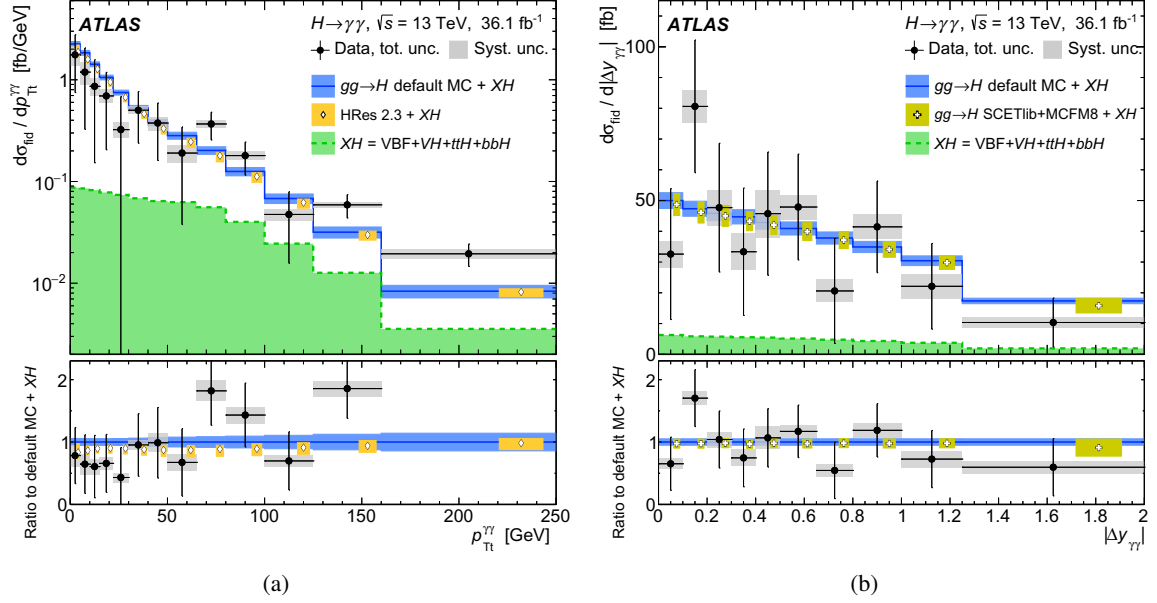
Figure 36: The differential cross sections for $pp \to H \to \gamma\gamma$ as a function of (a) $p_{\mathrm{Tt}}^{\gamma\gamma}$ and (b) $|\Delta y_{\gamma\gamma}|$ are shown and compared to the SM expectations. The data are shown as filled (black) circles. The vertical error bar on each data point represents the total uncertainty in the measured cross section and the shaded (gray) band is the systematic component. The SM prediction, defined using the Powheg NNLOPS prediction for gluon–gluon fusion and the default MC samples for the other production mechanisms, is presented as a hatched (blue) band, with the width of the band reflecting the total theoretical uncertainty (see text for details). The small contribution from VBF, VH $t\bar{t}H$ and $b\bar{b}H$ is also shown as a (green) histogram and denoted by XH. The default MC has been normalized with the N^3LO prediction of Refs. [7, 24, 31–34]. In addition, the Hres and SCETlib+MCFM8 predictions, described in Section 9.5, are displayed in (a) and (b), respectively.

both factors. Note though that no non-perturbative correction factors are applied to the SM predictions presented in this paper.

A summary of the binning of all differential variables is given in Table 26.

E Supplement to event categorization

Table 27 summarizes the number of expected signal events and measured background events in the smallest interval expected to contain 90% of the expected SM signal events, together with the expected signal purity and local significance in the same interval, for each of the event reconstruction categories. The definition of the categories can be found in Table 4 in Section 8.1.6.

Table 28 summarizes the fractions of signal events from the different production modes expected in each reconstruction category, as illustrated in Figure 8.

Table 29 summarizes the chosen background function used in each reconstruction category.
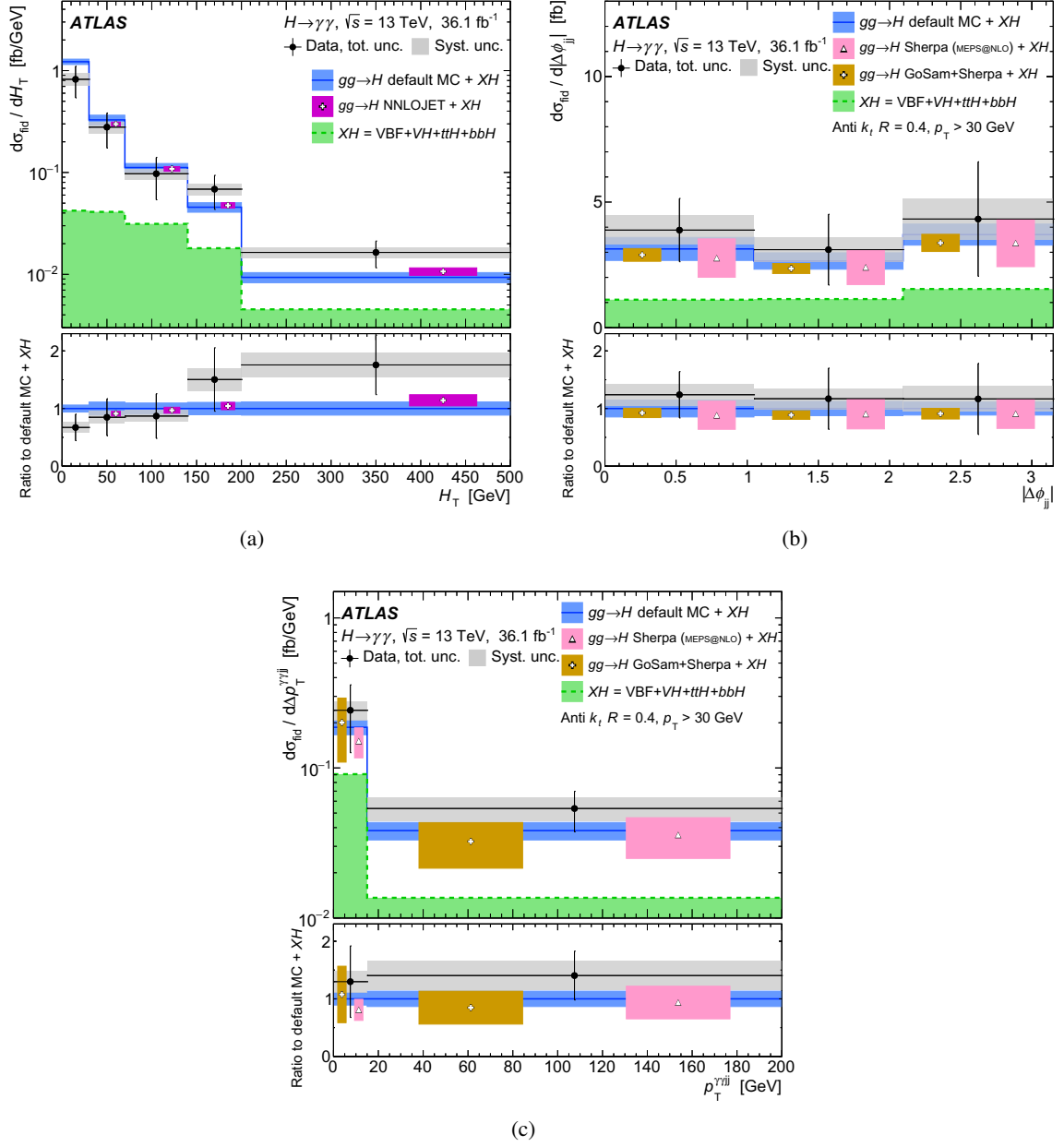
Figure 37: The differential cross sections for $pp \to H \to \gamma\gamma$ as a function of (a) H_T, (b) $|\Delta\phi_{jj}|$, and (c) $p_T^{\gamma\gamma jj}$ are shown and compared to the SM expectations. The data and theoretical predictions are presented in the same way as in Figure 36. In addition, the NNLOJET prediction is displayed in (a), and the SHERPA and GOSAM predictions are displayed in (b) and (c). More details of these predictions can be found in Section 9.5.1.

92
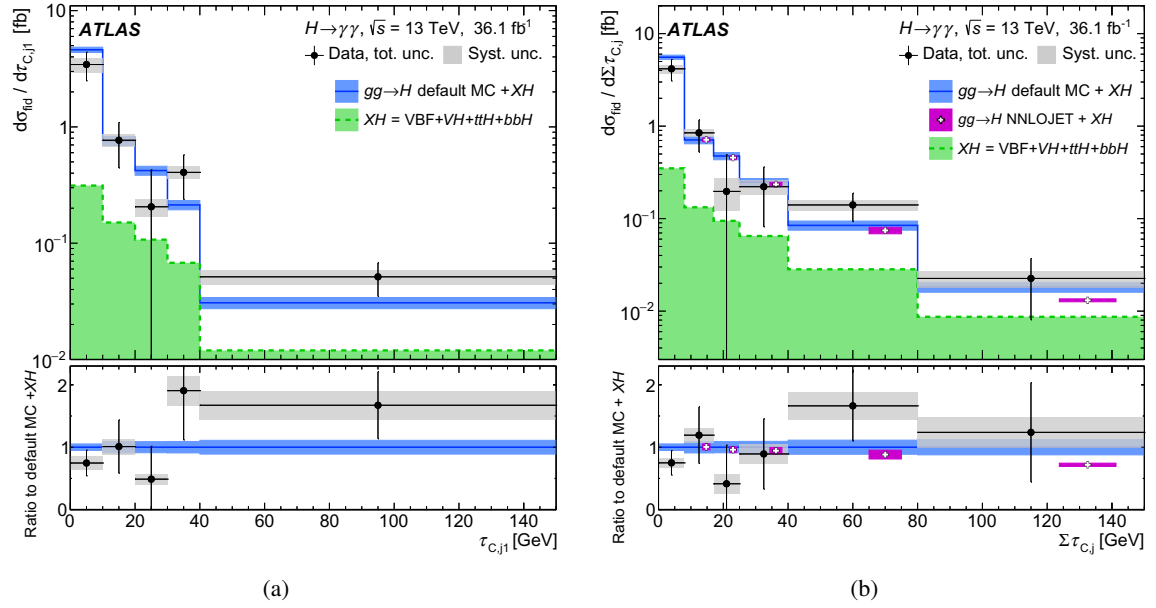
Figure 38: The differential cross sections for $pp \rightarrow H \rightarrow \gamma\gamma$ as a function of (a) $\tau_{C,j1}$ and (b) $\sum \tau_{C,j}$ are shown and compared to the SM expectations. The data and theoretical predictions are presented in the same way as in Figure 36. In addition, the NNLOJET prediction is displayed in (b).
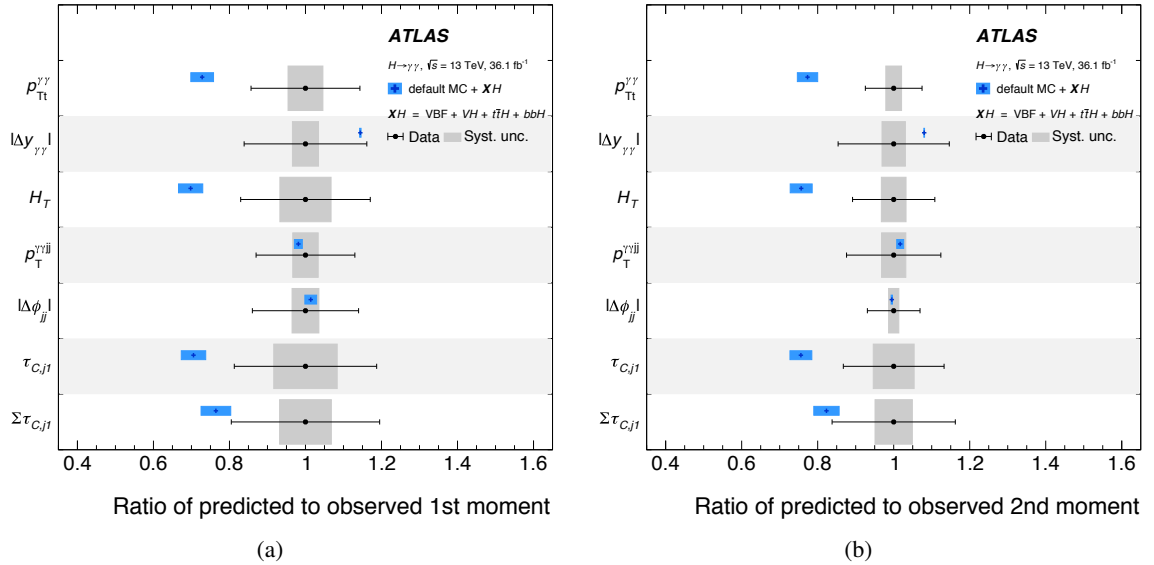
Figure 39: (a) The ratio of the first moment (mean) of each differential distribution predicted by the Standard Model to that observed in the data. The SM moment is calculated by using the PowHEG NNLOPS prediction for gluon–gluon fusion and the default MC samples for the other production mechanisms. (b) The ratio of the second moment (RMS) of each differential distribution predicted by the Standard Model to that observed in the data. The intervals on the vertical axes each represent one of the differential distributions. The band for the theoretical prediction represents the corresponding uncertainty in that prediction (see text for details). The error bar on the data represents the total uncertainty in the measurement, with the gray band representing only the systematic uncertainty.

Table 22: Diphoton kinematic acceptances in percent for gluon–gluon fusion for the diphoton fiducial region and all differential variable bins studied in this paper, defined as the probability to fulfill the diphoton kinematic criteria: $p_T/m_{\gamma\gamma} < 0.35\ (0.25)$ for the leading (subleading) photon and $|\eta_\gamma| < 2.37$. The factors are evaluated using the Powheg NNLOPS event generator. Uncertainties are taken from PDF variations. QCD scale variations have a negligible impact on these factors. The range of each bin is given in Table 26.

	Bin 1	Bin 2	Bin 3	Bin 4	Bin 5	Bin 6	Bin 7	Bin 8	Bin 9	Bin 10	Bin 11	Bin 12	Bin 13
Diphoton fiducial	51.9 ± 0.4	–	–	–	–	–	–	–	–	–	–	–	–
$p_T^{\gamma\gamma}$	52.3 ±0.5	52.9 ±0.5	52.0 ±0.4	50.8 ±0.4	50.0 ±0.3	48.6 ±0.3	51.0 ±0.3	57.7 ±0.3	65.2 ±0.3	–	–	–	–
$|y_{\gamma\gamma}|$	74.0 ±0.2	73.6 ±0.2	72.2 ±0.2	69.3 ±0.1	67.1 ±0.1	64.8 ±0.1	61.5 ±0.1	56.0 ±0.2	31.4 ±0.1	–	–	–	–
$p_{\mathrm{Tt}}^{\gamma\gamma}$	49.5 ±0.6	49.4 ±0.6	49.2 ±0.6	48.8 ±0.6	49.0 ±0.6	49.8 ±0.6	52.8 ±0.7	59.7 ±0.5	69.5 ±0.5	73.2 ±0.5	75.7 ±0.5	78.3 ±0.4	82.9 ±0.4
$|\cos\theta^*|$	78.8 ±0.6	74.9 ±0.6	73.3 ±0.6	71.7 ±0.6	69.6 ±0.6	67.6 ±0.7	65.8 ±0.7	60.4 ±0.7	23.6 ±0.5	–	–	–	–
$|\Delta y_{\gamma\gamma}|$	80.0 ±0.5	76.1 ±0.5	74.9 ±0.5	73.7 ±0.6	72.4 ±0.6	70.6 ±0.6	68.6 ±0.6	67.4 ±0.6	65.3 ±0.7	50.8 ±0.7	–	–	–
$N_{\mathrm{jets}},\, p_T>$ 30 GeV	51.8 ±0.5	51.8 ±0.4	52.3 ±0.4	54.2 ±0.7	–	–	–	–	–	–	–	–	–
$N_{\mathrm{jets}},\, p_T>$ 50 GeV	51.2 ±0.5	54.2 ±0.4	55.8 ±0.7	–	–	–	–	–	–	–	–	–	–
$p_T^{j_1}$	51.8 ±0.5	49.8 ±0.4	56.1 ±0.4	52.7 ±0.4	55.5 ±0.6	–	–	–	–	–	–	–	–
$p_T^{j_2}$	51.8 ±0.4	51.9 ±0.4	57.1 ±0.8	–	–	–	–	–	–	–	–	–	–
H_T	51.8 ±0.5	51.1 ±0.4	52.1 ±0.4	53.8 ±0.5	57.3 ±0.9	–	–	–	–	–	–	–	–
$|y_{j_1}|$	55.2 ±0.4	54.6 ±0.4	53.1 ±0.4	53.0 ±0.4	52.3 ±0.4	50.4 ±0.4	48.2 ±0.4	–	–	–	–	–	–
$|y_{j_2}|$	54.1 ±0.5	53.5 ±0.5	52.3 ±0.5	–	–	–	–	–	–	–	–	–	–
m_{jj}	52.8 ±0.5	53.3 ±0.6	51.6 ±0.6	–	–	–	–	–	–	–	–	–	–
$|\Delta y_{jj}|$	70.2 ±3.7	68.7 ±3.4	67.2 ±3.4	–	–	–	–	–	–	–	–	–	–
$|\Delta\phi_{jj}|$	53.8 ±0.6	53.3 ±0.5	51.6 ±0.4	–	–	–	–	–	–	–	–	–	–
$\Delta\phi_{jj}$	51.9 ±0.4	54.1 ±0.6	53.4 ±0.6	52.0 ±0.4	–	–	–	–	–	–	–	–	–
$p_T^{\gamma\gamma jj}$	47.6 ±0.4	54.4 ±0.5	–	–	–	–	–	–	–	–	–	–	–
$|\Delta\phi_{\gamma\gamma,jj}|$	50.9 ±0.6	54.0 ±0.4	54.0 ±0.4	–	–	–	–	–	–	–	–	–	–
$\tau_{C,j1}$	51.0 ±0.5	50.9 ±0.4	55.9 ±0.4	63.0 ±0.5	59.0 ±0.7	–	–	–	–	–	–	–	–
$\sum \tau_{C,j}$	51.0 ±0.5	50.5 ±0.4	52.3 ±0.4	59.5 ±0.4	57.6 ±0.5	61.7 ±0.9	–	–	–	–	–	–	–
$p_T^{\gamma\gamma}[|\cos\theta^*|<0.5]$	72.5 ±0.6	71.1 ±0.5	54.0 ±0.3	–	–	–	–	–	–	–	–	–	–
$p_T^{\gamma\gamma}[0.5 \le |\cos\theta^*|<1.0]$	32.4 ±0.4	30.4 ±0.3	55.1 ±0.6	–	–	–	–	–	–	–	–	–	–
$p_T^{\gamma\gamma}[N_{\mathrm{jets}}{=}0]$	51.2 ±0.5	52.1 ±0.5	52.2 ±0.5	59.9 ±1.9	–	–	–	–	–	–	–	–	–
$p_T^{\gamma\gamma}[N_{\mathrm{jets}}{=}1]$	58.4 ±0.5	49.6 ±0.4	48.8 ±0.4	51.6 ±0.5	–	–	–	–	–	–	–	–	–
$p_T^{\gamma\gamma}[N_{\mathrm{jets}}{=}2]$	52.5 ±0.4	50.1 ±0.4	63.1 ±0.3	–	–	–	–	–	–	–	–	–	–
$p_T^{\gamma\gamma}[N_{\mathrm{jets}}{\ge}3]$	52.2 ±0.4	63.0 ±0.3	–	–	–	–	–	–	–	–	–	–	–

Table 23: Isolation efficiencies in percent for gluon–gluon fusion $H \to \gamma\gamma$ for the diphoton fiducial region and all differential variable bins in this analysis.

	Bin 1	Bin 2	Bin 3	Bin 4	Bin 5	Bin 6	Bin 7	Bin 8	Bin 9	Bin 10	Bin 11	Bin 12	Bin 13
Diphoton fiducial	97.7 ±0.1	–	–	–	–	–	–	–	–	–	–	–	–
$p_T^{\gamma\gamma}$	98.4 ±0.1	97.6 ±0.1	97.2 ±0.0	96.9 ±0.0	97.0 ±0.0	97.7 ±0.1	98.5 ±0.0	98.7 ±0.1	98.9 ±0.2	–	–	–	–
$|y_{\gamma\gamma}|$	97.6 ±0.1	97.6 ±0.1	97.7 ±0.1	97.6 ±0.2	97.7 ±0.2	97.7 ±0.0	97.7 ±0.1	97.8 ±0.0	98.0 ±0.0	–	–	–	–
$p_{Tt}^{\gamma\gamma}$	97.2 ±0.2	97.4 ±0.0	97.5 ±0.1	97.7 ±0.0	97.9 ±0.0	97.9 ±0.0	98.0 ±0.1	98.0 ±0.1	98.2 ±0.1	98.5 ±0.1	98.9 ±0.0	99.1 ±0.0	99.2 ±0.2
$|\cos\theta^*|$	97.9 ±0.0	97.9 ±0.1	97.9 ±0.0	97.8 ±0.1	97.8 ±0.0	97.7 ±0.1	97.7 ±0.1	97.6 ±0.1	97.6 ±0.1	–	–	–	–
$|\Delta y_{\gamma\gamma}|$	97.7 ±0.1	98.0 ±0.1	97.9 ±0.1	97.9 ±0.1	97.9 ±0.2	97.9 ±0.1	97.8 ±0.0	97.7 ±0.1	97.7 ±0.1	97.4 ±0.1	–	–	–
$N_{\text{jets}}, p_T > 30$ GeV	97.7 ±0.1	97.8 ±0.1	97.8 ±0.1	97.8 ±0.1	–	–	–	–	–	–	–	–	–
$N_{\text{jets}}, p_T > 50$ GeV	97.7 ±0.1	97.8 ±0.1	98.1 ±0.0	–	–	–	–	–	–	–	–	–	–
$p_T^{j_1}$	97.7 ±0.1	97.6 ±0.1	97.8 ±0.0	97.8 ±0.2	98.3 ±0.0	–	–	–	–	–	–	–	–
$p_T^{j_2}$	97.8 ±0.1	97.7 ±0.1	98.3 ±0.0	–	–	–	–	–	–	–	–	–	–
H_T	97.7 ±0.1	97.7 ±0.1	97.8 ±0.1	98.0 ±0.2	98.2 ±0.0	97.7 ±0.4	97.8 ±0.1	–	–	–	–	–	–
$|y_{j_1}|$	97.7 ±0.1	97.7 ±0.1	97.8 ±0.1	97.8 ±0.1	97.8 ±0.1	–	–	–	–	–	–	–	–
$|y_{j_2}|$	97.8 ±0.1	97.8 ±0.1	98.2 ±0.1	–	–	–	–	–	–	–	–	–	–
m_{jj}	97.7 ±0.0	98.2 ±0.1	98.2 ±0.1	–	–	–	–	–	–	–	–	–	–
$|\Delta y_{jj}|$	97.8 ±0.1	97.8 ±0.0	97.8 ±0.3	–	–	–	–	–	–	–	–	–	–
$|\Delta\phi_{jj}|$	98.1 ±0.1	97.9 ±0.1	97.4 ±0.1	–	–	–	–	–	–	–	–	–	–
$\Delta\phi_{jjj}$	97.6 ±0.1	98.0 ±0.2	98.1 ±0.0	97.5 ±0.1	–	–	–	–	–	–	–	–	–
p_T^{jjj}	98.3 ±0.2	97.7 ±0.1	–	–	–	–	–	–	–	–	–	–	–
$|\Delta\phi_{\gamma\gamma,jj}|$	98.4 ±0.1	97.8 ±0.2	96.4 ±0.2	–	–	–	–	–	–	–	–	–	–
$\tau_{C,j1}$	97.7 ±0.1	97.8 ±0.1	97.7 ±0.1	97.6 ±0.1	97.9 ±0.0	98.1 ±0.2	–	–	–	–	–	–	–
$\sum \tau_{C,j}$	97.7 ±0.2	97.7 ±0.1	97.6 ±0.0	97.7 ±0.1	97.9 ±0.2	98.3 ±0.1	–	–	–	–	–	–	–
$p_T^{\gamma\gamma}[|\cos\theta^*| < 0.5]$	98.3 ±0.1	97.0 ±0.0	98.4 ±0.2	98.9 ±0.4	–	–	–	–	–	–	–	–	–
$p_T^{\gamma\gamma}[0.5 \leq |\cos\theta^*| < 1.0]$	97.6 ±0.1	97.4 ±0.1	98.9 ±0.0	99.0 ±1.0	100	–	–	–	–	–	–	–	–
$p_T^{\gamma\gamma}[N_{\text{jets}}=0]$	98.6 ±0.1	97.8 ±0.1	96.4 ±0.0	91.2 ±1.3	–	–	–	–	–	–	–	–	–
$p_T^{\gamma\gamma}[N_{\text{jets}}=1]$	97.5 ±0.3	97.6 ±0.2	97.7 ±0.0	98.4 ±0.1	–	–	–	–	–	–	–	–	–
$p_T^{\gamma\gamma}[N_{\text{jets}}=2]$	97.0 ±0.3	98.4 ±0.1	98.8 ±0.1	–	–	–	–	–	–	–	–	–	–
$p_T^{\gamma\gamma}[N_{\text{jets}}\geq3]$	97.4 ±0.2	98.5 ±0.7	–	–	–	–	–	–	–	–	–	–	–

Table 23: Isolation efficiencies in percent for gluon–gluon fusion $H \to \gamma\gamma$ for the diphoton fiducial region and all differential variable bins in this analysis. The isolation efficiency is defined as the probability for both photons to fulfill the isolation criteria (as described in Section 9.1) for events that satisfy the diphoton kinematic criteria. Regions of phase space where no reliable estimate could be obtained are listed as '100' without uncertainties. Uncertainties are assigned in the same way as for the non-perturbative correction factors: by varying the fragmentation and underlying-event modeling. These factors can be multiplied by the kinematic acceptance factors (see Table 22) to extrapolate an inclusive gluon–gluon fusion Higgs prediction to the fiducial volume used in this analysis. The range of each bin is given in Table 26.

	Bin 1	Bin 2	Bin 3	Bin 4	Bin 5	Bin 6	Bin 7	Bin 8	Bin 9	Bin 10	Bin 11	Bin 12	Bin 13
Diphoton fiducial	100 ±2	–	–	–	–	–	–	–	–	–	–	–	–
$p_T^{\gamma\gamma}$	99.7 ±0.4	100.3 ±0.3	100.2 ±0.4	99.7 ±0.6	100.0 ±0.7	99.8 ±0.5	100.4 ±0.6	99.9 ±0.9	100.1 ±0.6	–	–	–	–
$|y_{\gamma\gamma}|$	99.8 ±0.4	99.9 ±0.3	100.1 ±0.2	100.0 ±0.5	100.0 ±0.3	100.2 ±0.4	99.9 ±0.5	100.2 ±0.3	100.0 ±0.4	–	–	–	–
$p_T^{\gamma\gamma}$	100.0 ±0.5	100.1 ±0.3	100.0 ±0.4	100.3 ±0.3	100.0 ±0.8	100.3 ±0.7	99.8 ±0.7	100.0 ±0.3	99.9 ±1.1	99.8 ±0.8	99.8 ±1.1	100.6 ±0.9	100.4 ±1.5
$|\cos\theta^*|$	100.1 ±0.5	100.0 ±0.5	99.8 ±0.5	99.7 ±0.4	99.9 ±0.4	100.0 ±0.4	100.2 ±0.5	100.0 ±0.4	100.2 ±0.2	–	–	–	–
$|\Delta y_{\gamma\gamma}|$	99.9 ±0.7	100.0 ±0.5	100.0 ±0.9	99.7 ±0.5	99.7 ±0.4	100.1 ±0.4	99.9 ±0.3	100.0 ±0.5	100.1 ±0.7	100.1 ±0.2	–	–	–
$N_{\text{jets}}, p_T > 30$ GeV	102 ±4	99.2 ±2.8	98.2 ±7.3	94.4 ±11.9	–	–	–	–	–	–	–	–	–
$N_{\text{jets}}, p_T > 50$ GeV	100.7 ±2.2	98.7 ±3.6	96.4 ±6.5	–	–	–	–	–	–	–	–	–	–
$p_T^{j_1}$	102 ±4	98.7 ±5.2	98.0 ±4.7	98.1 ±4.3	97.4 ±3.7	–	–	–	–	–	–	–	–
$p_T^{j_2}$	99.2 ±2.8	97.2 ±9.2	97.3 ±6.2	–	–	–	–	–	–	–	–	–	–
H_T	102 ±4	99.1 ±3.8	98.1 ±5.3	97.0 ±6.7	96.7 ±6.5	–	–	–	–	–	–	–	–
$|y_{j_1}|$	98.5 ±4.6	98.9 ±4.4	98.5 ±4.7	98.0 ±4.5	98.4 ±4.3	99.3 ±4.9	97.9 ±4.9	–	–	–	–	–	–
$|y_{j_2}|$	96.7 ±8.6	97.6 ±8.4	97.0 ±8.9	–	–	–	–	–	–	–	–	–	–
m_{jj}	96.1 ±9.4	98.6 ±8.0	98.4 ±8.3	–	–	–	–	–	–	–	–	–	–
$|\Delta y_{jj}|$	96.5 ±8.3	98.5 ±9.0	96.5 ±10.4	–	–	–	–	–	–	–	–	–	–
$|\Delta\phi_{jj}|$	95.2 ±8.3	97.0 ±7.9	100.3 ±10.6	–	–	–	–	–	–	–	–	–	–
$\Delta\phi_{jj}$	99.0 ±9.6	95.8 ±8.0	95.5 ±8.3	98.7 ±9.5	–	–	–	–	–	–	–	–	–
$p_T^{\gamma\gamma jj}$	94.3 ±12.4	97.8 ±7.5	–	–	–	–	–	–	–	–	–	–	–
$|\Delta\phi_{\gamma\gamma,jj}|$	96.6 ±7.1	96.3 ±7.7	102.5 ±14.3	–	–	–	–	–	–	–	–	–	–
$\tau_{C,j1}$	102 ±4	98.1 ±4.3	98.0 ±5.1	99.2 ±5.0	99.9 ±4.9	98.8 ±4.1	–	–	–	–	–	–	–
$\sum \tau_{C,j}$	100.9 ±2.9	98.0 ±4.0	100.1 ±4.2	98.8 ±5.3	98.8 ±6.0	97.8 ±5.3	–	–	–	–	–	–	–
$p_T^{\gamma\gamma}[|\cos\theta^*| < 0.5]$	100.1 ±1.0	100.2 ±0.7	100.0 ±0.7	100.8 ±6.8	–	–	–	–	–	–	–	–	–
$p_T^{\gamma\gamma}[0.5 \le |\cos\theta^*| < 1.0]$	100.2 ±0.9	99.8 ±0.8	100.2 ±1.3	100.3 ±4.1	–	–	–	–	–	–	–	–	–
$p_T^{\gamma\gamma}[N_{\text{jets}}=0]$	98.6 ±2.3	99.8 ±0.7	103.1 ±4.7	110.1 ±23.7	–	–	–	–	–	–	–	–	–
$p_T^{\gamma\gamma}[N_{\text{jets}}=1]$	98.2 ±9.4	99.1 ±0.9	103.2 ±5.8	104.9 ±8.1	–	–	–	–	–	–	–	–	–
$p_T^{\gamma\gamma}[N_{\text{jets}}=2]$	99.9 ±5.2	102.5 ±7.9	106.1 ±12.3	–	–	–	–	–	–	–	–	–	–
$p_T^{\gamma\gamma}[N_{\text{jets}}\ge3]$	100.1 ±2.5	102 ±11	–	–	–	–	–	–	–	–	–	–	–

Table 24: Non-perturbative correction factors in percent accounting for the impact of hadronization and the underlying-event activity for the diphoton fiducial region and all differential variable bins. Uncertainties are evaluated by deriving these factors using different generators and tunes as described in the text. The range of each bin is given in Table 26.

	Bin 1	Bin 2	Bin 3	Bin 4	Bin 5	Bin 6	Bin 7	Bin 8	Bin 9	Bin 10	Bin 11	Bin 12	Bin 13
Diphoton fiducial	97.7 ±2.4	–	–	–	–	–	–	–	–	–	–	–	–
$p_T^{\gamma\gamma}$	97.8 ±0.5	97.7 ±0.6	97.2 ±1.0	96.3 ±1.0	96.5 ±0.9	96.9 ±0.7	98.4 ±1.0	98.3 ±1.1	99.1 ±0.7	–	–	–	–
$|y_{\gamma\gamma}|$	97.2 ±0.7	97.3 ±0.5	97.4 ±0.6	97.4 ±0.8	97.5 ±0.6	97.5 ±0.7	97.5 ±0.6	97.5 ±0.7	97.8 ±0.8	–	–	–	–
$p_{Tt}^{\gamma\gamma}$	97.0 ±0.6	97.4 ±0.7	97.2 ±0.6	97.6 ±0.7	97.1 ±0.9	97.8 ±1.0	97.5 ±0.9	97.6 ±0.6	97.8 ±1.4	98.0 ±0.8	98.1 ±1.2	99.6 ±1.0	99.5 ±1.6
$|\cos\theta^*|$	97.7 ±0.8	97.7 ±0.7	97.3 ±0.8	97.1 ±0.7	97.4 ±0.6	97.5 ±0.5	97.6 ±0.7	97.3 ±0.6	97.5 ±0.7	–	–	–	–
$|\Delta y_{\gamma\gamma}|$	97.6 ±0.9	97.9 ±0.5	97.6 ±1.1	97.4 ±0.7	97.1 ±0.6	97.7 ±0.7	97.4 ±0.7	97.5 ±0.9	97.3 ±0.6	97.3 ±0.8	–	–	–
$N_{\text{jets}}, p_T > 30$ GeV	99.3 ±3.8	96.5 ±3.1	95.5 ±7.6	91.9 ±12.2	–	–	–	–	–	–	–	–	–
$N_{\text{jets}}, p_T > 50$ GeV	98.4 ±1.5	96.1 ±3.9	94.2 ±6.9	–	–	–	–	–	–	–	–	–	–
p_T^{j1}	99.3 ±3.8	95.9 ±5.5	95.3 ±5.0	95.5 ±4.8	95.1 ±4.3	–	–	–	–	–	–	–	–
p_T^{j2}	96.5 ±3.1	94.4 ±9.5	95.1 ±6.5	–	–	–	–	–	–	–	–	–	–
H_T	99.3 ±3.8	96.4 ±4.1	95.4 ±5.7	94.5 ±7.0	94.5 ±6.8	–	–	–	–	–	–	–	–
$|y_{j1}|$	95.8 ±5.0	96.2 ±4.7	95.9 ±5.0	95.3 ±4.9	95.6 ±4.7	96.8 ±5.4	95.2 ±5.3	–	–	–	–	–	–
$|y_{j2}|$	94.1 ±9.0	94.8 ±8.7	94.3 ±9.2	–	–	–	–	–	–	–	–	–	–
m_{jj}	93.3 ±9.6	95.9 ±8.3	96.0 ±8.7	–	–	–	–	–	–	–	–	–	–
$|\Delta y_{jj}|$	93.8 ±8.6	95.8 ±9.3	93.8 ±10.8	–	–	–	–	–	–	–	–	–	–
$|\Delta\phi_{jj}|$	92.9 ±8.7	94.4 ±8.3	97.2 ±11.0	–	–	–	–	–	–	–	–	–	–
$\Delta\phi_{\gamma\gamma,jj}$	96.0 ±9.9	93.4 ±8.3	93.0 ±8.5	95.7 ±9.7	–	–	–	–	–	–	–	–	–
$p_T^{\gamma\gamma jj}$	92.3 ±12.6	–	–	–	–	–	–	–	–	–	–	–	–
$|\Delta\phi_{\gamma\gamma,jj}|$	94.6 ±7.4	93.6 ±8.0	97.9 ±14.7	–	–	–	–	–	–	–	–	–	–
$\tau_{C,j1}$	99.3 ±3.8	95.4 ±4.8	95.2 ±5.5	96.3 ±5.2	97.1 ±5.4	96.5 ±4.5	–	–	–	–	–	–	–
$\sum \tau_{C,j}$	98.7 ±2.3	95.3 ±4.5	97.2 ±4.6	96.0 ±5.6	96.3 ±6.2	95.7 ±5.8	–	–	–	–	–	–	–
$p_T^{\gamma\gamma}[|\cos\theta^*|< 0.5]$	98.1 ±0.7	97.0 ±0.7	98.2 ±1.0	99.8 ±6.8	–	–	–	–	–	–	–	–	–
$p_T^{\gamma\gamma}[0.5 \leq |\cos\theta^*|< 1.0]$	97.6 ±0.6	96.9 ±1.1	98.8 ±1.4	99.7 ±4.5	–	–	–	–	–	–	–	–	–
$p_T^{\gamma\gamma}[N_{\text{jets}}=0]$	96.7 ±2.4	97.3 ±1.1	99.0 ±4.6	102.0 ±24.5	–	–	–	–	–	–	–	–	–
$p_T^{\gamma\gamma}[N_{\text{jets}}=1]$	95.4 ±9.7	96.3 ±1.3	100.4 ±5.6	103.2 ±7.9	–	–	–	–	–	–	–	–	–
$p_T^{\gamma\gamma}[N_{\text{jets}}=2]$	96.5 ±5.4	100.5 ±7.7	104.5 ±12.2	–	–	–	–	–	–	–	–	–	–
$p_T^{\gamma\gamma}[N_{\text{jets}}\geq3]$	97.3 ±3.1	99.9 ±10.6	–	–	–	–	–	–	–	–	–	–	–

Table 25: Combined non-perturbative (Table 24) and particle-level isolation correction factors (Table 23) in percent accounting for the impact of hadronization and the underlying-event activity for the diphoton fiducial region and all differential variable bins. The uncertainties in the combined values properly take into account the correlations between both multiplicative factors.

97

Bin	1	2	3	4	5	6	7	8	9	10	11	12	13
$p_T^{\gamma\gamma}$ [GeV]	$0-20$	$20-30$	$30-45$	$45-60$	$60-80$	$80-120$	$120-170$	$170-220$	$220-350$				
$|y_{\gamma\gamma}|$	$0-0.15$	$0.15-0.3$	$0.3-0.45$	$0.45-0.6$	$0.6-0.75$	$0.75-0.9$	$0.9-1.2$	$1.2-1.6$	$1.6-2.4$				
$p_{T1}^{\gamma\gamma}$ [GeV]	$0-5$	$5-10$	$10-15$	$15-22$	$22-30$	$30-40$	$40-50$	$50-65$	$65-80$	$80-100$	$100-125$	$125-160$	$160-250$
$|\cos\theta^*|$	$0-0.0625$	$0.0625-0.125$	$0.125-0.1875$	$0.1875-0.25$	$0.25-0.3125$	$0.3125-0.375$	$0.375-0.5$	$0.5-0.625$	$0.625-1$				
$|\Delta y_{\gamma\gamma}|$	$0-0.1$	$0.1-0.2$	$0.2-0.3$	$0.3-0.4$	$0.4-0.5$	$0.5-0.65$	$0.65-0.8$	$0.8-1$	$1-1.25$	$1.25-2$			
$N_{\text{jets}}, p_T>30$ GeV	0	1	2	≥ 3									
$N_{\text{jets}}, p_T>50$ GeV	0	1	≥ 2										
p_T^{j1} [GeV]	$0-30$	$30-55$	$55-75$	$75-120$	$120-350$								
p_T^{j2} [GeV]	$0-30$	$30-70$	$70-120$										
H_T [GeV]	$0-30$	$30-70$	$70-140$	$140-200$	$200-500$								
$|y_{j1}|$	$0-0.5$	$0.5-1$	$1-1.5$	$1.5-1.9$	$1.9-2.3$	$2.3-2.5$							
$|y_{j2}|$	$0-1.2$	$1.2-2$	$2-4.4$										
m_{jj} [GeV]	$0-170$	$170-500$	$500-1500$										
$|\Delta y_{jj}|$	$0-2$	$2-4$	$4-8.8$										
$|\Delta\phi_{jj}|$	$0-\frac{\pi}{3}$	$\frac{\pi}{3}-\frac{2\pi}{3}$	$\frac{2\pi}{3}-\pi$										
$\Delta\phi_{jj}$	$-\pi--\frac{\pi}{2}$	$-\frac{\pi}{2}-0$	$0-\frac{\pi}{2}$	$\frac{\pi}{2}-\pi$									
$p_T^{\gamma\gamma jj}$ [GeV]	$0-15$	$15-200$											
$|\Delta\phi_{\gamma\gamma,jj}|$	$0-3.01$	$3.01-3.1$	$3.1-\pi$										
$\tau_{C,j1}$ [GeV]	$0-10$	$10-20$	$20-30$	$30-40$	$40-150$								
$\sum\tau_{C,j}$ [GeV]	$0-8$	$8-17$	$17-25$	$25-40$	$40-80$	$80-150$							
$p_T^{\gamma\gamma}[|\cos\theta^*|<0.5]$ [GeV]	$0-30$	$30-120$	$120-350$										
$p_T^{\gamma\gamma}[0.5\leq|\cos\theta^*|<1.0]$ [GeV]	$0-30$	$30-120$	$120-350$										
$p_T^{\gamma\gamma}[N_{\text{jets}}=0]$ [GeV]	$0-15$	$15-30$	$30-75$	$75-350$									
$p_T^{\gamma\gamma}[N_{\text{jets}}=1]$ [GeV]	$0-40$	$40-60$	$60-100$	$100-350$									
$p_T^{\gamma\gamma}[N_{\text{jets}}=2]$ [GeV]	$0-100$	$100-200$	$200-350$										
$p_T^{\gamma\gamma}[N_{\text{jets}}\geq3]$ [GeV]	$0-200$	$200-350$											

Table 26: Bin ranges for each of the studied variables.

Table 27: The effective signal mass resolutions σ_{68} (σ_{90}) in GeV defined as half the width containing 68% (90%) of the signal events for listed for each reconstructed category. Further, the numbers of background events B_{90}, measured by fits to the data, in the smallest interval expected to contain 90% of the SM signal events S_{90} are given, accompanied by the expected purities $f_{90} \equiv S_{90}/(S_{90} + B_{90})$ and expected significances $Z_{90} \equiv \sqrt{2((S_{90} + B_{90})\log(1 + S_{90}/B_{90}) - S_{90})}$.

Category	σ_{68} [GeV]	σ_{90} [GeV]	S_{90}	B_{90}	f_{90}	Z_{90}
ttH lep 0fwd	1.7	3.0	0.93	3.6	0.21	0.47
ttH lep 1fwd	1.7	3.0	0.99	1.9	0.34	0.67
ttH lep	1.6	2.9	2.1	2.7	0.44	1.16
ttH had BDT1	1.6	2.8	1.3	2.0	0.40	0.85
ttH had BDT2	1.6	2.9	1.6	3.9	0.29	0.75
ttH had BDT3	1.6	2.9	0.54	2.3	0.19	0.35
ttH had BDT4	1.6	2.9	2.2	14.0	0.14	0.58
tH had 4j1b	1.7	3.0	2.3	48	0.05	0.32
tH had 4j2b	1.7	3.1	0.56	6.8	0.08	0.21
VH dilep	1.7	3.0	0.84	1.1	0.43	0.72
VH lep High	1.5	2.8	1.4	2.4	0.37	0.82
VH lep Low	1.8	3.3	5.8	52	0.10	0.79
VH MET High	1.6	2.8	1.2	2.3	0.34	0.72
VH MET Low	1.8	3.3	0.56	3.4	0.14	0.30
jet BSM	1.4	2.6	24	280	0.08	1.41
VH had tight	1.5	2.8	11	47	0.19	1.55
VH had loose	1.7	3.1	15	220	0.06	0.98
VBF tight, high p_T^{Hjj}	1.7	2.8	18	120	0.13	1.62
VBF loose, high p_T^{Hjj}	1.8	3.1	15	250	0.06	0.93
VBF tight, low p_T^{Hjj}	1.6	2.9	12	12	0.50	3.12
VBF loose, low p_T^{Hjj}	1.8	3.3	17	110	0.14	1.62
ggH 2J BSM	1.4	2.6	6.8	26	0.21	1.29
ggH 2J High	1.6	2.9	26	280	0.08	1.53
ggH 2J Med	1.8	3.2	65	1700	0.04	1.56
ggH 2J Low	1.9	3.4	73	3100	0.02	1.30
ggH 1J BSM	1.4	2.6	2.0	7.1	0.22	0.72
ggH 1J High	1.6	2.9	28	240	0.11	1.80
ggH 1J Med	1.8	3.2	140	2900	0.05	2.61
ggH 1J Low	1.9	3.4	260	8000	0.03	2.89
ggH 0J Fwd	2.1	3.8	520	21000	0.02	3.62
ggH 0J Cen	1.6	2.7	300	5300	0.05	4.07

Table 28: Composition of the selected Higgs boson events, in terms of the different production modes, as expected for each reconstructed category. The total expected numbers of Higgs boson events are given in the column labeled N_H.

Category	N_H	Composition [%]								
		ggH	VBF	WH	ZH	ggZH	$t\bar{t}H$	$b\bar{b}H$	tHq	tHW
tH lep 0fwd	1.0	4.1	0.2	5.6	2.2	0.6	75.7	0.9	8.2	2.5
tH lep 1fwd	1.1	1.8	0.2	1.4	0.8	0.2	79.4	0.2	13.5	2.6
ttH lep	2.4	—	—	0.2	0.1	—	96.0	0.1	1.0	2.6
ttH had BDT1	1.4	1.2	0.1	0.1	0.5	0.2	95.0	0.1	0.7	2.1
ttH had BDT2	1.8	3.6	0.3	0.8	1.2	0.4	89.3	0.2	1.8	2.4
ttH had BDT3	0.6	3.5	0.5	1.0	2.0	1.1	86.1	0.5	3.1	2.2
ttH had BDT4	2.5	7.0	0.8	1.4	2.7	1.7	79.4	0.3	4.3	2.4
tH had 4j1b	2.5	35.4	4.0	4.3	5.7	2.2	36.4	2.2	8.5	1.3
tH had 4j2b	0.62	23.8	2.8	1.6	9.8	3.6	39.0	8.3	10.5	0.6
VH dilep	0.93	—	—	—	76.9	18.9	4.0	—	—	0.2
VH lep High	1.5	0.2	—	76.2	3.5	1.2	16.4	—	1.2	1.3
VH lep Low	6.4	11.4	1.1	68.0	6.8	1.3	8.5	0.9	1.6	0.4
VH MET High	1.3	1.3	0.1	22.4	48.1	18.5	8.3	—	0.6	0.7
VH MET Low	0.62	11.9	0.4	23.4	48.0	15.2	0.5	0.3	0.2	—
jet BSM	27	59.9	25.8	5.9	3.3	1.1	3.0	0.1	0.6	0.2
VH had tight	12	52.4	3.5	23.8	13.5	4.4	1.9	0.1	0.2	0.1
VH had loose	16	67.3	4.9	14.6	8.8	2.2	1.6	0.4	0.3	0.1
VBF tight, high p_T^{Hjj}	20	46.9	48.3	1.2	0.7	0.6	0.8	0.3	1.2	—
VBF loose, high p_T^{Hjj}	17	69.9	23.8	2.2	1.3	0.6	0.9	0.8	0.6	—
VBF tight, low p_T^{Hjj}	14	13.0	86.7	0.1	0.1	—	—	—	0.1	—
VBF loose, low p_T^{Hjj}	19	32.5	66.6	0.3	0.2	0.1	—	0.2	0.1	—
ggH 2J BSM	7.5	76.1	10.3	4.9	2.8	1.8	3.0	0.2	0.6	0.2
ggH 2J High	29	75.8	12.8	4.8	2.6	1.3	2.0	0.1	0.4	0.1
ggH 2J Med	72	77.6	12.2	4.4	2.6	0.6	1.5	0.7	0.4	—
ggH 2J Low	81	79.1	9.5	4.5	2.9	0.3	1.1	2.3	0.3	—
ggH 1J BSM	2.2	72.4	16.9	6.0	2.7	1.5	0.3	—	0.1	—
ggH 1J High	32	76.0	17.5	3.4	1.9	0.8	0.1	0.3	—	—
ggH 1J Med	160	83.6	11.7	2.6	1.5	0.2	—	0.4	—	—
ggH 1J Low	290	90.5	5.7	1.7	0.9	—	—	1.1	—	—
ggH 0J Fwd	580	97.0	1.2	0.5	0.4	—	—	0.9	—	—
ggH 0J Cen	330	97.3	1.1	0.4	0.3	—	—	0.9	—	—

Table 29: The used background functions are listed: Either a power law ($m_{\gamma\gamma}^{\alpha}$), exponential function of a first order polynomial ($e^{m_{\gamma\gamma}\alpha}$) or a second order polynomial ($e^{m_{\gamma\gamma}\alpha+m_{\gamma\gamma}^2\beta}$) are used to describe the non-resonant diphoton background.

Category	Background function
ttH lep 0fwd	Power law
ttH lep 1fwd	Power law
ttH lep	Power law
ttH had BDT1	Exponential of a first order polynomial
ttH had BDT2	Exponential of a first order polynomial
ttH had BDT3	Exponential of a first order polynomial
ttH had BDT4	Exponential of a first order polynomial
tH had 4j1b	Power law
tH had 4j2b	Power law
VH dilep	Power law
VH lep High	Exponential of a first order polynomial
VH lep Low	Exponential of a first order polynomial
VH MET High	Exponential of a first order polynomial
VH MET Low	Exponential of a first order polynomial
jet BSM	Exponential of a first order polynomial
VH had tight	Exponential of a first order polynomial
VH had loose	Exponential of a first order polynomial
VBF tight, high p_T^{Hjj}	Exponential of a first order polynomial
VBF loose, high p_T^{Hjj}	Exponential of a first order polynomial
VBF tight, low p_T^{Hjj}	Exponential of a first order polynomial
VBF loose, low p_T^{Hjj}	Exponential of a first order polynomial
ggH 2J BSM	Power law
ggH 2J High	Power law
ggH 2J Med	Exponential of a second order polynomial
ggH 2J Low	Exponential of a second order polynomial
ggH 1J BSM	Exponential of a first order polynomial
ggH 1J High	Power law
ggH 1J Med	Exponential of a second order polynomial
ggH 1J Low	Exponential of a second order polynomial
ggH 0J Fwd	Exponential of a second order polynomial
ggH 0J Cen	Exponential of a second order polynomial

Table 30: Observed and expected 95% CL limits for the signal strengths of the VH associated production processes. The observed asymptotic limit on μ_{VH} is compared to that obtained using an ensemble of pseudo-experiments (PEs). Separate observed limits obtained from toys are reported for μ_{ZH} and μ_{WH}. These are shown for the background-only case ($\mu_i = 0$), together with the $\pm 1\,\sigma$ and $\pm 2\,\sigma$ intervals.

Measurement	Observed	Expected Limit ($\mu = 1$)	Expected Limit ($\mu = 0$)	$+2\sigma$	$+1\sigma$	-1σ	-2σ
μ_{VH}	2.3	2.5	1.5	3.1	2.2	1.1	0.8
μ_{VH} (PE)	2.2		1.5	3.1	2.2	1.1	1.0
μ_{ZH} (PE)	2.3		3.1	6.2	4.4	2.2	1.9
μ_{WH} (PE)	4.5		2.7	4.9	3.8	1.8	1.4

Table 31: Observed and expected signal strengths for inclusive production and for various production modes. Uncertainties smaller than 0.5 (0.05) are displayed as 0 (0.0).

Production mode	Observed μ				Expected μ			
	Result	Stat	Exp	Theo	Result	Stat	Exp	Theo
Inclusive	0.99	$+0.12$ -0.12	$+0.06$ -0.05	$+0.07$ -0.05	1.00	$+0.12$ -0.12	$+0.07$ -0.06	$+0.07$ -0.05
ggH	0.81	$+0.16$ -0.16	$+0.07$ -0.06	$+0.07$ -0.05	1.00	$+0.16$ -0.17	$+0.08$ -0.06	$+0.08$ -0.06
VBF	2.0	$+0.5$ -0.5	$+0.3$ -0.2	$+0.3$ -0.2	1.0	$+0.4$ -0.4	$+0.2$ -0.1	$+0.2$ -0.1
VH	0.7	$+0.8$ -0.8	$+0.2$ -0.2	$+0.2$ -0.1	1.0	$+0.8$ -0.7	$+0.2$ -0.2	$+0.1$ -0.1
ttH + tH	0.5	$+0.6$ -0.5	$+0.1$ -0.1	$+0.1$ -0.0	1.0	$+0.7$ -0.6	$+0.1$ -0.1	$+0.2$ -0.0

F Limits on μ_{ZH} and μ_{WH} using pseudo-experiments

As discussed in Section 8.2.2, Table 30 shows the observed and expected limits for μ_{VH}, and separately for μ_{ZH} and μ_{WH}, as obtained using the asmptotic approximation and ensembles of pseudo-experiments.

G Summary of couplings results

In this Appendix the expected and observed central values and uncertainties of signal strength measurements, production mode cross section measurements, and simplified template cross section measurements from Section 8.2 and Appendix B are summarized.

G.1 Signal strengths

Table 31 summarizes the observed and expected signal strengths for inclusive production and for various production modes.

Table 32: Observed and expected cross sections times diphoton branching ratio for various production modes, in the fiducial region $|y_H| < 2.5$. Uncertainties smaller than 0.5 (0.05) are displayed as 0 (0.0).

Production mode ($|y_H| < 2.5$)	Observed $\sigma \times B(H \to \gamma\gamma)$ [fb]				Expected $\sigma \times B(H \to \gamma\gamma)$ [fb]			
	Result	Stat	Exp	Theo	Result	Stat	Exp	Theo
ggH	82	$^{+16}_{-16}$	$^{+7}_{-6}$	$^{+5}_{-4}$	102	$^{+17}_{-17}$	$^{+8}_{-6}$	$^{+5}_{-4}$
VBF	17	$^{+5}_{-4}$	$^{+2}_{-2}$	$^{+3}_{-2}$	8	$^{+3}_{-3}$	$^{+1}_{-1}$	$^{+2}_{-1}$
VH	3	$^{+4}_{-3}$	$^{+1}_{-1}$	$^{+1}_{-0}$	5	$^{+4}_{-3}$	$^{+1}_{-1}$	$^{+0}_{-0}$
$ttH + tH$	0.7	$^{+0.8}_{-0.7}$	$^{+0.2}_{-0.1}$	$^{+0.2}_{-0.0}$	1.3	$^{+0.9}_{-0.8}$	$^{+0.2}_{-0.1}$	$^{+0.3}_{-0.1}$

Table 33: Observed and expected simplified template cross sections times diphoton branching ratio, in the fiducial region $|y_H| < 2.5$.

Simplified fiducial region ($|y_H| < 2.5$)	Observed $\sigma \times B(H \to \gamma\gamma)$ [fb]			Expected $\sigma \times B(H \to \gamma\gamma)$ [fb]		
	Result	Stat	Syst	Result	Stat	Syst
ggH, 0 jet	37	$^{+14}_{-14}$	$^{+6}_{-5}$	63	$^{+15}_{-15}$	$^{+8}_{-6}$
ggH, 1 jet, $p_T^H < 60$ GeV	13	$^{+12}_{-12}$	$^{+5}_{-4}$	15	$^{+12}_{-12}$	$^{+6}_{-4}$
ggH, 1 jet, $60 \le p_T^H < 120$ GeV	5	$^{+6}_{-6}$	$^{+2}_{-1}$	10	$^{+6}_{-6}$	$^{+2}_{-1}$
ggH, 1 jet, $120 \le p_T^H < 200$ GeV	2.8	$^{+1.6}_{-1.5}$	$^{+0.7}_{-0.5}$	1.7	$^{+1.6}_{-1.6}$	$^{+0.5}_{-0.4}$
ggH, ≥ 2 jet	20	$^{+8}_{-8}$	$^{+4}_{-3}$	11	$^{+8}_{-8}$	$^{+3}_{-2}$
$qq \to Hqq$, $p_T^j < 200$ GeV	15	$^{+5}_{-5}$	$^{+3}_{-2}$	10	$^{+5}_{-5}$	$^{+2}_{-1}$
$ggH + qq \to Hqq$, BSM $-$ like	2.0	$^{+1.3}_{-1.3}$	$^{+0.6}_{-0.6}$	1.8	$^{+1.3}_{-1.3}$	$^{+0.5}_{-0.5}$
VH, leptonic	0.7	$^{+1.4}_{-1.2}$	$^{+0.4}_{-0.3}$	1.4	$^{+1.3}_{-1.2}$	$^{+0.3}_{-0.3}$
$ttH + tH$	0.7	$^{+0.8}_{-0.7}$	$^{+0.2}_{-0.1}$	1.3	$^{+0.9}_{-0.8}$	$^{+0.3}_{-0.1}$

G.2 Production mode cross sections

Table 32 summarizes the observed and expected cross sections times diphoton branching ratio for various production modes, in the fiducial region $|y_H| < 2.5$.

G.3 Simplified template cross sections

Table 33 summarizes the observed and expected simplified template cross sections times diphoton branching ratio, in the fiducial region $|y_H| < 2.5$.

Table 34: Observed and expected simplified template cross sections times diphoton branching ratio, in the fiducial region $|y_H| < 2.5$.

Simplified fiducial region ($|y_H| < 2.5$)	Observed $\sigma \times B(H \to \gamma\gamma)$ [fb]			Expected $\sigma \times B(H \to \gamma\gamma)$ [fb]		
	Result	Stat	Syst	Result	Stat	Syst
ggH, 0 jet	38	$+14$ -14	$+6$ -5	63	$+15$ -15	$+8$ -6
ggH, 1 jet, $p_T^H < 60$ GeV	23	$+13$ -13	$+5$ -4	15	$+12$ -13	$+6$ -4
ggH, 1 jet, $60 \leq p_T^H < 120$ GeV	11	$+7$ -7	$+3$ -2	10	$+8$ -8	$+2$ -2
ggH, 1 jet, $120 \leq p_T^H < 200$ GeV	4.0	$+1.8$ -1.8	$+0.9$ -0.6	1.7	$+1.9$ -1.8	$+0.6$ -0.4
ggH, 1 jet, $p_T^H \geq 200$ GeV	2.6	$+1.3$ -1.1	$+0.8$ -0.5	0.4	$+1.1$ -0.9	$+0.5$ -0.4
ggH, ≥ 2 jet, $p_T^H < 60$ GeV	0	$+8$ -8	$+3$ -2	3	$+8$ -8	$+4$ -2
ggH, ≥ 2 jet, $60 \leq p_T^H < 120$ GeV	12	$+7$ -7	$+3$ -2	4	$+7$ -7	$+2$ -1
ggH, ≥ 2 jet, $120 \leq p_T^H < 200$ GeV	7.9	$+3.3$ -3.3	$+1.1$ -0.9	2.3	$+3.4$ -3.3	$+0.8$ -0.7
ggH, ≥ 2 jet, $p_T^H \geq 200$ GeV	2.6	$+1.5$ -1.4	$+0.6$ -0.5	1.0	$+1.4$ -1.3	$+0.5$ -0.4
ggH, VBF $-$ like	6.2	$+4.1$ -4.1	$+1.2$ -1.2	1.5	$+3.9$ -3.8	$+1.4$ -1.0
$qq \to Hqq$, VBF $-$ like	3.8	$+2.2$ -2.0	$+1.2$ -1.2	2.7	$+2.0$ -1.8	$+0.8$ -0.5
$qq \to Hqq$, VH + Rest	-19	$+21$ -20	$+6$ -7	8	$+22$ -21	$+6$ -5
$qq \to Hqq$, $p_T^j > 200$ GeV	-3.2	$+1.7$ -1.7	$+0.7$ -0.9	0.5	$+1.7$ -1.7	$+0.6$ -0.6
VH leptonic	0.7	$+1.4$ -1.2	$+0.4$ -0.3	1.4	$+1.3$ -1.2	$+0.3$ -0.3
$ttH + tH$	0.7	$+0.8$ -0.7	$+0.2$ -0.1	1.3	$+0.9$ -0.8	$+0.3$ -0.1

G.4 Minimally merged simplified template cross sections

Table 34 summarizes the observed and expected minimally merged simplified template cross sections times diphoton branching ratio, in the fiducial region $|y_H| < 2.5$.

H Observed and expected correlation maps

This appendix summaries the observed and expected correlations between the parameters of interest of each of the measurements presented in Section 8.2 are given. The observed and expected correlations for the production-mode cross sections and production mode cross-section ratios are shown in Figures 40 and 41. The observed and expected correlations for the simplified template cross sections and minimally merged simplified template cross sections are shown in Figures 42 and 43.

Figure 40: Observed (left) and expected (right) correlations between the measured simplified template cross sections, including both the statistical and systematic uncertainties. The color indicates the size of the correlation.
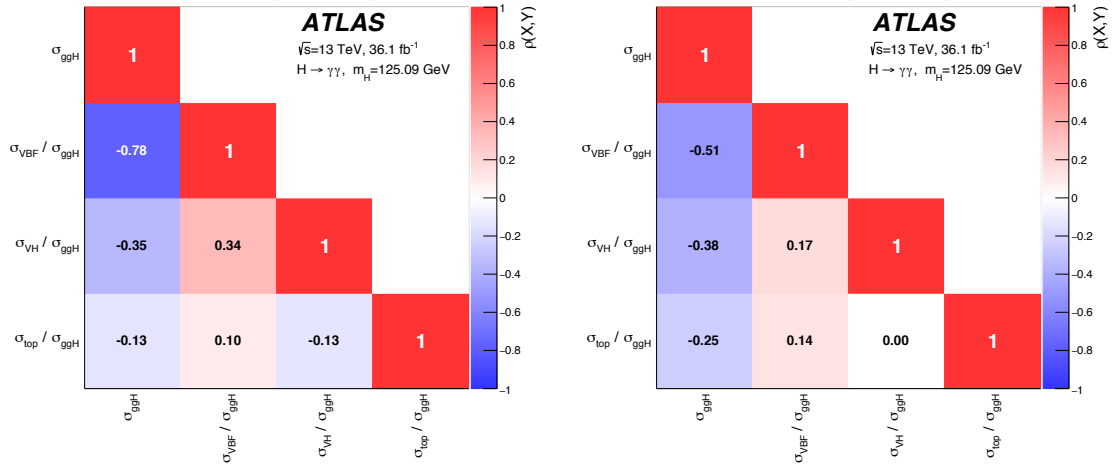
Figure 41: Observed (left) and expected (right) correlations between the measured simplified template cross section ratios, including both the statistical and systematic uncertainties. The color indicates the size of the correlation.

Figure 42: Observed (top) and expected (bottom) correlations between the measured simplified template cross sections, including both the statistical and systematic uncertainties. The color indicates the size of the correlation.
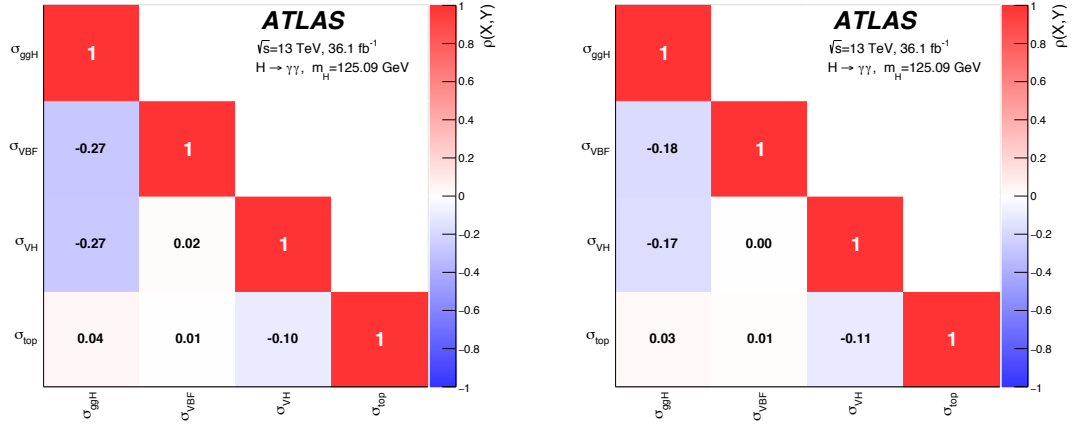
106

Figure 43: Observed (top) and expected (bottom) correlations between the measured simplified template cross sections, including both the statistical and systematic uncertainties. The color indicates the size of the correlation.
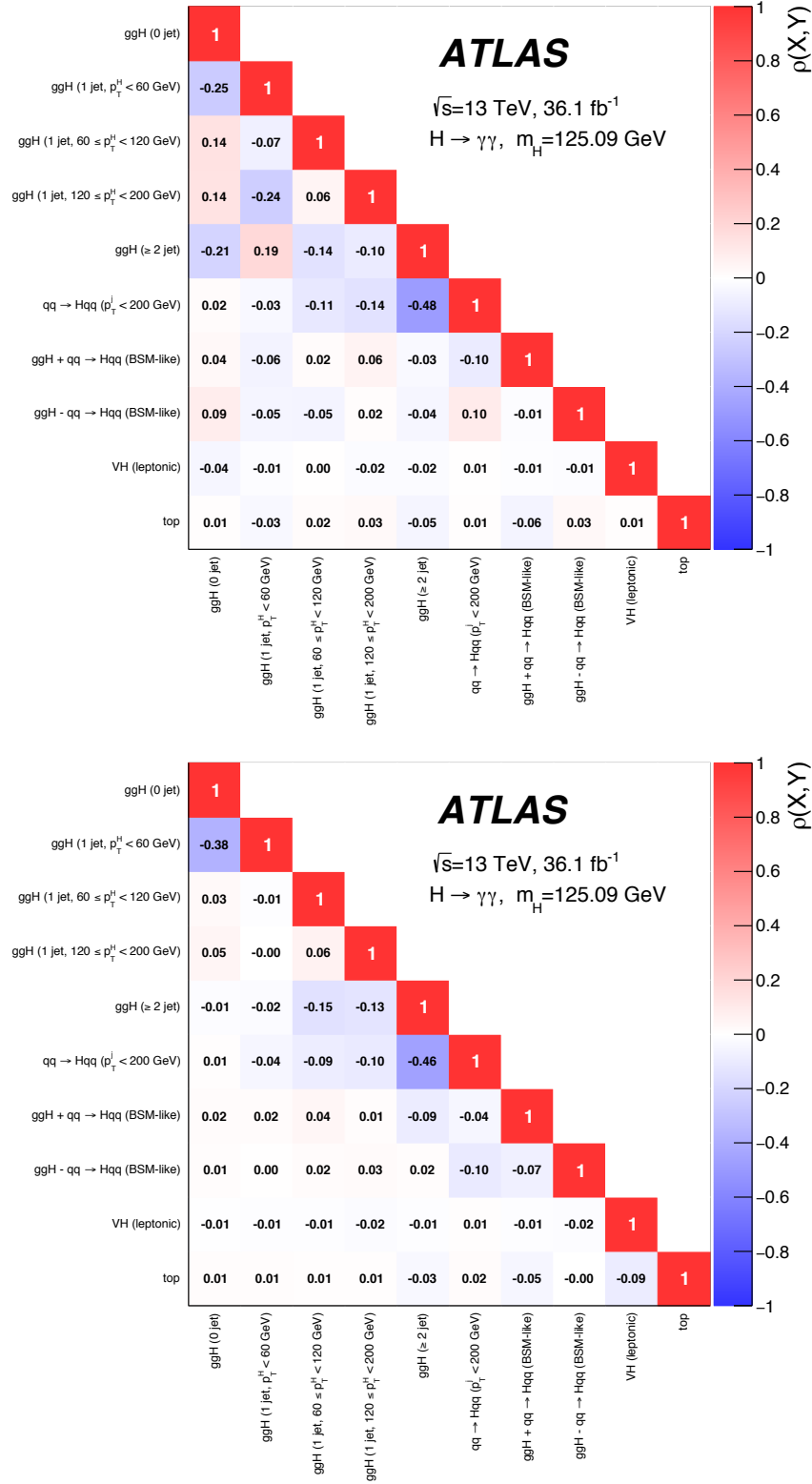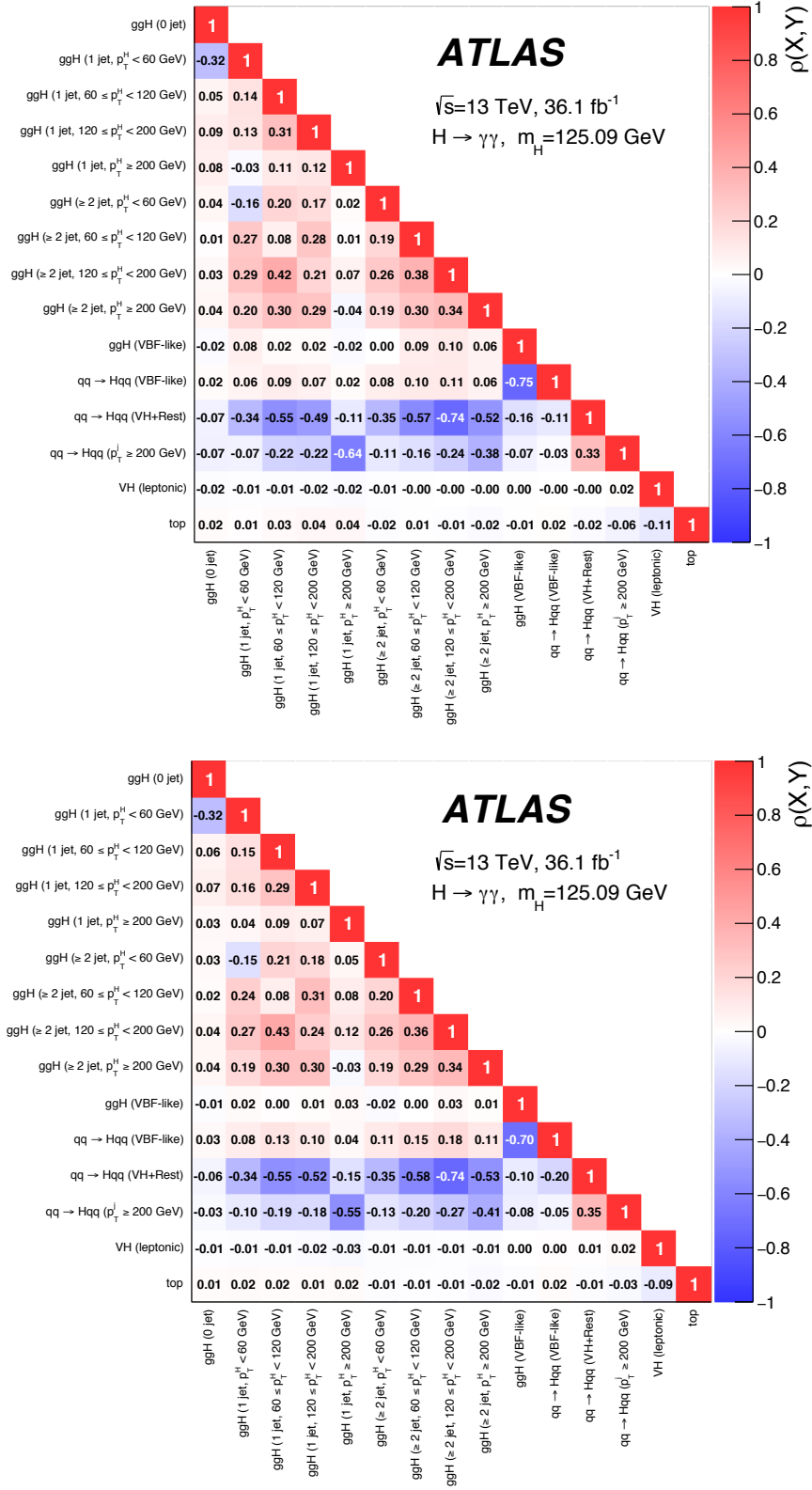
References

[1] ATLAS Collaboration, *The ATLAS Experiment at the CERN Large Hadron Collider*,
JINST **3** (2008) S08003.

[2] CMS Collaboration, *The CMS experiment at the CERN LHC*, JINST **3** (2008) S08004.

[3] ATLAS Collaboration, *Observation of a new particle in the search for the Standard Model
Higgs boson with the ATLAS detector at the LHC*, Phys. Lett. B **716** (2012) 1,
arXiv: `1207.7214 [hep-ex]`.

[4] CMS Collaboration,
Observation of a new boson at a mass of 125 GeV with the CMS experiment at the LHC,
Phys. Lett. B **716** (2012) 30, arXiv: `1207.7235 [hep-ex]`.

[5] ATLAS and CMS Collaborations, *Measurements of the Higgs boson production and decay
rates and constraints on its couplings from a combined ATLAS and CMS analysis of the LHC
pp collision data at $\sqrt{s}$ = 7 and 8 TeV*, JHEP **08** (2016) 045, arXiv: `1606.02266 [hep-ex]`.

[6] ATLAS and CMS Collaborations, *Combined Measurement of the Higgs Boson Mass in pp
Collisions at $\sqrt{s}$ = 7 and 8 TeV with the ATLAS and CMS Experiments*,
Phys. Rev. Lett. **114** (2015) 191803, arXiv: `1503.07589 [hep-ex]`.

[7] LHC Higgs Cross Section Working Group (D. de Florian et al.),
Handbook of LHC Higgs Cross Sections: 4. Deciphering the Nature of the Higgs Sector,
2016, arXiv: `1610.07922 [hep-ph]`.

[8] J. R. Andersen et al.,
Les Houches 2015: Physics at TeV Colliders Standard Model Working Group Report, 2016,
arXiv: `1605.04692 [hep-ph]`.

[9] ATLAS Collaboration, *Measurements of fiducial and differential cross sections for Higgs
boson production in the diphoton decay channel at $\sqrt{s}$ = 8 TeV with ATLAS*,
JHEP **09** (2014) 112, arXiv: `1407.4222 [hep-ex]`.

[10] CMS Collaboration, *Measurement of differential cross sections for Higgs boson production
in the diphoton decay channel in pp collisions at $\sqrt{s}$ = 8 TeV*, Eur. Phys. J. C **76** (2016) 13,
arXiv: `1508.07819 [hep-ex]`.

[11] J. C. Collins, D. E. Soper and G. F. Sterman,
Transverse Momentum Distribution in Drell-Yan Pair and W and Z Boson Production,
Nucl. Phys. B **250** (1985) 199.

[12] F. Bishara, U. Haisch, P. F. Monni and E. Re,
Constraining Light-Quark Yukawa Couplings from Higgs Distributions,
Phys. Rev. Lett. **118** (2017) 121801, arXiv: `1606.09253 [hep-ph]`.

[13] G. F. Giudice, C. Grojean, A. Pomarol and R. Rattazzi, *The strongly-interacting light Higgs*,
JHEP **06** (2007) 045, arXiv: `hep-ph/0703164`.

[14] ATLAS Collaboration, *Constraints on non-Standard Model Higgs boson interactions in an
effective Lagrangian using differential cross sections measured in the H → γγ decay channel
at $\sqrt{s}$ = 8 TeV with the ATLAS detector*, Phys. Lett. B **753** (2016) 69,
arXiv: `1508.02507 [hep-ex]`.

[15] ATLAS Collaboration, *ATLAS Insertable B-Layer Technical Design Report*,
ATLAS-TDR-19, 2010, URL: https://cds.cern.ch/record/1291633,
ATLAS Insertable B-Layer Technical Design Report Addendum, ATLAS-TDR-19-ADD-1,
2012, URL: https://cds.cern.ch/record/1451888.

[16] ATLAS Collaboration, *Performance of the ATLAS Trigger System in 2015*,
Eur. Phys. J. C **77** (2017) 317, arXiv: 1611.09661 [hep-ex].

[17] LHC Higgs Cross Section Working Group (S. Heinemeyer et al.),
Handbook of LHC Higgs Cross Sections: 3. Higgs Properties, 2013,
arXiv: 1307.1347 [hep-ph].

[18] A. Djouadi, J. Kalinowski and M. Spira, *HDECAY: a program for Higgs boson decays in the
Standard Model and its supersymmetric extension*, Comput. Phys. Commun. **108** (1998) 56,
arXiv: hep-ph/9704448.

[19] A. Djouadi, M. M. Mühlleitner and M. Spira, *Decays of supersymmetric particles: The
Program SUSY-HIT (SUspect-SdecaY-Hdecay-InTerface)*, Acta Phys. Polon. **B38** (2007) 635,
arXiv: hep-ph/0609292.

[20] A. Bredenstein, A. Denner, S. Dittmaier and M. M. Weber, *Radiative corrections to the
semileptonic and hadronic Higgs-boson decays $H \rightarrow WW/ZZ \rightarrow 4$ fermions*,
JHEP **02** (2007) 080, arXiv: hep-ph/0611234.

[21] A. Bredenstein, A. Denner, S. Dittmaier and M. M. Weber,
Precise predictions for the Higgs-boson decay $H \rightarrow WW/ZZ \rightarrow 4$ leptons,
Phys. Rev. D **74** (2006) 013004, arXiv: hep-ph/0604011.

[22] A. Bredenstein, A. Denner, S. Dittmaier and M. M. Weber,
Precision calculations for the Higgs decays $H \rightarrow ZZ/WW \rightarrow 4$ leptons,
Nucl. Phys. Proc. Suppl. **160** (2006) 131, arXiv: hep-ph/0607060.

[23] K. Hamilton, P. Nason, E. Re and G. Zanderighi,
NNLOPS simulation of Higgs boson production, JHEP **10** (2013) 222,
arXiv: 1309.0017 [hep-ph].

[24] J. Butterworth et al., *PDF4LHC recommendations for LHC Run II*,
J. Phys. G **43** (2016) 023001, arXiv: 1510.03865 [hep-ph].

[25] K. Hamilton, P. Nason, C. Oleari and G. Zanderighi, *Merging $H/W/Z + 0$ and 1 jet at NLO
with no merging scale: a path to parton shower + NNLO matching*, JHEP **05** (2013) 082,
arXiv: 1212.4504 [hep-ph].

[26] S. Catani and M. Grazzini, *An NNLO subtraction formalism in hadron collisions and its
application to Higgs boson production at the LHC*, Phys. Rev. Lett. **98** (2007) 222002,
arXiv: hep-ph/0703012.

[27] G. Bozzi, S. Catani, D. de Florian and M. Grazzini,
Transverse-momentum resummation and the spectrum of the Higgs boson at the LHC,
Nucl. Phys. B **737** (2006) 73, arXiv: hep-ph/0508068.

[28] D. de Florian, G. Ferrera, M. Grazzini and D. Tommasini,
Transverse-momentum resummation: Higgs boson production at the Tevatron and the LHC,
JHEP **11** (2011) 064, arXiv: 1109.2109 [hep-ph].

[29] T. Sjöstrand, S. Mrenna and P. Z. Skands, *A brief introduction to PYTHIA 8.1*,
Comput. Phys. Commun. **178** (2008) 852, arXiv: 0710.3820 [hep-ph].

[30] ATLAS Collaboration, *Measurement of the Z/γ^* boson transverse momentum distribution in pp collisions at $\sqrt{s}$ = 7 TeV with the ATLAS detector*, JHEP **09** (2014) 145, arXiv: `1406.3660 [hep-ex]`.

[31] C. Anastasiou, C. Duhr, F. Dulat, F. Herzog and B. Mistlberger, *Higgs Boson Gluon-Fusion Production in QCD at Three Loops*, Phys. Rev. Lett. **114** (2015) 212001, arXiv: `1503.06056 [hep-ph]`.

[32] C. Anastasiou et al., *High precision determination of the gluon fusion Higgs boson cross-section at the LHC*, JHEP **05** (2016) 058, arXiv: `1602.00695 [hep-ph]`.

[33] S. Actis, G. Passarino, C. Sturm and S. Uccirati, *NLO electroweak corrections to Higgs boson production at hadron colliders*, Phys. Lett. B **670** (2008) 12, arXiv: `0809.1301 [hep-ph]`.

[34] C. Anastasiou, R. Boughezal and F. Petriello, *Mixed QCD-electroweak corrections to Higgs boson production in gluon fusion*, JHEP **04** (2009) 003, arXiv: `0811.3458 [hep-ph]`.

[35] P. Nason, *A New method for combining NLO QCD with shower Monte Carlo algorithms*, JHEP **11** (2004) 040, arXiv: `hep-ph/0409146`.

[36] S. Frixione, P. Nason and C. Oleari, *Matching NLO QCD computations with parton shower simulations: the POWHEG method*, JHEP **11** (2007) 070, arXiv: `0709.2092 [hep-ph]`.

[37] S. Alioli, P. Nason, C. Oleari and E. Re, *A general framework for implementing NLO calculations in shower Monte Carlo programs: the POWHEG BOX*, JHEP **06** (2010) 043, arXiv: `1002.2581 [hep-ph]`.

[38] P. Nason and C. Oleari, *NLO Higgs boson production via vector-boson fusion matched with shower in POWHEG*, JHEP **02** (2010) 037, arXiv: `0911.5299 [hep-ph]`.

[39] M. Ciccolini, A. Denner and S. Dittmaier, *Strong and electroweak corrections to the production of Higgs + 2 jets via weak interactions at the LHC*, Phys. Rev. Lett. **99** (2007) 161803, arXiv: `0707.0381 [hep-ph]`.

[40] M. Ciccolini, A. Denner and S. Dittmaier, *Electroweak and QCD corrections to Higgs production via vector-boson fusion at the LHC*, Phys. Rev. D **77** (2008) 013002, arXiv: `0710.4749 [hep-ph]`.

[41] P. Bolzoni, F. Maltoni, S.-O. Moch and M. Zaro, *Higgs production via vector-boson fusion at NNLO in QCD*, Phys. Rev. Lett. **105** (2010) 011801, arXiv: `1003.4451 [hep-ph]`.

[42] K. Mimasu, V. Sanz and C. Williams, *Higher order QCD predictions for associated Higgs production with anomalous couplings to gauge bosons*, JHEP **08** (2016) 039, arXiv: `1512.02572 [hep-ph]`.

[43] O. Brein, A. Djouadi and R. Harlander, *NNLO QCD corrections to the Higgs-strahlung processes at hadron colliders*, Phys. Lett. B **579** (2004) 149, arXiv: `hep-ph/0307206`.

[44] L. Altenkamp, S. Dittmaier, R. V. Harlander, H. Rzehak and T. J. E. Zirke, *Gluon-induced Higgs-strahlung at next-to-leading order QCD*, JHEP **02** (2013) 078, arXiv: 1211.5015 [hep-ph].

[45] A. Denner, S. Dittmaier, S. Kallweit and A. Mück, *Electroweak corrections to Higgs-strahlung off W/Z bosons at the Tevatron and the LHC with HAWK*, JHEP **03** (2012) 075, arXiv: 1112.5142 [hep-ph].

[46] J. Alwall et al., *The automated computation of tree-level and next-to-leading order differential cross sections, and their matching to parton shower simulations*, JHEP **07** (2014) 079, arXiv: 1405.0301 [hep-ph].

[47] NNPDF Collaboration, *Parton distributions for the LHC Run II*, JHEP **04** (2015) 040, arXiv: 1410.8849 [hep-ph].

[48] ATLAS Collaboration, *ATLAS Run 1 Pythia8 tunes*, ATL-PHYS-PUB-2014-021 (2014), URL: https://cds.cern.ch/record/1966419.

[49] W. Beenakker et al., *NLO QCD corrections to $t\bar{t}H$ production in hadron collisions*, Nucl. Phys. B **653** (2003) 151, arXiv: hep-ph/0211352.

[50] S. Dawson, C. Jackson, L. Orr, L. Reina and D. Wackeroth, *Associated Higgs production with top quarks at the large hadron collider: NLO QCD corrections*, Phys. Rev. D **68** (2003) 034022, arXiv: hep-ph/0305087.

[51] Y. Zhang, W.-G. Ma, R.-Y. Zhang, C. Chen and L. Guo, *QCD NLO and EW NLO corrections to $t\bar{t}H$ production with top quark decays at hadron collider*, Phys. Lett. B **738** (2014) 1, arXiv: 1407.1110 [hep-ph].

[52] S. Frixione, V. Hirschi, D. Pagani, H.-S. Shao and M. Zaro, *Electroweak and QCD corrections to top-pair hadroproduction in association with heavy bosons*, JHEP **06** (2015) 184, arXiv: 1504.03446 [hep-ph].

[53] M. Wiesemann et al., *Higgs production in association with bottom quarks*, JHEP **02** (2015) 132, arXiv: 1409.5301 [hep-ph].

[54] H.-L. Lai et al., *New parton distributions for collider physics*, Phys. Rev. D **82** (2010) 074024, arXiv: 1007.2241 [hep-ph].

[55] S. Dawson, C. Jackson, L. Reina and D. Wackeroth, *Exclusive Higgs boson production with bottom quarks at hadron colliders*, Phys. Rev. D **69** (2004) 074027, arXiv: hep-ph/0311067.

[56] S. Dittmaier, M. Krämer and M. Spira, *Higgs radiation off bottom quarks at the Tevatron and the CERN LHC*, Phys. Rev. D **70** (2004) 074010, arXiv: hep-ph/0309204.

[57] R. Harlander, M. Kramer and M. Schumacher, *Bottom-quark associated Higgs-boson production: reconciling the four- and five-flavour scheme approach*, 2011, arXiv: 1112.3478 [hep-ph].

[58] S. Gieseke, A. Ribon, M. H. Seymour, P. Stephens and B. Webber, *Herwig++ 1.0: an event generator for $e^+ e^-$ annihilation*, JHEP **02** (2004) 005, arXiv: hep-ph/0311208.

[59] J. Bellm et al., *Herwig++ 2.7 release note*, 2013, arXiv: 1310.6877 [hep-ph].

[60] M. Bahr et al., *Herwig++ physics and manual*, 2008 639, arXiv: 0803.0883 [hep-ph].

[61] F. Demartin, F. Maltoni, K. Mawatari and M. Zaro,
Higgs production in association with a single top quark at the LHC,
Eur. Phys. J. C **75** (2015) 267, arXiv: 1504.00611 [hep-ph].

[62] GEANT4 Collaboration, *GEANT4: a simulation toolkit*,
Nucl. Instrum. Meth. A **506** (2003) 250.

[63] ATLAS Collaboration, *The ATLAS Simulation Infrastructure*, Eur. Phys. J. C **70** (2010) 823,
arXiv: 1005.4568 [hep-ex].

[64] T. Gleisberg et al., *Event generation with SHERPA 1.1*, JHEP **02** (2009) 007,
arXiv: 0811.4622 [hep-ph].

[65] S. Schumann and F. Krauss,
A Parton shower algorithm based on Catani-Seymour dipole factorisation,
JHEP **03** (2008) 038, arXiv: 0709.1027 [hep-ph].

[66] S. Höche, F. Krauss, S. Schumann and F. Siegert,
QCD matrix elements and truncated showers, JHEP **05** (2009) 053,
arXiv: 0903.1219 [hep-ph].

[67] ATLAS Collaboration, *The ATLAS Simulation Infrastructure*, Eur. Phys. J. C **70** (2010) 823,
arXiv: 1005.4568 [physics.ins-det].

[68] ATLAS Collaboration, *Summary of ATLAS Pythia 8 tunes*,
ATL-PHYS-PUB-2012-003 (2012), URL: https://cds.cern.ch/record/1474107.

[69] A. D. Martin, W. J. Stirling, R. S. Thorne and G. Watt, *Parton distributions for the LHC*,
Eur. Phys. J. C **63** (2009) 189, arXiv: 0901.0002 [hep-ph].

[70] ATLAS Collaboration, *Measurement of the photon identification efficiencies with the ATLAS
detector using LHC Run-1 data*, Eur. Phys. J. C **76** (2016) 666,
arXiv: 1606.01813 [hep-ex].

[71] ATLAS Collaboration,
Electron and photon energy calibration with the ATLAS detector using LHC Run 1 data,
Eur. Phys. J. C **74** (2014) 3071, arXiv: 1407.5063 [hep-ex].

[72] ATLAS Collaboration, *Electron and photon energy calibration with the ATLAS detector
using data collected in 2015 at $\sqrt{s}$ = 13 TeV*, ATL-PHYS-PUB-2016-015 (2016),
URL: https://cds.cern.ch/record/2203514.

[73] ATLAS Collaboration, *Photon identification in 2015 ATLAS data*,
ATL-PHYS-PUB-2016-014 (2016), URL: https://cds.cern.ch/record/2203125.

[74] ATLAS Collaboration,
Topological cell clustering in the ATLAS calorimeters and its performance in LHC Run 1,
Eur. Phys. J. C **77** (2017) 490, arXiv: 1603.02934 [hep-ex].

[75] M. Cacciari, G. P. Salam and S. Sapeta, *On the characterisation of the underlying event*,
JHEP **04** (2010) 065, arXiv: 0912.4926 [hep-ph].

[76] ATLAS Collaboration, *Measurement of Higgs boson production in the diphoton decay
channel in pp collisions at center-of-mass energies of 7 and 8 TeV with the ATLAS detector*,
Phys. Rev. D **90** (2014) 112015, arXiv: 1408.7084 [hep-ex].

[77] M. Cacciari, G. P. Salam and G. Soyez, *The anti-k_t jet clustering algorithm*,
JHEP **04** (2008) 063, arXiv: 0802.1189 [hep-ph].

[78] M. Cacciari and G. P. Salam, *Dispelling the N^3 myth for the k_t jet-finder*,
Phys. Lett. B **641** (2006) 57, arXiv: hep-ph/0512210.

[79] M. Cacciari, G. P. Salam and G. Soyez, *FastJet user manual*, Eur. Phys. J. C **72** (2012) 1896,
arXiv: 1111.6097 [hep-ph].

[80] ATLAS Collaboration, *Performance of pile-up mitigation techniques for jets in pp collisions at $\sqrt{s}$ = 8 TeV using the ATLAS detector*, Eur. Phys. J. **C76** (2016) 581,
arXiv: 1510.03823 [hep-ex].

[81] ATLAS Collaboration, *Jet Calibration and Systematic Uncertainties for Jets Reconstructed in the ATLAS Detector at $\sqrt{s}$ = 13 TeV*, ATLAS-PHYS-PUB-2015-015 (2015),
URL: https://cds.cern.ch/record/2037613.

[82] ATLAS Collaboration, *Jet energy measurement and its systematic uncertainty in proton-proton collisions at $\sqrt{s}$ = 7 TeV with the ATLAS detector*, Eur. Phys. J. C **75** (2015) 17,
arXiv: 1406.0076 [hep-ex].

[83] ATLAS Collaboration, *Tagging and suppression of pileup jets with the ATLAS detector*,
ATLAS-CONF-2014-018 (2014), URL: https://cds.cern.ch/record/1700870.

[84] ATLAS Collaboration, *Expected performance of the ATLAS b-tagging algorithms in Run-2*,
ATL-PHYS-PUB-2015-022 (2015), URL: https://cds.cern.ch/record/2037697.

[85] ATLAS Collaboration,
Optimisation of the ATLAS b-tagging performance for the 2016 LHC Run,
ATL-PHYS-PUB-2016-012 (2016), URL: https://cds.cern.ch/record/2160731.

[86] ATLAS Collaboration, *Electron efficiency measurements with the ATLAS detector using the 2015 LHC proton-proton collision data*, ATLAS-CONF-2016-024 (2016),
URL: https://cds.cern.ch/record/2157687.

[87] ATLAS Collaboration, *Muon reconstruction performance of the ATLAS detector in proton-proton collision data at $\sqrt{s}$ =13 TeV*, Eur. Phys. J. C **76** (2016) 292,
arXiv: 1603.05598 [hep-ex].

[88] ATLAS Collaboration, *Expected performance of missing transverse momentum reconstruction for the ATLAS detector at $\sqrt{s}$ = 13 TeV*,
ATLAS-PHYS-PUB-2015-023 (2015), URL: https://cds.cern.ch/record/2037700.

[89] ATLAS Collaboration, *Performance of missing transverse momentum reconstruction for the ATLAS detector in the first proton-proton collisions at $\sqrt{s}$ = 13 TeV*,
ATLAS-PHYS-PUB-2015-027 (2015), URL: https://cds.cern.ch/record/2037904.

[90] ATLAS Collaboration, *Measurement of the isolated di-photon cross-section in pp collisions at $\sqrt{s}$ = 7 TeV with the ATLAS detector*, Phys. Rev. D **85** (2012) 012003,
arXiv: 1107.0581 [hep-ex].

[91] ATLAS Collaboration, *Measurement of the inclusive isolated prompt photon cross section in pp collisions at $\sqrt{s}$ = 7 TeV with the ATLAS detector*, Phys. Rev. D **83** (2011) 052005,
arXiv: 1012.4389 [hep-ex].

[92] G. Cowan, K. Cranmer, E. Gross and O. Vitells,
Asymptotic formulae for likelihood-based tests of new physics,
Eur. Phys. J. C **71** (2011) 1554, arXiv: 1007.1727 [physics.data-an],
Erratum: Eur. Phys. J. C **73** (2013) 2501.

[93] ATLAS Collaboration, *Combined search for the Standard Model Higgs boson in pp collisions at $\sqrt{s}$ = 7 TeV with the ATLAS detector*, Phys. Rev. D **86** (2012) 032003, arXiv: 1207.0319 [hep-ex].

[94] A. L. Read, *Presentation of search results: The CL$_S$ technique*, J. Phys. G **28** (2002) 2693.

[95] ATLAS Collaboration, *Luminosity determination in pp collisions at $\sqrt{s}$ = 8 TeV using the ATLAS detector at the LHC*, Eur. Phys. J. C **76** (2016) 653, arXiv: 1608.03953 [hep-ex].

[96] ATLAS Collaboration, *Jet energy scale measurements and their systematic uncertainties in proton-proton collisions at $\sqrt{s}$ = 13 TeV with the ATLAS detector*, Phys. Rev. D **96** (2017) 072002, arXiv: 1703.09665 [hep-ex].

[97] ATLAS Collaboration, *Performance of b-jet identification in the ATLAS experiment*, JINST **11** (2016) P04008, arXiv: 1512.01094 [hep-ex].

[98] *Electron and photon energy calibration with the ATLAS detector using data collected in 2015 at $\sqrt{s}$ = 13 TeV*, (2016), URL: https://cds.cern.ch/record/2203514.

[99] I. W. Stewart, F. J. Tackmann, J. R. Walsh and S. Zuberi, *Jet p_T Resummation in Higgs Production at $NNLL' + NNLO$*, Phys. Rev. D **89** (2014) 054001, arXiv: 1307.1808 [hep-ph].

[100] X. Liu and F. Petriello, *Reducing theoretical uncertainties for exclusive Higgs-boson plus one-jet production at the LHC*, Phys. Rev. D **87** (2013) 094027, arXiv: 1303.4405 [hep-ph].

[101] R. Boughezal, X. Liu, F. Petriello, F. J. Tackmann and J. R. Walsh, *Combining resummed Higgs predictions across jet bins*, Phys. Rev. D **89** (2014) 074044, arXiv: 1312.4535 [hep-ph].

[102] J. M. Campbell and R. K. Ellis, *MCFM for the Tevatron and the LHC*, Nucl. Phys. Proc. Suppl. **205-206** (2010) 10, arXiv: 1007.3492 [hep-ph].

[103] I. W. Stewart and F. J. Tackmann, *Theory uncertainties for Higgs and other searches using jet bins*, Phys. Rev. D **85** (2012) 034011, arXiv: 1107.2117 [hep-ph].

[104] S. Gangal and F. J. Tackmann, *Next-to-leading-order uncertainties in Higgs+2 jets from gluon fusion*, Phys. Rev. D **87** (2013) 093008, arXiv: 1302.5437 [hep-ph].

[105] R. Frederix, S. Frixione, E. Vryonidou and M. Wiesemann, *Heavy-quark mass effects in Higgs plus jets production*, JHEP **08** (2016) 006, arXiv: 1604.03017 [hep-ph].

[106] R. Frederix and S. Frixione, *Merging meets matching in MC@NLO*, JHEP **12** (2012) 061, arXiv: 1209.6215 [hep-ph].

[107] ATLAS Collaboration, *Measurement of the cross-section for electroweak production of dijets in association with a Z boson in pp collisions at $\sqrt{s}$ = 13 TeV with the ATLAS detector*, Phys. Lett. B **775** (2017) 206, arXiv: 1709.10264 [hep-ex].

[108] ATLAS Collaboration, *Measurements of fiducial cross-sections for $t\bar{t}$ production with one or two additional b-jets in pp collisions at $\sqrt{s}$ =8 TeV using the ATLAS detector*, Eur. Phys. J. C **76** (2016) 11, arXiv: 1508.06868 [hep-ex].

114

[109] ATLAS Collaboration, *Measurement of differential production cross-sections for a Z boson in association with b-jets in 7 TeV proton-proton collisions with the ATLAS detector*, JHEP **10** (2014) 141, arXiv: 1407.3643 [hep-ex].

[110] ATLAS Collaboration, *Measurement of the cross-section for W boson production in association with b-jets in pp collisions at $\sqrt{s}$ = 7 TeV with the ATLAS detector*, JHEP **06** (2013) 084, arXiv: 1302.2929 [hep-ex].

[111] D. de Florian and M. Grazzini, *Higgs production at the LHC: updated cross sections at $\sqrt{s}$ = 8 TeV*, Phys. Lett. B **718** (2012) 117, arXiv: 1206.4133 [hep-ph].

[112] G. D'Agostini, *A Multidimensional unfolding method based on Bayes' theorem*, Nucl. Instrum. Meth. A **362** (1995) 487.

[113] A. Hoecker and V. Kartvelishvili, *SVD approach to data unfolding*, Nucl. Instrum. Meth. A **372** (1996) 469, arXiv: hep-ph/9509307.

[114] B. Malaescu, *An Iterative, dynamically stabilized method of data unfolding*, 2009, arXiv: 0907.3791 [physics.data-an].

[115] K. G. Hayes, M. L. Perl and B. Efron, *Application of the bootstrap statistical method to the tau-decay-mode problem*, Phys. Rev. D **39** (1989) 274.

[116] A. Banfi et al., *Jet-vetoed Higgs cross section in gluon fusion at N^3LO+NNLL with small-R resummation*, JHEP **04** (2016) 049, arXiv: 1511.02886 [hep-ph].

[117] X. Chen, T. Gehrmann, E. W. N. Glover and M. Jaquier, *Precise QCD predictions for the production of Higgs + jet final states*, Phys. Lett. B **740** (2015) 147, arXiv: 1408.5325 [hep-ph].

[118] X. Chen, J. Cruz-Martinez, T. Gehrmann, E. W. N. Glover and M. Jaquier, *NNLO QCD corrections to Higgs boson production at large transverse momentum*, JHEP **10** (2016) 066, arXiv: 1607.08817 [hep-ph].

[119] G. Cullen et al., *Automated one-loop calculations with GoSam*, Eur. Phys. J. C **72** (2012) 1889, arXiv: 1111.2034 [hep-ph].

[120] G. Cullen et al., *GOSAM-2.0: a tool for automated one-loop calculations within the Standard Model and beyond*, Eur. Phys. J. C **74** (2014) 3001, arXiv: 1404.7096 [hep-ph].

[121] N. Greiner et al., *Phenomenological analysis of Higgs boson production through gluon fusion in association with jets*, JHEP **01** (2016) 169, arXiv: 1506.01016 [hep-ph].

[122] S. Höche, F. Krauss, M. Schonherr and F. Siegert, *A critical appraisal of NLO+PS matching methods*, JHEP **09** (2012) 049, arXiv: 1111.1220 [hep-ph].

[123] S. Höche, F. Krauss, M. Schonherr and F. Siegert, *QCD matrix elements + parton showers: The NLO case*, JHEP **04** (2013) 027, arXiv: 1207.5030 [hep-ph].

[124] M. Buschmann et al., *Mass effects in the Higgs-gluon coupling: boosted vs off-shell production*, JHEP **02** (2015) 038, arXiv: 1410.5806 [hep-ph].

[125] E. Bothmann, M. Schonherr and S. Schumann,
Reweighting QCD matrix-element and parton-shower calculations,
Eur. Phys. J. C **76** (2016) 590, arXiv: 1606.08753 [hep-ph].

[126] T. Gleisberg and S. Höche, *Comix, a new matrix element generator*, JHEP **12** (2008) 039,
arXiv: 0808.3674 [hep-ph].

[127] F. Krauss, R. Kuhn and G. Soff, *AMEGIC++ 1.0: A matrix element generator in C++*,
JHEP **02** (2002) 044, arXiv: hep-ph/0109036.

[128] S. Höche and M. Schonherr, *Uncertainties in next-to-leading order plus parton shower
matched simulations of inclusive jet and dijet production*, Phys. Rev. D **86** (2012) 094042,
arXiv: 1208.2815 [hep-ph].

[129] S. Höche, F. Krauss and M. Schonherr, *Uncertainties in MEPS@NLO calculations of h+jets*,
Phys. Rev. D **90** (2014) 014012, arXiv: 1401.7971 [hep-ph].

[130] S. Dulat et al.,
New parton distribution functions from a global analysis of quantum chromodynamics,
Phys. Rev. D **93** (2016) 033006, arXiv: 1506.07443 [hep-ph].

[131] D. de Florian, G. Ferrera, M. Grazzini and D. Tommasini,
*Higgs boson production at the LHC: transverse momentum resummation effects in the
$H \to \gamma\gamma$, $H \to WW \to \ell\nu\ell\nu$ and $H \to ZZ \to 4\ell$ decay modes*, JHEP **06** (2012) 132,
arXiv: 1203.6321 [hep-ph].

[132] M. Grazzini and H. Sargsyan,
Heavy-quark mass effects in Higgs boson production at the LHC, JHEP **09** (2013) 129,
arXiv: 1306.4581 [hep-ph].

[133] P. F. Monni, E. Re and P. Torrielli,
Higgs Transverse-Momentum Resummation in Direct Space,
Phys. Rev. Lett. **116** (2016) 242001, arXiv: 1604.02191 [hep-ph].

[134] M. A. Ebert, J. K. L. Michel and F. J. Tackmann,
Resummation improved rapidity spectrum for gluon fusion Higgs production,
JHEP **05** (2017) 088, arXiv: 1702.00794 [hep-ph].

[135] M. A. Ebert et al., *SCETlib: A C++ Package for Numerical Calculations in QCD and
Soft-Collinear Effective Theory*, DESY-17-099, URL: http://scetlib.desy.de.

[136] R. Boughezal et al., *Color singlet production at NNLO in MCFM*,
Eur. Phys. J. C **77** (2017) 7, arXiv: 1605.08011 [hep-ph].

[137] J. Gaunt, M. Stahlhofen, F. J. Tackmann and J. R. Walsh,
N-jettiness Subtractions for NNLO QCD calculations, JHEP **09** (2015) 058,
arXiv: 1505.04794 [hep-ph].

[138] ATLAS Collaboration,
*Fiducial and differential cross sections of Higgs boson production measured in the
four-lepton decay channel in pp collisions at $\sqrt{s}$=8 TeV with the ATLAS detector*,
Phys. Lett. B **738** (2014) 234, arXiv: 1408.3226 [hep-ex].

[139] G. Klamke and D. Zeppenfeld,
Higgs plus two jet production via gluon fusion as a signal at the CERN LHC,
JHEP **04** (2007) 052, arXiv: hep-ph/0703202.

[140] T. Plehn, D. L. Rainwater and D. Zeppenfeld,
       Determining the structure of Higgs couplings at the LHC, Phys. Rev. Lett. **88** (2002) 051801,
       arXiv: `hep-ph/0105325`.

[141] J. R. Andersen, K. Arnold and D. Zeppenfeld,
       Azimuthal angle correlations for Higgs boson plus multi-jet events, JHEP **06** (2010) 091,
       arXiv: `1001.3822 [hep-ph]`.

[142] M. J. Dolan, P. Harris, M. Jankowiak and M. Spannowsky,
       Constraining CP-violating Higgs Sectors at the LHC using gluon fusion,
       Phys. Rev. D **90** (2014) 073008, arXiv: `1406.3322 [hep-ph]`.

[143] R. Contino, M. Ghezzi, C. Grojean, M. Muhlleitner and M. Spira,
       Effective Lagrangian for a light Higgs-like scalar, JHEP **07** (2013) 035,
       arXiv: `1303.3876 [hep-ph]`.

[144] A. Alloul, B. Fuks and V. Sanz,
       Phenomenology of the Higgs Effective Lagrangian via FEYNRULES, JHEP **04** (2014) 110,
       arXiv: `1310.5150 [hep-ph]`.

[145] A. Pomarol and F. Riva, *Towards the ultimate SM fit to close in on Higgs physics*,
       JHEP **01** (2014) 151, arXiv: `1308.2803 [hep-ph]`.

[146] J. Ellis, V. Sanz and T. You, *The effective Standard Model after LHC Run I*,
       JHEP **03** (2015) 157, arXiv: `1410.7703 [hep-ph]`.

[147] P. Artoisenet et al., *A framework for Higgs characterisation*, JHEP **11** (2013) 043,
       arXiv: `1306.6464 [hep-ph]`.

[148] M. L. Mangano, M. Moretti, F. Piccinini and M. Treccani, *Matching matrix elements and
       shower evolution for top-quark production in hadronic collisions*, JHEP **01** (2007) 013,
       arXiv: `hep-ph/0611129`.

[149] A. Buckley et al., *Rivet user manual*, Comput. Phys. Commun. **184** (2013) 2803,
       arXiv: `1003.0694 [hep-ph]`.

[150] A. Buckley, H. Hoeth, H. Lacker, H. Schulz and J. E. von Seggern,
       Systematic event generator tuning for the LHC, Eur. Phys. J. C **65** (2010) 331,
       arXiv: `0907.2973 [hep-ph]`.

[151] K. Arnold et al.,
       VBFNLO: A Parton level Monte Carlo for processes with electroweak bosons,
       Comput. Phys. Commun. **180** (2009) 1661, arXiv: `0811.4559 [hep-ph]`.

[152] ATLAS Collaboration, *Search for Higgs boson decays to a photon and a Z boson in pp
       collisions at $\sqrt{s} = 7$ and 8 TeV with the ATLAS detector*, Phys. Lett. B **732** (2014) 8,
       arXiv: `1402.3051 [hep-ex]`.

[153] ATLAS Collaboration, *Searches for the $Z\gamma$ decay mode of the Higgs boson and for new
       high-mass resonances in pp collisions at $\sqrt{s} = 13$ TeV with the ATLAS detector*,
       JHEP **10** (2017) 112, arXiv: `1708.00212 [hep-ex]`.

[154] ATLAS Collaboration, *Measurement of Higgs boson production in the diphoton decay
       channel in pp collisions at center-of-mass energies of 7 and 8 TeV with the ATLAS detector*,
       Phys. Rev. D **90** (2014) 112015, arXiv: `1408.7084 [hep-ex]`.

[155] ATLAS Collaboration, *ATLAS Computing Acknowledgements*, ATL-GEN-PUB-2016-002,
URL: https://cds.cern.ch/record/2202407.

[156] I. W. Stewart, F. J. Tackmann and W. J. Waalewijn,
Factorization at the LHC: from PDFs to initial state jets, Phys. Rev. D **81** (2010) 094035,
arXiv: 0910.0467 [hep-ph].

The ATLAS Collaboration

M. Aaboud[137d], G. Aad[88], B. Abbott[115], O. Abdinov[12,*], B. Abeloos[119], S.H. Abidi[161],
O.S. AbouZeid[139], N.L. Abraham[151], H. Abramowicz[155], H. Abreu[154], Y. Abulaiti[148a,148b],
B.S. Acharya[167a,167b,a], S. Adachi[157], L. Adamczyk[41a], J. Adelman[110], M. Adersberger[102],
T. Adye[133], A.A. Affolder[139], Y. Afik[154], C. Agheorghiesei[28c], J.A. Aguilar-Saavedra[128a,128f],
S.P. Ahlen[24], F. Ahmadov[68,b], G. Aielli[135a,135b], S. Akatsuka[71], H. Akerstedt[148a,148b],
T.P.A. Åkesson[84], E. Akilli[52], A.V. Akimov[98], G.L. Alberghi[22a,22b], J. Albert[172], P. Albicocco[50],
M.J. Alconada Verzini[74], S.C. Alderweireldt[108], M. Aleksa[32], I.N. Aleksandrov[68], C. Alexa[28b],
G. Alexander[155], T. Alexopoulos[10], M. Alhroob[115], B. Ali[130], M. Aliev[76a,76b], G. Alimonti[94a],
J. Alison[33], S.P. Alkire[38], B.M.M. Allbrooke[151], B.W. Allen[118], P.P. Allport[19], A. Aloisio[106a,106b],
A. Alonso[39], F. Alonso[74], C. Alpigiani[140], A.A. Alshehri[56], M.I. Alstaty[88], B. Alvarez Gonzalez[32],
D. Álvarez Piqueras[170], M.G. Alviggi[106a,106b], B.T. Amadio[16], Y. Amaral Coutinho[26a],
C. Amelung[25], D. Amidei[92], S.P. Amor Dos Santos[128a,128c], S. Amoroso[32], C. Anastopoulos[141],
L.S. Ancu[52], N. Andari[19], T. Andeen[11], C.F. Anders[60b], J.K. Anders[18], K.J. Anderson[33],
A. Andreazza[94a,94b], V. Andrei[60a], S. Angelidakis[37], I. Angelozzi[109], A. Angerami[38],
A.V. Anisenkov[111,c], N. Anjos[13], A. Annovi[126a], C. Antel[60a], M. Antonelli[50], A. Antonov[100,*],
D.J. Antrim[166], F. Anulli[134a], M. Aoki[69], L. Aperio Bella[32], G. Arabidze[93], Y. Arai[69],
J.P. Araque[128a], V. Araujo Ferraz[26a], A.T.H. Arce[48], R.E. Ardell[80], F.A. Arduh[74], J-F. Arguin[97],
S. Argyropoulos[66], M. Arik[20a], A.J. Armbruster[32], L.J. Armitage[79], O. Arnaez[161], H. Arnold[51],
M. Arratia[30], O. Arslan[23], A. Artamonov[99,*], G. Artoni[122], S. Artz[86], S. Asai[157], N. Asbah[45],
A. Ashkenazi[155], L. Asquith[151], K. Assamagan[27], R. Astalos[146a], M. Atkinson[169], N.B. Atlay[143],
K. Augsten[130], G. Avolio[32], B. Axen[16], M.K. Ayoub[35a], G. Azuelos[97,d], A.E. Baas[60a], M.J. Baca[19],
H. Bachacou[138], K. Bachas[76a,76b], M. Backes[122], P. Bagnaia[134a,134b], M. Bahmani[42],
H. Bahrasemani[144], J.T. Baines[133], M. Bajic[39], O.K. Baker[179], P.J. Bakker[109], D. Bakshi Gupta[82],
E.M. Baldin[111,c], P. Balek[175], F. Balli[138], W.K. Balunas[124], E. Banas[42], A. Bandyopadhyay[23],
Sw. Banerjee[176,e], A.A.E. Bannoura[178], L. Barak[155], E.L. Barberio[91], D. Barberis[53a,53b],
M. Barbero[88], T. Barillari[103], M-S Barisits[65], J.T. Barkeloo[118], T. Barklow[145], N. Barlow[30],
S.L. Barnes[36b], B.M. Barnett[133], R.M. Barnett[16], Z. Barnovska-Blenessy[36c], A. Baroncelli[136a],
G. Barone[25], A.J. Barr[122], L. Barranco Navarro[170], F. Barreiro[85], J. Barreiro Guimarães da Costa[35a],
R. Bartoldus[145], A.E. Barton[75], P. Bartos[146a], A. Basalaev[125], A. Bassalat[119,f], R.L. Bates[56],
S.J. Batista[161], J.R. Batley[30], M. Battaglia[139], M. Bauce[134a,134b], F. Bauer[138], K.T. Bauer[166],
H.S. Bawa[145,g], J.B. Beacham[113], M.D. Beattie[75], T. Beau[83], P.H. Beauchemin[165], P. Bechtle[23],
H.P. Beck[18,h], H.C. Beck[57], K. Becker[122], M. Becker[86], C. Becot[112], A.J. Beddall[20e], A. Beddall[20b],
V.A. Bednyakov[68], M. Bedognetti[109], C.P. Bee[150], T.A. Beermann[32], M. Begalli[26a], M. Begel[27],
J.K. Behr[45], A.S. Bell[81], G. Bella[155], L. Bellagamba[22a], A. Bellerive[31], M. Bellomo[154],
K. Belotskiy[100], O. Beltramello[32], N.L. Belyaev[100], O. Benary[155,*], D. Benchekroun[137a],
M. Bender[102], N. Benekos[10], Y. Benhammou[155], E. Benhar Noccioli[179], J. Benitez[66],
D.P. Benjamin[48], M. Benoit[52], J.R. Bensinger[25], S. Bentvelsen[109], L. Beresford[122], M. Beretta[50],
D. Berge[109], E. Bergeaas Kuutmann[168], N. Berger[5], L.J. Bergsten[25], J. Beringer[16], S. Berlendis[58],
N.R. Bernard[89], G. Bernardi[83], C. Bernius[145], F.U. Bernlochner[23], T. Berry[80], P. Berta[86],
C. Bertella[35a], G. Bertoli[148a,148b], I.A. Bertram[75], C. Bertsche[45], G.J. Besjes[39],
O. Bessidskaia Bylund[148a,148b], M. Bessner[45], N. Besson[138], A. Bethani[87], S. Bethke[103], A. Betti[23],
A.J. Bevan[79], J. Beyer[103], R.M. Bianchi[127], O. Biebel[102], D. Biedermann[17], R. Bielski[87],
K. Bierwagen[86], N.V. Biesuz[126a,126b], M. Biglietti[136a], T.R.V. Billoud[97], H. Bilokon[50], M. Bindi[57],
A. Bingul[20b], C. Bini[134a,134b], S. Biondi[22a,22b], T. Bisanz[57], C. Bittrich[47], D.M. Bjergaard[48],

J.E. Black[145], K.M. Black[24], R.E. Blair[6], T. Blazek[146a], I. Bloch[45], C. Blocker[25], A. Blue[56],
U. Blumenschein[79], Dr. Blunier[34a], G.J. Bobbink[109], V.S. Bobrovnikov[111,c], S.S. Bocchetta[84],
A. Bocci[48], C. Bock[102], M. Boehler[51], D. Boerner[178], D. Bogavac[102], A.G. Bogdanchikov[111],
C. Bohm[148a], V. Boisvert[80], P. Bokan[168,i], T. Bold[41a], A.S. Boldyrev[101], A.E. Bolz[60b], M. Bomben[83],
M. Bona[79], J.S. Bonilla[118], M. Boonekamp[138], A. Borisov[132], G. Borissov[75], J. Bortfeldt[32],
D. Bortoletto[122], V. Bortolotto[62a], D. Boscherini[22a], M. Bosman[13], J.D. Bossio Sola[29],
J. Boudreau[127], E.V. Bouhova-Thacker[75], D. Boumediene[37], C. Bourdarios[119], S.K. Boutle[56],
A. Boveia[113], J. Boyd[32], I.R. Boyko[68], A.J. Bozson[80], J. Bracinik[19], A. Brandt[8], G. Brandt[178],
O. Brandt[60a], F. Braren[45], U. Bratzler[158], B. Brau[89], J.E. Brau[118], W.D. Breaden Madden[56],
K. Brendlinger[45], A.J. Brennan[91], L. Brenner[109], R. Brenner[168], S. Bressler[175], D.L. Briglin[19],
T.M. Bristow[49], D. Britton[56], D. Britzger[60b], F.M. Brochu[30], I. Brock[23], R. Brock[93],
G. Brooijmans[38], T. Brooks[80], W.K. Brooks[34b], E. Brost[110], J.H Broughton[19],
P.A. Bruckman de Renstrom[42], D. Bruncko[146b], A. Bruni[22a], G. Bruni[22a], L.S. Bruni[109],
S. Bruno[135a,135b], BH Brunt[30], M. Bruschi[22a], N. Bruscino[127], P. Bryant[33], L. Bryngemark[45],
T. Buanes[15], Q. Buat[144], P. Buchholz[143], A.G. Buckley[56], I.A. Budagov[68], F. Buehrer[51],
M.K. Bugge[121], O. Bulekov[100], D. Bullock[8], T.J. Burch[110], S. Burdin[77], C.D. Burgard[109],
A.M. Burger[5], B. Burghgrave[110], K. Burka[42], S. Burke[133], I. Burmeister[46], J.T.P. Burr[122],
D. Büscher[51], V. Büscher[86], E. Buschmann[57], P. Bussey[56], J.M. Butler[24], C.M. Buttar[56],
J.M. Butterworth[81], P. Butti[32], W. Buttinger[27], A. Buzatu[153], A.R. Buzykaev[111,c],
Changqiao C.-Q.[36c], S. Cabrera Urbán[170], D. Caforio[130], H. Cai[169], V.M.M. Cairo[2], O. Cakir[4a],
N. Calace[52], P. Calafiura[16], A. Calandri[88], G. Calderini[83], P. Calfayan[64], G. Callea[40a,40b],
L.P. Caloba[26a], S. Calvente Lopez[85], D. Calvet[37], S. Calvet[37], T.P. Calvet[88], R. Camacho Toro[33],
S. Camarda[32], P. Camarri[135a,135b], D. Cameron[121], R. Caminal Armadans[169], C. Camincher[58],
S. Campana[32], M. Campanelli[81], A. Camplani[94a,94b], A. Campoverde[143], V. Canale[106a,106b],
M. Cano Bret[36b], J. Cantero[116], T. Cao[155], M.D.M. Capeans Garrido[32], I. Caprini[28b], M. Caprini[28b],
M. Capua[40a,40b], R.M. Carbone[38], R. Cardarelli[135a], F. Cardillo[51], I. Carli[131], T. Carli[32],
G. Carlino[106a], B.T. Carlson[127], L. Carminati[94a,94b], R.M.D. Carney[148a,148b], S. Caron[108],
E. Carquin[34b], S. Carrá[94a,94b], G.D. Carrillo-Montoya[32], D. Casadei[19], M.P. Casado[13,j],
A.F. Casha[161], M. Casolino[13], D.W. Casper[166], R. Castelijn[109], V. Castillo Gimenez[170],
N.F. Castro[128a,k], A. Catinaccio[32], J.R. Catmore[121], A. Cattai[32], J. Caudron[23], V. Cavaliere[169],
E. Cavallaro[13], D. Cavalli[94a], M. Cavalli-Sforza[13], V. Cavasinni[126a,126b], E. Celebi[20d],
F. Ceradini[136a,136b], L. Cerda Alberich[170], A.S. Cerqueira[26b], A. Cerri[151], L. Cerrito[135a,135b],
F. Cerutti[16], A. Cervelli[22a,22b], S.A. Cetin[20d], A. Chafaq[137a], D. Chakraborty[110], S.K. Chan[59],
W.S. Chan[109], Y.L. Chan[62a], P. Chang[169], J.D. Chapman[30], D.G. Charlton[19], C.C. Chau[31],
C.A. Chavez Barajas[151], S. Che[113], S. Cheatham[167a,167c], A. Chegwidden[93], S. Chekanov[6],
S.V. Chekulaev[163a], G.A. Chelkov[68,l], M.A. Chelstowska[32], C. Chen[36c], C. Chen[67], H. Chen[27],
J. Chen[36c], J. Chen[38], S. Chen[35b], S. Chen[157], X. Chen[35c,m], Y. Chen[70], H.C. Cheng[92],
H.J. Cheng[35a,35d], A. Cheplakov[68], E. Cheremushkina[132], R. Cherkaoui El Moursli[137e], E. Cheu[7],
K. Cheung[63], L. Chevalier[138], V. Chiarella[50], G. Chiarelli[126a], G. Chiodini[76a], A.S. Chisholm[32],
A. Chitan[28b], Y.H. Chiu[172], M.V. Chizhov[68], K. Choi[64], A.R. Chomont[37], S. Chouridou[156],
Y.S. Chow[62a], V. Christodoulou[81], M.C. Chu[62a], J. Chudoba[129], A.J. Chuinard[90], J.J. Chwastowski[42],
L. Chytka[117], A.K. Ciftci[4a], D. Cinca[46], V. Cindro[78], I.A. Cioară[23], A. Ciocio[16], F. Cirotto[106a,106b],
Z.H. Citron[175], M. Citterio[94a], M. Ciubancan[28b], A. Clark[52], M.R. Clark[38], P.J. Clark[49],
R.N. Clarke[16], C. Clement[148a,148b], Y. Coadou[88], M. Cobal[167a,167c], A. Coccaro[52], J. Cochran[67],
L. Colasurdo[108], B. Cole[38], A.P. Colijn[109], J. Collot[58], T. Colombo[166], P. Conde Muiño[128a,128b],
E. Coniavitis[51], S.H. Connell[147b], I.A. Connelly[87], S. Constantinescu[28b], G. Conti[32],
F. Conventi[106a,n], A.M. Cooper-Sarkar[122], F. Cormier[171], K.J.R. Cormier[161], M. Corradi[134a,134b],

E.E. Corrigan[84], F. Corriveau[90,o], A. Cortes-Gonzalez[32], M.J. Costa[170], D. Costanzo[141], G. Cottin[30],
G. Cowan[80], B.E. Cox[87], K. Cranmer[112], S.J. Crawley[56], R.A. Creager[124], G. Cree[31],
S. Crépé-Renaudin[58], F. Crescioli[83], W.A. Cribbs[148a,148b], M. Cristinziani[23], V. Croft[112],
G. Crosetti[40a,40b], A. Cueto[85], T. Cuhadar Donszelmann[141], A.R. Cukierman[145], J. Cummings[179],
M. Curatolo[50], J. Cúth[86], S. Czekierda[42], P. Czodrowski[32], G. D'amen[22a,22b], S. D'Auria[56],
L. D'eramo[83], M. D'Onofrio[77], M.J. Da Cunha Sargedas De Sousa[128a,128b], C. Da Via[87],
W. Dabrowski[41a], T. Dado[146a], S. Dahbi[137e], T. Dai[92], O. Dale[15], F. Dallaire[97], C. Dallapiccola[89],
M. Dam[39], J.R. Dandoy[124], M.F. Daneri[29], N.P. Dang[176,e], N.S. Dann[87], M. Danninger[171],
M. Dano Hoffmann[138], V. Dao[150], G. Darbo[53a], S. Darmora[8], J. Dassoulas[3], A. Dattagupta[118],
T. Daubney[45], W. Davey[23], C. David[45], T. Davidek[131], D.R. Davis[48], P. Davison[81], E. Dawe[91],
I. Dawson[141], K. De[8], R. de Asmundis[106a], A. De Benedetti[115], S. De Castro[22a,22b], S. De Cecco[83],
N. De Groot[108], P. de Jong[109], H. De la Torre[93], F. De Lorenzi[67], A. De Maria[57], D. De Pedis[134a],
A. De Salvo[134a], U. De Sanctis[135a,135b], A. De Santo[151], K. De Vasconcelos Corga[88],
J.B. De Vivie De Regie[119], R. Debbe[27], C. Debenedetti[139], D.V. Dedovich[68], N. Dehghanian[3],
I. Deigaard[109], M. Del Gaudio[40a,40b], J. Del Peso[85], D. Delgove[119], F. Deliot[138], C.M. Delitzsch[7],
A. Dell'Acqua[32], L. Dell'Asta[24], M. Della Pietra[106a,106b], D. della Volpe[52], M. Delmastro[5],
C. Delporte[119], P.A. Delsart[58], D.A. DeMarco[161], S. Demers[179], M. Demichev[68], A. Demilly[83],
S.P. Denisov[132], D. Denysiuk[138], D. Derendarz[42], J.E. Derkaoui[137d], F. Derue[83], P. Dervan[77],
K. Desch[23], C. Deterre[45], K. Dette[161], M.R. Devesa[29], P.O. Deviveiros[32], A. Dewhurst[133],
S. Dhaliwal[25], F.A. Di Bello[52], A. Di Ciaccio[135a,135b], L. Di Ciaccio[5], W.K. Di Clemente[124],
C. Di Donato[106a,106b], A. Di Girolamo[32], B. Di Girolamo[32], B. Di Micco[136a,136b], R. Di Nardo[32],
K.F. Di Petrillo[59], A. Di Simone[51], R. Di Sipio[161], D. Di Valentino[31], C. Diaconu[88], M. Diamond[161],
F.A. Dias[39], M.A. Diaz[34a], J. Dickinson[16], E.B. Diehl[92], J. Dietrich[17], S. Díez Cornell[45],
A. Dimitrievska[16], J. Dingfelder[23], P. Dita[28b], S. Dita[28b], F. Dittus[32], F. Djama[88], T. Djobava[54b],
J.I. Djuvsland[60a], M.A.B. do Vale[26c], M. Dobre[28b], D. Dodsworth[25], C. Doglioni[84], J. Dolejsi[131],
Z. Dolezal[131], M. Donadelli[26d], S. Donati[126a,126b], J. Donini[37], J. Dopke[133], A. Doria[106a],
M.T. Dova[74], A.T. Doyle[56], E. Drechsler[57], M. Dris[10], Y. Du[36a], J. Duarte-Campderros[155],
F. Dubinin[98], A. Dubreuil[52], E. Duchovni[175], G. Duckeck[102], A. Ducourthial[83], O.A. Ducu[97,p],
D. Duda[109], A. Dudarev[32], A.Chr. Dudder[86], E.M. Duffield[16], L. Duflot[119], M. Dührssen[32],
C. Dulsen[178], M. Dumancic[175], A.E. Dumitriu[28b], A.K. Duncan[56], M. Dunford[60a], A. Duperrin[88],
H. Duran Yildiz[4a], M. Düren[55], A. Durglishvili[54b], D. Duschinger[47], B. Dutta[45], D. Duvnjak[1],
M. Dyndal[45], B.S. Dziedzic[42], C. Eckardt[45], K.M. Ecker[103], R.C. Edgar[92], T. Eifert[32], G. Eigen[15],
K. Einsweiler[16], T. Ekelof[168], M. El Kacimi[137c], R. El Kosseifi[88], V. Ellajosyula[88], M. Ellert[168],
S. Elles[5], F. Ellinghaus[178], A.A. Elliot[172], N. Ellis[32], J. Elmsheuser[27], M. Elsing[32],
D. Emeliyanov[133], Y. Enari[157], J.S. Ennis[173], M.B. Epland[48], J. Erdmann[46], A. Ereditato[18],
M. Ernst[27], S. Errede[169], M. Escalier[119], C. Escobar[170], B. Esposito[50], O. Estrada Pastor[170],
A.I. Etienvre[138], E. Etzion[155], H. Evans[64], A. Ezhilov[125], M. Ezzi[137e], F. Fabbri[22a,22b],
L. Fabbri[22a,22b], V. Fabiani[108], G. Facini[81], R.M. Fakhrutdinov[132], S. Falciano[134a], R.J. Falla[81],
J. Faltova[32], Y. Fang[35a], M. Fanti[94a,94b], A. Farbin[8], A. Farilla[136a], E.M. Farina[123a,123b],
T. Farooque[93], S. Farrell[16], S.M. Farrington[173], P. Farthouat[32], F. Fassi[137e], P. Fassnacht[32],
D. Fassouliotis[9], M. Faucci Giannelli[49], A. Favareto[53a,53b], W.J. Fawcett[122], L. Fayard[119],
O.L. Fedin[125,q], W. Fedorko[171], S. Feigl[121], L. Feligioni[88], C. Feng[36a], E.J. Feng[32], M. Feng[48],
M.J. Fenton[56], A.B. Fenyuk[132], L. Feremenga[8], P. Fernandez Martinez[170], J. Ferrando[45],
A. Ferrari[168], P. Ferrari[109], R. Ferrari[123a], D.E. Ferreira de Lima[60b], A. Ferrer[170], D. Ferrere[52],
C. Ferretti[92], F. Fiedler[86], A. Filipčič[78], M. Filipuzzi[45], F. Filthaut[108], M. Fincke-Keeler[172],
K.D. Finelli[24], M.C.N. Fiolhais[128a,128c,r], L. Fiorini[170], C. Fischer[13], J. Fischer[178], W.C. Fisher[93],
N. Flaschel[45], I. Fleck[143], P. Fleischmann[92], R.R.M. Fletcher[124], T. Flick[178], B.M. Flierl[102],

L.R. Flores Castillo[62a], N. Fomin[15], G.T. Forcolin[87], A. Formica[138], F.A. Förster[13], A. Forti[87],
A.G. Foster[19], D. Fournier[119], H. Fox[75], S. Fracchia[141], P. Francavilla[126a,126b], M. Franchini[22a,22b],
S. Franchino[60a], D. Francis[32], L. Franconi[121], M. Franklin[59], M. Frate[166], M. Fraternali[123a,123b],
D. Freeborn[81], S.M. Fressard-Batraneanu[32], B. Freund[97], W.S. Freund[26a], D. Froidevaux[32],
J.A. Frost[122], C. Fukunaga[158], T. Fusayasu[104], J. Fuster[170], O. Gabizon[154], A. Gabrielli[22a,22b],
A. Gabrielli[16], G.P. Gach[41a], S. Gadatsch[32], S. Gadomski[80], G. Gagliardi[53a,53b], L.G. Gagnon[97],
C. Galea[108], B. Galhardo[128a,128c], E.J. Gallas[122], B.J. Gallop[133], P. Gallus[130], G. Galster[39],
K.K. Gan[113], S. Ganguly[175], Y. Gao[77], Y.S. Gao[145,g], F.M. Garay Walls[34a], C. García[170],
J.E. García Navarro[170], J.A. García Pascual[35a], M. Garcia-Sciveres[16], R.W. Gardner[33], N. Garelli[145],
V. Garonne[121], A. Gascon Bravo[45], K. Gasnikova[45], C. Gatti[50], A. Gaudiello[53a,53b], G. Gaudio[123a],
I.L. Gavrilenko[98], C. Gay[171], G. Gaycken[23], E.N. Gazis[10], C.N.P. Gee[133], J. Geisen[57], M. Geisen[86],
M.P. Geisler[60a], K. Gellerstedt[148a,148b], C. Gemme[53a], M.H. Genest[58], C. Geng[92], S. Gentile[134a,134b],
C. Gentsos[156], S. George[80], D. Gerbaudo[13], G. Geßner[46], S. Ghasemi[143], M. Ghneimat[23],
B. Giacobbe[22a], S. Giagu[134a,134b], N. Giangiacomi[22a,22b], P. Giannetti[126a], S.M. Gibson[80],
M. Gignac[171], M. Gilchriese[16], D. Gillberg[31], G. Gilles[178], D.M. Gingrich[3,d], M.P. Giordani[167a,167c],
F.M. Giorgi[22a], P.F. Giraud[138], P. Giromini[59], G. Giugliarelli[167a,167c], D. Giugni[94a], F. Giuli[122],
M. Giulini[60b], B.K. Gjelsten[121], S. Gkaitatzis[156], I. Gkialas[9,s], E.L. Gkougkousis[13],
P. Gkountoumis[10], L.K. Gladilin[101], C. Glasman[85], J. Glatzer[13], P.C.F. Glaysher[45], A. Glazov[45],
M. Goblirsch-Kolb[25], J. Godlewski[42], S. Goldfarb[91], T. Golling[52], D. Golubkov[132],
A. Gomes[128a,128b,128d], R. GonCcalo[128a], R. Goncalves Gama[26a],
J. Goncalves Pinto Firmino Da Costa[138], G. Gonella[51], L. Gonella[19], A. Gongadze[68], F. Gonnella[19],
J.L. Gonski[59], S. González de la Hoz[170], S. Gonzalez-Sevilla[52], L. Goossens[32], P.A. Gorbounov[99],
H.A. Gordon[27], B. Gorini[32], E. Gorini[76a,76b], A. Gorišek[78], A.T. Goshaw[48], C. Gössling[46],
M.I. Gostkin[68], C.A. Gottardo[23], C.R. Goudet[119], D. Goujdami[137c], A.G. Goussiou[140],
N. Govender[147b,t], C. Goy[5], E. Gozani[154], I. Grabowska-Bold[41a], P.O.J. Gradin[168], E.C. Graham[77],
J. Gramling[166], E. Gramstad[121], S. Grancagnolo[17], V. Gratchev[125], P.M. Gravila[28f], C. Gray[56],
H.M. Gray[16], Z.D. Greenwood[82,u], C. Grefe[23], K. Gregersen[81], I.M. Gregor[45], P. Grenier[145],
K. Grevtsov[5], J. Griffiths[8], A.A. Grillo[139], K. Grimm[75], S. Grinstein[13,v], Ph. Gris[37], J.-F. Grivaz[119],
S. Groh[86], E. Gross[175], J. Grosse-Knetter[57], G.C. Grossi[82], Z.J. Grout[81], A. Grummer[107], L. Guan[92],
W. Guan[176], J. Guenther[32], F. Guescini[163a], D. Guest[166], O. Gueta[155], B. Gui[113], E. Guido[53a,53b],
T. Guillemin[5], S. Guindon[32], U. Gul[56], C. Gumpert[32], J. Guo[36b], W. Guo[92], Y. Guo[36c,w], R. Gupta[43],
S. Gurbuz[20a], G. Gustavino[115], B.J. Gutelman[154], P. Gutierrez[115], N.G. Gutierrez Ortiz[81],
C. Gutschow[81], C. Guyot[138], M.P. Guzik[41a], C. Gwenlan[122], C.B. Gwilliam[77], A. Haas[112],
C. Haber[16], H.K. Hadavand[8], N. Haddad[137e], A. Hadef[88], S. Hageböck[23], M. Hagihara[164],
H. Hakobyan[180,*], M. Haleem[45], J. Haley[116], G. Halladjian[93], G.D. Hallewell[88], K. Hamacher[178],
P. Hamal[117], K. Hamano[172], A. Hamilton[147a], G.N. Hamity[141], P.G. Hamnett[45], K. Han[36c,x],
L. Han[36c], S. Han[35a,35d], K. Hanagaki[69,y], K. Hanawa[157], M. Hance[139], D.M. Handl[102], B. Haney[124],
P. Hanke[60a], J.B. Hansen[39], J.D. Hansen[39], M.C. Hansen[23], P.H. Hansen[39], K. Hara[164], A.S. Hard[176],
T. Harenberg[178], F. Hariri[119], S. Harkusha[95], P.F. Harrison[173], N.M. Hartmann[102], Y. Hasegawa[142],
A. Hasib[49], S. Hassani[138], S. Haug[18], R. Hauser[93], L. Hauswald[47], L.B. Havener[38], M. Havranek[130],
C.M. Hawkes[19], R.J. Hawkings[32], D. Hayden[93], C.P. Hays[122], J.M. Hays[79], H.S. Hayward[77],
S.J. Haywood[133], T. Heck[86], V. Hedberg[84], L. Heelan[8], S. Heer[23], K.K. Heidegger[51], S. Heim[45],
T. Heim[16], B. Heinemann[45,z], J.J. Heinrich[102], L. Heinrich[112], C. Heinz[55], J. Hejbal[129], L. Helary[32],
A. Held[171], S. Hellman[148a,148b], C. Helsens[32], R.C.W. Henderson[75], Y. Heng[176], S. Henkelmann[171],
A.M. Henriques Correia[32], S. Henrot-Versille[119], G.H. Herbert[17], H. Herde[25], V. Herget[177],
Y. Hernández Jiménez[147c], H. Herr[86], G. Herten[51], R. Hertenberger[102], L. Hervas[32], T.C. Herwig[124],
G.G. Hesketh[81], N.P. Hessey[163a], J.W. Hetherly[43], S. Higashino[69], E. Higón-Rodriguez[170],

K. Hildebrand[33], E. Hill[172], J.C. Hill[30], K.H. Hiller[45], S.J. Hillier[19], M. Hils[47], I. Hinchliffe[16],
M. Hirose[51], D. Hirschbuehl[178], B. Hiti[78], O. Hladik[129], D.R. Hlaluku[147c], X. Hoad[49], J. Hobbs[150],
N. Hod[163a], M.C. Hodgkinson[141], P. Hodgson[141], A. Hoecker[32], M.R. Hoeferkamp[107], F. Hoenig[102],
D. Hohn[23], T.R. Holmes[33], M. Holzbock[102], M. Homann[46], S. Honda[164], T. Honda[69], T.M. Hong[127],
B.H. Hooberman[169], W.H. Hopkins[118], Y. Horii[105], A.J. Horton[144], J-Y. Hostachy[58], A. Hostiuc[140],
S. Hou[153], A. Hoummada[137a], J. Howarth[87], J. Hoya[74], M. Hrabovsky[117], J. Hrdinka[32], I. Hristova[17],
J. Hrivnac[119], T. Hryn'ova[5], A. Hrynevich[96], P.J. Hsu[63], S.-C. Hsu[140], Q. Hu[27], S. Hu[36b],
Y. Huang[35a], Z. Hubacek[130], F. Hubaut[88], F. Huegging[23], T.B. Huffman[122], E.W. Hughes[38],
M. Huhtinen[32], R.F.H. Hunter[31], P. Huo[150], N. Huseynov[68,b], J. Huston[93], J. Huth[59], R. Hyneman[92],
G. Iacobucci[52], G. Iakovidis[27], I. Ibragimov[143], L. Iconomidou-Fayard[119], Z. Idrissi[137e], P. Iengo[32],
O. Igonkina[109,aa], T. Iizawa[174], Y. Ikegami[69], M. Ikeno[69], Y. Ilchenko[11,ab], D. Iliadis[156], N. Ilic[145],
F. Iltzsche[47], G. Introzzi[123a,123b], P. Ioannou[9,*], M. Iodice[136a], K. Iordanidou[38], V. Ippolito[59],
M.F. Isacson[168], N. Ishijima[120], M. Ishino[157], M. Ishitsuka[159], C. Issever[122], S. Istin[20a], F. Ito[164],
J.M. Iturbe Ponce[62a], R. Iuppa[162a,162b], H. Iwasaki[69], J.M. Izen[44], V. Izzo[106a], S. Jabbar[3], P. Jackson[1],
R.M. Jacobs[23], V. Jain[2], G. Jakel[178], K.B. Jakobi[86], K. Jakobs[51], S. Jakobsen[65], T. Jakoubek[129],
D.O. Jamin[116], D.K. Jana[82], R. Jansky[52], J. Janssen[23], M. Janus[57], P.A. Janus[41a], G. Jarlskog[84],
N. Javadov[68,b], T. Javůrek[51], M. Javurkova[51], F. Jeanneau[138], L. Jeanty[16], J. Jejelava[54a,ac],
A. Jelinskas[173], P. Jenni[51,ad], C. Jeske[173], S. Jézéquel[5], H. Ji[176], J. Jia[150], H. Jiang[67], Y. Jiang[36c],
Z. Jiang[145], S. Jiggins[81], J. Jimenez Pena[170], S. Jin[35b], A. Jinaru[28b], O. Jinnouchi[159], H. Jivan[147c],
P. Johansson[141], K.A. Johns[7], C.A. Johnson[64], W.J. Johnson[140], K. Jon-And[148a,148b], R.W.L. Jones[75],
S.D. Jones[151], S. Jones[7], T.J. Jones[77], J. Jongmanns[60a], P.M. Jorge[128a,128b], J. Jovicevic[163a], X. Ju[176],
A. Juste Rozas[13,v], A. Kaczmarska[42], M. Kado[119], H. Kagan[113], M. Kagan[145], S.J. Kahn[88], T. Kaji[174],
E. Kajomovitz[154], C.W. Kalderon[84], A. Kaluza[86], S. Kama[43], A. Kamenshchikov[132], N. Kanaya[157],
L. Kanjir[78], Y. Kano[157], V.A. Kantserov[100], J. Kanzaki[69], B. Kaplan[112], L.S. Kaplan[176], D. Kar[147c],
K. Karakostas[10], N. Karastathis[10], M.J. Kareem[163b], E. Karentzos[10], S.N. Karpov[68], Z.M. Karpova[68],
V. Kartvelishvili[75], A.N. Karyukhin[132], K. Kasahara[164], L. Kashif[176], R.D. Kass[113], A. Kastanas[149],
Y. Kataoka[157], C. Kato[157], A. Katre[52], J. Katzy[45], K. Kawade[70], K. Kawagoe[73], T. Kawamoto[157],
G. Kawamura[57], E.F. Kay[77], V.F. Kazanin[111,c], R. Keeler[172], R. Kehoe[43], J.S. Keller[31],
E. Kellermann[84], J.J. Kempster[80], J Kendrick[19], H. Keoshkerian[161], O. Kepka[129], B.P. Kerševan[78],
S. Kersten[178], R.A. Keyes[90], M. Khader[169], F. Khalil-zada[12], A. Khanov[116], A.G. Kharlamov[111,c],
T. Kharlamova[111,c], A. Khodinov[160], T.J. Khoo[52], V. Khovanskiy[99,*], E. Khramov[68], J. Khubua[54b,ae],
S. Kido[70], M. Kiehn[52], C.R. Kilby[80], H.Y. Kim[8], S.H. Kim[164], Y.K. Kim[33], N. Kimura[167a,167c],
O.M. Kind[17], B.T. King[77], D. Kirchmeier[47], J. Kirk[133], A.E. Kiryunin[103], T. Kishimoto[157],
D. Kisielewska[41a], V. Kitali[45], O. Kivernyk[5], E. Kladiva[146b], T. Klapdor-Kleingrothaus[51],
M.H. Klein[92], M. Klein[77], U. Klein[77], K. Kleinknecht[86], P. Klimek[110], A. Klimentov[27],
R. Klingenberg[46,*], T. Klingl[23], T. Klioutchnikova[32], F.F. Klitzner[102], E.-E. Kluge[60a], P. Kluit[109],
S. Kluth[103], E. Kneringer[65], E.B.F.G. Knoops[88], A. Knue[51], A. Kobayashi[157], D. Kobayashi[73],
T. Kobayashi[157], M. Kobel[47], M. Kocian[145], P. Kodys[131], T. Koffas[31], E. Koffeman[109],
N.M. Köhler[103], T. Koi[145], M. Kolb[60b], I. Koletsou[5], T. Kondo[69], N. Kondrashova[36b], K. Köneke[51],
A.C. König[108], T. Kono[69,af], R. Konoplich[112,ag], N. Konstantinidis[81], B. Konya[84], R. Kopeliansky[64],
S. Koperny[41a], K. Korcyl[42], K. Kordas[156], A. Korn[81], I. Korolkov[13], E.V. Korolkova[141],
O. Kortner[103], S. Kortner[103], T. Kosek[131], V.V. Kostyukhin[23], A. Kotwal[48], A. Koulouris[10],
A. Kourkoumeli-Charalampidi[123a,123b], C. Kourkoumelis[9], E. Kourlitis[141], V. Kouskoura[27],
A.B. Kowalewska[42], R. Kowalewski[172], T.Z. Kowalski[41a], C. Kozakai[157], W. Kozanecki[138],
A.S. Kozhin[132], V.A. Kramarenko[101], G. Kramberger[78], D. Krasnopevtsev[100], M.W. Krasny[83],
A. Krasznahorkay[32], D. Krauss[103], J.A. Kremer[41a], J. Kretzschmar[77], K. Kreutzfeldt[55], P. Krieger[161],
K. Krizka[16], K. Kroeninger[46], H. Kroha[103], J. Kroll[129], J. Kroll[124], J. Kroseberg[23], J. Krstic[14],

U. Kruchonak[68], H. Krüger[23], N. Krumnack[67], M.C. Kruse[48], T. Kubota[91], H. Kucuk[81], S. Kuday[4b],
J.T. Kuechler[178], S. Kuehn[32], A. Kugel[60a], F. Kuger[177], T. Kuhl[45], V. Kukhtin[68], R. Kukla[88],
Y. Kulchitsky[95], S. Kuleshov[34b], Y.P. Kulinich[169], M. Kuna[11], T. Kunigo[71], A. Kupco[129], T. Kupfer[46],
O. Kuprash[155], H. Kurashige[70], L.L. Kurchaninov[163a], Y.A. Kurochkin[95], M.G. Kurth[35a,35d],
E.S. Kuwertz[172], M. Kuze[159], J. Kvita[117], T. Kwan[172], A. La Rosa[103], J.L. La Rosa Navarro[26d],
L. La Rotonda[40a,40b], F. La Ruffa[40a,40b], C. Lacasta[170], F. Lacava[134a,134b], J. Lacey[45], D.P.J. Lack[87],
H. Lacker[17], D. Lacour[83], E. Ladygin[68], R. Lafaye[5], B. Laforge[83], S. Lai[57], S. Lammers[64],
W. Lampl[7], E. LanÇcon[27], U. Landgraf[51], M.P.J. Landon[79], M.C. Lanfermann[52], V.S. Lang[45],
J.C. Lange[13], R.J. Langenberg[32], A.J. Lankford[166], F. Lanni[27], K. Lantzsch[23], A. Lanza[123a],
A. Lapertosa[53a,53b], S. Laplace[83], J.F. Laporte[138], T. Lari[94a], F. Lasagni Manghi[22a,22b], M. Lassnig[32],
T.S. Lau[62a], P. Laurelli[50], W. Lavrijsen[16], A.T. Law[139], P. Laycock[77], T. Lazovich[59],
M. Lazzaroni[94a,94b], B. Le[91], O. Le Dortz[83], E. Le Guirriec[88], E.P. Le Quilleuc[138], M. LeBlanc[7],
T. LeCompte[6], F. Ledroit-Guillon[58], C.A. Lee[27], G.R. Lee[34a], S.C. Lee[153], L. Lee[59], B. Lefebvre[90],
G. Lefebvre[83], M. Lefebvre[172], F. Legger[102], C. Leggett[16], G. Lehmann Miotto[32], X. Lei[7],
W.A. Leight[45], M.A.L. Leite[26d], R. Leitner[131], D. Lellouch[175], B. Lemmer[57], K.J.C. Leney[81],
T. Lenz[23], B. Lenzi[32], R. Leone[7], S. Leone[126a], C. Leonidopoulos[49], G. Lerner[151], C. Leroy[97],
R. Les[161], A.A.J. Lesage[138], C.G. Lester[30], M. Levchenko[125], J. Levêque[5], D. Levin[92],
L.J. Levinson[175], M. Levy[19], D. Lewis[79], B. Li[36c,w], H. Li[150], L. Li[36b], Q. Li[35a,35d], Q. Li[36c], S. Li[48],
X. Li[36b], Y. Li[143], Z. Liang[35a], B. Liberti[135a], A. Liblong[161], K. Lie[62c], A. Limosani[152], C.Y. Lin[30],
K. Lin[93], S.C. Lin[182], T.H. Lin[86], R.A. Linck[64], B.E. Lindquist[150], A.E. Lionti[52], E. Lipeles[124],
A. Lipniacka[15], M. Lisovyi[60b], T.M. Liss[169,ah], A. Lister[171], A.M. Litke[139], B. Liu[67], H. Liu[92],
H. Liu[27], J.K.K. Liu[122], J. Liu[36a], J.B. Liu[36c], K. Liu[88], L. Liu[169], M. Liu[36c], Y.L. Liu[36c], Y. Liu[36c],
M. Livan[123a,123b], A. Lleres[58], J. Llorente Merino[35a], S.L. Lloyd[79], C.Y. Lo[62b], F. Lo Sterzo[43],
E.M. Lobodzinska[45], P. Loch[7], F.K. Loebinger[87], A. Loesle[51], K.M. Loew[25], T. Lohse[17],
K. Lohwasser[141], M. Lokajicek[129], B.A. Long[24], J.D. Long[169], R.E. Long[75], L. Longo[76a,76b],
K.A. Looper[113], J.A. Lopez[34b], I. Lopez Paz[13], A. Lopez Solis[83], J. Lorenz[102], N. Lorenzo Martinez[5],
M. Losada[21], P.J. Lösel[102], X. Lou[35a], A. Lounis[119], J. Love[6], P.A. Love[75], H. Lu[62a], N. Lu[92],
Y.J. Lu[63], H.J. Lubatti[140], C. Luci[134a,134b], A. Lucotte[58], C. Luedtke[51], F. Luehring[64], W. Lukas[65],
L. Luminari[134a], B. Lund-Jensen[149], M.S. Lutz[89], P.M. Luzi[83], D. Lynn[27], R. Lysak[129], E. Lytken[84],
F. Lyu[35a], V. Lyubushkin[68], H. Ma[27], L.L. Ma[36a], Y. Ma[36a], G. Maccarrone[50], A. Macchiolo[103],
C.M. Macdonald[141], B. Maček[78], J. Machado Miguens[124,128b], D. Madaffari[170], R. Madar[37],
W.F. Mader[47], A. Madsen[45], N. Madysa[47], J. Maeda[70], S. Maeland[15], T. Maeno[27], A.S. Maevskiy[101],
V. Magerl[51], C. Maiani[119], C. Maidantchik[26a], T. Maier[102], A. Maio[128a,128b,128d], O. Majersky[146a],
S. Majewski[118], Y. Makida[69], N. Makovec[119], B. Malaescu[83], Pa. Malecki[42], V.P. Maleev[125],
F. Malek[58], U. Mallik[66], D. Malon[6], C. Malone[30], S. Maltezos[10], S. Malyukov[32], J. Mamuzic[170],
G. Mancini[50], I. Mandić[78], J. Maneira[128a,128b], L. Manhaes de Andrade Filho[26b],
J. Manjarres Ramos[47], K.H. Mankinen[84], A. Mann[102], A. Manousos[32], B. Mansoulie[138],
J.D. Mansour[35a], R. Mantifel[90], M. Mantoani[57], S. Manzoni[94a,94b], L. Mapelli[32], G. Marceca[29],
L. March[52], L. Marchese[122], G. Marchiori[83], M. Marcisovsky[129], C.A. Marin Tobon[32],
M. Marjanovic[37], D.E. Marley[92], F. Marroquim[26a], S.P. Marsden[87], Z. Marshall[16],
M.U.F Martensson[168], S. Marti-Garcia[170], C.B. Martin[113], T.A. Martin[173], V.J. Martin[49],
B. Martin dit Latour[15], M. Martinez[13,v], V.I. Martinez Outschoorn[169], S. Martin-Haugh[133],
V.S. Martoiu[28b], A.C. Martyniuk[81], A. Marzin[32], L. Masetti[86], T. Mashimo[157], R. Mashinistov[98],
J. Masik[87], A.L. Maslennikov[111,c], L.H. Mason[91], L. Massa[135a,135b], P. Mastrandrea[5],
A. Mastroberardino[40a,40b], T. Masubuchi[157], P. Mättig[178], J. Maurer[28b], S.J. Maxfield[77],
D.A. Maximov[111,c], R. Mazini[153], I. Maznas[156], S.M. Mazza[94a,94b], N.C. Mc Fadden[107],
G. Mc Goldrick[161], S.P. Mc Kee[92], A. McCarn[92], R.L. McCarthy[150], T.G. McCarthy[103],

124

L.I. McClymont[81], E.F. McDonald[91], J.A. Mcfayden[32], G. Mchedlidze[57], S.J. McMahon[133],
P.C. McNamara[91], C.J. McNicol[173], R.A. McPherson[172,o], Z.A. Meadows[89], S. Meehan[140],
T.J. Megy[51], S. Mehlhase[102], A. Mehta[77], T. Meideck[58], K. Meier[60a], B. Meirose[44], D. Melini[170,ai],
B.R. Mellado Garcia[147c], J.D. Mellenthin[57], M. Melo[146a], F. Meloni[18], A. Melzer[23], S.B. Menary[87],
L. Meng[77], X.T. Meng[92], A. Mengarelli[22a,22b], S. Menke[103], E. Meoni[40a,40b], S. Mergelmeyer[17],
C. Merlassino[18], P. Mermod[52], L. Merola[106a,106b], C. Meroni[94a], F.S. Merritt[33], A. Messina[134a,134b],
J. Metcalfe[6], A.S. Mete[166], C. Meyer[124], J-P. Meyer[138], J. Meyer[109], H. Meyer Zu Theenhausen[60a],
F. Miano[151], R.P. Middleton[133], S. Miglioranzi[53a,53b], L. Mijović[49], G. Mikenberg[175],
M. Mikestikova[129], M. Mikuž[78], M. Milesi[91], A. Milic[161], D.A. Millar[79], D.W. Miller[33], A. Milov[175],
D.A. Milstead[148a,148b], A.A. Minaenko[132], Y. Minami[157], I.A. Minashvili[54b], A.I. Mincer[112],
B. Mindur[41a], M. Mineev[68], Y. Minegishi[157], Y. Ming[176], L.M. Mir[13], A. Mirto[76a,76b], K.P. Mistry[124],
T. Mitani[174], J. Mitrevski[102], V.A. Mitsou[170], A. Miucci[18], P.S. Miyagawa[141], A. Mizukami[69],
J.U. Mjörnmark[84], T. Mkrtchyan[180], M. Mlynarikova[131], T. Moa[148a,148b], K. Mochizuki[97], P. Mogg[51],
S. Mohapatra[38], S. Molander[148a,148b], R. Moles-Valls[23], M.C. Mondragon[93], K. Mönig[45], J. Monk[39],
E. Monnier[88], A. Montalbano[150], J. Montejo Berlingen[32], F. Monticelli[74], S. Monzani[94a],
R.W. Moore[3], N. Morange[119], D. Moreno[21], M. Moreno Llácer[32], P. Morettini[53a],
M. Morgenstern[109], S. Morgenstern[32], D. Mori[144], T. Mori[157], M. Morii[59], M. Morinaga[174],
V. Morisbak[121], A.K. Morley[32], G. Mornacchi[32], J.D. Morris[79], L. Morvaj[150], P. Moschovakos[10],
M. Mosidze[54b], H.J. Moss[141], J. Moss[145,aj], K. Motohashi[159], R. Mount[145], E. Mountricha[27],
E.J.W. Moyse[89], S. Muanza[88], F. Mueller[103], J. Mueller[127], R.S.P. Mueller[102], D. Muenstermann[75],
P. Mullen[56], G.A. Mullier[18], F.J. Munoz Sanchez[87], W.J. Murray[173,133], H. Musheghyan[32],
M. Muškinja[78], C. Mwewa[147a], A.G. Myagkov[132,ak], J. Myers[118], M. Myska[130], B.P. Nachman[16],
O. Nackenhorst[46], K. Nagai[122], R. Nagai[69,af], K. Nagano[69], Y. Nagasaka[61], K. Nagata[164],
M. Nagel[51], E. Nagy[88], A.M. Nairz[32], Y. Nakahama[105], K. Nakamura[69], T. Nakamura[157],
I. Nakano[114], R.F. Naranjo Garcia[45], R. Narayan[11], D.I. Narrias Villar[60a], I. Naryshkin[125],
T. Naumann[45], G. Navarro[21], R. Nayyar[7], H.A. Neal[92], P.Yu. Nechaeva[98], T.J. Neep[138],
A. Negri[123a,123b], M. Negrini[22a], S. Nektarijevic[108], C. Nellist[57], A. Nelson[166], M.E. Nelson[122],
S. Nemecek[129], P. Nemethy[112], M. Nessi[32,al], M.S. Neubauer[169], M. Neumann[178], P.R. Newman[19],
T.Y. Ng[62c], Y.S. Ng[17], T. Nguyen Manh[97], R.B. Nickerson[122], R. Nicolaidou[138], J. Nielsen[139],
N. Nikiforou[11], V. Nikolaenko[132,ak], I. Nikolic-Audit[83], K. Nikolopoulos[19], P. Nilsson[27],
Y. Ninomiya[69], A. Nisati[134a], N. Nishu[36b], R. Nisius[103], I. Nitsche[46], T. Nitta[174], T. Nobe[157],
Y. Noguchi[71], M. Nomachi[120], I. Nomidis[31], M.A. Nomura[27], T. Nooney[79], M. Nordberg[32],
N. Norjoharuddeen[122], O. Novgorodova[47], R. Novotny[130], M. Nozaki[69], L. Nozka[117], K. Ntekas[166],
E. Nurse[81], F. Nuti[91], K. O'connor[25], D.C. O'Neil[144], A.A. O'Rourke[45], V. O'Shea[56],
F.G. Oakham[31,d], H. Oberlack[103], T. Obermann[23], J. Ocariz[83], A. Ochi[70], I. Ochoa[38],
J.P. Ochoa-Ricoux[34a], S. Oda[73], S. Odaka[69], A. Oh[87], S.H. Oh[48], C.C. Ohm[149], H. Ohman[168],
H. Oide[53a,53b], H. Okawa[164], Y. Okumura[157], T. Okuyama[69], A. Olariu[28b], L.F. Oleiro Seabra[128a],
S.A. Olivares Pino[34a], D. Oliveira Damazio[27], J.L. Oliver[1], M.J.R. Olsson[33], A. Olszewski[42],
J. Olszowska[42], A. Onofre[128a,128e], K. Onogi[105], P.U.E. Onyisi[11,ab], H. Oppen[121], M.J. Oreglia[33],
Y. Oren[155], D. Orestano[136a,136b], E.C. Orgill[87], N. Orlando[62b], R.S. Orr[161], B. Osculati[53a,53b,*],
R. Ospanov[36c], G. Otero y Garzon[29], H. Otono[73], M. Ouchrif[137d], F. Ould-Saada[121], A. Ouraou[138],
K.P. Oussoren[109], Q. Ouyang[35a], M. Owen[56], R.E. Owen[19], V.E. Ozcan[20a], N. Ozturk[8], K. Pachal[144],
A. Pacheco Pages[13], L. Pacheco Rodriguez[138], C. Padilla Aranda[13], S. Pagan Griso[16],
M. Paganini[179], F. Paige[27], G. Palacino[64], S. Palazzo[40a,40b], S. Palestini[32], M. Palka[41b], D. Pallin[37],
E.St. Panagiotopoulou[10], I. Panagoulias[10], C.E. Pandini[52], J.G. Panduro Vazquez[80], P. Pani[32],
S. Panitkin[27], D. Pantea[28b], L. Paolozzi[52], Th.D. Papadopoulou[10], K. Papageorgiou[9,s],
A. Paramonov[6], D. Paredes Hernandez[179], T.H. Park[31], A.J. Parker[75], M.A. Parker[30], K.A. Parker[45],

F. Parodi[53a,53b], J.A. Parsons[38], U. Parzefall[51], V.R. Pascuzzi[161], J.M. Pasner[139], E. Pasqualucci[134a],
S. Passaggio[53a], Fr. Pastore[80], S. Pataraia[86], J.R. Pater[87], T. Pauly[32], B. Pearson[103],
S. Pedraza Lopez[170], R. Pedro[128a,128b], S.V. Peleganchuk[111,c], O. Penc[129], C. Peng[35a,35d], H. Peng[36c],
J. Penwell[64], B.S. Peralva[26b], M.M. Perego[138], D.V. Perepelitsa[27], F. Peri[17], L. Perini[94a,94b],
H. Pernegger[32], S. Perrella[106a,106b], R. Peschke[45], V.D. Peshekhonov[68,∗], K. Peters[45], R.F.Y. Peters[87],
B.A. Petersen[32], T.C. Petersen[39], E. Petit[58], A. Petridis[1], C. Petridou[156], P. Petroff[119], E. Petrolo[134a],
M. Petrov[122], F. Petrucci[136a,136b], N.E. Pettersson[89], A. Peyaud[138], R. Pezoa[34b], T. Pham[91],
F.H. Phillips[93], P.W. Phillips[133], G. Piacquadio[150], E. Pianori[173], A. Picazio[89], M.A. Pickering[122],
R. Piegaia[29], J.E. Pilcher[33], A.D. Pilkington[87], M. Pinamonti[135a,135b], J.L. Pinfold[3], H. Pirumov[45],
M. Pitt[175], L. Plazak[146a], M.-A. Pleier[27], V. Pleskot[86], E. Plotnikova[68], D. Pluth[67], P. Podberezko[111],
R. Poettgen[84], R. Poggi[123a,123b], L. Poggioli[119], I. Pogrebnyak[93], D. Pohl[23], I. Pokharel[57],
G. Polesello[123a], A. Poley[45], A. Policicchio[40a,40b], R. Polifka[32], A. Polini[22a], C.S. Pollard[45],
V. Polychronakos[27], K. Pommès[32], D. Ponomarenko[100], L. Pontecorvo[134a], G.A. Popeneciu[28d],
D.M. Portillo Quintero[83], S. Pospisil[130], K. Potamianos[45], I.N. Potrap[68], C.J. Potter[30], H. Potti[11],
T. Poulsen[84], J. Poveda[32], M.E. Pozo Astigarraga[32], P. Pralavorio[88], A. Pranko[16], S. Prell[67],
D. Price[87], M. Primavera[76a], S. Prince[90], N. Proklova[100], K. Prokofiev[62c], F. Prokoshin[34b],
S. Protopopescu[27], J. Proudfoot[6], M. Przybycien[41a], A. Puri[169], P. Puzo[119], J. Qian[92], Y. Qin[87],
A. Quadt[57], M. Queitsch-Maitland[45], D. Quilty[56], S. Raddum[121], V. Radeka[27], V. Radescu[122],
S.K. Radhakrishnan[150], P. Radloff[118], P. Rados[91], F. Ragusa[94a,94b], G. Rahal[181], J.A. Raine[87],
S. Rajagopalan[27], T. Rashid[119], S. Raspopov[5], M.G. Ratti[94a,94b], D.M. Rauch[45], F. Rauscher[102],
S. Rave[86], I. Ravinovich[175], J.H. Rawling[87], M. Raymond[32], A.L. Read[121], N.P. Readioff[58],
M. Reale[76a,76b], D.M. Rebuzzi[123a,123b], A. Redelbach[177], G. Redlinger[27], R. Reece[139], R.G. Reed[147c],
K. Reeves[44], L. Rehnisch[17], J. Reichert[124], A. Reiss[86], C. Rembser[32], H. Ren[35a,35d], M. Rescigno[134a],
S. Resconi[94a], E.D. Resseguie[124], S. Rettie[171], E. Reynolds[19], O.L. Rezanova[111,c], P. Reznicek[131],
R. Rezvani[97], R. Richter[103], S. Richter[81], E. Richter-Was[41b], O. Ricken[23], M. Ridel[83], P. Rieck[103],
C.J. Riegel[178], J. Rieger[57], O. Rifki[115], M. Rijssenbeek[150], A. Rimoldi[123a,123b], M. Rimoldi[18],
L. Rinaldi[22a], G. Ripellino[149], B. Ristić[32], E. Ritsch[32], I. Riu[13], F. Rizatdinova[116], E. Rizvi[79],
C. Rizzi[13], R.T. Roberts[87], S.H. Robertson[90,o], A. Robichaud-Veronneau[90], D. Robinson[30],
J.E.M. Robinson[45], A. Robson[56], E. Rocco[86], C. Roda[126a,126b], Y. Rodina[88,am],
S. Rodriguez Bosca[170], A. Rodriguez Perez[13], D. Rodriguez Rodriguez[170], A.M. Rodríguez Vera[163b],
S. Roe[32], C.S. Rogan[59], O. Røhne[121], J. Roloff[59], A. Romaniouk[100], M. Romano[22a,22b],
S.M. Romano Saez[37], E. Romero Adam[170], N. Rompotis[77], M. Ronzani[51], L. Roos[83], S. Rosati[134a],
K. Rosbach[51], P. Rose[139], N.-A. Rosien[57], E. Rossi[106a,106b], L.P. Rossi[53a], J.H.N. Rosten[30],
R. Rosten[140], M. Rotaru[28b], J. Rothberg[140], D. Rousseau[119], D. Roy[147c], A. Rozanov[88], Y. Rozen[154],
X. Ruan[147c], F. Rubbo[145], F. Rühr[51], A. Ruiz-Martinez[31], Z. Rurikova[51], N.A. Rusakovich[68],
H.L. Russell[90], J.P. Rutherfoord[7], N. Ruthmann[32], E.M. Rüttinger[45], Y.F. Ryabov[125], M. Rybar[169],
G. Rybkin[119], S. Ryu[6], A. Ryzhov[132], G.F. Rzehorz[57], A.F. Saavedra[152], G. Sabato[109], S. Sacerdoti[29],
H.F-W. Sadrozinski[139], R. Sadykov[68], F. Safai Tehrani[134a], P. Saha[110], M. Sahinsoy[60a],
M. Saimpert[45], M. Saito[157], T. Saito[157], H. Sakamoto[157], Y. Sakurai[174], G. Salamanna[136a,136b],
J.E. Salazar Loyola[34b], D. Salek[109], P.H. Sales De Bruin[168], D. Salihagic[103], A. Salnikov[145],
J. Salt[170], D. Salvatore[40a,40b], F. Salvatore[151], A. Salvucci[62a,62b,62c], A. Salzburger[32], D. Sammel[51],
D. Sampsonidis[156], D. Sampsonidou[156], J. Sánchez[170], A. Sanchez Pineda[167a,167c], H. Sandaker[121],
R.L. Sandbach[79], C.O. Sander[45], M. Sandhoff[178], C. Sandoval[21], D.P.C. Sankey[133],
M. Sannino[53a,53b], Y. Sano[105], A. Sansoni[50], C. Santoni[37], H. Santos[128a], I. Santoyo Castillo[151],
A. Sapronov[68], J.G. Saraiva[128a,128d], O. Sasaki[69], K. Sato[164], E. Sauvan[5], G. Savage[80], P. Savard[161,d],
N. Savic[103], C. Sawyer[133], L. Sawyer[82,u], C. Sbarra[22a], A. Sbrizzi[22a,22b], T. Scanlon[81],
D.A. Scannicchio[166], J. Schaarschmidt[140], P. Schacht[103], B.M. Schachtner[102], D. Schaefer[33],

L. Schaefer[124], J. Schaeffer[86], S. Schaepe[32], U. Schäfer[86], A.C. Schaffer[119], D. Schaile[102], R.D. Schamberger[150], V.A. Schegelsky[125], D. Scheirich[131], F. Schenck[17], M. Schernau[166], C. Schiavi[53a,53b], S. Schier[139], L.K. Schildgen[23], C. Schillo[51], E.J. Schioppa[32], M. Schioppa[40a,40b], S. Schlenker[32], K.R. Schmidt-Sommerfeld[103], K. Schmieden[32], C. Schmitt[86], S. Schmitt[45], S. Schmitz[86], U. Schnoor[51], L. Schoeffel[138], A. Schoening[60b], B.D. Schoenrock[93], E. Schopf[23], M. Schott[86], J.F.P. Schouwenberg[108], J. Schovancova[32], S. Schramm[52], N. Schuh[86], A. Schulte[86], M.J. Schultens[23], H.-C. Schultz-Coulon[60a], M. Schumacher[51], B.A. Schumm[139], Ph. Schune[138], A. Schwartzman[145], T.A. Schwarz[92], H. Schweiger[87], Ph. Schwemling[138], R. Schwienhorst[93], J. Schwindling[138], A. Sciandra[23], G. Sciolla[25], M. Scornajenghi[40a,40b], F. Scuri[126a], F. Scutti[91], J. Searcy[92], P. Seema[23], S.C. Seidel[107], A. Seiden[139], J.M. Seixas[26a], G. Sekhniaidze[106a], K. Sekhon[92], S.J. Sekula[43], N. Semprini-Cesari[22a,22b], S. Senkin[37], C. Serfon[121], L. Serin[119], L. Serkin[167a,167b], M. Sessa[136a,136b], R. Seuster[172], H. Severini[115], T. Šfiligoj[78], F. Sforza[165], A. Sfyrla[52], E. Shabalina[57], N.W. Shaikh[148a,148b], L.Y. Shan[35a], R. Shang[169], J.T. Shank[24], M. Shapiro[16], P.B. Shatalov[99], K. Shaw[167a,167b], S.M. Shaw[87], A. Shcherbakova[148a,148b], C.Y. Shehu[151], Y. Shen[115], N. Sherafati[31], A.D. Sherman[24], P. Sherwood[81], L. Shi[153,an], S. Shimizu[70], C.O. Shimmin[179], M. Shimojima[104], I.P.J. Shipsey[122], S. Shirabe[73], M. Shiyakova[68,ao], J. Shlomi[175], A. Shmeleva[98], D. Shoaleh Saadi[97], M.J. Shochet[33], S. Shojaii[94a,94b], D.R. Shope[115], S. Shrestha[113], E. Shulga[100], M.A. Shupe[7], P. Sicho[129], A.M. Sickles[169], P.E. Sidebo[149], E. Sideras Haddad[147c], O. Sidiropoulou[177], A. Sidoti[22a,22b], F. Siegert[47], Dj. Sijacki[14], J. Silva[128a,128d], M. Silva Jr.[176], S.B. Silverstein[148a], V. Simak[130], L. Simic[68], S. Simion[119], E. Simioni[86], B. Simmons[81], M. Simon[86], P. Sinervo[161], N.B. Sinev[118], M. Sioli[22a,22b], G. Siragusa[177], I. Siral[92], S.Yu. Sivoklokov[101], J. Sjölin[148a,148b], M.B. Skinner[75], P. Skubic[115], M. Slater[19], T. Slavicek[130], M. Slawinska[42], K. Sliwa[165], R. Slovak[131], V. Smakhtin[175], B.H. Smart[5], J. Smiesko[146a], N. Smirnov[100], S.Yu. Smirnov[100], Y. Smirnov[100], L.N. Smirnova[101,ap], O. Smirnova[84], J.W. Smith[57], M.N.K. Smith[38], R.W. Smith[38], M. Smizanska[75], K. Smolek[130], A.A. Snesarev[98], I.M. Snyder[118], S. Snyder[27], R. Sobie[172,o], F. Socher[47], A.M. Soffa[166], A. Soffer[155], A. Søgaard[49], D.A. Soh[153], G. Sokhrannyi[78], C.A. Solans Sanchez[32], M. Solar[130], E.Yu. Soldatov[100], U. Soldevila[170], A.A. Solodkov[132], A. Soloshenko[68], O.V. Solovyanov[132], V. Solovyev[125], P. Sommer[141], H. Son[165], W. Song[133], A. Sopczak[130], D. Sosa[60b], C.L. Sotiropoulou[126a,126b], S. Sottocornola[123a,123b], R. Soualah[167a,167c], A.M. Soukharev[111,c], D. South[45], B.C. Sowden[80], S. Spagnolo[76a,76b], M. Spalla[126a,126b], M. Spangenberg[173], F. Spanò[80], D. Sperlich[17], F. Spettel[103], T.M. Spieker[60a], R. Spighi[22a], G. Spigo[32], L.A. Spiller[91], M. Spousta[131], R.D. St. Denis[56,*], A. Stabile[94a,94b], R. Stamen[60a], S. Stamm[17], E. Stanecka[42], R.W. Stanek[6], C. Stanescu[136a], M.M. Stanitzki[45], B.S. Stapf[109], S. Stapnes[121], E.A. Starchenko[132], G.H. Stark[33], J. Stark[58], S.H Stark[39], P. Staroba[129], P. Starovoitov[60a], S. Stärz[32], R. Staszewski[42], M. Stegler[45], P. Steinberg[27], B. Stelzer[144], H.J. Stelzer[32], O. Stelzer-Chilton[163a], H. Stenzel[55], T.J. Stevenson[79], G.A. Stewart[56], M.C. Stockton[118], M. Stoebe[90], G. Stoicea[28b], P. Stolte[57], S. Stonjek[103], A.R. Stradling[8], A. Straessner[47], M.E. Stramaglia[18], J. Strandberg[149], S. Strandberg[148a,148b], M. Strauss[115], P. Strizenec[146b], R. Ströhmer[177], D.M. Strom[118], R. Stroynowski[43], A. Strubig[49], S.A. Stucci[27], B. Stugu[15], N.A. Styles[45], D. Su[145], J. Su[127], S. Suchek[60a], Y. Sugaya[120], M. Suk[130], V.V. Sulin[98], DMS Sultan[52], S. Sultansoy[4c], T. Sumida[71], S. Sun[59], X. Sun[3], K. Suruliz[151], C.J.E. Suster[152], M.R. Sutton[151], S. Suzuki[69], M. Svatos[129], M. Swiatlowski[33], S.P. Swift[2], A. Sydorenko[86], I. Sykora[146a], T. Sykora[131], D. Ta[51], K. Tackmann[45], J. Taenzer[155], A. Taffard[166], R. Tafirout[163a], E. Tahirovic[79], N. Taiblum[155], H. Takai[27], R. Takashima[72], E.H. Takasugi[103], K. Takeda[70], T. Takeshita[142], Y. Takubo[69], M. Talby[88], A.A. Talyshev[111,c], J. Tanaka[157], M. Tanaka[159], R. Tanaka[119], R. Tanioka[70], B.B. Tannenwald[113], S. Tapia Araya[34b], S. Tapprogge[86], A.T. Tarek Abouelfadl Mohamed[83], S. Tarem[154], G.F. Tartarelli[94a], P. Tas[131], M. Tasevsky[129],

T. Tashiro[71], E. Tassi[40a,40b], A. Tavares Delgado[128a,128b], Y. Tayalati[137e], A.C. Taylor[107],
A.J. Taylor[49], G.N. Taylor[91], P.T.E. Taylor[91], W. Taylor[163b], P. Teixeira-Dias[80], D. Temple[144],
H. Ten Kate[32], P.K. Teng[153], J.J. Teoh[120], F. Tepel[178], S. Terada[69], K. Terashi[157], J. Terron[85],
S. Terzo[13], M. Testa[50], R.J. Teuscher[161,o], S.J. Thais[179], T. Theveneaux-Pelzer[88], F. Thiele[39],
J.P. Thomas[19], J. Thomas-Wilsker[80], P.D. Thompson[19], A.S. Thompson[56], L.A. Thomsen[179],
E. Thomson[124], Y. Tian[38], R.E. Ticse Torres[57], V.O. Tikhomirov[98,aq], Yu.A. Tikhonov[111,c],
S. Timoshenko[100], P. Tipton[179], S. Tisserant[88], K. Todome[159], S. Todorova-Nova[5], S. Todt[47],
J. Tojo[73], S. Tokár[146a], K. Tokushuku[69], E. Tolley[113], L. Tomlinson[87], M. Tomoto[105],
L. Tompkins[145,ar], K. Toms[107], B. Tong[59], P. Tornambe[51], E. Torrence[118], H. Torres[47],
E. Torró Pastor[140], J. Toth[88,as], F. Touchard[88], D.R. Tovey[141], C.J. Treado[112], T. Trefzger[177],
F. Tresoldi[151], A. Tricoli[27], I.M. Trigger[163a], S. Trincaz-Duvoid[83], M.F. Tripiana[13], W. Trischuk[161],
B. Trocmé[58], A. Trofymov[45], C. Troncon[94a], M. Trovatelli[172], L. Truong[147b], M. Trzebinski[42],
A. Trzupek[42], K.W. Tsang[62a], J.C-L. Tseng[122], P.V. Tsiareshka[95], N. Tsirintanis[9], S. Tsiskaridze[13],
V. Tsiskaridze[51], E.G. Tskhadadze[54a], I.I. Tsukerman[99], V. Tsulaia[16], S. Tsuno[69], D. Tsybychev[150],
Y. Tu[62b], A. Tudorache[28b], V. Tudorache[28b], T.T. Tulbure[28a], A.N. Tuna[59], S. Turchikhin[68],
D. Turgeman[175], I. Turk Cakir[4b,at], R. Turra[94a], P.M. Tuts[38], G. Ucchielli[22a,22b], I. Ueda[69],
M. Ughetto[148a,148b], F. Ukegawa[164], G. Unal[32], A. Undrus[27], G. Unel[166], F.C. Ungaro[91], Y. Unno[69],
K. Uno[157], J. Urban[146b], P. Urquijo[91], P. Urrejola[86], G. Usai[8], J. Usui[69], L. Vacavant[88], V. Vacek[130],
B. Vachon[90], K.O.H. Vadla[121], A. Vaidya[81], C. Valderanis[102], E. Valdes Santurio[148a,148b],
M. Valente[52], S. Valentinetti[22a,22b], A. Valero[170], L. Valéry[13], A. Vallier[5], J.A. Valls Ferrer[170],
W. Van Den Wollenberg[109], H. van der Graaf[109], P. van Gemmeren[6], J. Van Nieuwkoop[144],
I. van Vulpen[109], M.C. van Woerden[109], M. Vanadia[135a,135b], W. Vandelli[32], A. Vaniachine[160],
P. Vankov[109], G. Vardanyan[180], R. Vari[134a], E.W. Varnes[7], C. Varni[53a,53b], T. Varol[43],
D. Varouchas[119], A. Vartapetian[8], K.E. Varvell[152], J.G. Vasquez[179], G.A. Vasquez[34b], F. Vazeille[37],
D. Vazquez Furelos[13], T. Vazquez Schroeder[90], J. Veatch[57], V. Veeraraghavan[7], L.M. Veloce[161],
F. Veloso[128a,128c], S. Veneziano[134a], A. Ventura[76a,76b], M. Venturi[172], N. Venturi[32], V. Vercesi[123a],
M. Verducci[136a,136b], W. Verkerke[109], A.T. Vermeulen[109], J.C. Vermeulen[109], M.C. Vetterli[144,d],
N. Viaux Maira[34b], O. Viazlo[84], I. Vichou[169,*], T. Vickey[141], O.E. Vickey Boeriu[141],
G.H.A. Viehhauser[122], S. Viel[16], L. Vigani[122], M. Villa[22a,22b], M. Villaplana Perez[94a,94b],
E. Vilucchi[50], M.G. Vincter[31], V.B. Vinogradov[68], A. Vishwakarma[45], C. Vittori[22a,22b],
I. Vivarelli[151], S. Vlachos[10], M. Vogel[178], P. Vokac[130], G. Volpi[13], S.E. von Buddenbrock[147c],
H. von der Schmitt[103], E. von Toerne[23], V. Vorobel[131], K. Vorobev[100], M. Vos[170], R. Voss[32],
J.H. Vossebeld[77], N. Vranjes[14], M. Vranjes Milosavljevic[14], V. Vrba[130], M. Vreeswijk[109],
R. Vuillermet[32], I. Vukotic[33], P. Wagner[23], W. Wagner[178], J. Wagner-Kuhr[102], H. Wahlberg[74],
S. Wahrmund[47], K. Wakamiya[70], J. Walder[75], R. Walker[102], W. Walkowiak[143], V. Wallangen[148a,148b],
A.M. Wang[59], C. Wang[36a,au], F. Wang[176], H. Wang[16], H. Wang[3], J. Wang[60b], J. Wang[152],
Q. Wang[115], R.-J. Wang[83], R. Wang[6], S.M. Wang[153], T. Wang[38], W. Wang[153,av], W. Wang[36c,aw],
Z. Wang[36b], C. Wanotayaroj[45], A. Warburton[90], C.P. Ward[30], D.R. Wardrope[81], A. Washbrook[49],
P.M. Watkins[19], A.T. Watson[19], M.F. Watson[19], G. Watts[140], S. Watts[87], B.M. Waugh[81],
A.F. Webb[11], S. Webb[86], M.S. Weber[18], S.M. Weber[60a], S.A. Weber[31], J.S. Webster[6],
A.R. Weidberg[122], B. Weinert[64], J. Weingarten[57], M. Weirich[86], C. Weiser[51], P.S. Wells[32],
T. Wenaus[27], T. Wengler[32], S. Wenig[32], N. Wermes[23], M.D. Werner[67], P. Werner[32], M. Wessels[60a],
T.D. Weston[18], K. Whalen[118], N.L. Whallon[140], A.M. Wharton[75], A.S. White[92], A. White[8],
M.J. White[1], R. White[34b], D. Whiteson[166], B.W. Whitmore[75], F.J. Wickens[133], W. Wiedenmann[176],
M. Wielers[133], C. Wiglesworth[39], L.A.M. Wiik-Fuchs[51], A. Wildauer[103], F. Wilk[87], H.G. Wilkens[32],
H.H. Williams[124], S. Williams[30], C. Willis[93], S. Willocq[89], J.A. Wilson[19], I. Wingerter-Seez[5],
E. Winkels[151], F. Winklmeier[118], O.J. Winston[151], B.T. Winter[23], M. Wittgen[145], M. Wobisch[82,u],

A. Wolf[86], T.M.H. Wolf[109], R. Wolff[88], M.W. Wolter[42], H. Wolters[128a,128c], V.W.S. Wong[171], N.L. Woods[139], S.D. Worm[19], B.K. Wosiek[42], J. Wotschack[32], K.W. Wozniak[42], M. Wu[33], S.L. Wu[176], X. Wu[52], Y. Wu[92], T.R. Wyatt[87], B.M. Wynne[49], S. Xella[39], Z. Xi[92], L. Xia[35c], D. Xu[35a], L. Xu[27], T. Xu[138], W. Xu[92], B. Yabsley[152], S. Yacoob[147a], K. Yajima[120], D.P. Yallup[81], D. Yamaguchi[159], Y. Yamaguchi[159], A. Yamamoto[69], S. Yamamoto[157], T. Yamanaka[157], F. Yamane[70], M. Yamatani[157], T. Yamazaki[157], Y. Yamazaki[70], Z. Yan[24], H. Yang[36b], H. Yang[16], S. Yang[66], Y. Yang[153], Z. Yang[15], W-M. Yao[16], Y.C. Yap[45], Y. Yasu[69], E. Yatsenko[5], K.H. Yau Wong[23], J. Ye[43], S. Ye[27], I. Yeletskikh[68], E. Yigitbasi[24], E. Yildirim[86], K. Yorita[174], K. Yoshihara[124], C. Young[145], C.J.S. Young[32], J. Yu[8], J. Yu[67], S.P.Y. Yuen[23], I. Yusuff[30,ax], B. Zabinski[42], G. Zacharis[10], R. Zaidan[13], A.M. Zaitsev[132,ak], N. Zakharchuk[45], J. Zalieckas[15], A. Zaman[150], S. Zambito[59], D. Zanzi[32], C. Zeitnitz[178], G. Zemaityte[122], J.C. Zeng[169], Q. Zeng[145], O. Zenin[132], T. Ženiš[146a], D. Zerwas[119], D. Zhang[36a], D. Zhang[92], F. Zhang[176], G. Zhang[36c,aw], H. Zhang[119], J. Zhang[6], L. Zhang[51], L. Zhang[36c], M. Zhang[169], P. Zhang[35b], R. Zhang[23], R. Zhang[36c,au], X. Zhang[36a], Y. Zhang[35a,35d], Z. Zhang[119], X. Zhao[43], Y. Zhao[36a,x], Z. Zhao[36c], A. Zhemchugov[68], B. Zhou[92], C. Zhou[176], L. Zhou[43], M. Zhou[35a,35d], M. Zhou[150], N. Zhou[36b], Y. Zhou[7], C.G. Zhu[36a], H. Zhu[35a], J. Zhu[92], Y. Zhu[36c], X. Zhuang[35a], K. Zhukov[98], A. Zibell[177], D. Zieminska[64], N.I. Zimine[68], S. Zimmermann[51], Z. Zinonos[103], M. Zinser[86], M. Ziolkowski[143], L. Živković[14], G. Zobernig[176], A. Zoccoli[22a,22b], R. Zou[33], M. zur Nedden[17], L. Zwalinski[32].

[1] Department of Physics, University of Adelaide, Adelaide, Australia

[2] Physics Department, SUNY Albany, Albany NY, United States of America

[3] Department of Physics, University of Alberta, Edmonton AB, Canada

[4] [(a)] Department of Physics, Ankara University, Ankara; [(b)] Istanbul Aydin University, Istanbul; [(c)] Division of Physics, TOBB University of Economics and Technology, Ankara, Turkey

[5] LAPP, CNRS/IN2P3 and Université Savoie Mont Blanc, Annecy-le-Vieux, France

[6] High Energy Physics Division, Argonne National Laboratory, Argonne IL, United States of America

[7] Department of Physics, University of Arizona, Tucson AZ, United States of America

[8] Department of Physics, The University of Texas at Arlington, Arlington TX, United States of America

[9] Physics Department, National and Kapodistrian University of Athens, Athens, Greece

[10] Physics Department, National Technical University of Athens, Zografou, Greece

[11] Department of Physics, The University of Texas at Austin, Austin TX, United States of America

[12] Institute of Physics, Azerbaijan Academy of Sciences, Baku, Azerbaijan

[13] Institut de Física d'Altes Energies (IFAE), The Barcelona Institute of Science and Technology, Barcelona, Spain

[14] Institute of Physics, University of Belgrade, Belgrade, Serbia

[15] Department for Physics and Technology, University of Bergen, Bergen, Norway

[16] Physics Division, Lawrence Berkeley National Laboratory and University of California, Berkeley CA, United States of America

[17] Department of Physics, Humboldt University, Berlin, Germany

[18] Albert Einstein Center for Fundamental Physics and Laboratory for High Energy Physics, University of Bern, Bern, Switzerland

[19] School of Physics and Astronomy, University of Birmingham, Birmingham, United Kingdom

[20] [(a)] Department of Physics, Bogazici University, Istanbul; [(b)] Department of Physics Engineering, Gaziantep University, Gaziantep; [(d)] Istanbul Bilgi University, Faculty of Engineering and Natural Sciences, Istanbul; [(e)] Bahcesehir University, Faculty of Engineering and Natural Sciences, Istanbul, Turkey

[21] Centro de Investigaciones, Universidad Antonio Narino, Bogota, Colombia

[22] [a] INFN Sezione di Bologna; [b] Dipartimento di Fisica e Astronomia, Università di Bologna, Bologna, Italy

[23] Physikalisches Institut, University of Bonn, Bonn, Germany

[24] Department of Physics, Boston University, Boston MA, United States of America

[25] Department of Physics, Brandeis University, Waltham MA, United States of America

[26] [a] Universidade Federal do Rio De Janeiro COPPE/EE/IF, Rio de Janeiro; [b] Electrical Circuits Department, Federal University of Juiz de Fora (UFJF), Juiz de Fora; [c] Federal University of Sao Joao del Rei (UFSJ), Sao Joao del Rei; [d] Instituto de Fisica, Universidade de Sao Paulo, Sao Paulo, Brazil

[27] Physics Department, Brookhaven National Laboratory, Upton NY, United States of America

[28] [a] Transilvania University of Brasov, Brasov; [b] Horia Hulubei National Institute of Physics and Nuclear Engineering, Bucharest; [c] Department of Physics, Alexandru Ioan Cuza University of Iasi, Iasi; [d] National Institute for Research and Development of Isotopic and Molecular Technologies, Physics Department, Cluj Napoca; [e] University Politehnica Bucharest, Bucharest; [f] West University in Timisoara, Timisoara, Romania

[29] Departamento de Física, Universidad de Buenos Aires, Buenos Aires, Argentina

[30] Cavendish Laboratory, University of Cambridge, Cambridge, United Kingdom

[31] Department of Physics, Carleton University, Ottawa ON, Canada

[32] CERN, Geneva, Switzerland

[33] Enrico Fermi Institute, University of Chicago, Chicago IL, United States of America

[34] [a] Departamento de Física, Pontificia Universidad Católica de Chile, Santiago; [b] Departamento de Física, Universidad Técnica Federico Santa María, Valparaíso, Chile

[35] [a] Institute of High Energy Physics, Chinese Academy of Sciences, Beijing; [b] Department of Physics, Nanjing University, Jiangsu; [c] Physics Department, Tsinghua University, Beijing 100084; [d] University of Chinese Academy of Science (UCAS), Beijing, China

[36] [a] School of Physics, Shandong University, Shandong; [b] School of Physics and Astronomy, Key Laboratory for Particle Physics, Astrophysics and Cosmology, Ministry of Education; Shanghai Key Laboratory for Particle Physics and Cosmology, Tsung-Dao Lee Institute, Shanghai Jiao Tong University; [c] Department of Modern Physics and State Key Laboratory of Particle Detection and Electronics, University of Science and Technology of China, Anhui, China

[37] Université Clermont Auvergne, CNRS/IN2P3, LPC, Clermont-Ferrand, France

[38] Nevis Laboratory, Columbia University, Irvington NY, United States of America

[39] Niels Bohr Institute, University of Copenhagen, Kobenhavn, Denmark

[40] [a] INFN Gruppo Collegato di Cosenza, Laboratori Nazionali di Frascati; [b] Dipartimento di Fisica, Università della Calabria, Rende, Italy

[41] [a] AGH University of Science and Technology, Faculty of Physics and Applied Computer Science, Krakow; [b] Marian Smoluchowski Institute of Physics, Jagiellonian University, Krakow, Poland

[42] Institute of Nuclear Physics Polish Academy of Sciences, Krakow, Poland

[43] Physics Department, Southern Methodist University, Dallas TX, United States of America

[44] Physics Department, University of Texas at Dallas, Richardson TX, United States of America

[45] DESY, Hamburg and Zeuthen, Germany

[46] Lehrstuhl für Experimentelle Physik IV, Technische Universität Dortmund, Dortmund, Germany

[47] Institut für Kern- und Teilchenphysik, Technische Universität Dresden, Dresden, Germany

[48] Department of Physics, Duke University, Durham NC, United States of America

[49] SUPA - School of Physics and Astronomy, University of Edinburgh, Edinburgh, United Kingdom

[50] INFN e Laboratori Nazionali di Frascati, Frascati, Italy

[51] Fakultät für Mathematik und Physik, Albert-Ludwigs-Universität, Freiburg, Germany

[52] Departement de Physique Nucleaire et Corpusculaire, Université de Genève, Geneva, Switzerland

[53] [a] INFN Sezione di Genova; [b] Dipartimento di Fisica, Università di Genova, Genova, Italy

[54] [a] E. Andronikashvili Institute of Physics, Iv. Javakhishvili Tbilisi State University, Tbilisi; [b] High Energy Physics Institute, Tbilisi State University, Tbilisi, Georgia

[55] II Physikalisches Institut, Justus-Liebig-Universität Giessen, Giessen, Germany

[56] SUPA - School of Physics and Astronomy, University of Glasgow, Glasgow, United Kingdom

[57] II Physikalisches Institut, Georg-August-Universität, Göttingen, Germany

[58] Laboratoire de Physique Subatomique et de Cosmologie, Université Grenoble-Alpes, CNRS/IN2P3, Grenoble, France

[59] Laboratory for Particle Physics and Cosmology, Harvard University, Cambridge MA, United States of America

[60] [a] Kirchhoff-Institut für Physik, Ruprecht-Karls-Universität Heidelberg, Heidelberg; [b] Physikalisches Institut, Ruprecht-Karls-Universität Heidelberg, Heidelberg, Germany

[61] Faculty of Applied Information Science, Hiroshima Institute of Technology, Hiroshima, Japan

[62] [a] Department of Physics, The Chinese University of Hong Kong, Shatin, N.T., Hong Kong; [b] Department of Physics, The University of Hong Kong, Hong Kong; [c] Department of Physics and Institute for Advanced Study, The Hong Kong University of Science and Technology, Clear Water Bay, Kowloon, Hong Kong, China

[63] Department of Physics, National Tsing Hua University, Hsinchu, Taiwan

[64] Department of Physics, Indiana University, Bloomington IN, United States of America

[65] Institut für Astro- und Teilchenphysik, Leopold-Franzens-Universität, Innsbruck, Austria

[66] University of Iowa, Iowa City IA, United States of America

[67] Department of Physics and Astronomy, Iowa State University, Ames IA, United States of America

[68] Joint Institute for Nuclear Research, JINR Dubna, Dubna, Russia

[69] KEK, High Energy Accelerator Research Organization, Tsukuba, Japan

[70] Graduate School of Science, Kobe University, Kobe, Japan

[71] Faculty of Science, Kyoto University, Kyoto, Japan

[72] Kyoto University of Education, Kyoto, Japan

[73] Research Center for Advanced Particle Physics and Department of Physics, Kyushu University, Fukuoka, Japan

[74] Instituto de Física La Plata, Universidad Nacional de La Plata and CONICET, La Plata, Argentina

[75] Physics Department, Lancaster University, Lancaster, United Kingdom

[76] [a] INFN Sezione di Lecce; [b] Dipartimento di Matematica e Fisica, Università del Salento, Lecce, Italy

[77] Oliver Lodge Laboratory, University of Liverpool, Liverpool, United Kingdom

[78] Department of Experimental Particle Physics, Jožef Stefan Institute and Department of Physics, University of Ljubljana, Ljubljana, Slovenia

[79] School of Physics and Astronomy, Queen Mary University of London, London, United Kingdom

[80] Department of Physics, Royal Holloway University of London, Surrey, United Kingdom

[81] Department of Physics and Astronomy, University College London, London, United Kingdom

[82] Louisiana Tech University, Ruston LA, United States of America

[83] Laboratoire de Physique Nucléaire et de Hautes Energies, UPMC and Université Paris-Diderot and CNRS/IN2P3, Paris, France

[84] Fysiska institutionen, Lunds universitet, Lund, Sweden

[85] Departamento de Fisica Teorica C-15, Universidad Autonoma de Madrid, Madrid, Spain

[86] Institut für Physik, Universität Mainz, Mainz, Germany

[87] School of Physics and Astronomy, University of Manchester, Manchester, United Kingdom

[88] CPPM, Aix-Marseille Université and CNRS/IN2P3, Marseille, France

[89] Department of Physics, University of Massachusetts, Amherst MA, United States of America

[90] Department of Physics, McGill University, Montreal QC, Canada

[91] School of Physics, University of Melbourne, Victoria, Australia

[92] Department of Physics, The University of Michigan, Ann Arbor MI, United States of America

[93] Department of Physics and Astronomy, Michigan State University, East Lansing MI, United States of America

[94] [a] INFN Sezione di Milano; [b] Dipartimento di Fisica, Università di Milano, Milano, Italy

[95] B.I. Stepanov Institute of Physics, National Academy of Sciences of Belarus, Minsk, Republic of Belarus

[96] Research Institute for Nuclear Problems of Byelorussian State University, Minsk, Republic of Belarus

[97] Group of Particle Physics, University of Montreal, Montreal QC, Canada

[98] P.N. Lebedev Physical Institute of the Russian Academy of Sciences, Moscow, Russia

[99] Institute for Theoretical and Experimental Physics (ITEP), Moscow, Russia

[100] National Research Nuclear University MEPhI, Moscow, Russia

[101] D.V. Skobeltsyn Institute of Nuclear Physics, M.V. Lomonosov Moscow State University, Moscow, Russia

[102] Fakultät für Physik, Ludwig-Maximilians-Universität München, München, Germany

[103] Max-Planck-Institut für Physik (Werner-Heisenberg-Institut), München, Germany

[104] Nagasaki Institute of Applied Science, Nagasaki, Japan

[105] Graduate School of Science and Kobayashi-Maskawa Institute, Nagoya University, Nagoya, Japan

[106] [a] INFN Sezione di Napoli; [b] Dipartimento di Fisica, Università di Napoli, Napoli, Italy

[107] Department of Physics and Astronomy, University of New Mexico, Albuquerque NM, United States of America

[108] Institute for Mathematics, Astrophysics and Particle Physics, Radboud University Nijmegen/Nikhef, Nijmegen, Netherlands

[109] Nikhef National Institute for Subatomic Physics and University of Amsterdam, Amsterdam, Netherlands

[110] Department of Physics, Northern Illinois University, DeKalb IL, United States of America

[111] Budker Institute of Nuclear Physics, SB RAS, Novosibirsk, Russia

[112] Department of Physics, New York University, New York NY, United States of America

[113] Ohio State University, Columbus OH, United States of America

[114] Faculty of Science, Okayama University, Okayama, Japan

[115] Homer L. Dodge Department of Physics and Astronomy, University of Oklahoma, Norman OK, United States of America

[116] Department of Physics, Oklahoma State University, Stillwater OK, United States of America

[117] Palacký University, RCPTM, Olomouc, Czech Republic

[118] Center for High Energy Physics, University of Oregon, Eugene OR, United States of America

[119] LAL, Univ. Paris-Sud, CNRS/IN2P3, Université Paris-Saclay, Orsay, France

[120] Graduate School of Science, Osaka University, Osaka, Japan

[121] Department of Physics, University of Oslo, Oslo, Norway

[122] Department of Physics, Oxford University, Oxford, United Kingdom

[123] [a] INFN Sezione di Pavia; [b] Dipartimento di Fisica, Università di Pavia, Pavia, Italy

[124] Department of Physics, University of Pennsylvania, Philadelphia PA, United States of America

[125] National Research Centre "Kurchatov Institute" B.P.Konstantinov Petersburg Nuclear Physics

Institute, St. Petersburg, Russia

[126] [a] INFN Sezione di Pisa; [b] Dipartimento di Fisica E. Fermi, Università di Pisa, Pisa, Italy

[127] Department of Physics and Astronomy, University of Pittsburgh, Pittsburgh PA, United States of America

[128] [a] Laboratório de InstrumentaCcão e Física Experimental de Partículas - LIP, Lisboa; [b] Faculdade de Ciências, Universidade de Lisboa, Lisboa; [c] Department of Physics, University of Coimbra, Coimbra; [d] Centro de Física Nuclear da Universidade de Lisboa, Lisboa; [e] Departamento de Fisica, Universidade do Minho, Braga; [f] Departamento de Fisica Teorica y del Cosmos, Universidad de Granada, Granada; [g] Dep Fisica and CEFITEC of Faculdade de Ciencias e Tecnologia, Universidade Nova de Lisboa, Caparica, Portugal

[129] Institute of Physics, Academy of Sciences of the Czech Republic, Praha, Czech Republic

[130] Czech Technical University in Prague, Praha, Czech Republic

[131] Charles University, Faculty of Mathematics and Physics, Prague, Czech Republic

[132] State Research Center Institute for High Energy Physics (Protvino), NRC KI, Russia

[133] Particle Physics Department, Rutherford Appleton Laboratory, Didcot, United Kingdom

[134] [a] INFN Sezione di Roma; [b] Dipartimento di Fisica, Sapienza Università di Roma, Roma, Italy

[135] [a] INFN Sezione di Roma Tor Vergata; [b] Dipartimento di Fisica, Università di Roma Tor Vergata, Roma, Italy

[136] [a] INFN Sezione di Roma Tre; [b] Dipartimento di Matematica e Fisica, Università Roma Tre, Roma, Italy

[137] [a] Faculté des Sciences Ain Chock, Réseau Universitaire de Physique des Hautes Energies - Université Hassan II, Casablanca; [b] Centre National de l'Energie des Sciences Techniques Nucleaires, Rabat; [c] Faculté des Sciences Semlalia, Université Cadi Ayyad, LPHEA-Marrakech; [d] Faculté des Sciences, Université Mohamed Premier and LPTPM, Oujda; [e] Faculté des sciences, Université Mohammed V, Rabat, Morocco

[138] DSM/IRFU (Institut de Recherches sur les Lois Fondamentales de l'Univers), CEA Saclay (Commissariat à l'Energie Atomique et aux Energies Alternatives), Gif-sur-Yvette, France

[139] Santa Cruz Institute for Particle Physics, University of California Santa Cruz, Santa Cruz CA, United States of America

[140] Department of Physics, University of Washington, Seattle WA, United States of America

[141] Department of Physics and Astronomy, University of Sheffield, Sheffield, United Kingdom

[142] Department of Physics, Shinshu University, Nagano, Japan

[143] Department Physik, Universität Siegen, Siegen, Germany

[144] Department of Physics, Simon Fraser University, Burnaby BC, Canada

[145] SLAC National Accelerator Laboratory, Stanford CA, United States of America

[146] [a] Faculty of Mathematics, Physics & Informatics, Comenius University, Bratislava; [b] Department of Subnuclear Physics, Institute of Experimental Physics of the Slovak Academy of Sciences, Kosice, Slovak Republic

[147] [a] Department of Physics, University of Cape Town, Cape Town; [b] Department of Physics, University of Johannesburg, Johannesburg; [c] School of Physics, University of the Witwatersrand, Johannesburg, South Africa

[148] [a] Department of Physics, Stockholm University; [b] The Oskar Klein Centre, Stockholm, Sweden

[149] Physics Department, Royal Institute of Technology, Stockholm, Sweden

[150] Departments of Physics & Astronomy and Chemistry, Stony Brook University, Stony Brook NY, United States of America

[151] Department of Physics and Astronomy, University of Sussex, Brighton, United Kingdom

[152] School of Physics, University of Sydney, Sydney, Australia

[153] Institute of Physics, Academia Sinica, Taipei, Taiwan

[154] Department of Physics, Technion: Israel Institute of Technology, Haifa, Israel

[155] Raymond and Beverly Sackler School of Physics and Astronomy, Tel Aviv University, Tel Aviv, Israel

[156] Department of Physics, Aristotle University of Thessaloniki, Thessaloniki, Greece

[157] International Center for Elementary Particle Physics and Department of Physics, The University of Tokyo, Tokyo, Japan

[158] Graduate School of Science and Technology, Tokyo Metropolitan University, Tokyo, Japan

[159] Department of Physics, Tokyo Institute of Technology, Tokyo, Japan

[160] Tomsk State University, Tomsk, Russia

[161] Department of Physics, University of Toronto, Toronto ON, Canada

[162] (a) INFN-TIFPA; (b) University of Trento, Trento, Italy

[163] (a) TRIUMF, Vancouver BC; (b) Department of Physics and Astronomy, York University, Toronto ON, Canada

[164] Faculty of Pure and Applied Sciences, and Center for Integrated Research in Fundamental Science and Engineering, University of Tsukuba, Tsukuba, Japan

[165] Department of Physics and Astronomy, Tufts University, Medford MA, United States of America

[166] Department of Physics and Astronomy, University of California Irvine, Irvine CA, United States of America

[167] (a) INFN Gruppo Collegato di Udine, Sezione di Trieste, Udine; (b) ICTP, Trieste; (c) Dipartimento di Chimica, Fisica e Ambiente, Università di Udine, Udine, Italy

[168] Department of Physics and Astronomy, University of Uppsala, Uppsala, Sweden

[169] Department of Physics, University of Illinois, Urbana IL, United States of America

[170] Instituto de Fisica Corpuscular (IFIC), Centro Mixto Universidad de Valencia - CSIC, Spain

[171] Department of Physics, University of British Columbia, Vancouver BC, Canada

[172] Department of Physics and Astronomy, University of Victoria, Victoria BC, Canada

[173] Department of Physics, University of Warwick, Coventry, United Kingdom

[174] Waseda University, Tokyo, Japan

[175] Department of Particle Physics, The Weizmann Institute of Science, Rehovot, Israel

[176] Department of Physics, University of Wisconsin, Madison WI, United States of America

[177] Fakultät für Physik und Astronomie, Julius-Maximilians-Universität, Würzburg, Germany

[178] Fakultät für Mathematik und Naturwissenschaften, Fachgruppe Physik, Bergische Universität Wuppertal, Wuppertal, Germany

[179] Department of Physics, Yale University, New Haven CT, United States of America

[180] Yerevan Physics Institute, Yerevan, Armenia

[181] Centre de Calcul de l'Institut National de Physique Nucléaire et de Physique des Particules (IN2P3), Villeurbanne, France

[182] Academia Sinica Grid Computing, Institute of Physics, Academia Sinica, Taipei, Taiwan

[a] Also at Department of Physics, King's College London, London, United Kingdom

[b] Also at Institute of Physics, Azerbaijan Academy of Sciences, Baku, Azerbaijan

[c] Also at Novosibirsk State University, Novosibirsk, Russia

[d] Also at TRIUMF, Vancouver BC, Canada

[e] Also at Department of Physics & Astronomy, University of Louisville, Louisville, KY, United States of America

[f] Also at Physics Department, An-Najah National University, Nablus, Palestine

[g] Also at Department of Physics, California State University, Fresno CA, United States of America

[h] Also at Department of Physics, University of Fribourg, Fribourg, Switzerland

[i] Also at II Physikalisches Institut, Georg-August-Universität, Göttingen, Germany

[j] Also at Departament de Fisica de la Universitat Autonoma de Barcelona, Barcelona, Spain

[k] Also at Departamento de Fisica e Astronomia, Faculdade de Ciencias, Universidade do Porto, Portugal

[l] Also at Tomsk State University, Tomsk, and Moscow Institute of Physics and Technology State University, Dolgoprudny, Russia

[m] Also at The Collaborative Innovation Center of Quantum Matter (CICQM), Beijing, China

[n] Also at Universita di Napoli Parthenope, Napoli, Italy

[o] Also at Institute of Particle Physics (IPP), Canada

[p] Also at Horia Hulubei National Institute of Physics and Nuclear Engineering, Bucharest, Romania

[q] Also at Department of Physics, St. Petersburg State Polytechnical University, St. Petersburg, Russia

[r] Also at Borough of Manhattan Community College, City University of New York, New York City, United States of America

[s] Also at Department of Financial and Management Engineering, University of the Aegean, Chios, Greece

[t] Also at Centre for High Performance Computing, CSIR Campus, Rosebank, Cape Town, South Africa

[u] Also at Louisiana Tech University, Ruston LA, United States of America

[v] Also at Institucio Catalana de Recerca i Estudis Avancats, ICREA, Barcelona, Spain

[w] Also at Department of Physics, The University of Michigan, Ann Arbor MI, United States of America

[x] Also at LAL, Univ. Paris-Sud, CNRS/IN2P3, Université Paris-Saclay, Orsay, France

[y] Also at Graduate School of Science, Osaka University, Osaka, Japan

[z] Also at Fakultät für Mathematik und Physik, Albert-Ludwigs-Universität, Freiburg, Germany

[aa] Also at Institute for Mathematics, Astrophysics and Particle Physics, Radboud University Nijmegen/Nikhef, Nijmegen, Netherlands

[ab] Also at Department of Physics, The University of Texas at Austin, Austin TX, United States of America

[ac] Also at Institute of Theoretical Physics, Ilia State University, Tbilisi, Georgia

[ad] Also at CERN, Geneva, Switzerland

[ae] Also at Georgian Technical University (GTU),Tbilisi, Georgia

[af] Also at Ochadai Academic Production, Ochanomizu University, Tokyo, Japan

[ag] Also at Manhattan College, New York NY, United States of America

[ah] Also at The City College of New York, New York NY, United States of America

[ai] Also at Departamento de Fisica Teorica y del Cosmos, Universidad de Granada, Granada, Portugal

[aj] Also at Department of Physics, California State University, Sacramento CA, United States of America

[ak] Also at Moscow Institute of Physics and Technology State University, Dolgoprudny, Russia

[al] Also at Departement de Physique Nucleaire et Corpusculaire, Université de Genève, Geneva, Switzerland

[am] Also at Institut de Física d'Altes Energies (IFAE), The Barcelona Institute of Science and Technology, Barcelona, Spain

[an] Also at School of Physics, Sun Yat-sen University, Guangzhou, China

[ao] Also at Institute for Nuclear Research and Nuclear Energy (INRNE) of the Bulgarian Academy of Sciences, Sofia, Bulgaria

[ap] Also at Faculty of Physics, M.V.Lomonosov Moscow State University, Moscow, Russia

[aq] Also at National Research Nuclear University MEPhI, Moscow, Russia

[ar] Also at Department of Physics, Stanford University, Stanford CA, United States of America

[as] Also at Institute for Particle and Nuclear Physics, Wigner Research Centre for Physics, Budapest, Hungary

[at] Also at Giresun University, Faculty of Engineering, Turkey

[au] Also at CPPM, Aix-Marseille Université and CNRS/IN2P3, Marseille, France

[av] Also at Department of Physics, Nanjing University, Jiangsu, China

[aw] Also at Institute of Physics, Academia Sinica, Taipei, Taiwan

[ax] Also at University of Malaya, Department of Physics, Kuala Lumpur, Malaysia

* Deceased